

UNCLASSIFIED

SECURITY CLASSIFICATION OF THIS PAGE (When Data Entered)

REPORT DOCUMENTATION PAGE		READ INSTRUCTIONS BEFORE COMPLETING FORM
1. REPORT NUMBER AFFDL-TR-78-117	2. GOVT ACCESSION NO.	3. RECIPIENT'S CATALOG NUMBER
4. TITLE (and Subtitle) PRELIMINARY DESIGN AERODYNAMIC PREDICTION METHODOLOGY FOR MISSILES WITH NOSE BLUNTNESS		5. TYPE OF REPORT & PERIOD COVERED Final Report, Apr 77 - Jun 78
7. AUTHOR(s) Charles W. Ingram Karlheinz O. W. Ball Carter Dinkeloo David Shida		6. PERFORMING ORG. REPORT NUMBER
9. PERFORMING ORGANIZATION NAME AND ADDRESS Systems Research Laboratories, Inc. 2800 Indian Ripple Road Dayton, OH 45433		8. CONTRACT OR GRANT NUMBER(s) F33615-75-D-0089/0030
11. CONTROLLING OFFICE NAME AND ADDRESS Air Force Flight Dynamics Laboratory (FGC) Wright-Patterson AF Base, OH 45433		10. PROGRAM ELEMENT, PROJECT, TASK AREA & WORK UNIT NUMBERS 2403-05-07
14. MONITORING AGENCY NAME & ADDRESS (if different from Controlling Office)		12. REPORT DATE Sep 1978
		13. NUMBER OF PAGES 181
		15. SECURITY CLASS. (of this report) Unclassified
16. DISTRIBUTION STATEMENT (of this Report) Approved for public release, distribution unlimited.		15a. DECLASSIFICATION/DOWNGRADING SCHEDULE
17. DISTRIBUTION STATEMENT (of the abstract entered in Block 20, if different from Report)		
18. SUPPLEMENTARY NOTES		
19. KEY WORDS (Continue on reverse side if necessary and identify by block number) Aerodynamic Prediction Axial Force Coefficient Normal Force Coefficient Nose Bluntness Effects Center of Pressure Missiles		
20. ABSTRACT (Continue on reverse side if necessary and identify by block number) A semi-empirical methodology is presented for predicting the axial and normal force coefficients and the center of pressure to include nose bluntness effects for missiles. This methodology includes the transonic and supersonic Mach number regime with angles of attack from 0 to 180 degrees. This methodology correlates well with wind tunnel test data.		

DD FORM 1 JAN 73 1473

EDITION OF 1 NOV 65 IS OBSOLETE

UNCLASSIFIED

SECURITY CLASSIFICATION OF THIS PAGE (When Data Entered)

Contrails

FOREWORD

This report, Preliminary Design Aerodynamic Prediction Methodology for Missiles with Nose Bluntness, was developed by Systems Research Laboratories, Inc. (SRL) under Contract No. F-33615-75-D-0089/0030 with the Air Force Flight Dynamics Laboratory, Control Dynamics Branch (AFFDL/FGC). The work reported herein was performed during the period April 1977 to June 1978.

SRL's project personnel were Dr. Charles W. Ingram, Dr. Karlheinz O. W. Ball, Mr. Carter Dinkeloo, Mr. David Shida, and Ms. Diane Dimiduk. Mr. James Jenkins was SRL's program manager. The AFFDL/FGC project engineer was Mr. William H. Lane.

Contrails

TABLE OF CONTENTS

SECTION		PAGE
I	INTRODUCTION	1
II	WIND TUNNEL DATA BASE	2
III	NOSE BLUNTNESS EFFECTS	4
	Axial Force Coefficient	4
	Normal Force Coefficient	13
	Center of Pressure	20
IV	FINNED BODY	26
	Axial Force Coefficient	26
	Normal Force Coefficient	31
	Center of Pressure	38
V	CONCLUSIONS	42
APPENDIX:	WIND TUNNEL DATA USED FOR NOSE BLUNTNESS METHODOLOGY DEVELOPMENT	43
REFERENCES		181

LIST OF ILLUSTRATIONS

FIGURE		PAGE
1	Nose Configurations from Reference 2	3
2	ΔC_{A_0} Versus Mach Number	5
3	Comparison of Prediction Methods with Wind Tunnel Data, Body-Alone	8
4A	C_{A_α} as Function of Mach Number	10
4B	C_{A_π} as Function of Mach Number	10
5	Variation of C_{N_α} with Mach Number of $\ell_A/d = 6$	15
6	Variation of C_{N_α} with Mach Number of $\ell_A/d = 8$	16
7	Variation of C_{N_α} with Mach Number of $\ell_A/d = 10$	17
8	Change in Normal Force Slope Coefficient Due to Nose Bluntness	18
9	Variation of X_0 with Mach Number for $\ell_A/d = 6$	21
10	Variation of X_0 with Mach Number for $\ell_A/d = 8$	22
11	Variation of X_0 with Mach Number for $\ell_A/d = 10$	23
12	ΔX_0 Due to Nose Bluntness	25
13	Fin Geometry for a Slender Body Model	29
14	Ten-Caliber Finned Body	29
15	Comparison Prediction Method with Wind Tunnel Data, Finned Body	32
16	Normal Force Coefficient Versus Angle of Attack for the 10-Caliber Finned Body	35
17	$C_{NT} \times R_{T(B)}$ Versus Angle of Attack for a 10-Caliber Finned Body Using Prediction Method (Reference 1)	37
18	Center of Pressure Versus Angle of Attack for 10-Caliber Finned Body	40
19	Tail Only Center of Pressure Versus Angle of Attack for 10-Caliber Finned Body	41

LIST OF ILLUSTRATIONS (CONT'D)

APPENDIX

FIGURE		PAGE
A-1	Axial Force Coefficient Versus Angle of Attack for $\ell_A/d = 6$, $M = 0.6$	45
A-2	Axial Force Coefficient Versus Angle of Attack for $\ell_A/d = 10$, $M = 0.6$	46
A-3	Axial Force Coefficient Versus Angle of Attack for $\ell_A/d = 6$, $M = 0.8$	47
A-4	Axial Force Coefficient Versus Angle of Attack for $\ell_A/d = 10$, $M = 0.8$	48
A-5	Axial Force Coefficient Versus Angle of Attack for $\ell_A/d = 6$, $M = 1.0$	49
A-6	Axial Force Coefficient Versus Angle of Attack for $\ell_A/d = 10$, $M = 1.0$	50
A-7	Axial Force Coefficient Versus Angle of Attack for $\ell_A/d = 6$, $M = 1.2$	51
A-8	Axial Force Coefficient Versus Angle of Attack for $\ell_A/d = 10$, $M = 1.2$	52
A-9	Axial Force Coefficient Versus Angle of Attack for $\ell_A/d = 6$, $M = 1.5$	53
A-10	Axial Force Coefficient Versus Angle of Attack for $\ell_A/d = 6$, $M = 1.5$	54
A-11	Axial Force Coefficient Versus Angle of Attack for $\ell_A/d = 10$, $M = 1.5$	55
A-12	Axial Force Coefficient Versus Angle of Attack for $\ell_A/d = 6$, $M = 2.0$	56
A-13	Axial Force Coefficient Versus Angle of Attack for $\ell_A/d = 8$, $M = 2.0$	57
A-14	Axial Force Coefficient Versus Angle of Attack for $\ell_A/d = 10$, $M = 2.0$	58
A-15	Axial Force Coefficient Versus Angle of Attack for $\ell_A/d = 6$, $M = 3.0$	59

LIST OF ILLUSTRATIONS (CONT'D)

APPENDIX

FIGURE		PAGE
A-16	Axial Force Coefficient Versus Angle of Attack for $l_A/d = 8$, $M = 3.0$	60
A-17	Axial Force Coefficient Versus Angle of Attack for $l_A/d = 10$, $M = 3.0$	61
A-18	Axial Force Coefficient Versus Angle of Attack for $l_A/d = 8$, $M = 4.0$	62
A-19	Axial Force Coefficient Versus Angle of Attack for $l_A/d = 10$, $M = 4.0$	63
A-20	Axial Force Coefficient Versus Nose Bluntness Ratio for $l_A/d = 6$	64
A-21	Axial Force Coefficient Versus Nose Bluntness Ratio for $l_A/d = 8$	65
A-22	Axial Force Coefficient Versus Nose Bluntness Ratio for $l_A/d = 10$	66
A-23	Normal Force Coefficient Versus Angle of Attack for $l_N/d = 2$, $l_A/d = 6$, $M = 0.6$	67
A-24	Normal Force Coefficient Versus Angle of Attack for $l_N/d = 3$, $l_A = 6$, $M = 0.6$	68
A-25	Normal Force Coefficient Versus Angle of Attack for $l_N/d = 4$, $l_A/d = 6$, $M = 0.6$	69
A-26	Normal Force Coefficient Versus Angle of Attack for $l_N/d = 2$, $l_A/d = 10$, $M = 0.6$	70
A-27	Normal Force Coefficient Versus Angle of Attack for $l_N/d = 3$, $l_A/d = 10$, $M = 0.6$	71
A-28	Normal Force Coefficient Versus Angle of Attack for $l_N/d = 4$, $l_A/d = 10$, $M = 0.6$	72
A-29	Normal Force Coefficient Versus Angle of Attack for $l_N/d = 2$, $l_A/d = 6$, $M = 0.8$	73
A-30	Normal Force Coefficient Versus Angle of Attack for $l_N/d = 3$, $l_A/d = 6$, $M = 0.8$	74

LIST OF ILLUSTRATIONS (CONT'D)

APPENDIX

FIGURE		PAGE
A-31	Normal Force Coefficient Versus Angle of Attack for $\ell_N/d = 4$, $\ell_A/d = 6$, $M = 0.8$	75
A-32	Normal Force Coefficient Versus Angle of Attack for $\ell_N/d = 2$, $\ell_A/d = 10$, $M = 0.8$	76
A-33	Normal Force Coefficient Versus Angle of Attack for $\ell_N/d = 3$, $\ell_A/d = 10$, $M = 0.8$	77
A-34	Normal Force Coefficient Versus Angle of Attack for $\ell_N/d = 4$, $\ell_A/d = 10$, $M = 0.8$	78
A-35	Normal Force Coefficient Versus Angle of Attack for $\ell_N/d = 2$, $\ell_A/d = 6$, $M = 1.0$	79
A-36	Normal Force Coefficient Versus Angle of Attack for $\ell_N/d = 3$, $\ell_A/d = 6$, $M = 1.0$	80
A-37	Normal Force Coefficient Versus Angle of Attack for $\ell_N/d = 4$, $\ell_A/d = 6$, $M = 1.0$	81
A-38	Normal Force Coefficient Versus Angle of Attack for $\ell_N/d = 2$, $\ell_A/d = 10$, $M = 1.0$	82
A-39	Normal Force Coefficient Versus Angle of Attack for $\ell_N/d = 3$, $\ell_A/d = 10$, $M = 1.0$	83
A-40	Normal Force Coefficient Versus Angle of Attack for $\ell_N/d = 4$, $\ell_A/d = 10$, $M = 1.0$	84
A-41	Normal Force Coefficient Versus Angle of Attack for $\ell_N/d = 2$, $\ell_A/d = 6$, $M = 1.2$	85
A-42	Normal Force Coefficient Versus Angle of Attack for $\ell_N/d = 3$, $\ell_A/d = 6$, $M = 1.2$	86
A-43	Normal Force Coefficient Versus Angle of Attack for $\ell_N/d = 4$, $\ell_A/d = 6$, $M = 1.2$	87
A-44	Normal Force Coefficient Versus Angle of Attack for $\ell_N/d = 2$, $\ell_A/d = 10$, $M = 1.2$	88
A-45	Normal Force Coefficient Versus Angle of Attack for $\ell_N/d = 3$, $\ell_A/d = 10$, $M = 1.2$	89

LIST OF ILLUSTRATIONS (CONT'D)

APPENDIX

FIGURE		PAGE
A-46	Normal Force Coefficient Versus Angle of Attack for $\ell_N/d = 4$, $\ell_A/d = 10$, $M = 1.2$	90
A-47	Normal Force Coefficient Versus Angle of Attack for $\ell_N/d = 2$, $\ell_A/d = 6$, $M = 1.5$	91
A-48	Normal Force Coefficient Versus Angle of Attack for $\ell_N/d = 3$, $\ell_A/d = 6$, $M = 1.5$	92
A-49	Normal Force Coefficient Versus Angle of Attack for $\ell_N/d = 4$, $\ell_A/d = 6$, $M = 1.5$	93
A-50	Normal Force Coefficient Versus Angle of Attack for $\ell_N/d = 3$, $\ell_A/d = 8$, $M = 1.5$	94
A-51	Normal Force Coefficient Versus Angle of Attack for $\ell_N/d = 2$, $\ell_A/d = 8$, $M = 1.5$	95
A-52	Normal Force Coefficient Versus Angle of Attack for $\ell_N/d = 4$, $\ell_A/d = 8$, $M = 1.5$	96
A-53	Normal Force Coefficient Versus Angle of Attack for $\ell_N/d = 2$, $\ell_A/d = 10$, $M = 1.5$	97
A-54	Normal Force Coefficient Versus Angle of Attack for $\ell_N/d = 3$, $\ell_A/d = 10$, $M = 1.5$	98
A-55	Normal Force Coefficient Versus Angle of Attack for $\ell_N/d = 4$, $\ell_A/d = 10$, $M = 1.5$	99
A-56	Normal Force Coefficient Versus Angle of Attack for $\ell_N/d = 2$, $\ell_A/d = 6$, $M = 2.0$	100
A-57	Normal Force Coefficient Versus Angle of Attack for $\ell_N/d = 3$, $\ell_A/d = 6$, $M = 2.0$	101
A-58	Normal Force Coefficient Versus Angle of Attack for $\ell_N/d = 4$, $\ell_A/d = 6$, $M = 2.0$	102
A-59	Normal Force Coefficient Versus Angle of Attack for $\ell_N/d = 2$, $\ell_A/d = 8$, $M = 2.0$	103
A-60	Normal Force Coefficient Versus Angle of Attack for $\ell_N/d = 3$, $\ell_A/d = 8$, $M = 2.0$	104

LIST OF ILLUSTRATIONS (CONT'D)

APPENDIX

FIGURE		PAGE
A-61	Normal Force Coefficient Versus Angle of Attack for $\ell_N/d = 4$, $\ell_A/d = 8$, $M = 2.0$	105
A-62	Normal Force Coefficient Versus Angle of Attack for $\ell_N/d = 2$, $\ell_A/d = 10$, $M = 2.0$	106
A-63	Normal Force Coefficient Versus Angle of Attack for $\ell_N/d = 3$, $\ell_A/d = 10$, $M = 2.0$	107
A-64	Normal Force Coefficient Versus Angle of Attack for $\ell_N/d = 4$, $\ell_A/d = 10$, $M = 2.0$	108
A-65	Normal Force Coefficient Versus Angle of Attack for $\ell_N/d = 2$, $\ell_A/d = 6$, $M = 3.0$	109
A-66	Normal Force Coefficient Versus Angle of Attack for $\ell_N/d = 3$, $\ell_A/d = 6$, $M = 3.0$	110
A-67	Normal Force Coefficient Versus Angle of Attack for $\ell_N/d = 4$, $\ell_A/d = 6$, $M = 3.0$	111
A-68	Normal Force Coefficient Versus Angle of Attack for $\ell_N/d = 2$, $\ell_A/d = 8$, $M = 3.0$	112
A-69	Normal Force Coefficient Versus Angle of Attack for $\ell_N/d = 3$, $\ell_A/d = 8$, $M = 3.0$	113
A-70	Normal Force Coefficient Versus Angle of Attack for $\ell_N/d = 4$, $\ell_A/d = 8$, $M = 3.0$	114
A-71	Normal Force Coefficient Versus Angle of Attack for $\ell_N/d = 2$, $\ell_A/d = 10$, $M = 3.0$	115
A-72	Normal Force Coefficient Versus Angle of Attack for $\ell_N/d = 3$, $\ell_A/d = 10$, $M = 3.0$	116
A-73	Normal Force Coefficient Versus Angle of Attack for $\ell_N/d = 4$, $\ell_A/d = 10$, $M = 3.0$	117
A-74	Normal Force Coefficient Versus Angle of Attack for $\ell_N/d = 2$, $\ell_A/d = 8$, $M = 4.0$	118
A-75	Normal Force Coefficient Versus Angle of Attack for $\ell_N/d = 3$, $\ell_A/d = 8$, $M = 4.0$	119

LIST OF ILLUSTRATIONS (CONT'D)

APPENDIX

FIGURE		PAGE
A-76	Normal Force Coefficient Versus Angle of Attack for $\ell_N/d = 4$, $\ell_A/d = 8$, $M = 4.0$	120
A-77	Normal Force Coefficient Versus Angle of Attack for $\ell_N/d = 2$, $\ell_A/d = 10$, $M = 4.0$	121
A-78	Normal Force Coefficient Versus Angle of Attack for $\ell_N/d = 3$, $\ell_A/d = 10$, $M = 4.0$	122
A-79	Normal Force Coefficient Versus Angle of Attack for $\ell_N/d = 4$, $\ell_A/d = 10$, $M = 4.0$	123
A-80	Center of Pressure Versus Angle of Attack for $\ell_N/d = 2$, $\ell_A/d = 6$, $M = 0.6$	124
A-81	Center of Pressure Versus Angle of Attack for $\ell_N/d = 3$, $\ell_A/d = 6$, $M = 0.6$	125
A-82	Center of Pressure Versus Angle of Attack for $\ell_N/d = 4$, $\ell_A/d = 6$, $M = 0.6$	126
A-83	Center of Pressure Versus Angle of Attack for $\ell_N/d = 2$, $\ell_A/d = 10$, $M = 0.6$	127
A-84	Center of Pressure Versus Angle of Attack for $\ell_N/d = 3$, $\ell_A/d = 10$, $M = 0.6$	128
A-85	Center of Pressure Versus Angle of Attack for $\ell_N/d = 4$, $\ell_A/d = 10$, $M = 0.6$	129
A-86	Center of Pressure Versus Angle of Attack for $\ell_N/d = 2$, $\ell_A/d = 6$, $M = 0.8$	130
A-87	Center of Pressure Versus Angle of Attack for $\ell_N/d = 3$, $\ell_A/d = 6$, $M = 0.8$	131
A-88	Center of Pressure Versus Angle of Attack for $\ell_N/d = 4$, $\ell_A/d = 6$, $M = 0.8$	132
A-89	Center of Pressure Versus Angle of Attack for $\ell_N/d = 2$, $\ell_A/d = 6$, $M = 0.8$	133
A-90	Center of Pressure Versus Angle of Attack for $\ell_N/d = 3$, $\ell_A/d = 10$, $M = 0.8$	134

LIST OF ILLUSTRATIONS (CONT'D)

APPENDIX

FIGURE		PAGE
A-91	Center of Pressure Versus Angle of Attack for $\ell_N/d = 4$, $\ell_A/d = 10$, $M = 0.8$	135
A-92	Center of Pressure Versus Angle of Attack for $\ell_N/d = 2$, $\ell_A/d = 6$, $M = 1.0$	136
A-93	Center of Pressure Versus Angle of Attack for $\ell_N/d = 3$, $\ell_A/d = 6$, $M = 1.0$	137
A-94	Center of Pressure Versus Angle of Attack for $\ell_N/d = 4$, $\ell_A/d = 6$, $M = 1.0$	138
A-95	Center of Pressure Versus Angle of Attack for $\ell_N/d = 2$, $\ell_A/d = 10$, $M = 1.0$	139
A-96	Center of Pressure Versus Angle of Attack for $\ell_N/d = 3$, $\ell_A/d = 10$, $M = 1.0$	140
A-97	Center of Pressure Versus Angle of Attack for $\ell_N/d = 4$, $\ell_A/d = 10$, $M = 1.0$	141
A-98	Center of Pressure Versus Angle of Attack for $\ell_N/d = 2$, $\ell_A/d = 6$, $M = 1.2$	142
A-99	Center of Pressure Versus Angle of Attack for $\ell_N/d = 3$, $\ell_A/d = 6$, $M = 1.2$	143
A-100	Center of Pressure Versus Angle of Attack for $\ell_N/d = 4$, $\ell_A/d = 6$, $M = 1.2$	144
A-101	Center of Pressure Versus Angle of Attack for $\ell_N/d = 2$, $\ell_A/d = 10$, $M = 1.2$	145
A-102	Center of Pressure Versus Angle of Attack for $\ell_N/d = 3$, $\ell_A/d = 10$, $M = 1.2$	146
A-103	Center of Pressure Versus Angle of Attack for $\ell_N/d = 4$, $\ell_A/d = 10$, $M = 1.2$	147
A-104	Center of Pressure Versus Angle of Attack for $\ell_N/d = 2$, $\ell_A/d = 6$, $M = 1.5$	148
A-105	Center of Pressure Versus Angle of Attack for $\ell_N/d = 3$, $\ell_A/d = 6$, $M = 1.5$	149

LIST OF ILLUSTRATIONS (CONT'D)

APPENDIX

FIGURE		PAGE
A-106	Center of Pressure Versus Angle of Attack for $\ell_N/d = 4$, $\ell_A/d = 6$, $M = 1.5$	150
A-107	Center of Pressure Versus Angle of Attack for $\ell_N/d = 2$, $\ell_A/d = 8$, $M = 1.5$	151
A-108	Center of Pressure Versus Angle of Attack for $\ell_N/d = 3$, $\ell_A/d = 8$, $M = 1.5$	152
A-109	Center of Pressure Versus Angle of Attack for $\ell_N/d = 4$, $\ell_A/d = 8$, $M = 1.5$	153
A-110	Center of Pressure Versus Angle of Attack for $\ell_N/d = 2$, $\ell_A/d = 10$, $M = 1.5$	154
A-111	Center of Pressure Versus Angle of Attack for $\ell_N/d = 3$, $\ell_A/d = 10$, $M = 1.5$	155
A-112	Center of Pressure Versus Angle of Attack for $\ell_N/d = 4$, $\ell_A/d = 10$, $M = 1.5$	156
A-113	Center of Pressure Versus Angle of Attack for $\ell_N/d = 2$, $\ell_A/d = 6$, $M = 2.0$	157
A-114	Center of Pressure Versus Angle of Attack for $\ell_N/d = 3$, $\ell_A/d = 6$, $M = 2.0$	158
A-115	Center of Pressure Versus Angle of Attack for $\ell_N/d = 4$, $\ell_A/d = 6$, $M = 2.0$	159
A-116	Center of Pressure Versus Angle of Attack for $\ell_N/d = 2$, $\ell_A/d = 8$, $M = 2.0$	160
A-117	Center of Pressure Versus Angle of Attack for $\ell_N/d = 3$, $\ell_A/d = 8$, $M = 2.0$	161
A-118	Center of Pressure Versus Angle of Attack for $\ell_N/d = 4$, $\ell_A/d = 8$, $M = 2.0$	162
A-119	Center of Pressure Versus Angle of Attack for $\ell_N/d = 2$, $\ell_A/d = 10$, $M = 2.0$	163
A-120	Center of Pressure Versus Angle of Attack for $\ell_N/d = 3$, $\ell_A/d = 10$, $M = 2.0$	164

LIST OF ILLUSTRATIONS (CONCL'D)

APPENDIX

FIGURE		PAGE
A-121	Center of Pressure Versus Angle of Attack for $l_N/d = 4$, $l_A/d = 10$, $M = 2.0$	165
A-122	Center of Pressure Versus Angle of Attack for $l_N/d = 2$, $l_A/d = 6$, $M = 3.0$	166
A-123	Center of Pressure Versus Angle of Attack for $l_N/d = 3$, $l_A/d = 6$, $M = 3.0$	167
A-124	Center of Pressure Versus Angle of Attack for $l_N/d = 4$, $l_A/d = 6$, $M = 3.0$	168
A-125	Center of Pressure Versus Angle of Attack for $l_N/d = 2$, $l_A/d = 8$, $M = 3.0$	169
A-126	Center of Pressure Versus Angle of Attack for $l_N/d = 3$, $l_A/d = 8$, $M = 3.0$	170
A-127	Center of Pressure Versus Angle of Attack for $l_N/d = 4$, $l_A/d = 8$, $M = 3.0$	171
A-128	Center of Pressure Versus Angle of Attack for $l_N/d = 2$, $l_A/d = 10$, $M = 3.0$	172
A-129	Center of Pressure Versus Angle of Attack for $l_N/d = 3$, $l_A/d = 10$, $M = 3.0$	173
A-130	Center of Pressure Versus Angle of Attack for $l_N/d = 4$, $l_A/d = 10$, $M = 3.0$	174
A-131	Center of Pressure Versus Angle of Attack for $l_N/d = 2$, $l_A/d = 8$, $M = 4.0$	175
A-132	Center of Pressure Versus Angle of Attack for $l_N/d = 3$, $l_A/d = 8$, $M = 4.0$	176
A-133	Center of Pressure Versus Angle of Attack for $l_N/d = 4$, $l_A/d = 8$, $M = 4.0$	177
A-134	Center of Pressure Versus Angle of Attack for $l_N/d = 2$, $l_A/d = 10$, $M = 4.0$	178
A-135	Center of Pressure Versus Angle of Attack for $l_N/d = 3$, $l_A/d = 10$, $M = 4.0$	179
A-136	Center of Pressure Versus Angle of Attack for $l_N/d = 4$, $l_A/d = 10$, $M = 4.0$	180

LIST OF TABLES

TABLE		PAGE
1	Comparison of Prediction Methodology Due to ΔC_{A0} with Wind Tunnel Data	6
2	Comparison of Prediction Methodology Due to ΔC_{A0} with Wind Tunnel Data for a Hemispherical Body	6
3	Sample Calculation of $C_A(\alpha)$, $0 \leq \alpha \leq \bar{\alpha}$	12
4	Sample Calculation of $C_A(\alpha)$, $\bar{\alpha} < \alpha \leq 160^\circ$	12
5	Comparison of ΔC_{NB_α} Prediction Methodology with Wind Tunnel Data for a 2.25 Caliber, $R_N/R_B = 0.575$ Pointed Ogive Nose, 6-Caliber Afterbody Model	19
6	Comparison of ΔC_{NB_α} Prediction Methodology with Wind Tunnel Data for Varying Nose Bluntness	20
7	Comparison of ΔX_0 Prediction Methodology with Wind Tunnel Data for 2.25 Caliber, $R_N/R_B = 0.675$ Pointed Ogive Nose, 6-Caliber Afterbody Model	24
8	Comparison of ΔX_0 Prediction Methodology with Wind Tunnel Data for Varying Nose Bluntness	24
9	Sample Calculation of $C_A(\alpha)$, $0 \leq \alpha \leq \bar{\alpha}$	30
10	Sample Calculation of $C_A(\alpha)$, $\bar{\alpha} < \alpha \leq 160^\circ$	31

LIST OF SYMBOLS

C_A	Axial force coefficient, F_A/QS
$C_A(\alpha)$	Axial force coefficient as a function of angle of attack
C_{AF}	Axial force coefficient of forebody $C_{AF} = C_A - C_{Abase}$
C_{A0}	Axial force coefficient at zero angle of attack
ΔC_{A0}	Change in zero axial force coefficient due to nose bluntness
$C_{A\alpha}$	Variation of the axial force coefficient with change in angle of attack, $C_{A\alpha} \equiv \left. \frac{\partial C_A}{\partial \alpha} \right _{\alpha \rightarrow 0}$
$C_{A\pi}$	The axial force coefficient at 180-degrees angle of attack
C_N	Normal force coefficient, F_N/QS
C_{NB}	Normal Force coefficient for body alone
$C_{NB\alpha}$	The variation of normal force coefficient on the body alone, $C_{NB\alpha} \equiv \left. \frac{\partial C_{NB}}{\partial \alpha} \right _{\alpha \rightarrow 0}$
$C_{NB(T)}$	Total normal force coefficient for a finned body
$C_{N\alpha}$	Variation of the normal force coefficient with angle of attack, $C_{N\alpha} \equiv \left. \frac{\partial C_N}{\partial \alpha} \right _{\alpha \rightarrow 0}$
$C_{N\pi/2}$	Normal force coefficient due to viscous cross flow drag coefficient at 90-degree angle of attack
C_{NT}	Normal force coefficient for tail only (fin normal force coefficient)
$C_{NT(B)}$	Normal force coefficient on the tail including body effects
$\Delta C_{NB\alpha}$	Change due to more bluntness in the slope of the normal force coefficient

LIST OF SYMBOLS (cont)

$C_{NB\alpha_{NB}}$	Variation of $C_{NB\alpha}$ with nose bluntness
	$C_{NB\alpha_{NB}} \equiv \frac{\partial C_{NB\alpha}}{\partial R_N/R_B} = \frac{\partial}{\partial R_N/R_B} \left(\frac{\partial C_{NB\alpha}}{\partial \alpha} \right)$
X_{CP} or X_0	Center of pressure measured from the tip of the pointed ogive nose in body diameters
ΔX_0	Change in center of pressure due to nose bluntness
$R_T(B)$	Tail-body interference factor
$I_B(T)$	Tail contribution to carry-over C_N on body, jet-off and jet-on
ℓ_N	Length of nose, in.
ℓ_A	Length of missile cylindrical section, in.
M	Mach number
Q	Dynamic pressure, lb/ft ²
S_{ref} or S_B	Reference area, $S = \frac{\pi d^2}{4}$, sq ft
S_T	Area of a single exposed tail panel, sq ft
d	Body diameter, ft
α	Angle of attack
$\bar{\alpha}$	Angle of attack value at which $C_A(\alpha) = 0$
R_N	Radius of nose bluntness
R_B	Radius of base

SECTION I
INTRODUCTION

This report documents the work of Systems Research Laboratories, Inc. (SRL) conducted as part of the development of a preliminary design aerodynamic prediction methodology for missiles. This project is part of a continuing effort by the Air Force Flight Dynamics Laboratory, Control Dynamics Branch (AFFDL/FGC). The objective of this effort was to extend the semi-empirical methodology of Reference 1 to incorporate the effects of spherical nose bluntness in the prediction of the axial and normal force coefficients and the center of pressure for missiles. The methodology is applicable over the transonic and supersonic Mach number regime, and the 0- to 180-degree angle of attack range. The effects of spherical nose bluntness were obtained from analysis of the wind tunnel test data contained in Reference 2.

The approach used for the extended methodology was to identify the empirical parameters used in Reference 1 for aerodynamic prediction. Next, the data of Reference 2 were analyzed to determine the effects of spherical nose bluntness on these empirical parameters. Where nose bluntness effects were identified, tables or equations were developed for computing the incremental effect due to nose bluntness.

This report supplements the methodology presented in Reference 1. In addition, an analysis of a finned body configuration was conducted to give some insight into the sensitivity of the methodology of Reference 1.

SECTION II
WIND TUNNEL DATA BASE

The extended methodology was developed using the data contained in Reference 2 for the three families of nose shapes shown in Figure 1.

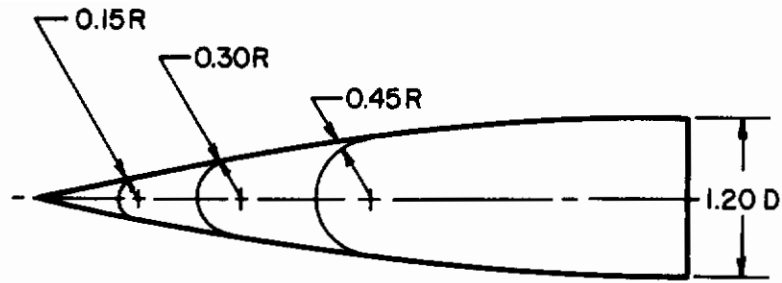
These data were obtained over a range in angle of attack from 0 to 14 degrees and Mach numbers of 0.6, 0.8, 1.0, 1.2, 1.5, 2.0, 3.0, and 4.0. The geometric properties varied during this test program were nose and after-body fineness ratio, ℓ_N/d and ℓ_A/d , respectively; and nose bluntness ratio, R_N/R_B , and are summarized as follows:

$$\frac{R_N}{R_B} = 0, 0.25, 0.50, 0.75$$

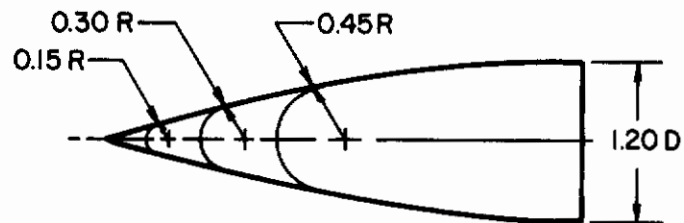
$$\frac{\ell_N}{d} = 2, 3, 4$$

$$\frac{\ell_A}{d} = 6, 8, 10$$

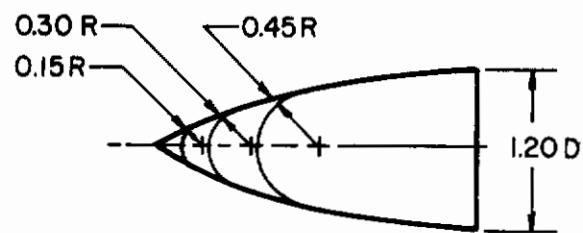
Plots of these data are presented in the Appendix, including procedures used for analysis.



4-CALIBER NOSE



3-CALIBER NOSE



2-CALIBER NOSE

Figure 1. Nose Configurations from Reference 2

SECTION III
NOSE BLUNTNESS EFFECTS

AXIAL FORCE COEFFICIENT

The methodology developed in Reference 1 for predicting C_A at transonic Mach numbers agreed extremely well with experimental data. However, at supersonic Mach numbers, the variation of C_A with angle of attack was not predicted well. As a matter of fact, C_A for angles of attack between 30 and 60 degrees at the higher Mach numbers was severely underpredicted. Furthermore, analysis of the data contained in Reference 2 indicated that the changes in C_A due to nose bluntness were limited to the supersonic Mach regime. Hence, an extended methodology was developed for predicting C_A at supersonic Mach numbers ($1.5 \leq M \leq 4.0$) and angles of attack from 0 to 180 degrees, including the effects of nose bluntness.

Zero Angle of Attack

Using the pointed-ogive nose as the base configuration, the change, ΔC_{A_0} , in the axial force coefficient at zero angle of attack, C_{A_0} , due to nose bluntness was determined. ΔC_{A_0} was found to be independent of ℓ_A/d . These results are summarized in Figure 2 as functions of Mach number, R_N/R_B , and ℓ_N/d . A regression analysis of these data indicated that the change in axial force coefficient at zero angle of attack, ΔC_{A_0} , due to nose bluntness could be represented by the following relationship:

$$\Delta C_{A_0} = \frac{0.5}{M} \left[(M^2 - 1)^{1/2} \left(\frac{\ell_N}{d} \right)^{1/2} \left(\frac{R_N}{R_B} \right)^{2.5} \right] \quad (1)$$

for $1.5 \leq M \leq 4.0$ and $0 < R_N/R_B \leq 0.75$, where ℓ_N/d is the fineness ratio of the pointed-ogive nose to which spherical nose bluntness, R_N/R_B , is added. Table 1 gives a comparison of ΔC_{A_0} determined from Equation (1) with the wind tunnel data of Reference 3.

The percent differences indicate good agreement for a preliminary design method. It should be noted that Equation (1) has been extended beyond the

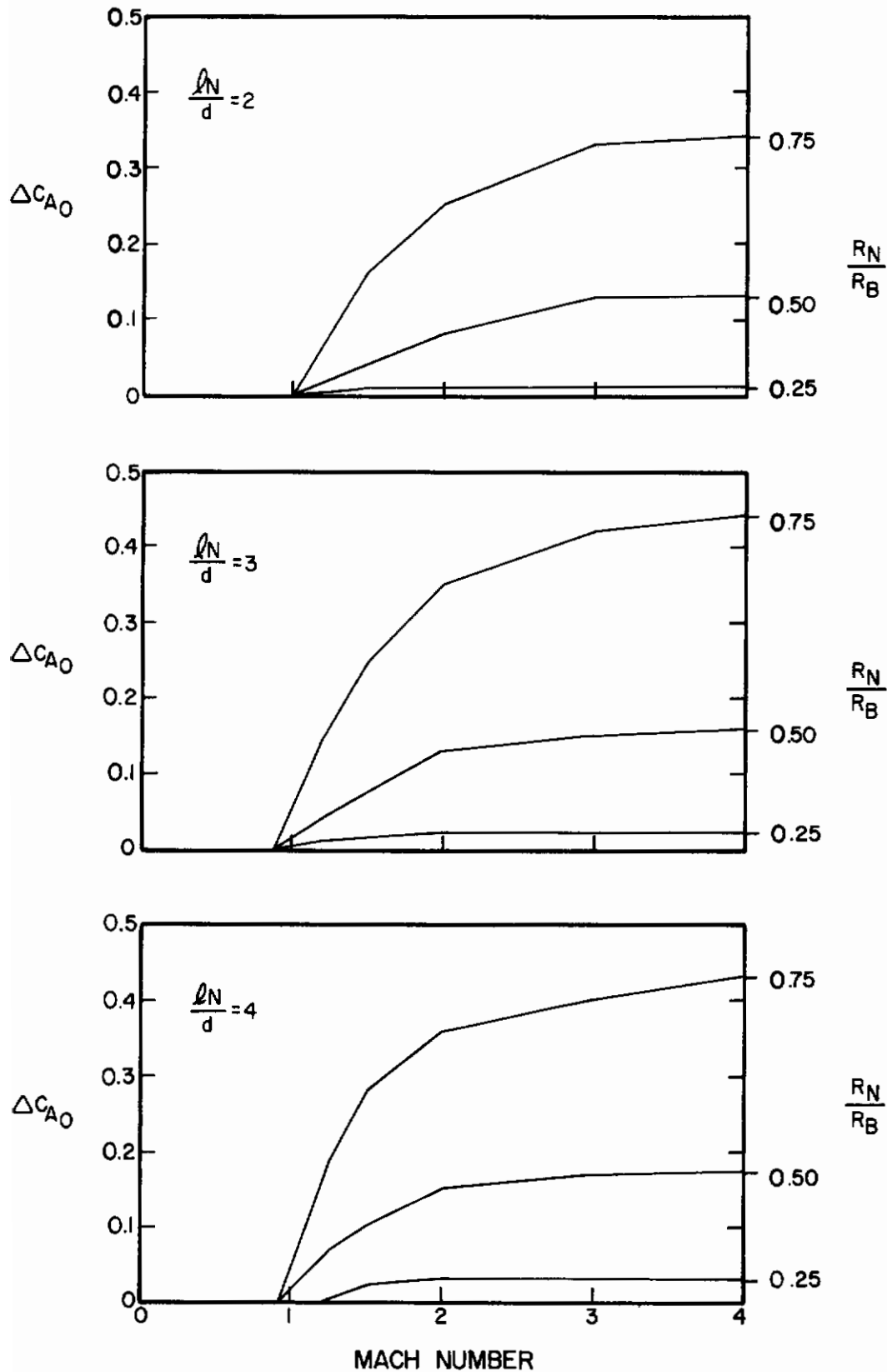


Figure 2. ΔC_{A0} Versus Mach Number

TABLE 1. COMPARISON OF PREDICTION METHODOLOGY
DUE TO ΔC_{A_0} WITH WIND TUNNEL DATA

M	$\frac{R_N}{R_B}$	ΔC_{A_0} Eq. (1)	ΔC_{A_0} Ref. 3	Percent Difference
1.50	0.45	0.078	0.065	20
1.50	0.70	0.237	0.200	18
1.50	1.0	0.578	0.540	7
2.86	0.45	0.097	0.086	13
2.86	0.70	0.283	0.280	1
2.86	1.0	0.705	0.672	5

original limit of $R_N/R_B = 0.75$, the maximum nose bluntness ratio of the data in Reference 2, to $R_N/R_B = 1$ (hemispherical nose) and represents the limiting case for Equation (1). Comparison of ΔC_{A_0} calculated from Equation (1) with wind tunnel data for a hemispherical body (Reference 4) is given in Table 2.

TABLE 2. COMPARISON OF PREDICTION METHODOLOGY DUE TO
 ΔC_{A_0} WITH WIND TUNNEL DATA FOR A HEMISPHERICAL BODY

M	ΔC_{A_0} Eq. (1)	ΔC_{A_0} Ref. 4	Percent Difference
1.5	0.527	0.561	9
2.0	0.612	0.636	4
3.0	0.667	0.674	1
4.0	0.684	0.691	1

These comparisons indicate that Equation (1) gives the best results for the larger Mach numbers and nose bluntness ratios.

Angle of Attack Variation

Analysis of the data in References 3 and 7 indicated that $C_A(\alpha)$ for supersonic Mach numbers follows the basic trends shown in Figure 3. With increasing angle of attack, $C_A(\alpha)$ increases from C_{A_0} , reaching a maximum value between 60 and 80 degrees. $C_A(\alpha)$ then decreases to 105 degrees angle of attack where $C_A(\alpha) = 0$. From 105 to 160 degrees $C_A(\alpha)$ decreases monotonically, and from 160- to 180-degrees angle of attack $C_A(\alpha)$ is a constant. Using the mathematical approach presented in Reference 1, the functional dependence of C_A with angle of attack, α , for a body-alone configuration was found to be expressible as a second order polynomial in angle of attack as follows:

$$C_A(\alpha) = b_0 + b_1\alpha + b_2\alpha^2 \quad (2)$$

The following conditions are defined:

$$\text{at } \alpha = 0,$$

$$\left. \frac{\partial C_A}{\partial \alpha} \right|_{\alpha \rightarrow 0} = C_{A_\alpha} \text{ and } C_A = C_{A_0}$$

and at

$$C_A = 0,$$

$$\alpha = \bar{\alpha}$$

By studying the wind tunnel data in Reference 5 for body-alone configurations at supersonic Mach numbers, $\bar{\alpha}$ values remained constant at

$$\bar{\alpha} = 105^\circ$$

Employing the above conditions to Equation (2), $C_A(\alpha)$ was derived as follows:

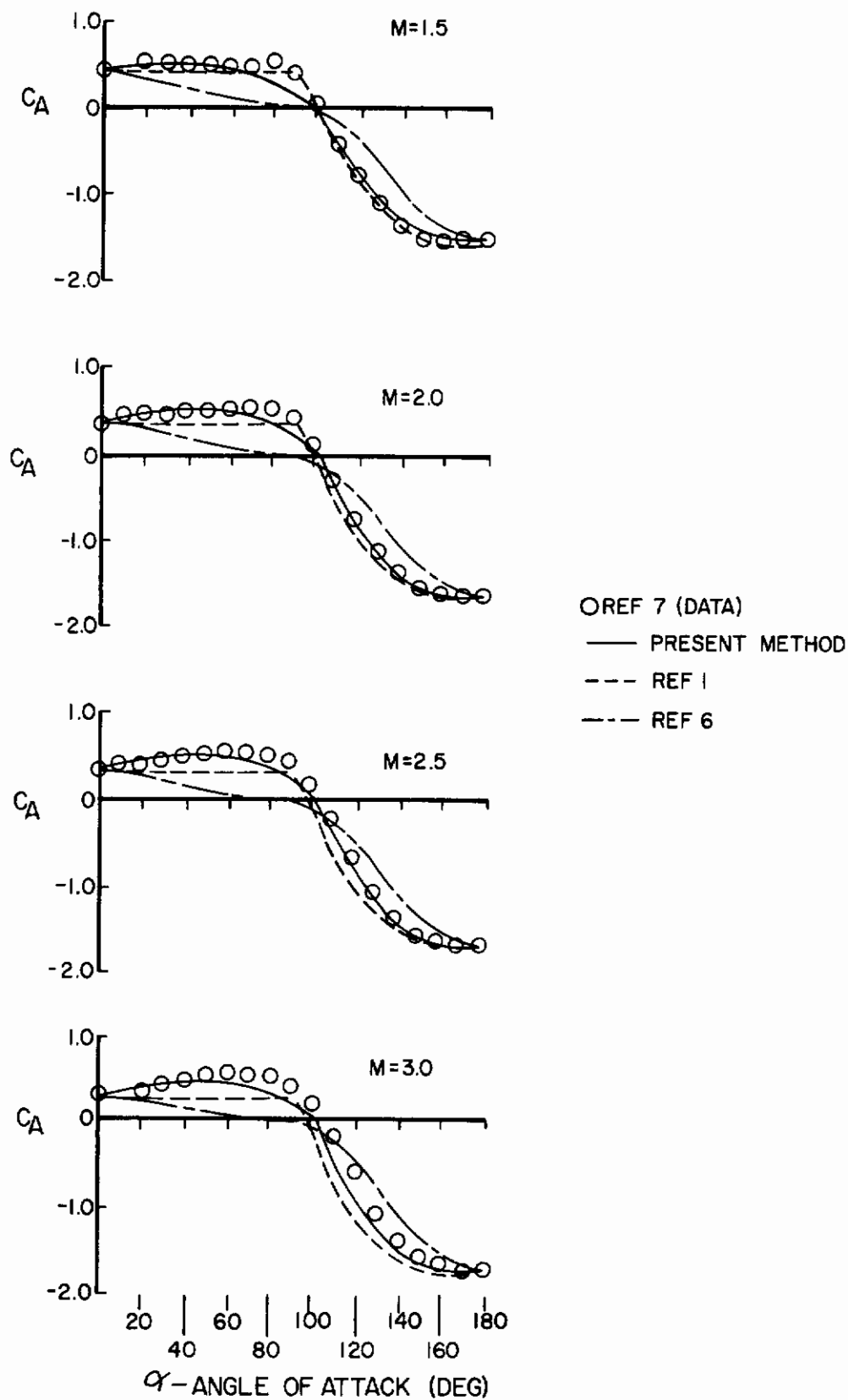


Figure 3. Comparison of Prediction Methods with Wind Tunnel Data, Body Alone

$$C_A(\alpha) \Big|_0^{\bar{\alpha}} = C_{A_0} \left(1 - \frac{\alpha^2}{\bar{\alpha}^2} \right) + C_{A_\alpha} \left(\alpha - \frac{\alpha^2}{\bar{\alpha}^2} \right) \quad \begin{matrix} (0^\circ \text{ to } 105^\circ \\ \text{angle of attack} \\ \text{range}) \end{matrix} \quad (3a)$$

$$C_A(\alpha) \Big|_{\bar{\alpha}}^{2.792} = -C_{A_\pi} \left[1 - \frac{(2.792 - \alpha)^2}{(2.792 - \bar{\alpha})^2} \right] \quad \begin{matrix} (105^\circ \text{ to } 160^\circ \\ \text{angle of} \\ \text{attack range}) \end{matrix} \quad (3b)$$

$$C_A(\alpha) \Big|_{2.792}^{\pi} = -C_{A_\pi} \quad (160^\circ \text{ to } 180^\circ \text{ angle of attack range}) \quad (3c)$$

where

α is in radians

$\bar{\alpha} = 1.83$ radians (105 degrees)

C_{A_α} was determined from the analysis of the wind tunnel data contained in Reference 2. These results are presented in Figure 4A. This analysis indicated that C_{A_α} is independent of ℓ_N/d , ℓ_A/d , and R_N/R_B , and dependent only on the Mach number.

Figure 4B also charts the axial force coefficient at 180-degrees angle of attack. These data are taken from page 84, Reference 1, and are presented to complete the methodology.

By summing C_{A_0} (pointed-ogive nose) and ΔC_{A_0} , that is

$$C_{A_0} = C_{A_0} \text{ (pointed-ogive nose)} + \Delta C_{A_0}, \quad (4)$$

the effective C_A value for axial force coefficient at 0-degree angle of attack is developed. C_{A_0} for pointed ogive-nose configurations is determined from Reference 6; and ΔC_{A_0} is determined from Equation (1).

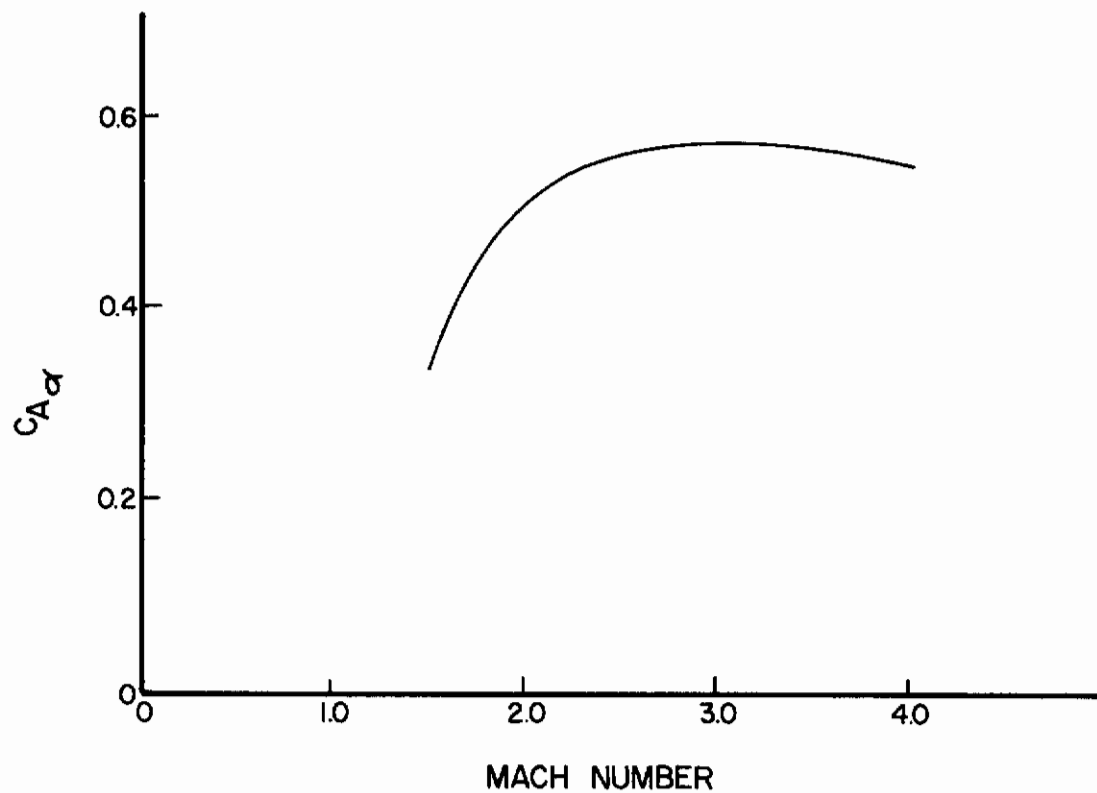


Figure 4A. $C_{A\alpha}$ as Function of Mach Number

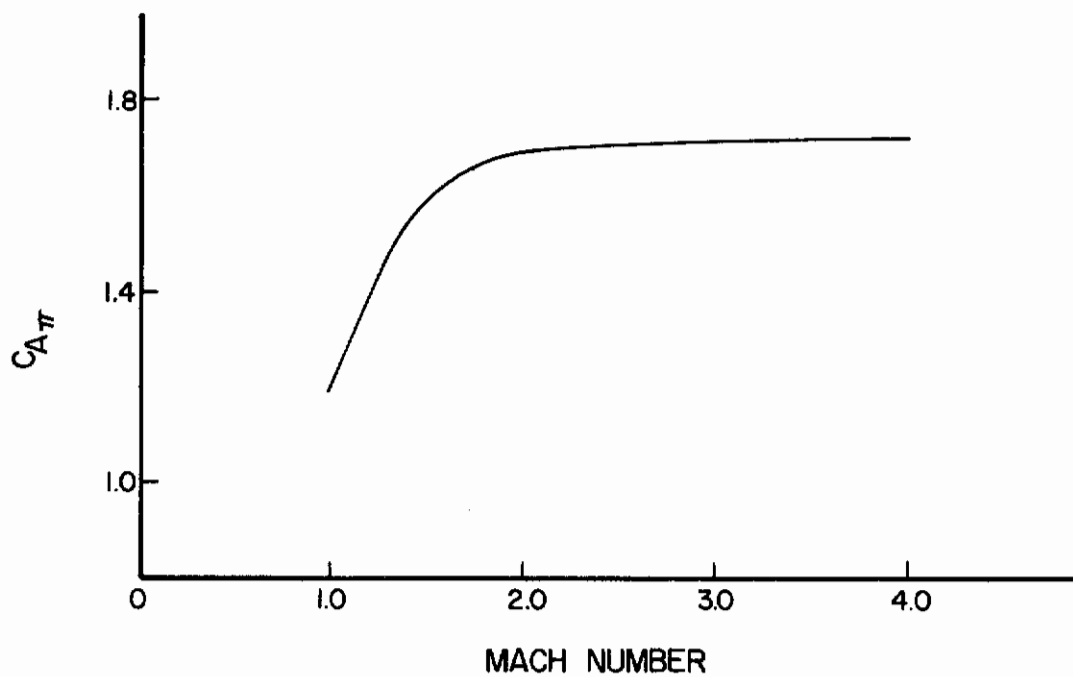


Figure 4B. $C_{A\pi}$ as Function of Mach Number

$C_A(\alpha)$ can now be determined. Using Equation (4), Equation (3a) is solved. Using Figure 4B, Equations (3b) and 3(c) are solved. A sample calculation is presented in the following numerical example.

Numerical Example

Problem:

Calculate the axial force coefficient between 0- and 180-degrees angle of attack for a missile body having a 2.5 caliber tangent ogive nose and a 7.5 caliber cylindrical body. The Mach number is 2.5 and the Reynolds number is 4.17×10^6 .

Solution:

- (1) From the method of Reference 6, $C_{A0} = 0.342$
- (2) From Figure 4A, $C_{A\alpha} = 0.560/\text{radian}$
- (3) From Figure 4B, $C_{A\pi} = 1.710/\text{radian}$
- (4) For the body alone $\bar{\alpha} = 105^\circ$ (1.833 radian)
- (5) Use Equation (3) to calculate $C_A(\alpha)$ from 0- to 180-degrees angle of attack
 - (a) $C_A(\alpha)$ from 0 to $\bar{\alpha}$ (105°) is shown in Table 3
 - (b) $C_A(\alpha)$ from $\bar{\alpha}$ to (105° to 160°) is shown in Table 4
 - (c) $C_A(\alpha)$ from 160° to 180° is $C_A(\alpha) = -C_{A\pi} = 1.710$

$C_A(\alpha)$ for pointed-ogive nose cylinder configurations computed from Equation (3) is compared with wind tunnel data and other semi-empirical methodologies, and is presented in Figure 3. For the 0- to 60-degree angle of attack range, as these results show, the present method yields significant improvement over the methods of References 1 and 6. These previous methods did not predict the increase in axial force coefficient occurring between 30- and 60-degrees angle of attack. This increase, as shown in the figures, can be as high as C_{A0} itself.

TABLE 3. SAMPLE CALCULATION OF $C_A(\alpha)$, $0 \leq \alpha \leq \bar{\alpha}$

α	$1 - \frac{\alpha^2}{\bar{\alpha}^2}$	$\alpha - \frac{\alpha^2}{\bar{\alpha}}$	$C_{A0} \left(1 - \frac{\alpha^2}{\bar{\alpha}^2} \right)$	$C_{A\alpha} \left(\alpha - \frac{\alpha^2}{\bar{\alpha}} \right)$	$C_A(\alpha)$
0	1.000	0.000	0.342	0.000	0.342
10	0.991	0.158	0.339	0.088	0.427
20	0.968	0.283	0.331	0.158	0.489
30	0.918	0.374	0.314	0.209	0.523
40	0.855	0.432	0.292	0.242	0.534
50	0.773	0.457	0.264	0.256	0.520
60	0.673	0.449	0.230	0.251	0.481
70	0.555	0.407	0.190	0.228	0.418
80	0.420	0.332	0.144	0.186	0.330
90	0.265	0.224	0.091	0.125	0.216
100	0.093	0.083	0.032	0.046	0.078
105	0.000	0.000	0.000	0.000	0.000

TABLE 4. SAMPLE CALCULATION OF $C_A(\alpha)$, $\bar{\alpha} \leq \alpha \leq 160^\circ$

α	$1 - \frac{(160 - \alpha)^2}{(160 - \bar{\alpha})^2}$	$-C_{A\pi} \left[1 - \frac{(160 - \alpha)^2}{(160 - \bar{\alpha})^2} \right]$	$C_A(\alpha)$
105	0.000	0.000	0.000
110	0.174	-0.298	-0.298
120	0.471	-0.805	-0.805
130	0.702	-1.200	-1.200
140	0.868	-1.484	-1.484
150	0.967	-1.654	-1.654
160	1.000	-1.710	-1.710

NORMAL FORCE COEFFICIENT

The methodology developed in Reference 1 for predicting the variation of C_N for pointed-ogive nose configurations with angle of attack and Mach number agrees well with experimental data. Hence, a semi-empirical approach is presented in the following section for incorporating the effect of nose bluntness in the computation of $C_N(\alpha)$. The methodology of Reference 1 utilizes a polynomial expansion in angle of attack to predict $C_N(\alpha)$ with two free variables, C_{N_α} and $C_{N_{\pi/2}}$, where C_{N_α} is the slope of the normal force coefficient as the angle of attack approaches 0 degrees

$$C_{N_\alpha} = \left. \frac{\partial C_N}{\partial \alpha} \right|_{\alpha \rightarrow 0}$$

and $C_{N_{\pi/2}}$ is the viscous crossflow drag coefficient at 90-degrees angle of attack.

To incorporate the effect of spherical nose bluntness into the methodology of Reference 1, it is assumed that:

$$1. \quad C_{NB_\alpha} = C_{NB_\alpha} \text{ (pointed ogive nose)} + \Delta C_{NB_\alpha} \quad (5)$$

where

C_{NB_α} (pointed-ogive nose) is the variation of the normal force coefficient obtained from pages 51 through 55 of Reference 1, and ΔC_{NB_α} is the change in C_{NB_α} due to spherical nose bluntness as indicated in Reference 2;

2. The viscous crossflow drag coefficient at 90-degrees angle of attack is independent of nose bluntness effects.

The following section presents the method developed for determining ΔC_{NB_α} from the data of Reference 2.

Change Due to Spherical Nose Bluntness

Analysis of the data contained in Reference 2 indicated that C_N was independent of nose bluntness effects for Mach numbers of 0.6 to 1.5. Only at the higher Mach numbers did the effect of nose bluntness become apparent. The slope of the normal force coefficient curve, C_{NB_α} , as a function of Mach number and nose bluntness ratio is presented in Figures 5 through 7. The C_{NB_α} values presented in the figures indicate significant changes due to nose bluntness occurred at Mach numbers of 3.0 and 4.0. For example, a nose fineness ratio of 4, afterbody fineness ratio of 10, and a Mach number of 3.0 indicates C_{NB_α} is decreased by 16 percent with 0.75 nose bluntness. For the same configurations at a Mach number of 4.0, 22 percent decrease occurs.

Analysis of the data of Reference 2 indicated that the change in C_{NB_α} at Mach numbers of 2 and above was independent of afterbody fineness ratio. Furthermore, it was found that the change in C_{NB_α} with respect to nose bluntness, ΔC_{NB_α} , is linear, and can be represented as a second derivative, $C_{NB_{\alpha N_B}}$. The effect of nose bluntness for the body alone added to C_{NB_α} , as determined in Reference 1, is computed as follows:

$$\Delta C_{NB_\alpha} = \left(C_{NB_{\alpha N_B}} \right) \left(\frac{R_N}{R_B} \right) \quad (6)$$

for

$$0 \leq \frac{R_N}{R_B} \leq 0.75$$

and

$$2.0 \leq M \leq 4.0$$

$C_{NB_{\alpha N_B}}$ as a function of Mach number is presented in Figure 8. From the test data of References 2 and 3, it was found that the change in normal force coefficient due to nose bluntness was influenced by the presence of the fins, as shown in this figure. Additional data are required to substantiate these findings. An average value of $C_{NB_{\alpha N_B}}$ was determined for prediction purposes. A sample calculation is presented in the following numerical example.

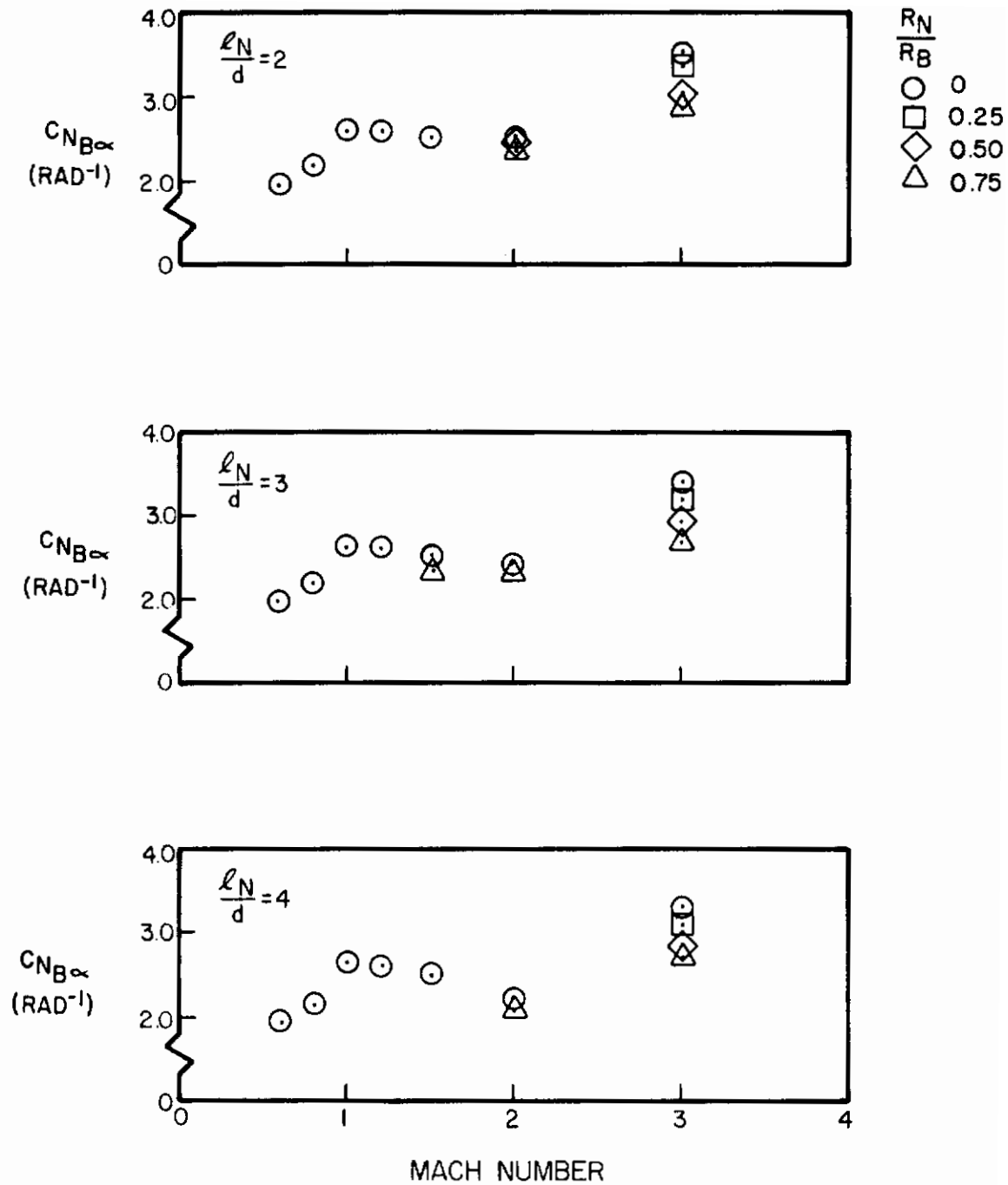


Figure 5. Variation of $C_{N_{B\alpha}}$ with Mach Number for $\ell_A/d = 6$

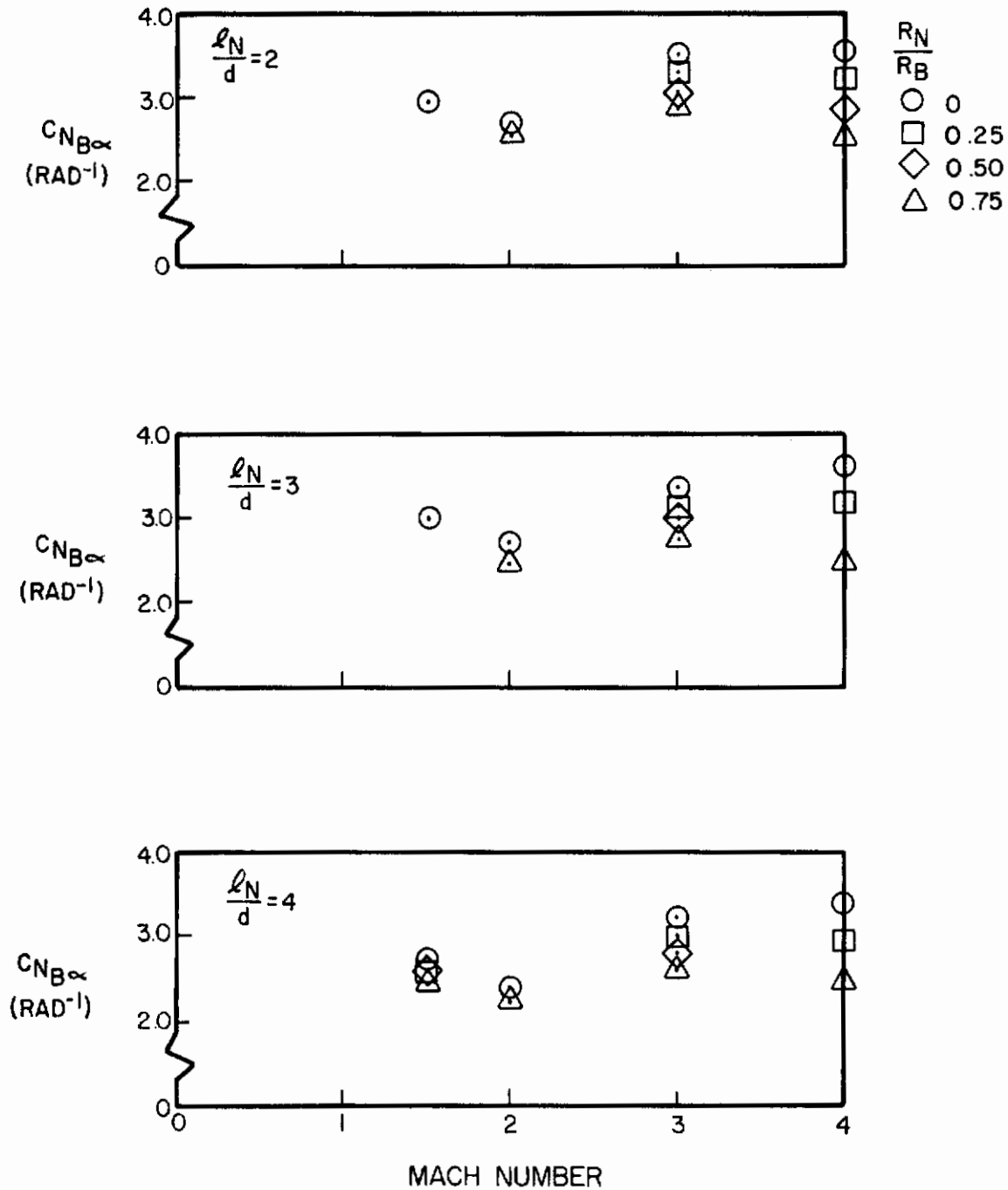


Figure 6. Variation of $C_{N_{B\alpha}}$ with Mach Number for $\ell_A/d = 8$

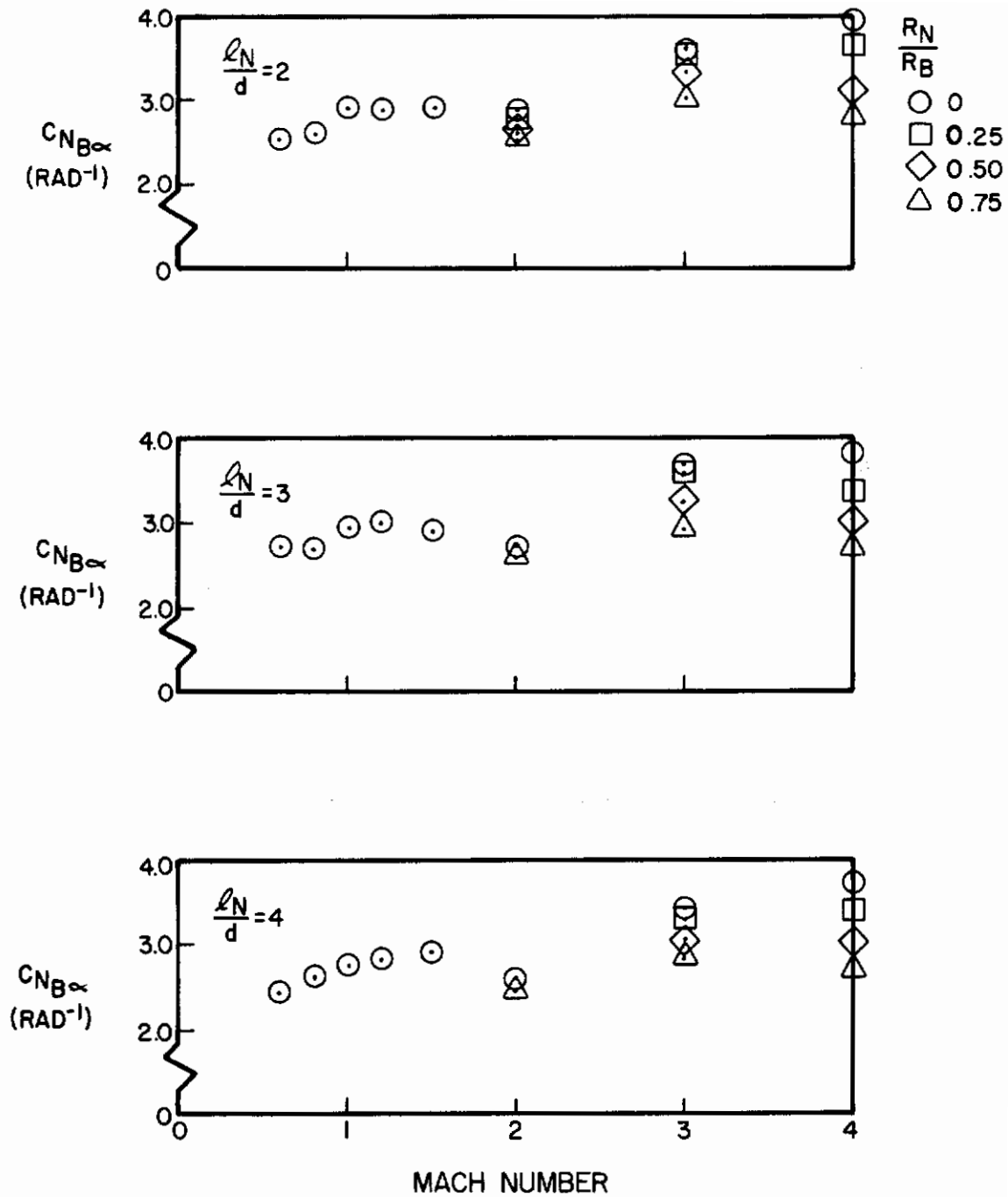


Figure 7. Variation of $C_{N\alpha}$ with Mach Number for $\ell_A/d = 10$

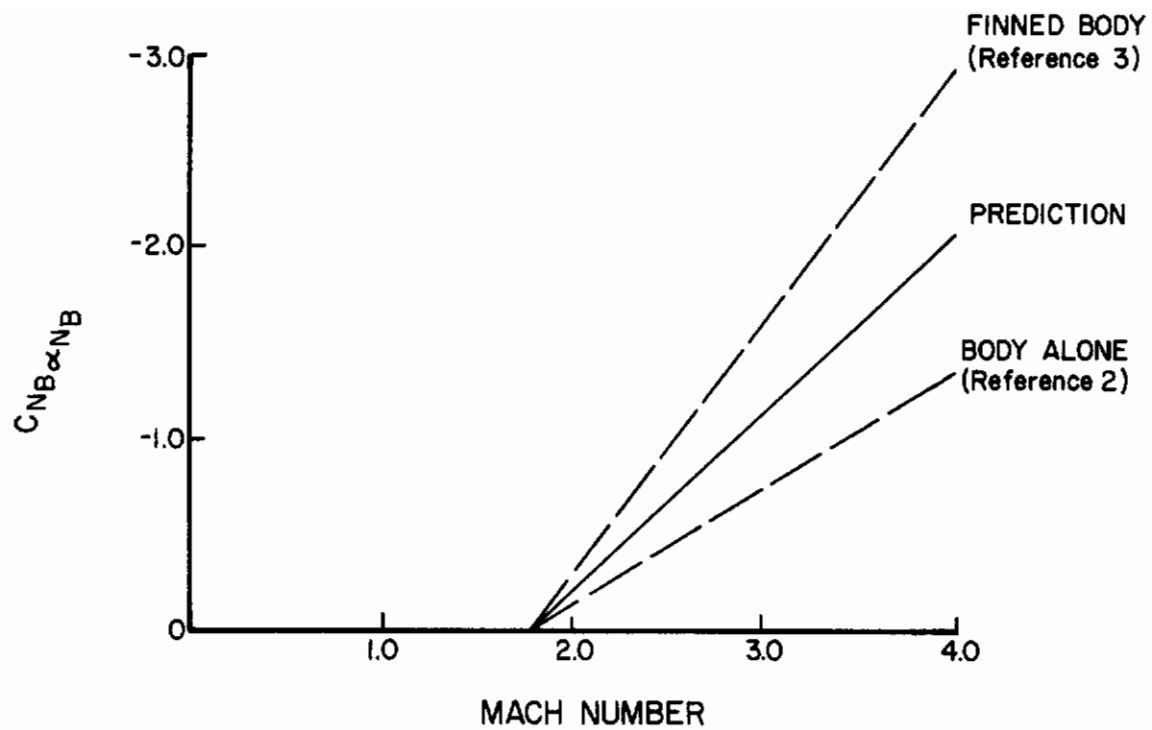


Figure 8. Change in Normal Force Slope Coefficient Due to Nose Bluntness

Numerical Example

Problem:

Calculate $\Delta C_{N_{B\alpha}}$ for a 2.25 caliber pointed-ogive nose with $R_N/R_B = 0.575$ and 6-caliber afterbody at Mach 3.5. Compare the calculated value with the wind tunnel data.

Solution:

- Using Figure 8 for a Mach number of 3.5,

$$C_{N_{B\alpha N_B}} = 1.57$$

- Using Equation (6)

$$\begin{aligned} \Delta C_{N_{B\alpha}} &= (-1.57) (.575) \\ &= -.90 \end{aligned}$$

The comparison of the predicted $\Delta C_{N_{B\alpha}}$ change in normal force coefficient with wind tunnel data is presented in Tables 5 and 6; Table 5 compares Mach number changes while Table 6 compares nose bluntness.

TABLE 5. COMPARISON OF $\Delta C_{N_{B\alpha}}$ PREDICTION METHODOLOGY WITH WIND TUNNEL DATA FOR A 2.25 CALIBER, $R_N/R_B = 0.575$ POINTED-OGIVE NOSE, 6-CALIBER AFTERBODY MODEL

Mach No.	$\Delta C_{N_{B\alpha}}$ Ref. 2	$\Delta C_{N_{B\alpha}}$ Eq. 6	Percent Difference
3.0	-0.65	-0.67	3
3.5	-0.80	-0.90	12

TABLE 6. COMPARISON OF ΔC_{NB_α} PREDICTION METHODOLOGY WITH
WIND TUNNEL DATA FOR VARYING NOSE BLUNTNESSES

$\frac{R_N}{R_B}$	ΔC_{NB_α} Ref. 3	ΔC_{NB_α} Eq. 6	Difference
0.45	-0.57	-0.46	19
0.70	-0.75	-0.71	5
1.00	-1.15	-1.01	12

CENTER OF PRESSURE

The methodology developed in Reference 1 for predicting the variation of the center of pressure, X_{CP} , for pointed-ogive nose configurations with angle of attack and Mach number agrees well with experimental data. Hence, a semi-empirical approach is presented in the following section for incorporating the effect of nose bluntness in the computation of $X_{CP}(\alpha)$. The methodology of Reference 1 utilizes a polynomial expansion in angle of attack to predict $X_{CP}(\alpha)$ with several "free-variables."

Since the data of Reference 2 was limited to a maximum 14-degree angle of attack, it was assumed that only the zero angle of attack value of the center of pressure, X_0 , was affected by nose shape. Therefore, using the methodology of Reference 1, the spherical nose bluntness effects become:

$$X_0 = X_0 \text{ (pointed-ogive nose)} + \Delta X_0 \quad (7)$$

where X_0 (pointed-ogive nose) is the zero angle of attack value of the center of pressure for the pointed-ogive nose, obtained from pages 70 and 71 of Reference 1, and ΔX_0 is the change due to spherical nose bluntness. It should be noted that X_0 and ΔX_0 are measured from the nose of the pointed ogive.

Change Due to Spherical Nose Bluntness

X_0 obtained from the data of Reference 2 is presented as a function of Mach number, nose and afterbody fineness ratio, and nose bluntness ratio in Figures 9 through 11.

Contrails

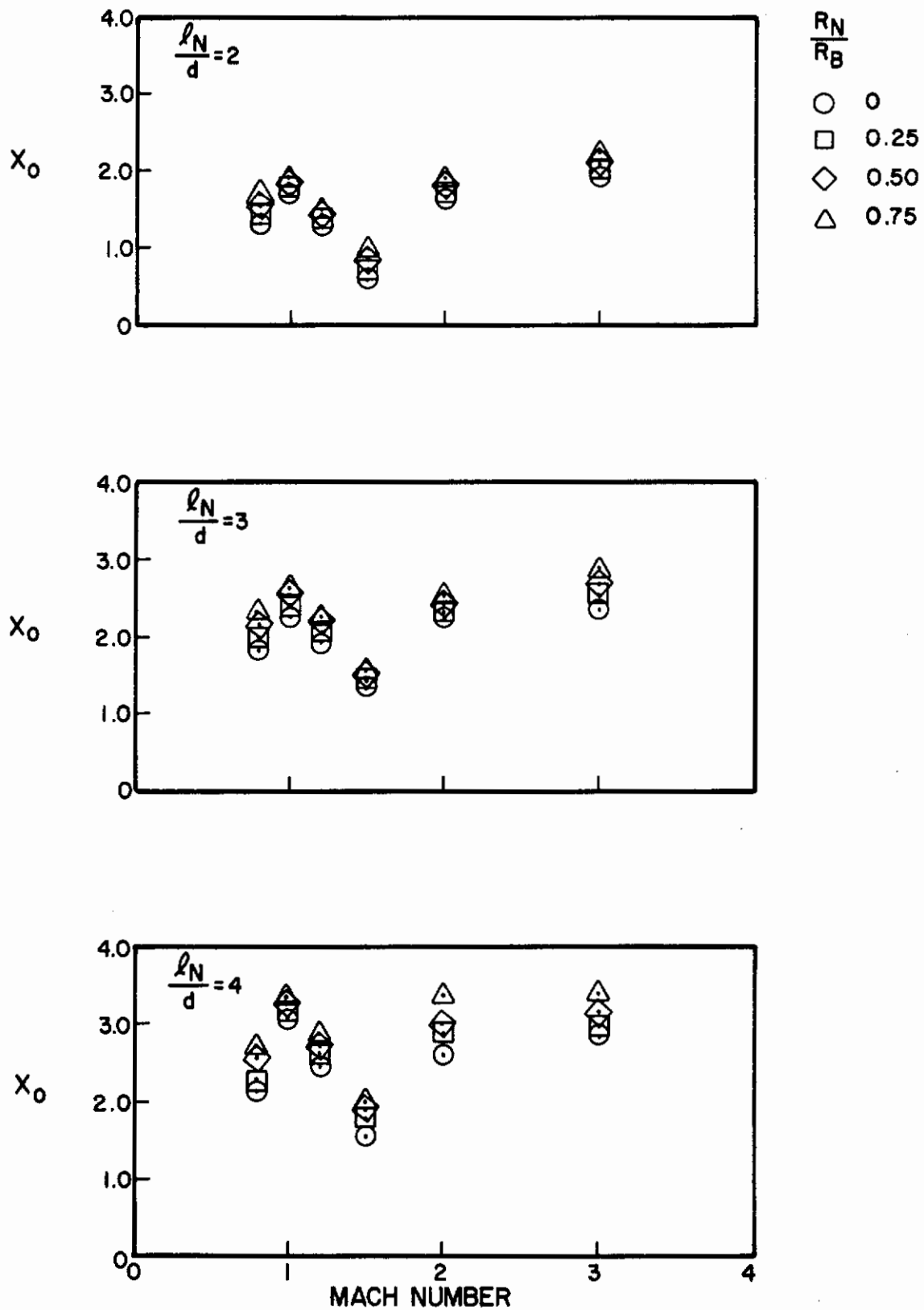


Figure 9. Variation of X_0 with Mach Number for $\frac{l_A}{d} = 6$

Contrails

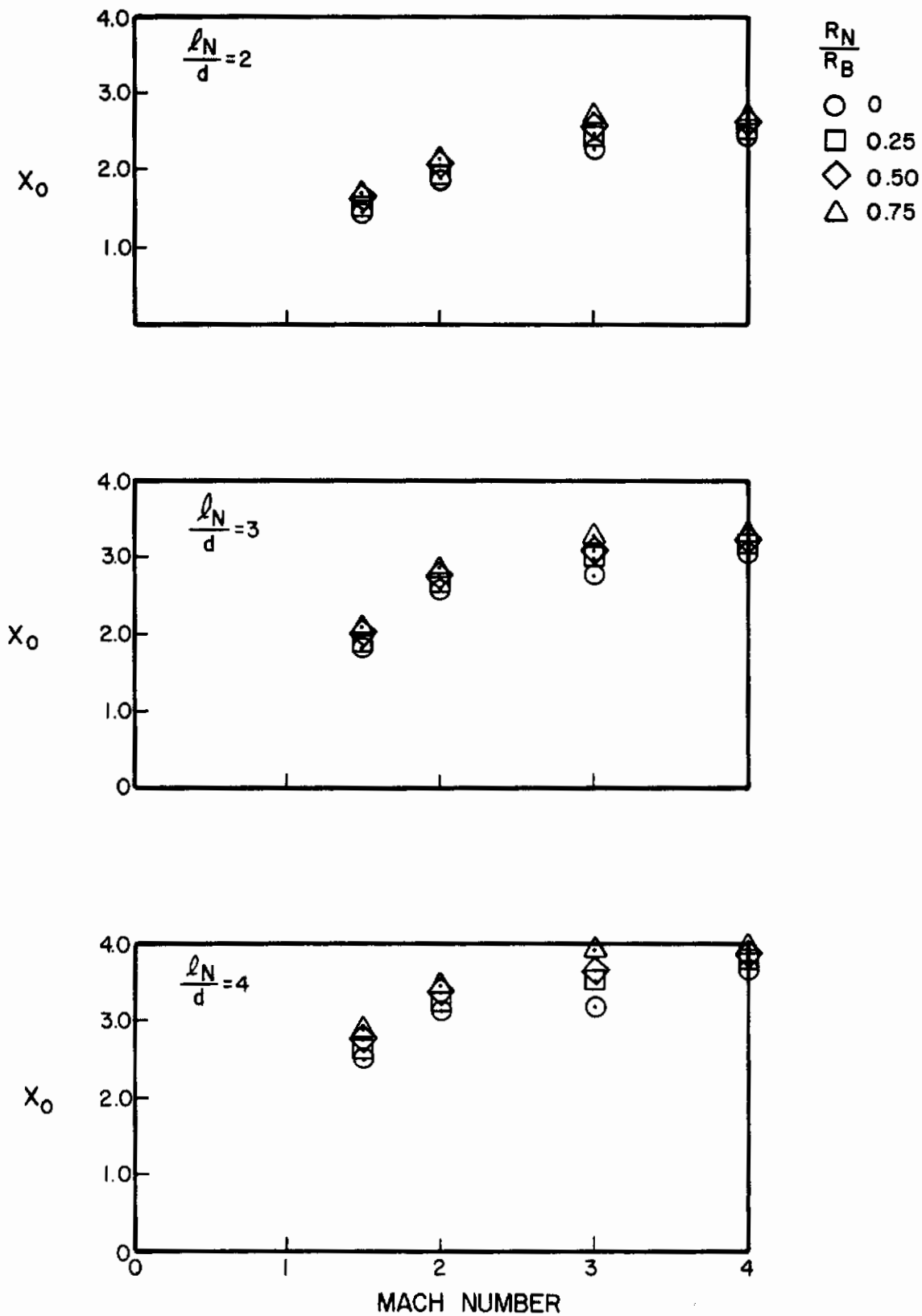


Figure 10. Variation of X_0 with Mach Number for $\frac{l_A}{d} = 8$

Contrails

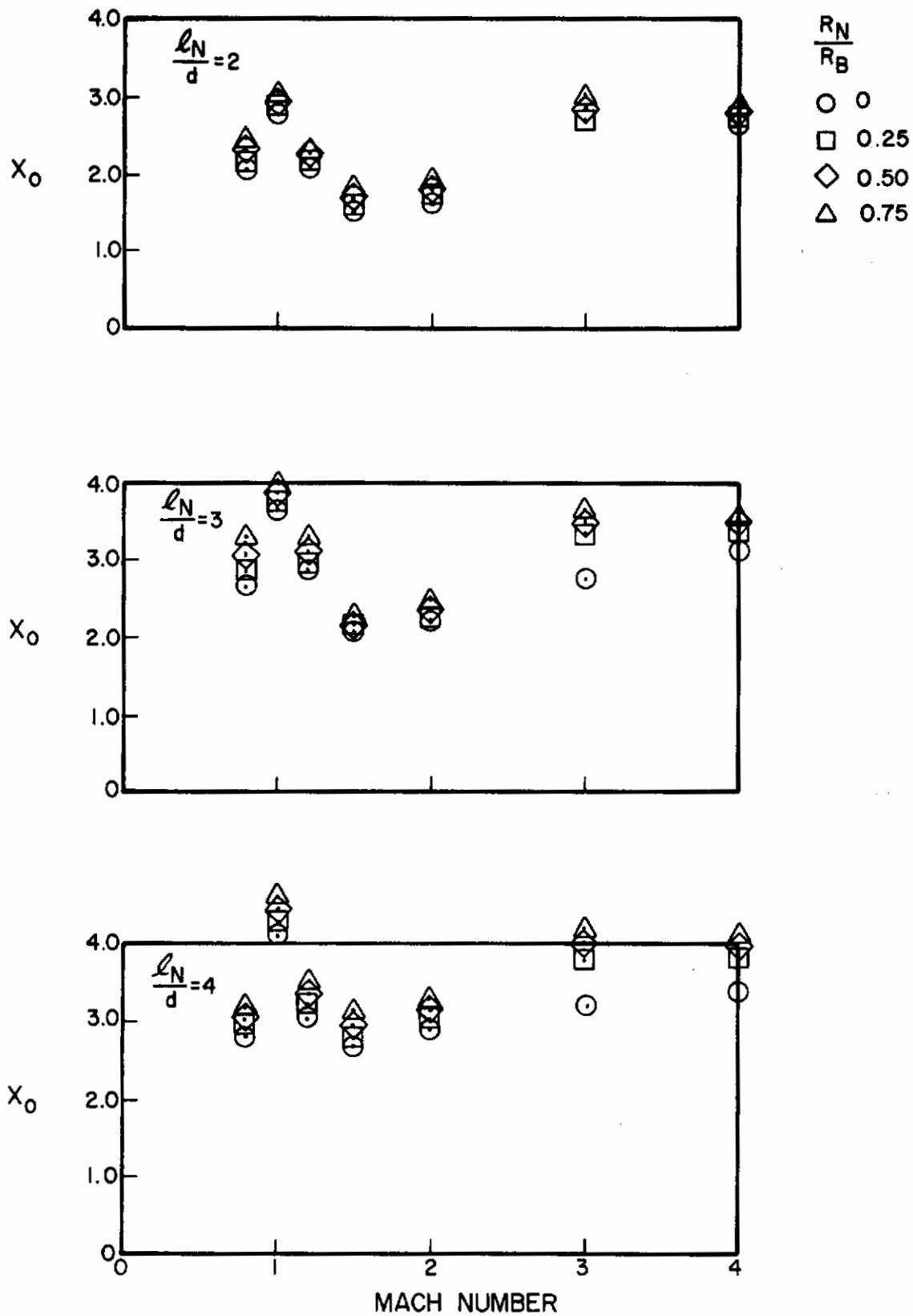


Figure 11. Variation of X_0 with Mach Number for $\frac{l_A}{d} = 10$

Analysis of these data indicated that the change in X_0 due to nose bluntness is independent of nose and afterbody fineness ratios. These results are summarized in Figure 12, which presents ΔX_0 as a function of Mach number and nose bluntness ratio.

Table 7 gives a comparison of ΔX_0 for a 2.25-caliber pointed-ogive nose with $R_N/R_B = 0.575$ and 6-caliber afterbody determined from Figure 12 with the wind tunnel data of Reference 2.

TABLE 7. COMPARISON OF ΔX_0 PREDICTION METHODOLOGY WITH WIND TUNNEL DATA FOR 2.25 CALIBER, $R_N/R_B = 0.575$ POINTED-OGIVE NOSE, 6-CALIBER AFTERBODY MODEL

Mach Number	ΔX_0 Ref. 2	ΔX_0 Fig. 13	Percent Difference
3.0	0.41	0.38	6
3.5	0.31	0.32	3

The data for this configuration were not included in the development of Figure 12. As seen here, good agreement is achieved.

Table 8 gives a comparison of ΔX_0 determined from Figure 12 with the wind tunnel data of Reference 3, for $M = 2.36$.

TABLE 8. COMPARISON OF ΔX_0 PREDICTION METHODOLOGY WITH WIND TUNNEL DATA FOR VARYING NOSE BLUNTNESS

$\frac{R_N}{R_B}$	ΔX_0 Ref. 3	ΔX_0 Fig. 12	Percent Difference
0.45	0.11	0.13	18
0.70	0.37	0.39	5
1.0	0.53	0.51	4

The percent difference shown above indicates that the extended methodology will yield good results for preliminary design.

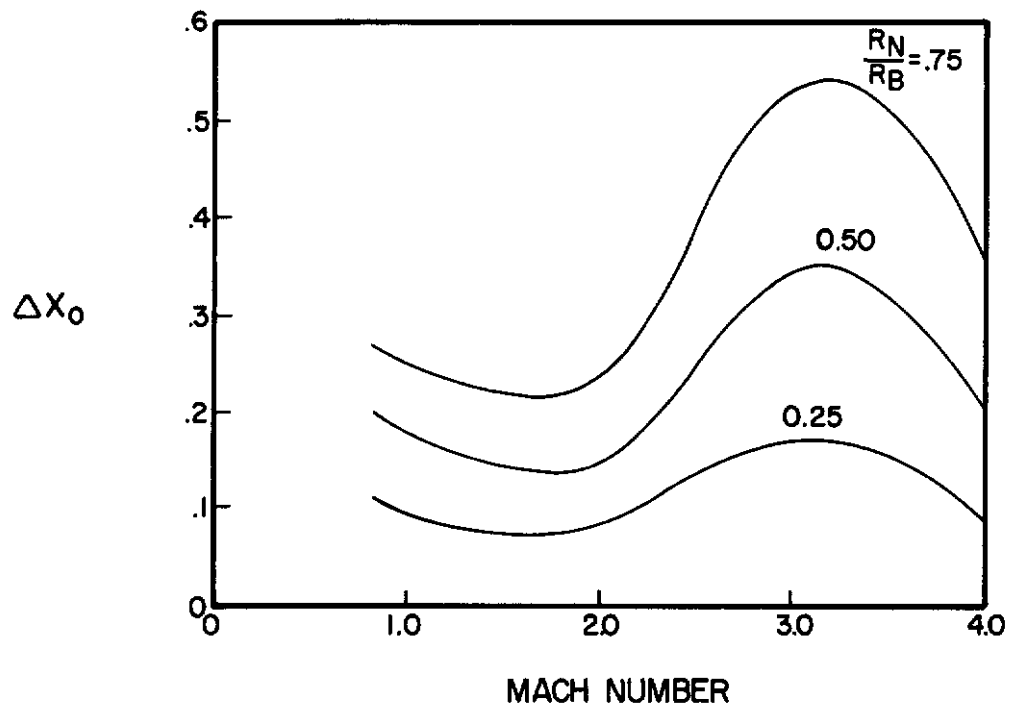


Figure 12. ΔX_0 Due to Nose Bluntness

SECTION IV
FINNED BODY

Reference 1 deals exclusively with the prediction of C_N and X_{CP} for finned and wing-tail bodies, and omits entirely any consideration of C_A . In the following section, a methodology is presented for predicting $C_A(\alpha)$ at supersonic speeds for finned bodies. Also, C_N and X_{CP} determined by the methodology of Reference 1 are compared with wind tunnel data to give some insight into the sensitivity of these calculations for finned bodies.

AXIAL FORCE COEFFICIENT

Analysis of the data in Reference 7 showed that C_A displayed the same variation with angle of attack for a finned body at supersonic Mach numbers as did the body-alone configuration discussed in Section III of this report. Initial compilations of $C_A(\alpha)$ using Equation (3) yielded poor agreement with the wind tunnel data for angles of attack from 20 to 100 degrees. However, from 110 to 130 degrees, Equation (3) gave excellent correlation with the wind tunnel test data. Close examination of these data showed that $\bar{\alpha}$, the value of α at which $C_A = 0$, was weakly dependent on Mach number. Furthermore, it was discovered that $C_A(\alpha)$ in the angle of attack range from 0 to $\bar{\alpha}$ would correlate better with the wind tunnel data if it were expressed as a cubic rather than a quadratic function of α . That is

$$C_A(\alpha) = b_0 + b_1\alpha + b_2\alpha^2 + b_3\alpha^3 \quad (8)$$

for a finned body for the angle of attack range from 0 to $\bar{\alpha}$. For the angle of attack range from $\bar{\alpha}$ to 180° , the applicable portions of Equation (3) were used. Analysis of the data of References 5 and 7 indicated that the $C_A(\alpha)$ trends for the body-with-fin configuration is identical to the trends for the body-alone configuration except that $\bar{\alpha}$, angle of attack when $C_A(\alpha) = 0$, is dependent upon Mach number as

$$\bar{\alpha} = 0.096M + \frac{\pi}{2}$$

Therefore, the following boundary conditions were established:

$$\text{at } \alpha = 0 \\ C_A = C_{A_0} \text{ and } \left. \frac{\partial C_A}{\partial \alpha} \right|_{\alpha \rightarrow 0} = C_{A_\alpha}$$

and at

$$C_A = 0, \alpha = \bar{\alpha}$$

where

$$C_{A_{\bar{\alpha}}} = \left. \frac{\partial C_A}{\partial \alpha} \right|_{\alpha \rightarrow \bar{\alpha}}$$

Applying the above conditions to Equation (8), $C_A(\alpha)$ for low aspect ratio finned bodies with 0- to 180-degree angles of attack was determined to be:

$$\begin{aligned} C_A(\alpha) \Big|_0^{\bar{\alpha}} &= C_{A_0} \left(1 - \frac{3\alpha^2}{\bar{\alpha}^2} + \frac{2\alpha^3}{\bar{\alpha}^3} \right) \quad (0^\circ \text{ to } \bar{\alpha} \text{ angle of attack range}) \\ &+ C_{A_\alpha} \left(\alpha - \frac{2\alpha^2}{\bar{\alpha}} + \frac{\alpha^3}{\bar{\alpha}^2} \right) \\ &- 1.84 \left(\frac{\alpha^3}{\bar{\alpha}^2} - \frac{\alpha^2}{\bar{\alpha}} \right) \end{aligned} \quad (9a)$$

$$C_A(\alpha) \Big|_{\bar{\alpha}}^{2.792} = C_{A_\pi} \left[1 - \frac{(2.792 - \alpha)^2}{(2.792 - \bar{\alpha})^2} \right] \quad (\bar{\alpha} \text{ to } 160^\circ \text{ angle of attack range}) \quad (9b)$$

$$C_A(\alpha) \Big|_{2.792}^{\pi} = -C_{A_\pi} \quad (160^\circ \text{ to } 180^\circ \text{ angle of attack range}) \quad (9c)$$

where

$$\bar{\alpha} = 0.096M + \frac{\pi}{2} \quad (10)$$

at

$$1.5 \leq M \leq 3.0; C_{A_{\alpha}} = 1.84 \text{ (radians}^{-1}\text{)}$$

The procedure of computing $C_A(\alpha)$ for a finned body is:

1. Determine C_{A_0} for the pointed-ogive nose, body alone, using the methods of Reference 6.
2. Determine ΔC_{A_0} from Equation (1), if spherical nose bluntness is present.
3. Determine C_{A_0} for the fin alone, using the methods of Reference 8.
4. Sum the C_{A_0} values obtained from 1, 2, and 3 above.
5. Determine $C_A(\alpha)$ from Equation (9) using C_{A_0} from Step 4 and $C_{A_{\alpha}}$ and $C_{A_{\pi}}$ from Figure 3.

A sample calculation is presented in the following numerical example.

Numerical Example

Problem:

Calculate the axial force coefficient between 0- and 180-degrees angle of attack for a missile having a 2.5-caliber tangent ogive nose, a 7.5-caliber cylindrical body, and fins of $AR = 1.0$. The Mach number is 3.0, the Reynolds number is 4.17×10^6 , and $R_N/R_B = 0.0$. The fin geometry is shown in Figure 13.

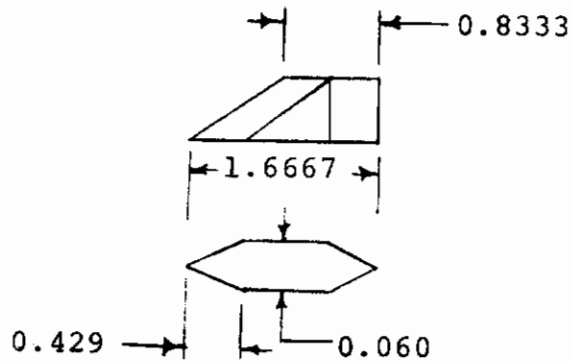


Figure 13. Fin Geometry for a Slender Body Model

Solution:

Steps 1-4. From the method of Reference 6 for the body alone, and method of Reference 8 for the fin alone, $C_{A_0} = 3.000$.

From Figure 3A, $C_{A_\alpha} = 0.580/\text{radian}$

From Figure 3B, $C_{A_\pi} = 1.750$

From Figure 11, $\bar{\alpha} = 106.5^\circ$ (1.859 radian)

Step 5. Equation (9) to calculate $C_A(\alpha)$ from 0- to 180-degrees angle of attack.

(a) $C_A(\alpha)$ from 0 to $\bar{\alpha}$ (106.5°) is shown in Table 9

(b) $C_A(\alpha)$ from 0 to $\bar{\alpha}$ (106.5° to 160°) is shown in Table 10.

(c) $C_A(\alpha)$ from 160° to 180° is $C_A(\alpha) = -C_{A_\pi} = -1.750$.

Employing the outlined procedure, $C_A(\alpha)$ was determined for the 10-caliber finned body shown in Figure 14, for a Mach number range from 1.5 to 3.0.

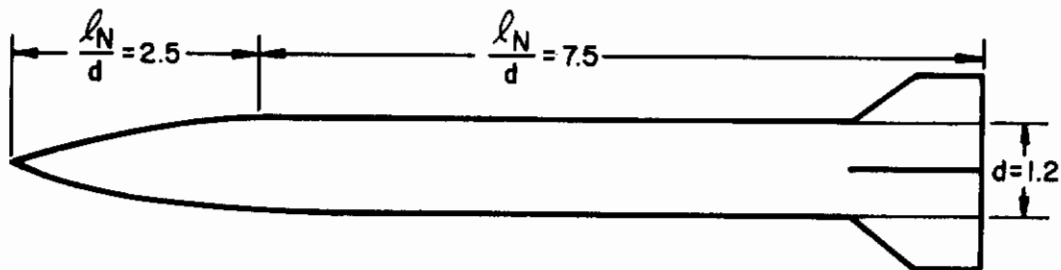


Figure 14. Ten-Caliber Finned Body

TABLE 9. SAMPLE CALCULATION OF $C_A(\alpha)$, $0 \leq \alpha \leq 160.5^\circ$

α	$\left[1 - \frac{3\alpha^2}{2} + \frac{2\alpha^3}{3}\right]$	$\left[\alpha - \frac{2\alpha^2}{3} + \frac{\alpha^3}{6}\right]$	$\left[\frac{\alpha^3}{2} - \frac{\alpha^2}{\alpha}\right]$	$C_{A_0} \left[1 - \frac{3\alpha^2}{2} + \frac{2\alpha^3}{3}\right]$	$C_{A_\alpha} \left[\alpha - \frac{2\alpha^2}{3} + \frac{\alpha^3}{6}\right]$	$C_{A_{\overline{\alpha}}} \left[\frac{\alpha^3}{2} - \frac{\alpha^2}{\alpha}\right]$	$C_A(\alpha)$
0	1.000	.000	.000	.300	.000	.000	.300
10	.975	.143	-.015	.293	.083	.028	.404
20	.907	.230	-.053	.272	.133	.098	.503
30	.807	.270	-.106	.242	.157	.195	.594
40	.683	.272	-.164	.205	.158	.302	.665
50	.546	.246	-.217	.164	.143	.399	.706
60	.406	.200	-.258	.122	.116	.474	.712
70	.272	.144	-.275	.082	.084	.506	.672
80	.155	.086	-.261	.047	.050	.480	.577
90	.065	.038	-.206	.020	.022	.379	.421
100	.011	.006	.100	.003	.003	.184	.190
160.5	.000	.000	.000	.000	.000	.000	.000

TABLE 10. SAMPLE CALCULATION OF $C_A(\alpha)$, $\bar{\alpha} < \alpha \leq 160^\circ$

α	$\left[1 - \frac{(160 - \alpha)^2}{(160 - \bar{\alpha})^2} \right]$	$-C_{A\pi} \left[1 - \frac{(160 - \alpha)^2}{(160 - \bar{\alpha})^2} \right]$	$C_A(\alpha)$
106.5	0.000	0.000	0.000
110	0.127	-0.222	-0.222
120	0.441	-0.772	-0.772
130	0.686	-1.200	-1.200
140	0.860	-1.505	-1.505
150	0.965	-1.689	-1.689
160	1.000	-1.750	-1.750

Figure 15 presents a comparison of the predicted values with the wind tunnel data, and clearly shows that C_A as a cubic function of α , Equation (8), yields better correlation than a quadratic.

NORMAL FORCE COEFFICIENT

The basic assumption in the semi-empirical method used by Reference 1 is that the total aerodynamic force acting on a missile configuration can be represented by the sum of each individual element and interference effect. For example, the normal force coefficient for a fin-body configuration, $C_{NB(T)}$ would be the sum of the body alone plus tail and interference effects. Therefore,

$$C_{NB(T)} = C_{NB} + 2C_{NT} R_{T(B)} \frac{S_T}{S_B} + I_{B(T)} \quad (11)$$

Each term is derived by using a power series expansion and establishing boundary conditions based upon wind tunnel test data. Validity of the prediction methods, i.e., Equation (11), was confirmed by comparisons with wind tunnel experiments.

To gain some insight into the prediction methodology developed in Reference 1, comparisons were made with the body buildup wind tunnel data of

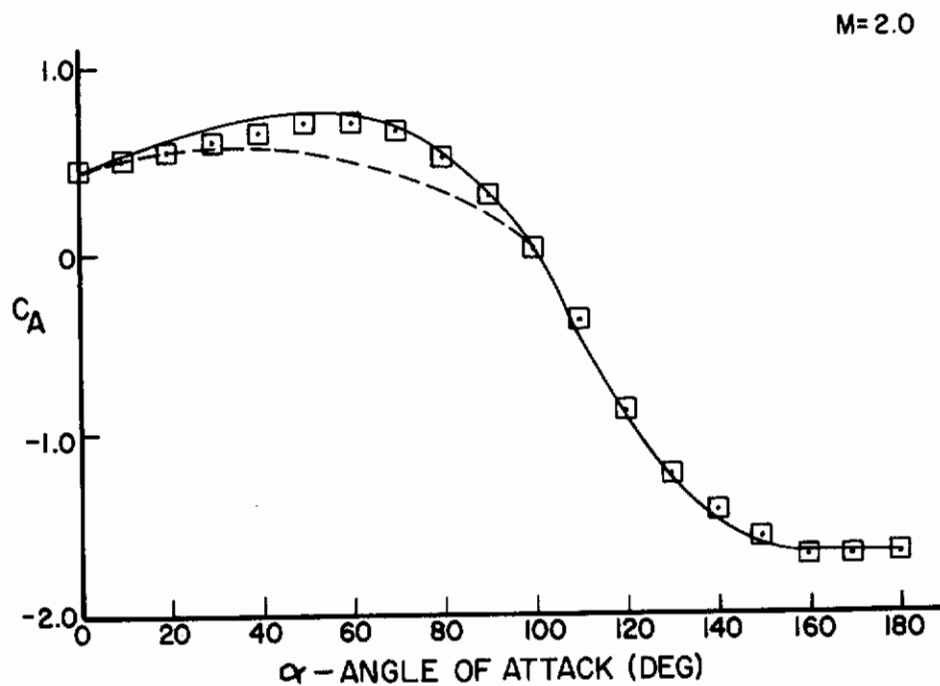
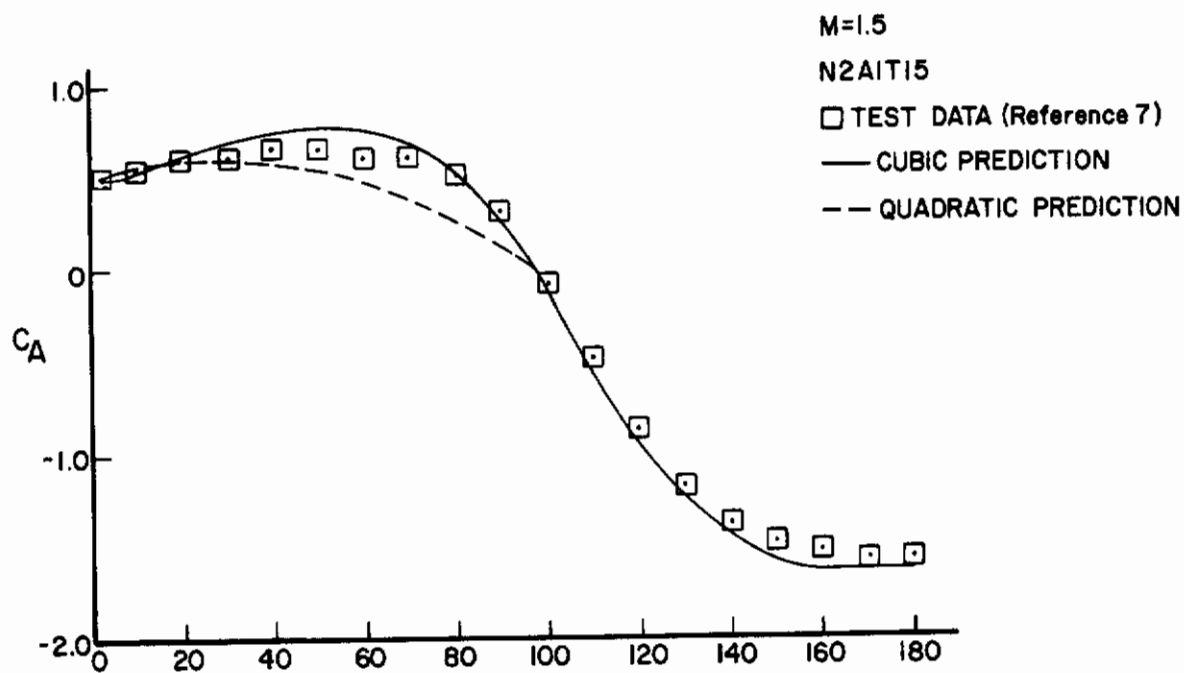


Figure 15. Comparison Prediction Method with Wind Tunnel Data, Finned Body

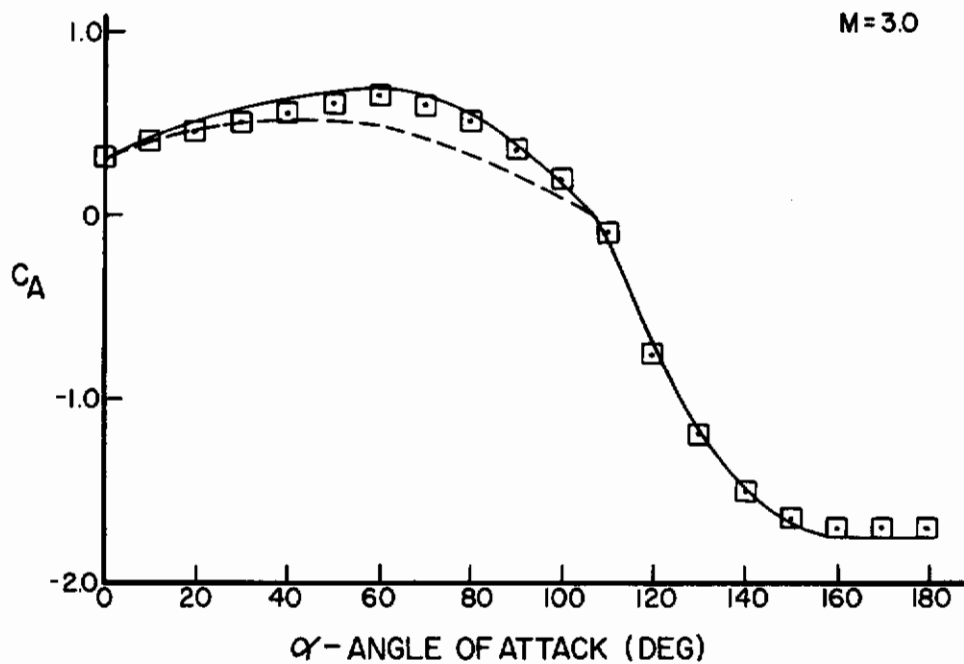
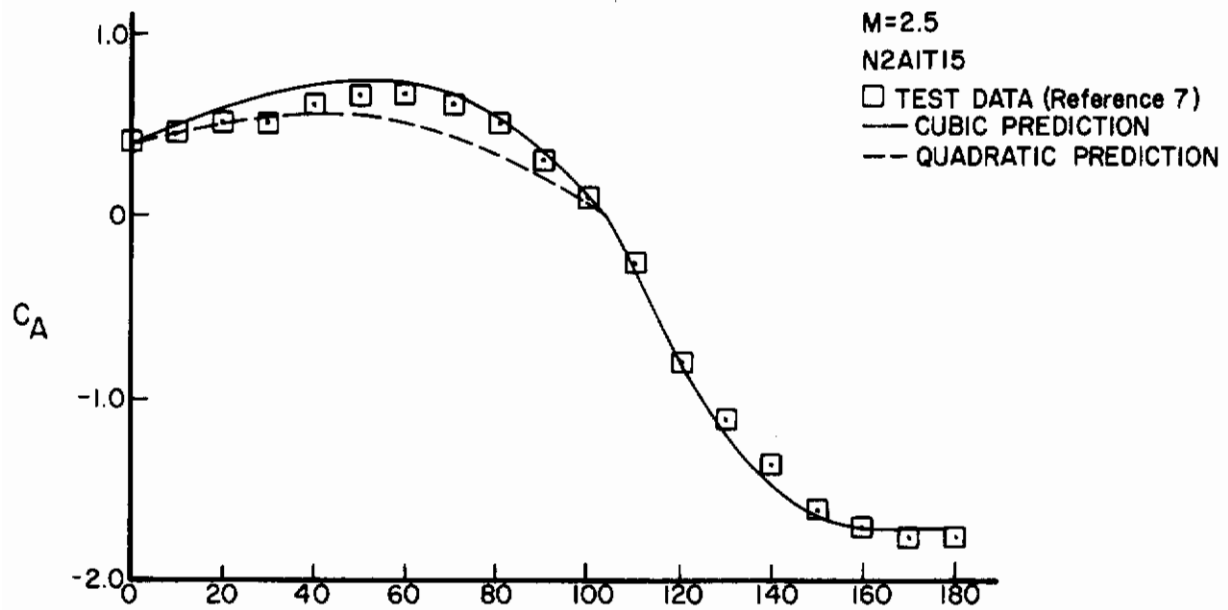


Figure 15. Comparison Prediction Method with Wind Tunnel Data, Finned Body (concluded)

the Air Slew Flight Demonstration Missile, References 7 and 9. As previously shown in Figure 14, this configuration is a 10-caliber finned body. The normal force coefficient, C_N , and the center of pressure were evaluated as a function of angle of attack at a Mach number of 2.0.

Effects on Tail Only

Figure 16(a) compares wind tunnel data to the Reference 1 prediction method of the tail-only normal force coefficient, C_{N_T} , at Mach 2.0. In order to isolate the fin/tail contribution from the total body effects, a reflection plane technique was used in wind tunnel tests. This reflection plane caused the air flow ahead of the fin to separate between 65- and 125-degrees angle of attack. This air flow separation caused a net reduction in measured C_{N_T} values, thus creating the drop in the C_{N_T} wind tunnel curve between 65 and 125 degrees [see Reference 7 and Figure 16(a)].

The normal force coefficient prediction method aligned itself closely with the wind tunnel data. The divergence in data between 65- and 125-degrees angle of attack, discussed above, prevents precise determination of the maximum normal force coefficient value and angle of attack. However, the smooth curve trend of the prediction method indicates a high accuracy probability.

Tail with Body Effects

There are three variables which affect the overall normal force on the tail of a body-tail configuration (Reference 1): load carrying carryover effects due to external lifting surfaces (C_{N_T}); normal force acting on the "undeflected" tail configuration ($I_{B(T)}$); and interference due to body-indirect upwash and lee-side vortex downwash with tail flow field ($R_{T(B)}$).

Using the Reference 1 prediction technique, the normal force relationship becomes:

$$C_{N_{T(B)}} = C_{N_T} \times R_{T(B)} + \frac{1}{2} I_{B(T)} \quad (12)$$

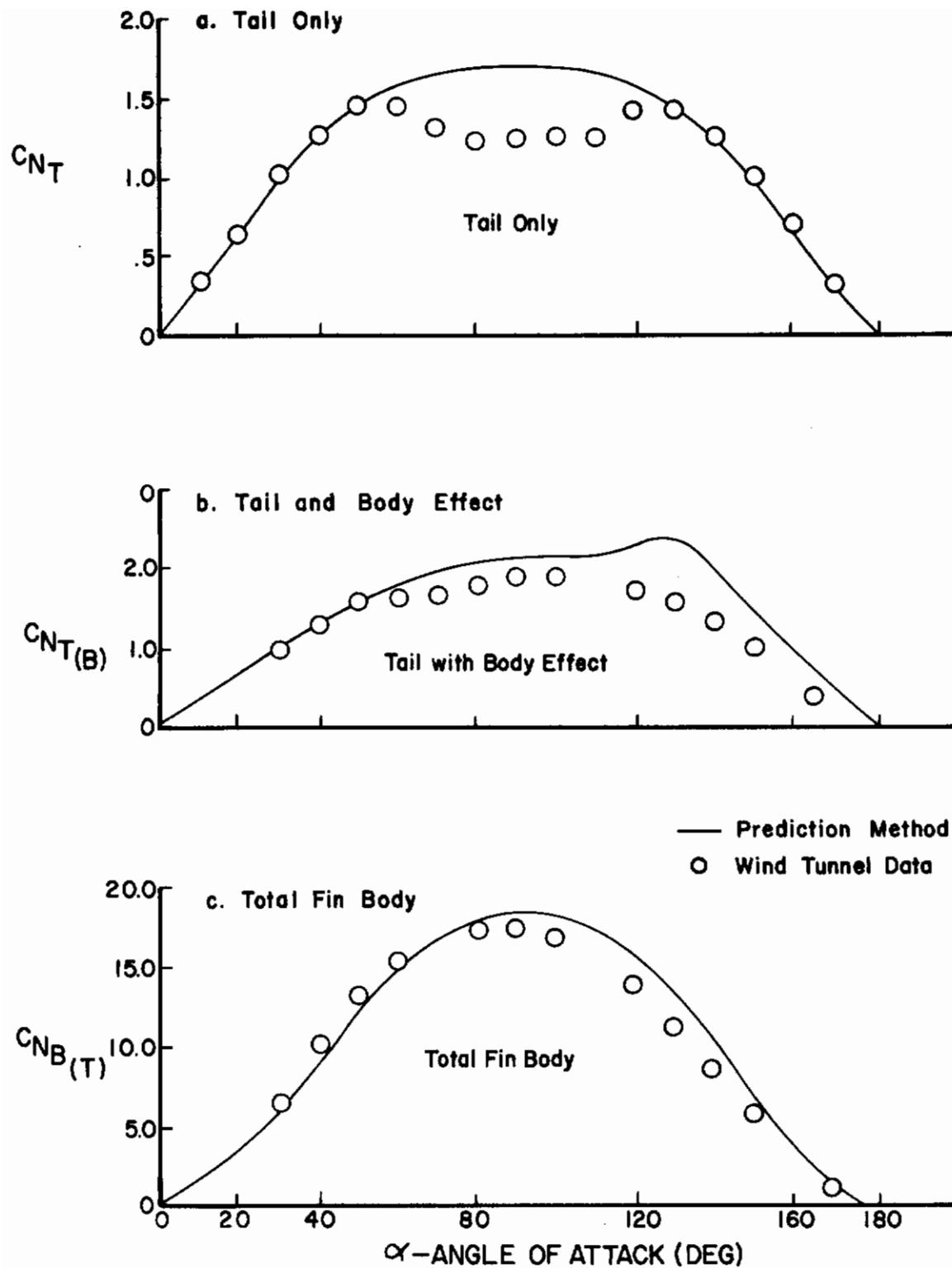


Figure 16. Normal Force Coefficient Versus Angle of Attack for the 10-Caliber Finned Body

From Equation (12), $C_{NT(B)}$ is predicted and compared to the wind tunnel results found in Reference 9. Figure 16(b) shows the comparison of wind tunnel data and the prediction method of Equation (12) for the 10-caliber body in Figure 14 at Mach 2. There is good agreement up to 50-degrees angle of attack. At angles greater than 50 degrees, the prediction method and the experimental data start to diverge. Equation (12) and the wind tunnel data showed poor correlation between 120 and 140 degrees. Evaluating each term in Equation (12), the following conclusions were made:

1. C_{NT} term is probably a representative value throughout the 0- to 180-degree angle of attack range. The C_{NT} prediction method has shown consistently good comparisons with wind tunnel results. Pages 120 and 121 in Reference 1 plus Figure 16 are examples of the C_{NT} prediction and wind tunnel results.
2. The $C_{NT} \times R(B)$ term whose results are presented in Figure 17 seems to replicate wind tunnel results. Though no $C_{NT} \times R_{T(B)}$ wind tunnel data for the Figure 14 configuration were available, similar configurations tested in the supersonic Mach ranges were found in Reference 1, pages 156-159. These data showed close resemblance to the predicted values.
3. There are limited data on $I_{B(T)}$. Reference 1 divides the $I_{B(T)}$ function into three regions: they are angles of attack 0 to 90 degrees, 90 to 115 degrees, and 115 to 180 degrees. The greatest variance between experimental and predicted $C_{NT(B)}$ occurs between 110 and 140 degrees. Also, the overall $C_{NT(B)}$ differences seem to increase as the angles of attack increase through the $I_{B(T)}$ regions. Therefore, it is believed that further analysis of wind tunnel data would develop better $I_{B(T)}$ results, thus leading to a better predictability of $C_{NT(B)}$.

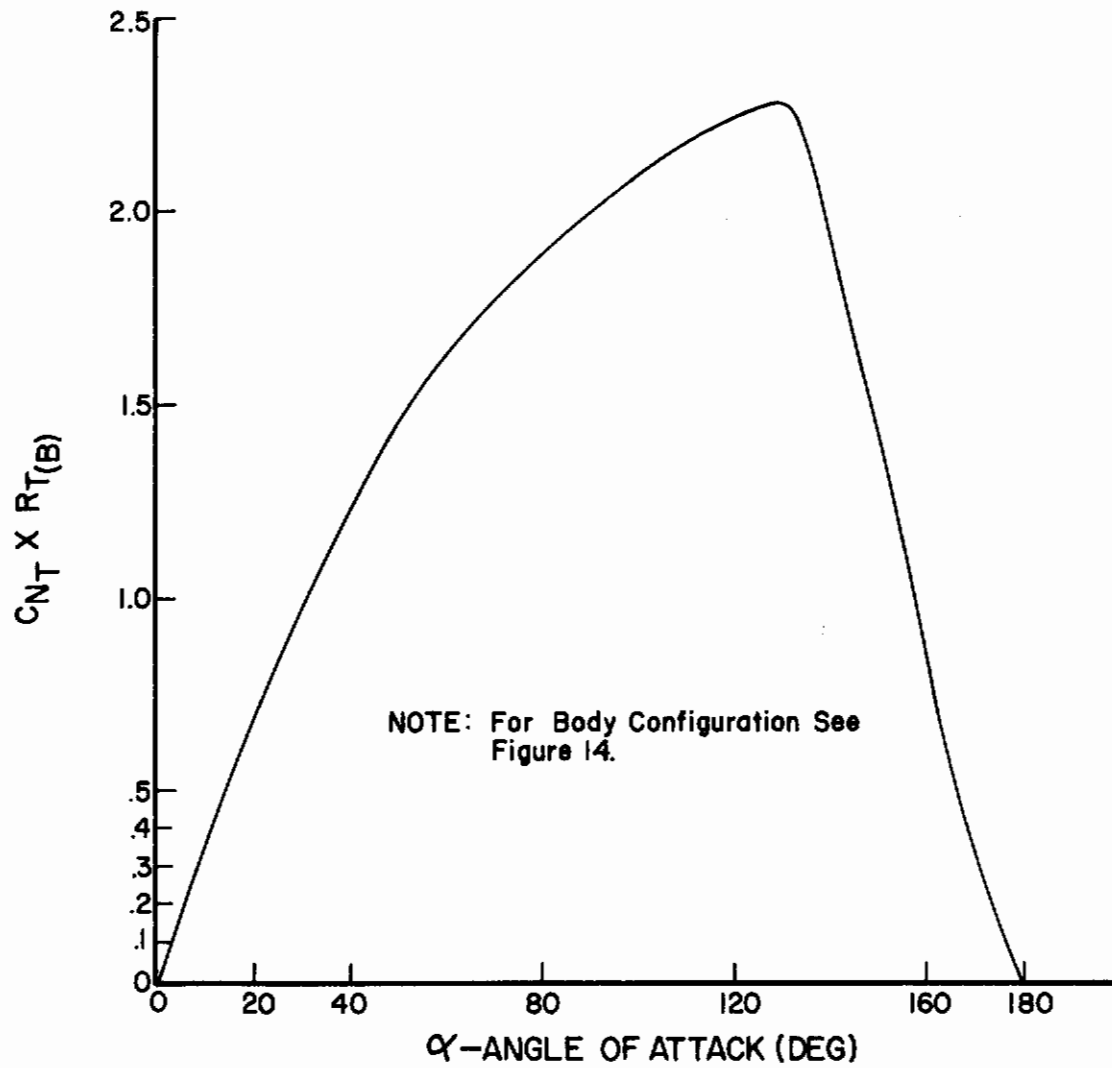


Figure 17. $C_{N_T} \times R_{T(B)}$ Versus Angle of Attack for a 10-Caliber Finned Body Using Prediction Method (Reference 1)

Body with Tail Effect

Figure 16 shows the Reference 1 prediction and wind tunnel data comparison for normal force coefficient for the total body tail configuration, $C_{NB(T)}$. The wind tunnel data were taken from Reference 9.

The Reference 1 prediction method shows good correlation with the wind tunnel results for the 10-caliber configuration shown in Figure 13 at Mach 2. For 0- to 100-degree angles of attack, the two sets of data were in agreement. For angles greater than 100 degrees, the Reference 1 prediction showed higher $C_{NB(T)}$ values than the wind tunnel results. The higher $C_{NB(T)}$ values for the prediction method was felt to be caused by the $I_{B(T)}$ effects, thus suggesting that the $I_{B(T)}$ term should be considered for future wind tunnel investigations.

Summary

A complete evaluation of the technique developed in Reference 1 is beyond the scope of this report; however, the importance of the Reference 1 method warrants some comments. The method developed by Reference 1 is good for making $C_{NB(T)}$ and $X_{CPB(T)}$ predictions and correlates well with wind tunnel results.

Examining the data in Figure 16, there are slight differences between wind tunnel and the Reference 1 prediction method at the higher angle of attack region. It is believed that the differences are affected by the interference and carry-over effects parameters used in the methodology (see subsection Tail with Body Effects). As previously stated, adequate data were not available for in-depth analysis and further testing on the interference/carry-over effects should be carried out.

CENTER OF PRESSURE

Like the normal force coefficient, the center of pressure methodology was also studied by comparing the wind tunnel data to the Reference 1 prediction technique. This section discusses the results from this analysis. Again the wind tunnel data of Reference 7 and 9 were used.

Figure 18 shows the center of pressure comparison between the predicted method and wind tunnel results. Figure 19 shows the same comparison but for the fin-only configuration--no body effects were present. The conclusions were that the tail-only center of pressure, X_{CP_T} , prediction methods were identical to the wind tunnel data; and the centers of pressure prediction method for the total configuration, i.e., overall fin body configuration, $X_{CP_{B(T)}}$, and the tail configuration including body effects, $X_{CP_{T(B)}}$, were also very representative of the wind tunnel results.

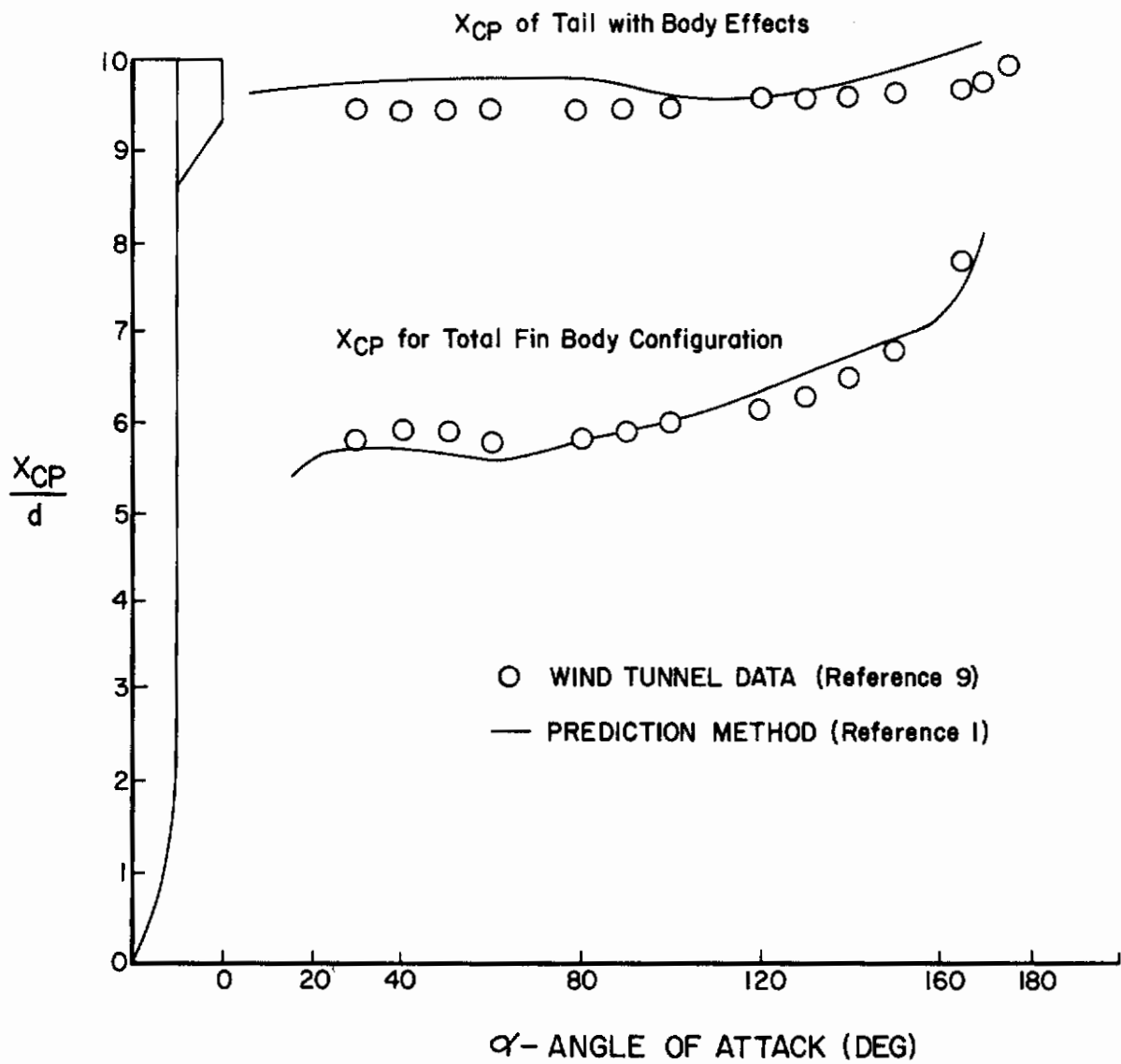


Figure 18. Center of Pressure Versus Angle of Attack for 10-Caliber Finned Body

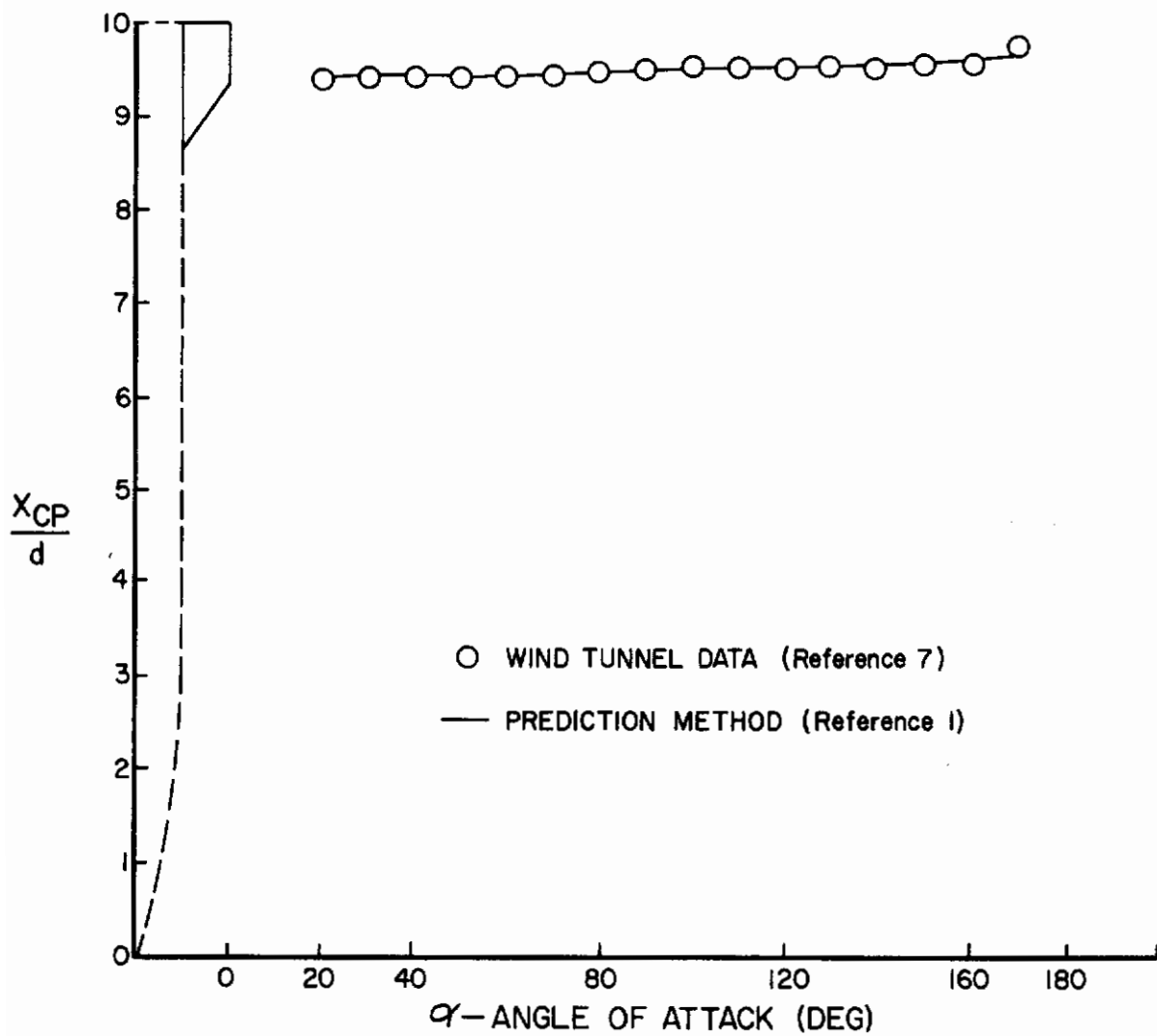


Figure 19. Tail Only Center of Pressure Versus Angle of Attack for 10-Caliber Finned Body

SECTION V
CONCLUSIONS

The semi-empirical methodology of Reference 1 for predicting the axial and normal force coefficients and the center of pressure for missile has been extended to include the effects of nose bluntness. The extended methodology was developed using the wind tunnel data contained in Reference 2. In addition, a method was developed for predicting the axial force coefficient for finned bodies at supersonic speeds. These methods correlated well with wind tunnel test data over the 0- to 180-degree angle of attack range.

For a 10-caliber finned body, calculation of the normal force coefficient and the center of pressure were determined from Reference 1. This analysis showed that overall, good agreement was obtained. However, the prediction of the fin normal force in the presence of the body showed a peculiar digression at high angles of attack. This digression was attributed to the effects of the body-fin interference and carry-over terms.

Based on the analysis of the methodology of Reference 1, with the extensions contained in this study, preliminary design aerodynamic prediction techniques have been developed for finned missiles with varying nose bluntness. Initial evaluations of these techniques indicate that good agreement is obtained; however, more analysis is required to thoroughly evaluate the applicability of the methodology. It is recommended that a detailed sensitivity analysis be conducted to identify the most influential parameters of the methodology. Further analysis of the prediction methodology compared to wind tunnel test data of missiles such as the Sidewinder and Sparrow would identify the critical areas needing improvement.

APPENDIX

WIND TUNNEL DATA USED FOR NOSE
BLUNTNESS METHODOLOGY DEVELOPMENT

Plots of the tabulated data contained in Reference 2 are presented in the following pages. It is felt that these data furnish a valuable base for missile aerodynamic analyses. The axial and normal force coefficients and center of pressure were obtained for a 0- to 14-degree range in angle of attack, Mach numbers from 0.6 to 4.0, nose calibers of 2, 3, and 4, nose bluntness ratios of 0.0, 0.25, 0.50, and 0.75, and afterbody fineness ratios of 6 and 10. For the afterbody fineness ratio of 8, the aerodynamic data were obtained for the same nose shapes and angles of attack, but the Mach number range was limited to only the supersonic regime, 1.5 to 4.0.

Axial Force Coefficients

Figures A-1 through A-19 present C_A as a function of angle of attack and Mach number for the range in configurational parameters previously stated. For Mach Numbers of 0.6, 0.8, and 1.0, nose bluntness is seen to have little or no effect on the axial force coefficient. However, significant variations in C_A are apparent for the Mach numbers from 1.2 to 4.0. It is noted for the latter Mach numbers that the change in C_A with angle of attack is approximately the same for all nose bluntness ratios.

C_{A_0} is presented in Figures A-20 through A-22 as a function of R_N/R_B for the Mach numbers and the various nose and afterbody fineness ratios of the test program. These data indicate that the change in C_{A_0} with R_N/R_B increases with increasing Mach number. As would be expected, these data show C_{A_0} increasing with decreased ℓ_N/d and increased ℓ_A/d for a given Mach number and nose bluntness ratio.

Normal Force Coefficient

Figures A-23 through A-79 present C_{N_B} as a function of angle of attack and Mach number for the range in configurational parameters previously stated. Most figures contain only the 0.0 and 0.75 nose bluntness ratio data point to indicate the variations. These data indicate that at small angles of attack and Mach numbers from 0.6 to 1.5 C_{N_B} is insensitive to nose bluntness effect. Only at the higher angles of attack and Mach numbers does the effect of nose bluntness become apparent.

Center of Pressure

Figures A-80 through A-136 present the nondimensional center of pressure, X_{CP} , as a function of angle of attack and Mach number for the various configurations tested. In some instances, only those nose bluntness data which best represent the trends are presented. All values of X_{CP} are measured from the tip of the pointed ogive configurations, thus using the same reference point for each of the three families of nose configurations shown in Figure 1. X_{CP} was obtained over a positive and negative range in angle of attack, as shown in Figure A-80. The large variation in X_{CP} shown here was typical in the transonic region, with both transonic and supersonic data showing a wide range of scatter for the angles of attack near zero.

In order to extend the methodology of Reference 1 to include the effects of nose bluntness, it was necessary to obtain the zero angle of attack center of pressure, X_0 . To determine X_0 , a second order polynomial was fitted to the results contained in Figures A-80 through A-136 using a least squares fitting routine available of the CDC-6600. All these data, contained in the Appendix, were used with the exception of Mach 0.6, since it was not included in the methodology of Reference 1.

To successfully fit the transonic data, only the positive angle of attack information could be used, excluding the points from 0 to 2 degrees. Figures A-86 through A-103 present the data points used in the fits, and the resultant X_0 is indicated by a flagged symbol. For the supersonic Mach numbers, the positive and negative angle of attack data were used excluding the points from -2 to +2 degrees. Figures A-104 through A-136 show the data used in the least squares fits, and the flagged symbols indicate the resultant X_0 values.

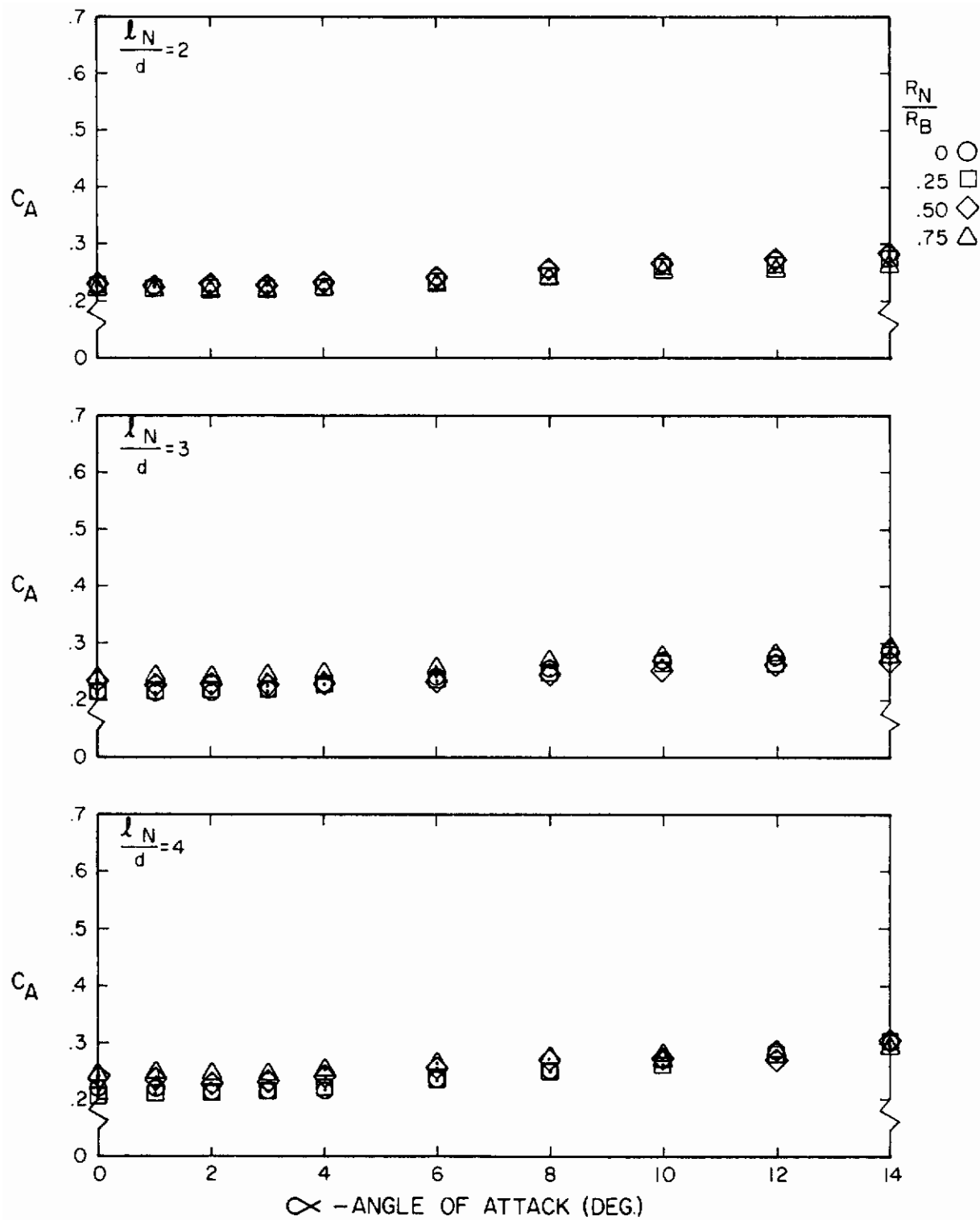


Figure A-1. Axial Force Coefficient Versus Angle of Attack for $l_A/d = 6$, $M = 0.6$

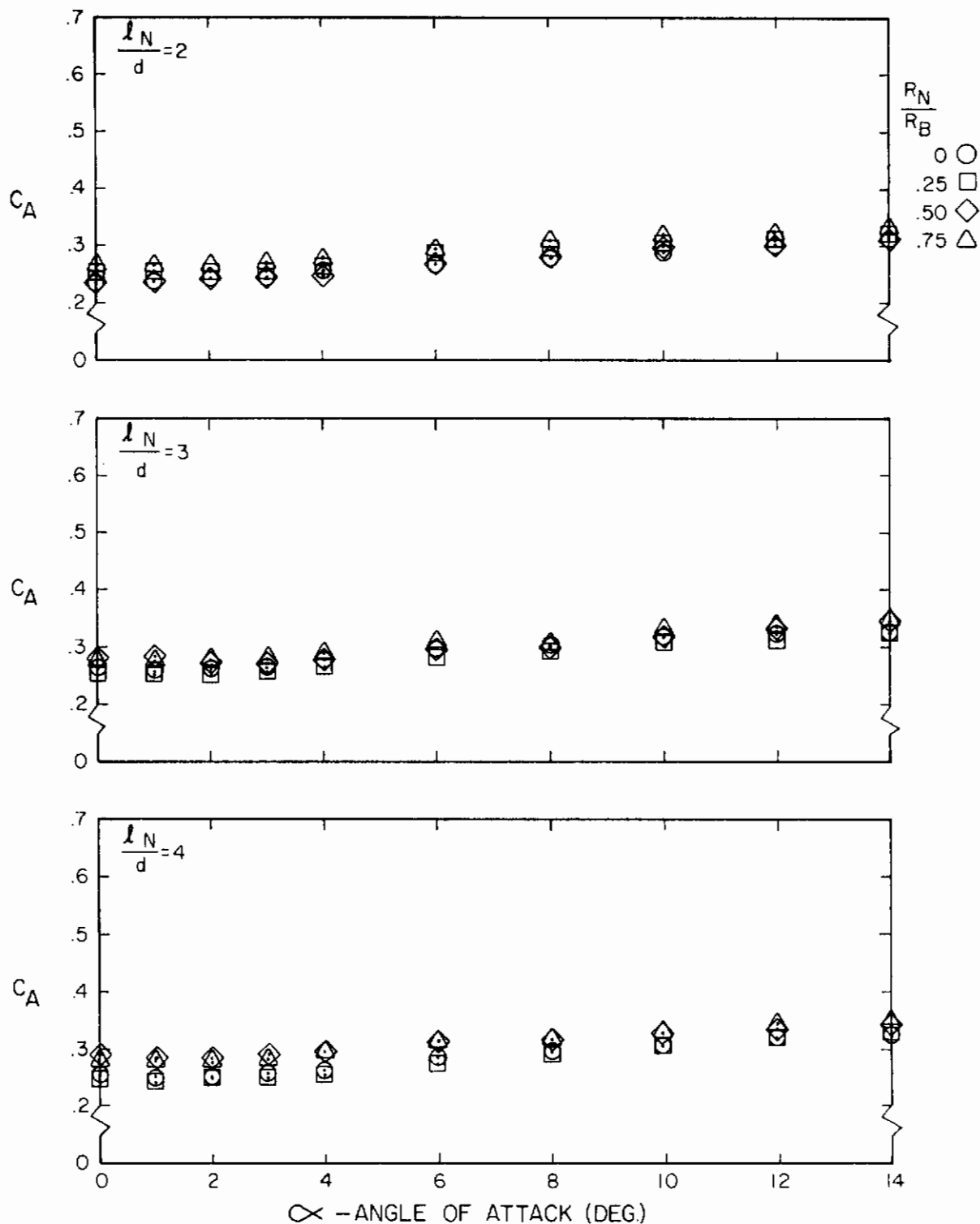


Figure A-2. Axial Force Coefficient Versus Angle of Attack for $l_A/d = 10$, $M = 0.6$

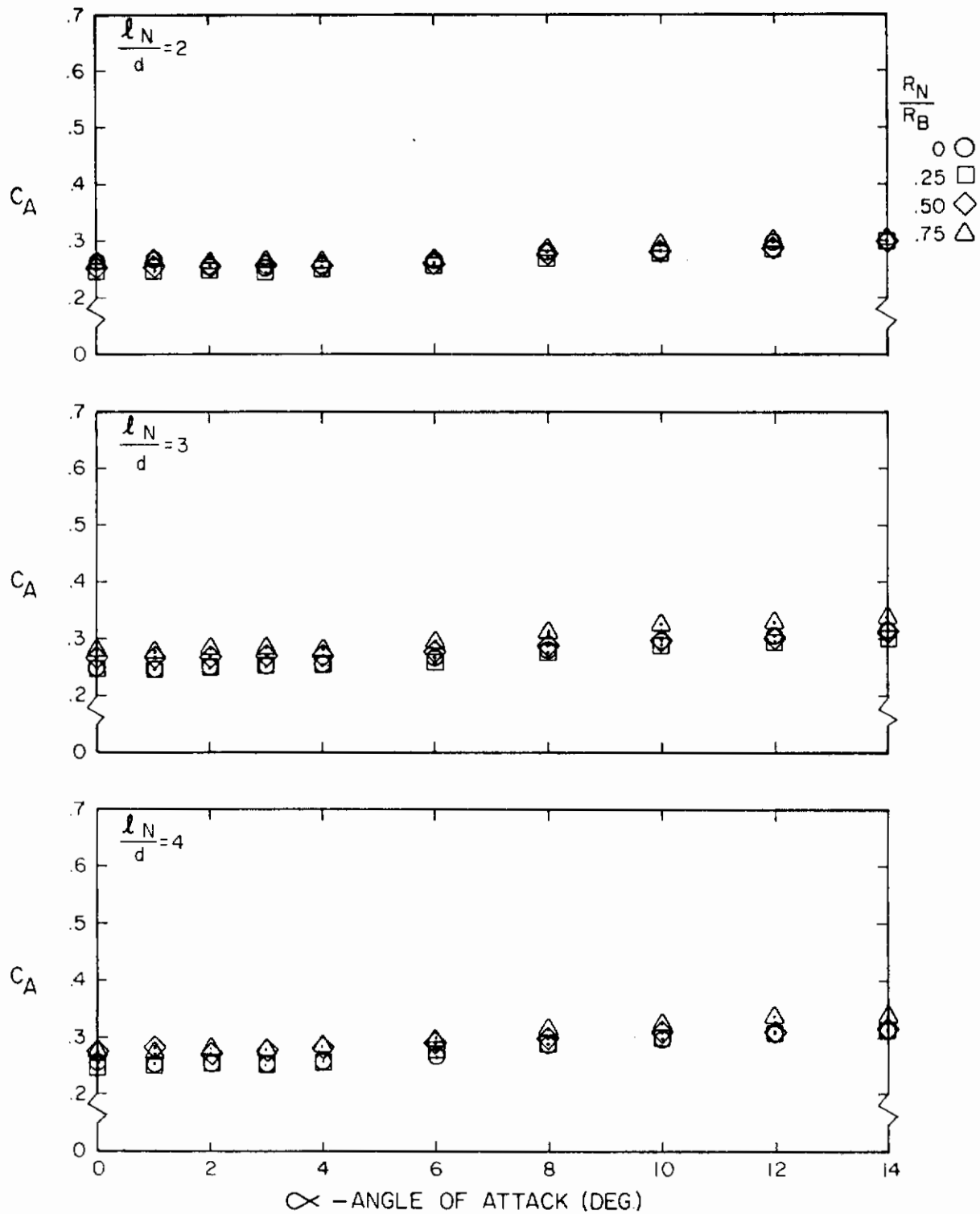


Figure A-3. Axial Force Coefficient Versus Angle of Attack for $l_A/d = 6$, $M = 0.8$

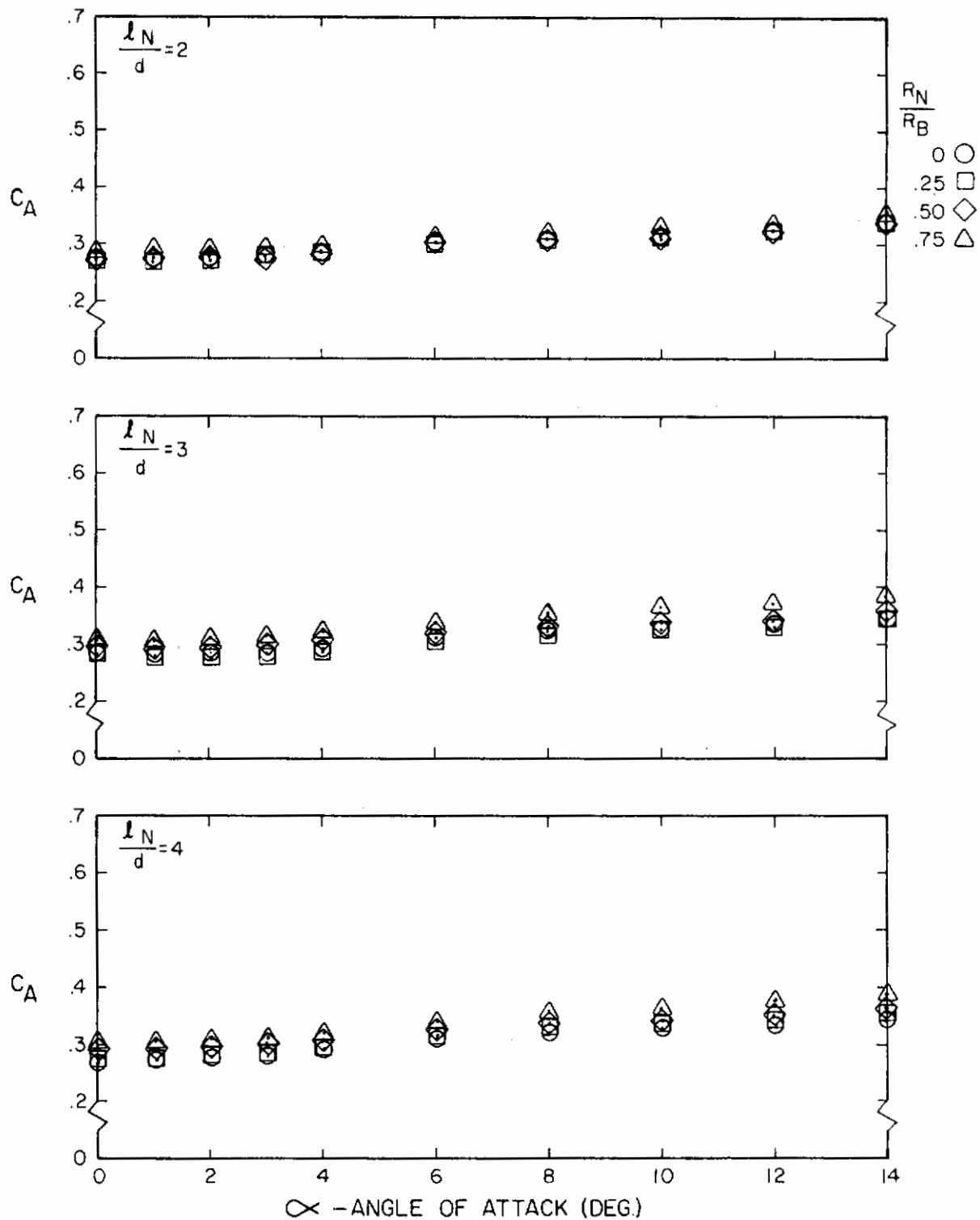


Figure A-4. Axial Force Coefficient Versus Angle of Attack for $l_A/d = 10$, $M = 0.8$

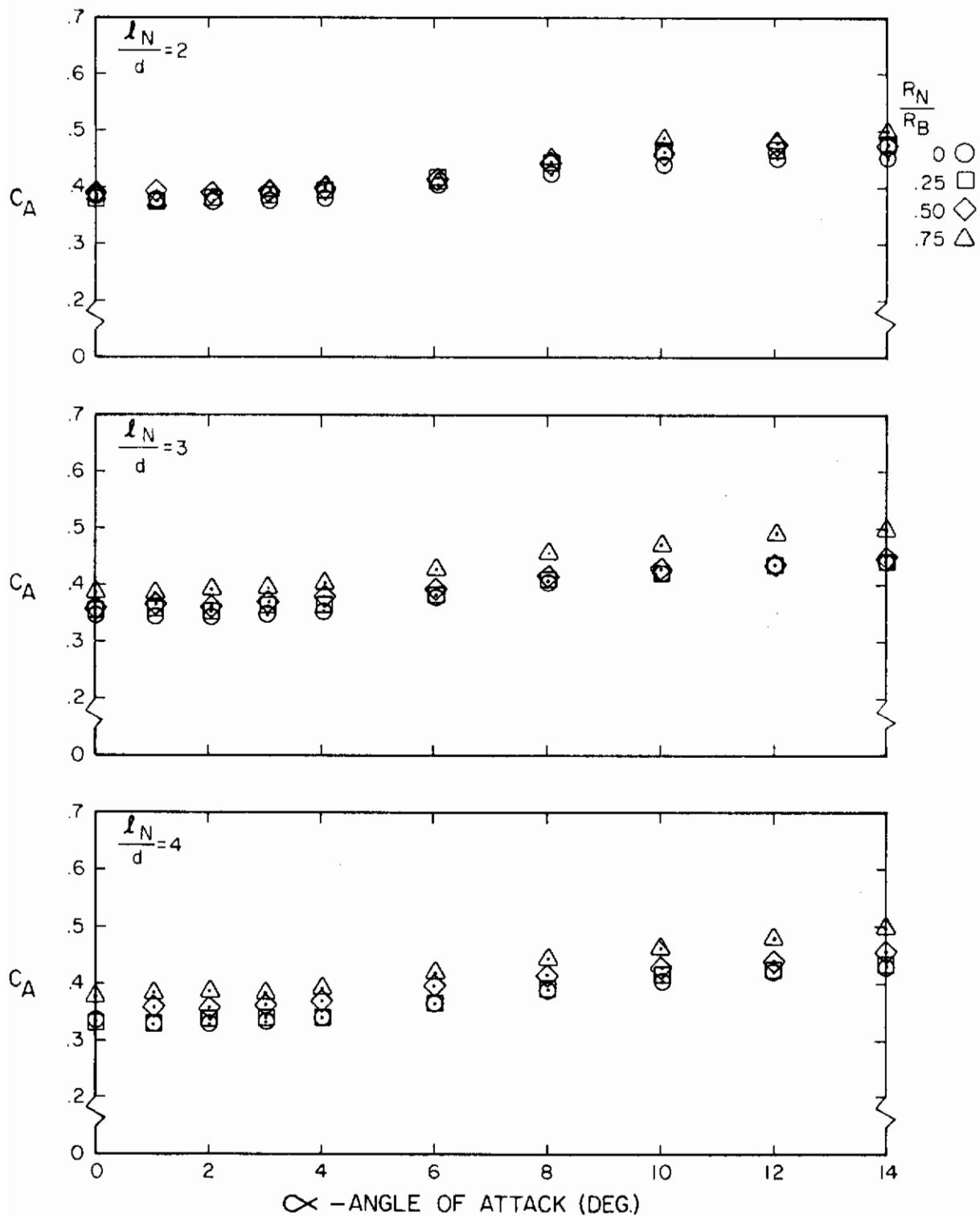


Figure A-5. Axial Force Coefficient Versus Angle of Attack for $l_A/d = 6$, $M = 1.0$

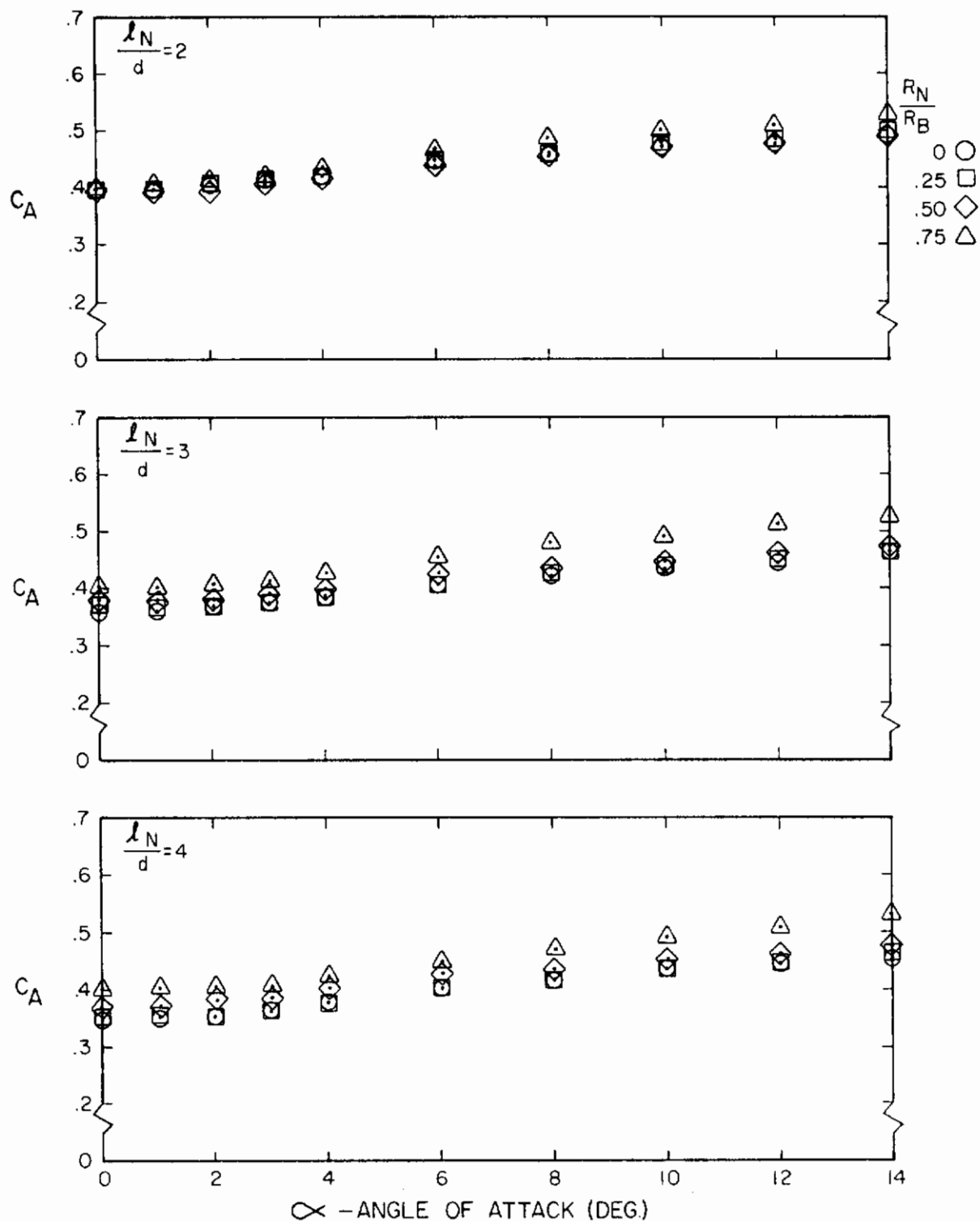


Figure A-6. Axial Force Coefficient Versus Angle of Attack for $l_A/d = 10$, $M = 1.0$

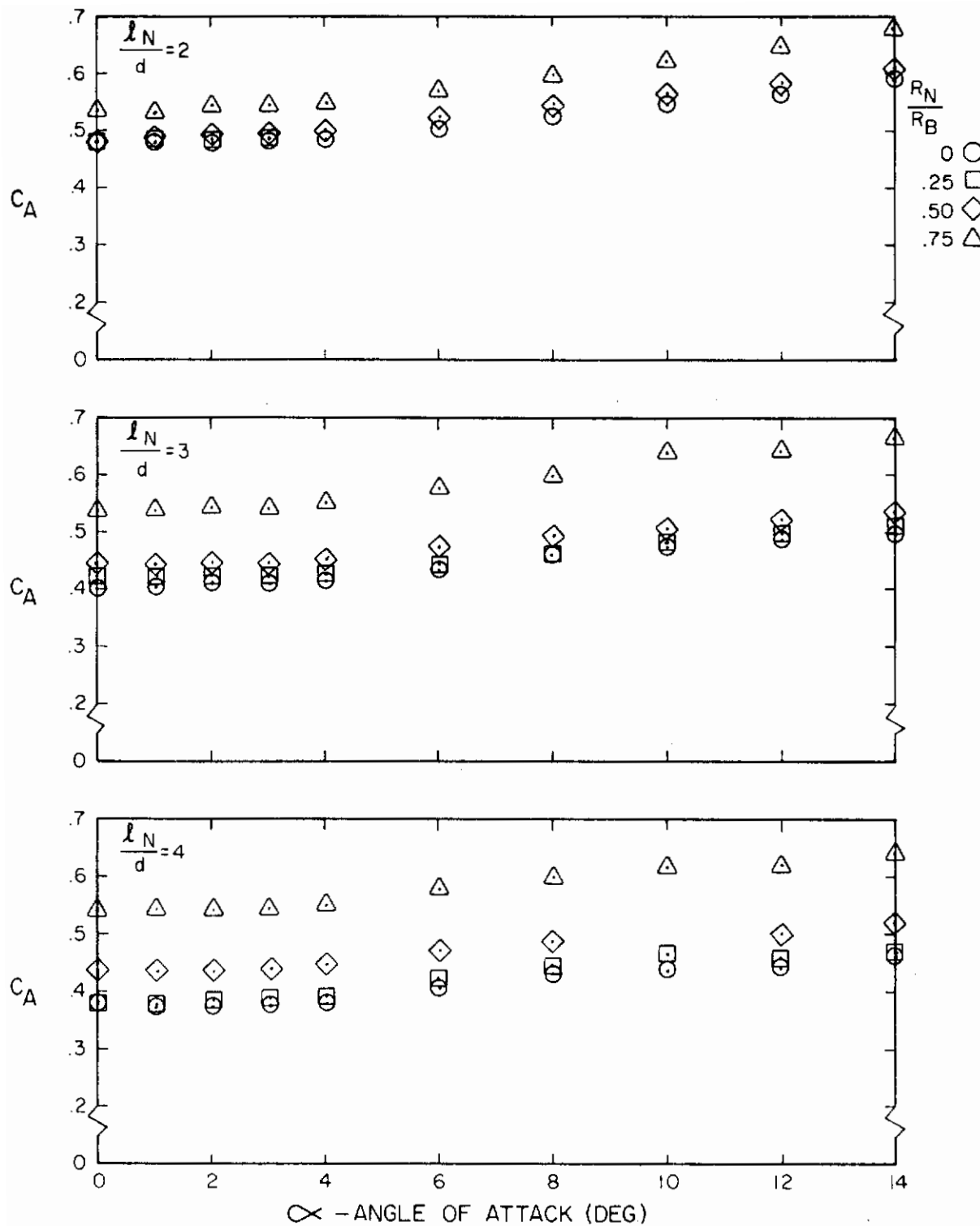


Figure A-7. Axial Force Coefficient Versus Angle of Attack for $\frac{l_A}{d} = 6$, $M = 1.2$

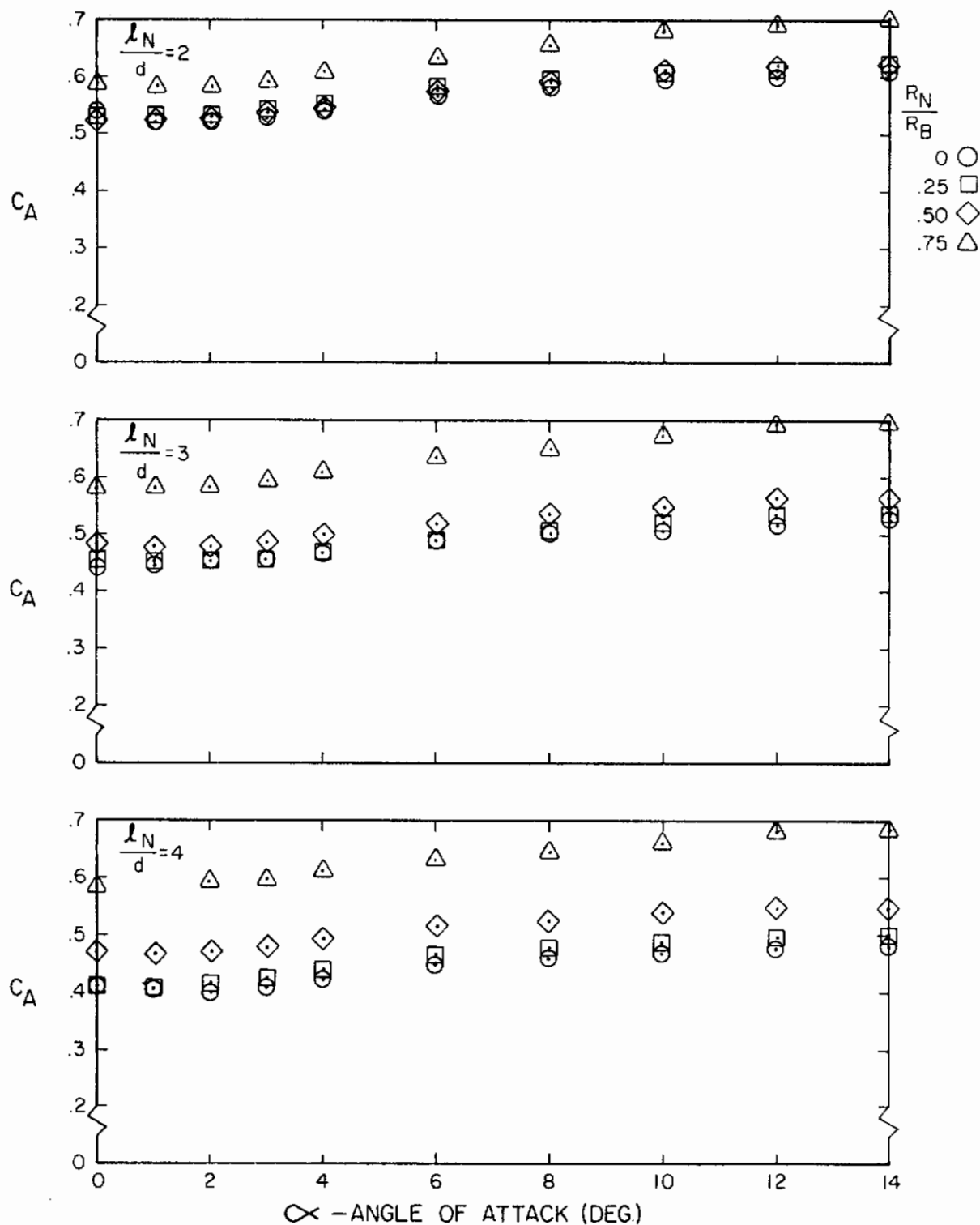


Figure A-8. Axial Force Coefficient Versus Angle of Attack for $\frac{l_A}{d} = 10$, $M = 1.2$

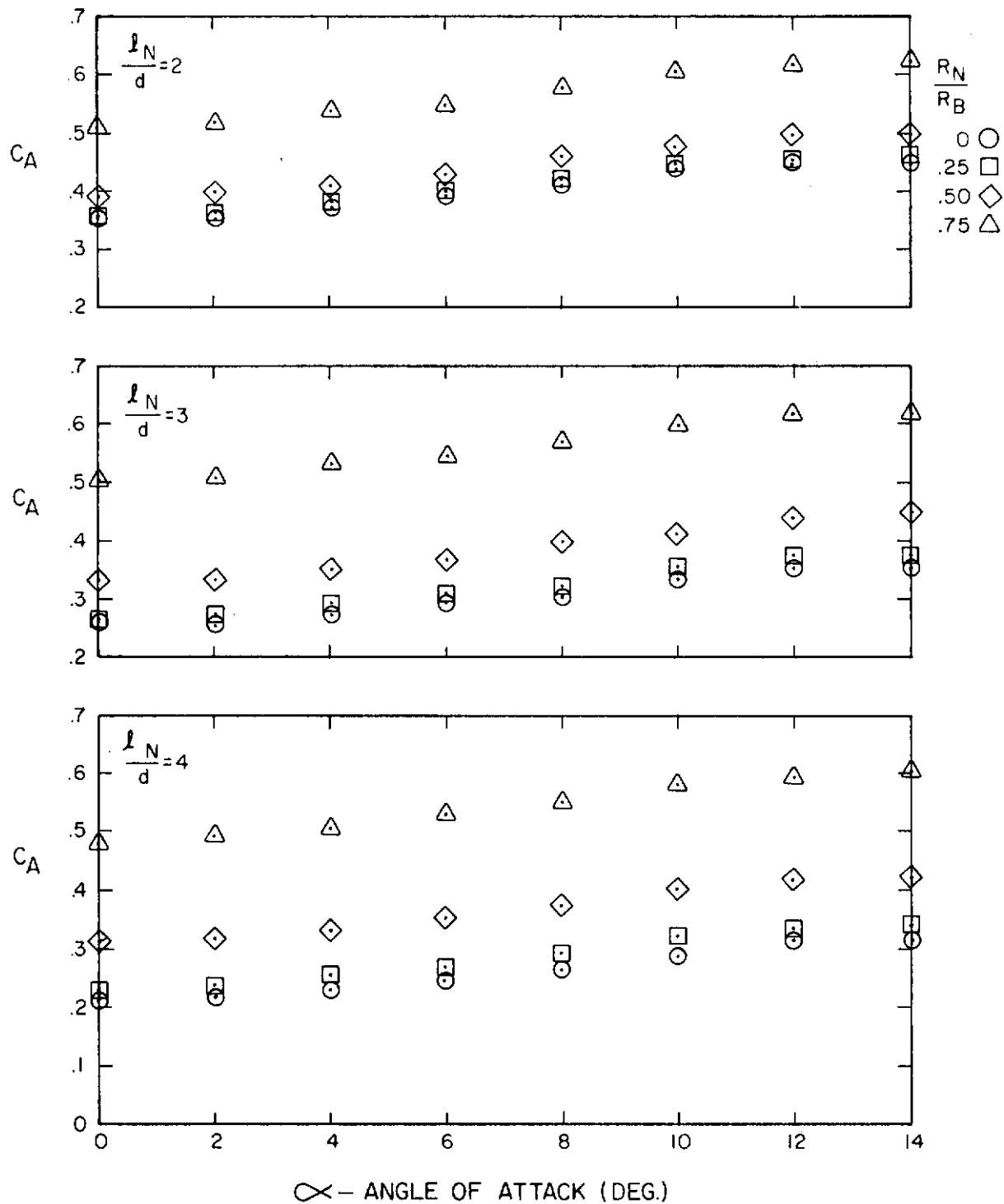


Figure A-9. Axial Force Coefficient Versus Angle of Attack for $\frac{l_A}{d} = 6$, $M = 1.5$

Contrails

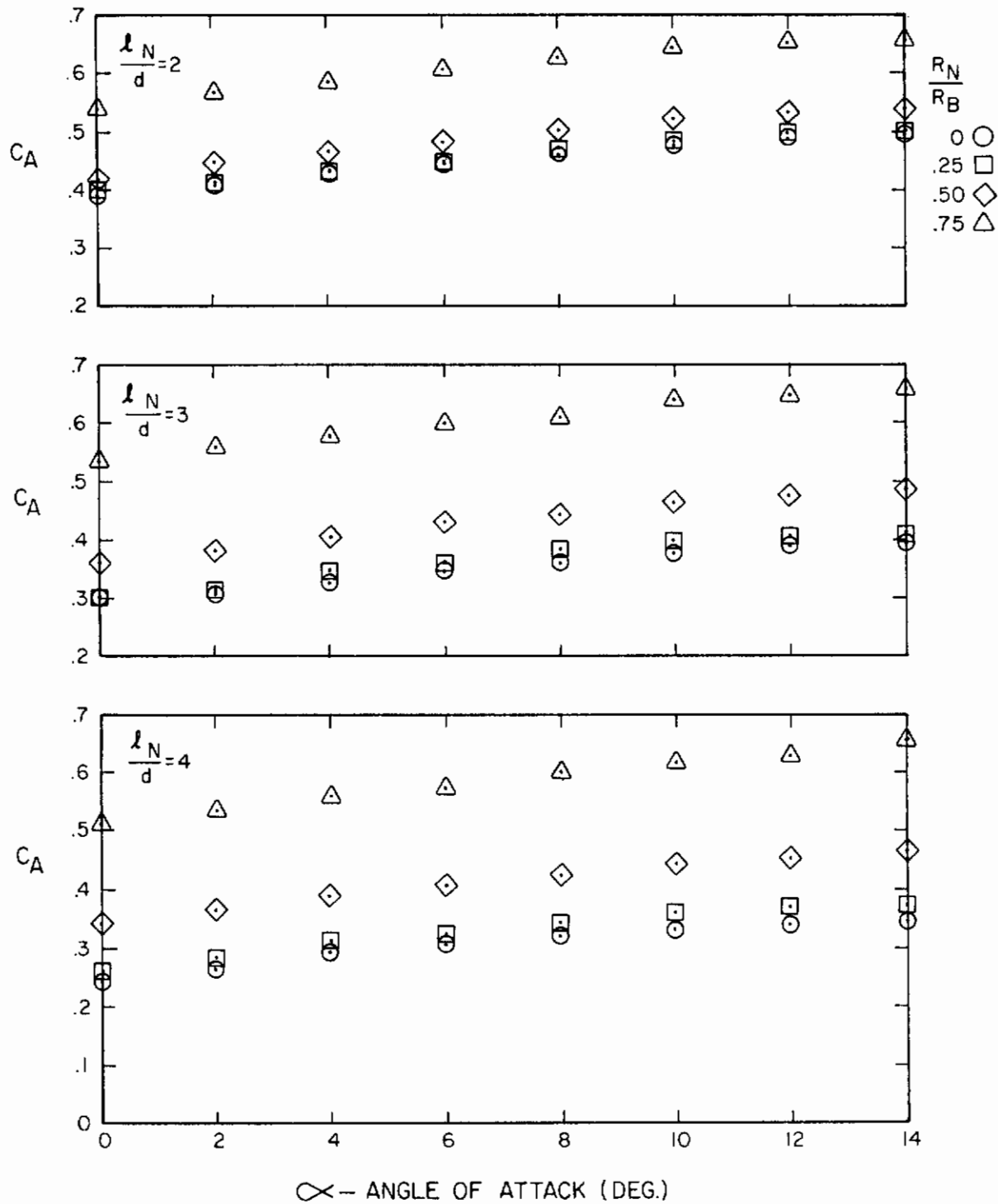


Figure A-10. Axial Force Coefficient Versus Angle of Attack for $l_A/d = 6$, $M = 1.5$

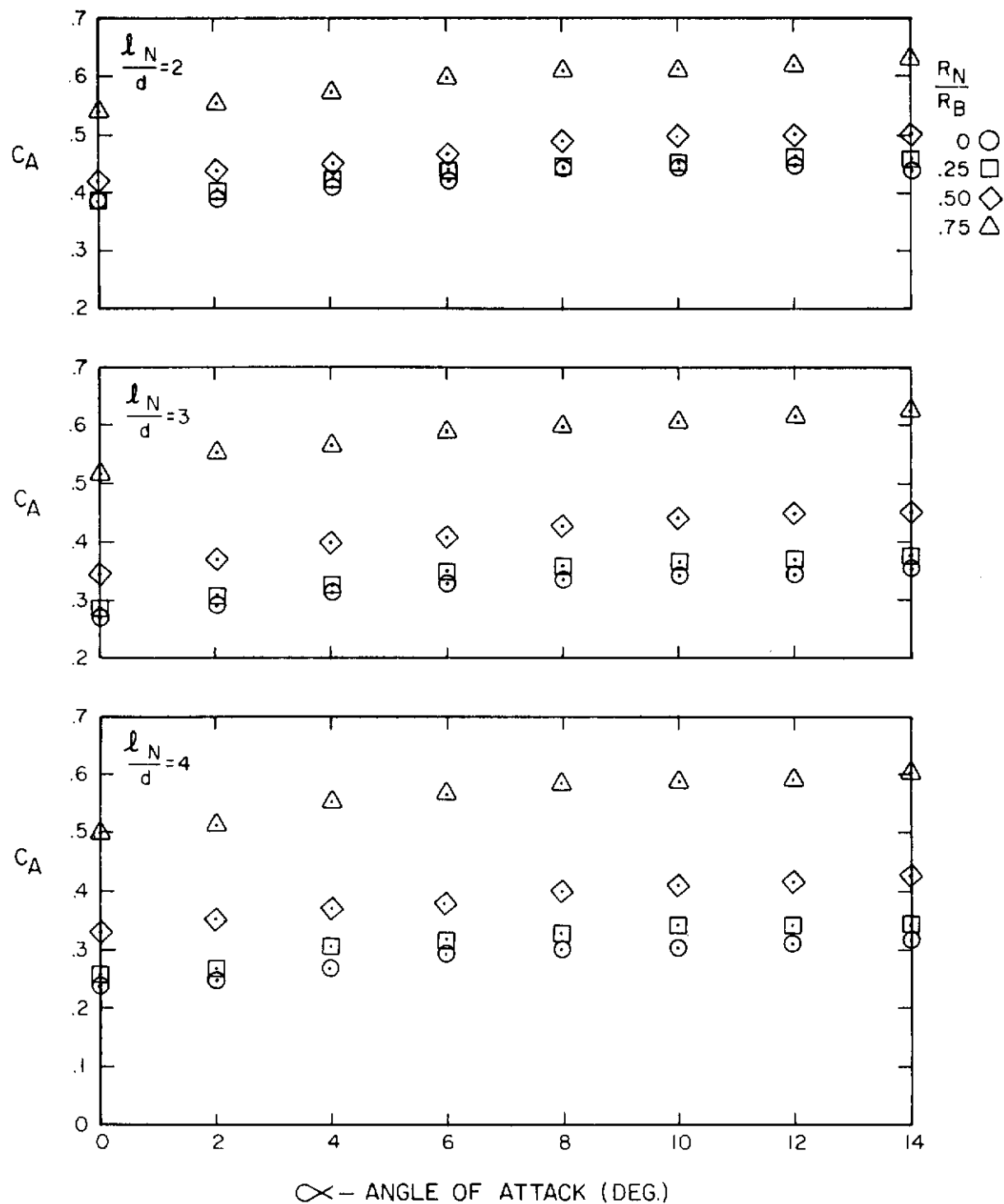


Figure A-11. Axial Force Coefficient Versus Angle of Attack for $\frac{l_A}{d} = 10$, $M = 1.5$

Contrails

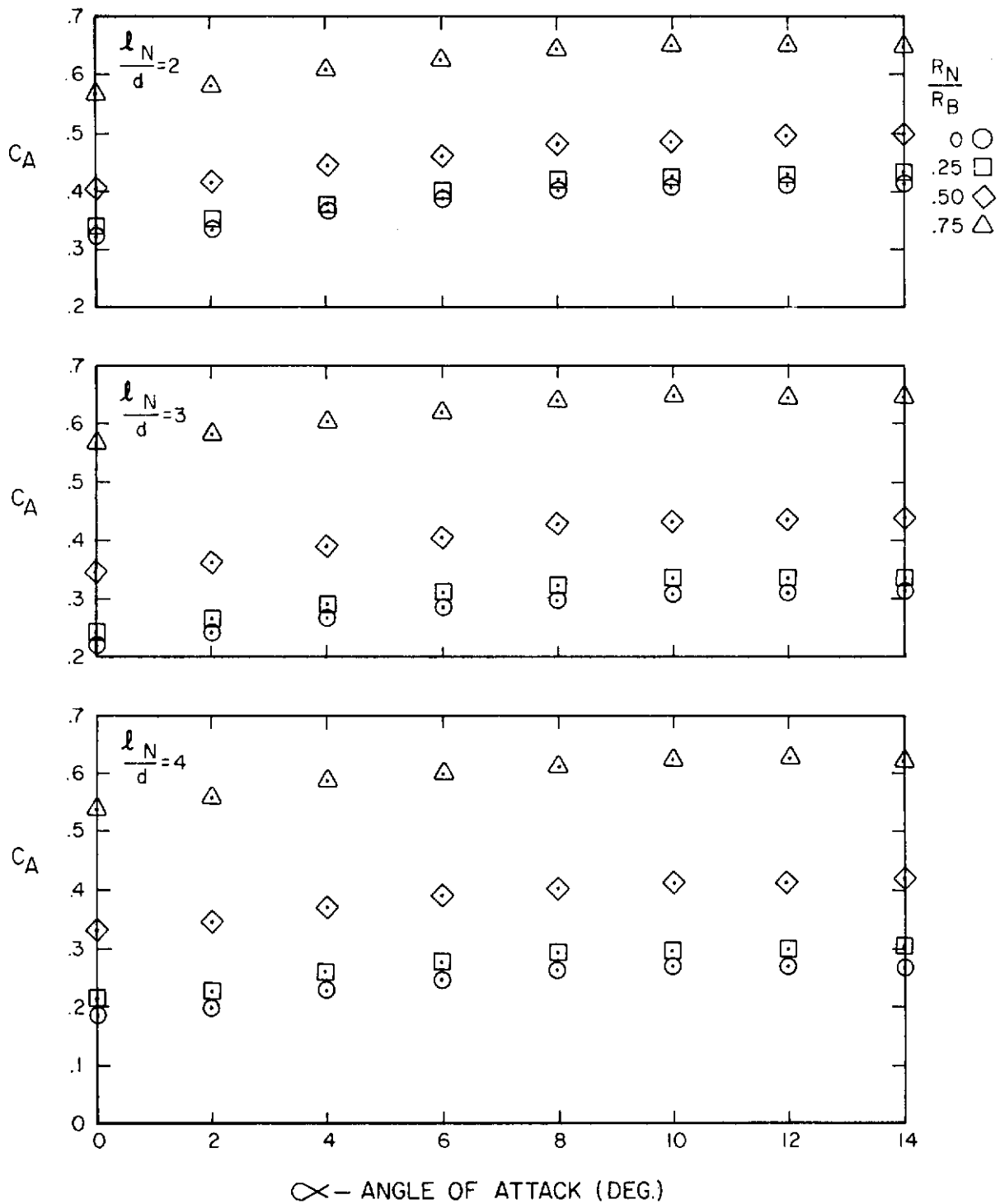


Figure A-12. Axial Force Coefficient Versus Angle of Attack for $l_A/d = 6$, $M = 2.0$

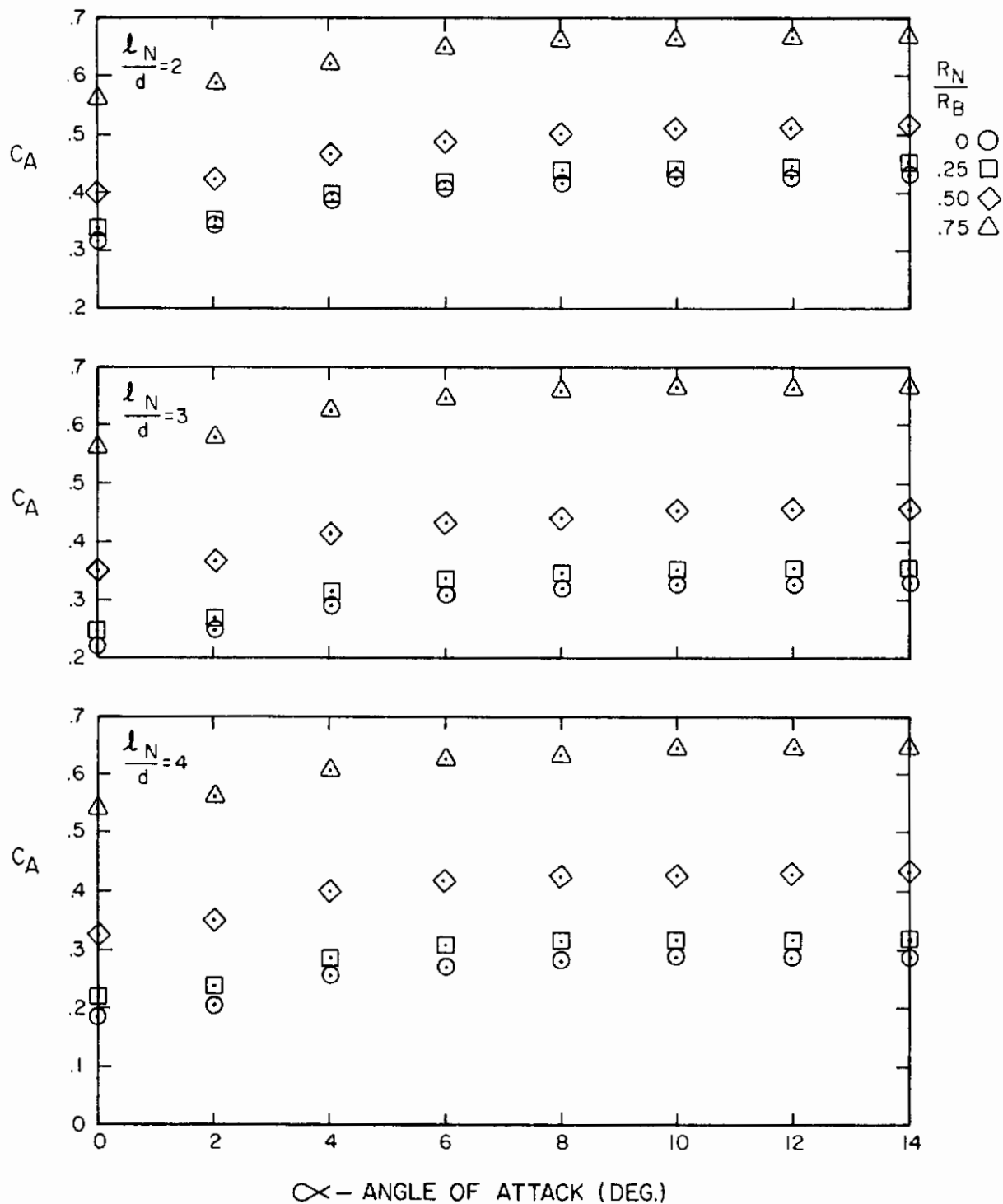


Figure A-13. Axial Force Coefficient Versus Angle of Attack for $\frac{l_A}{d} = 8$, $M = 2.0$

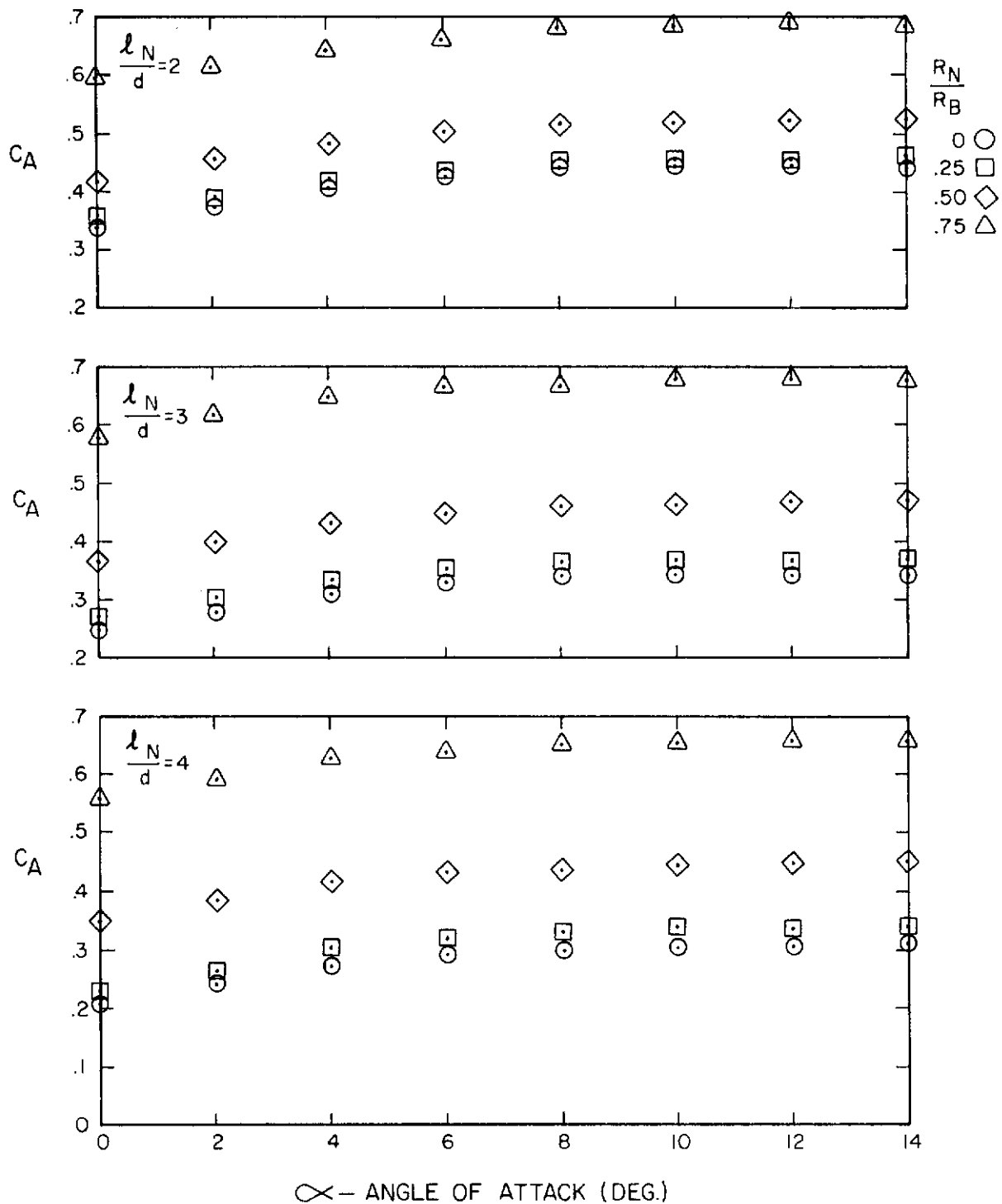


Figure A-14. Axial Force Coefficient Versus Angle of Attack for $l_A/d = 10$, $M = 2.0$

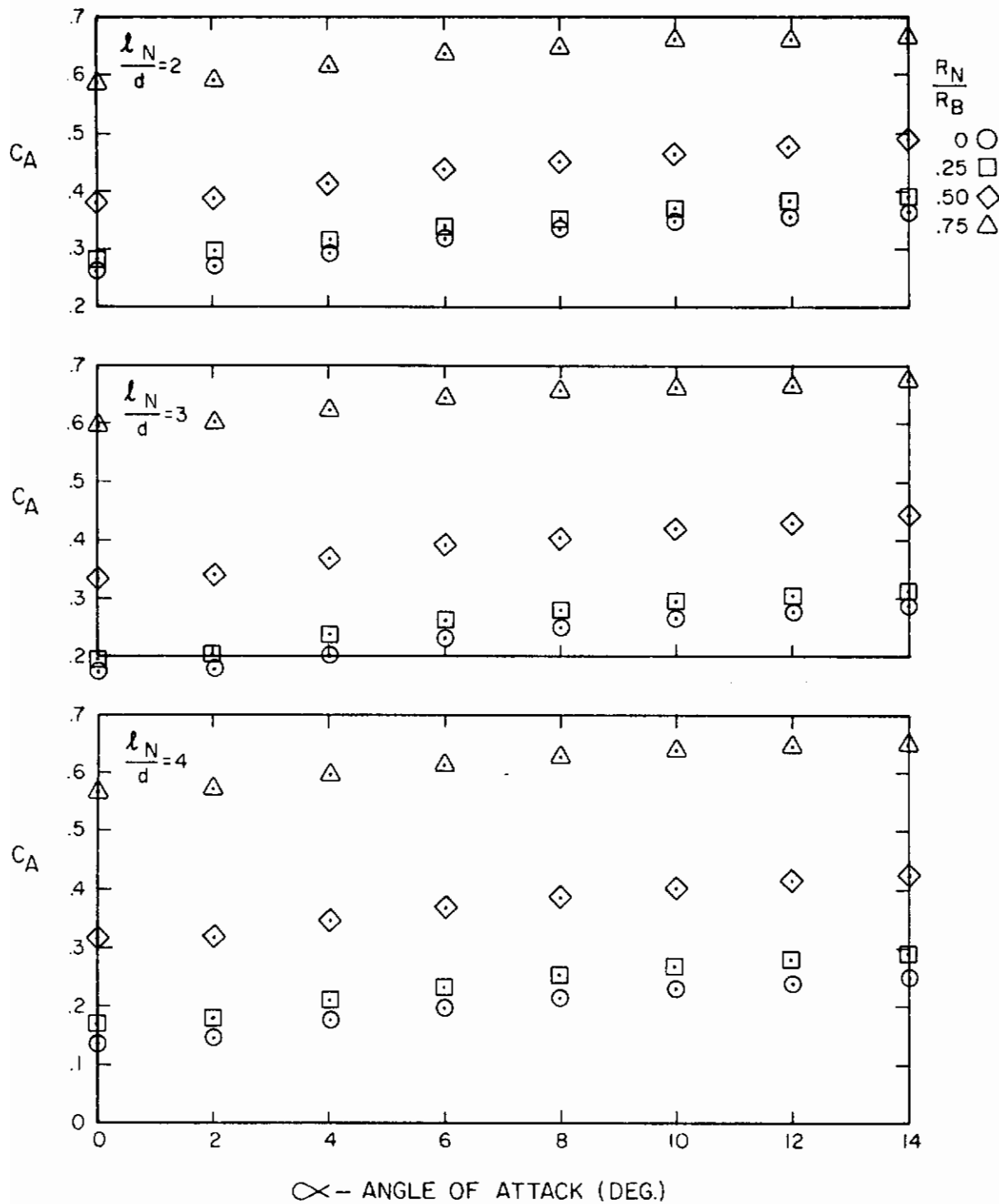


Figure A-15. Axial Force Coefficient Versus Angle of Attack for $\frac{l_A}{d} = 6$, $M = 3.0$

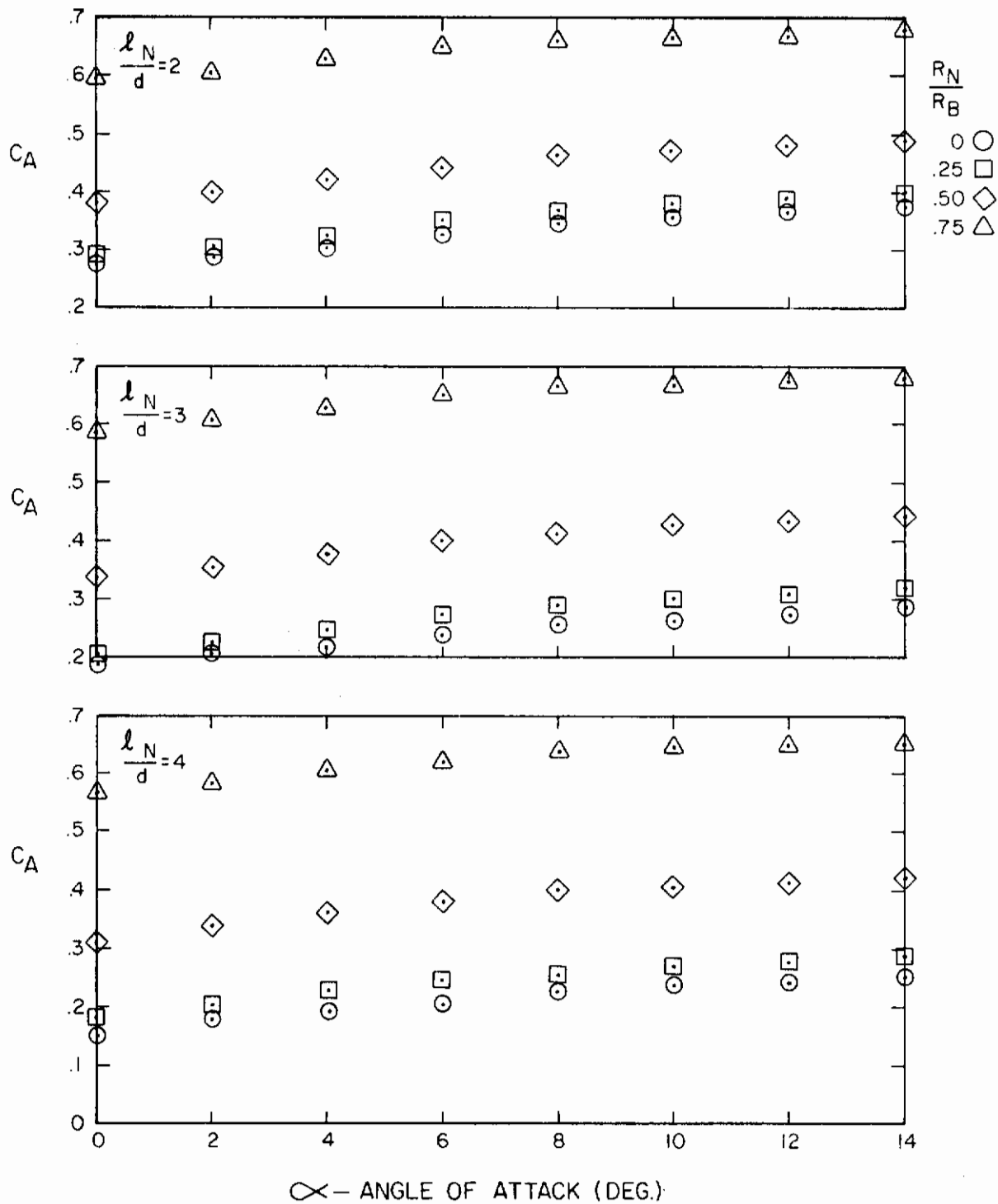


Figure A-16. Axial Force Coefficient Versus Angle of Attack for $l_A/d = 8$, $M = 3.0$

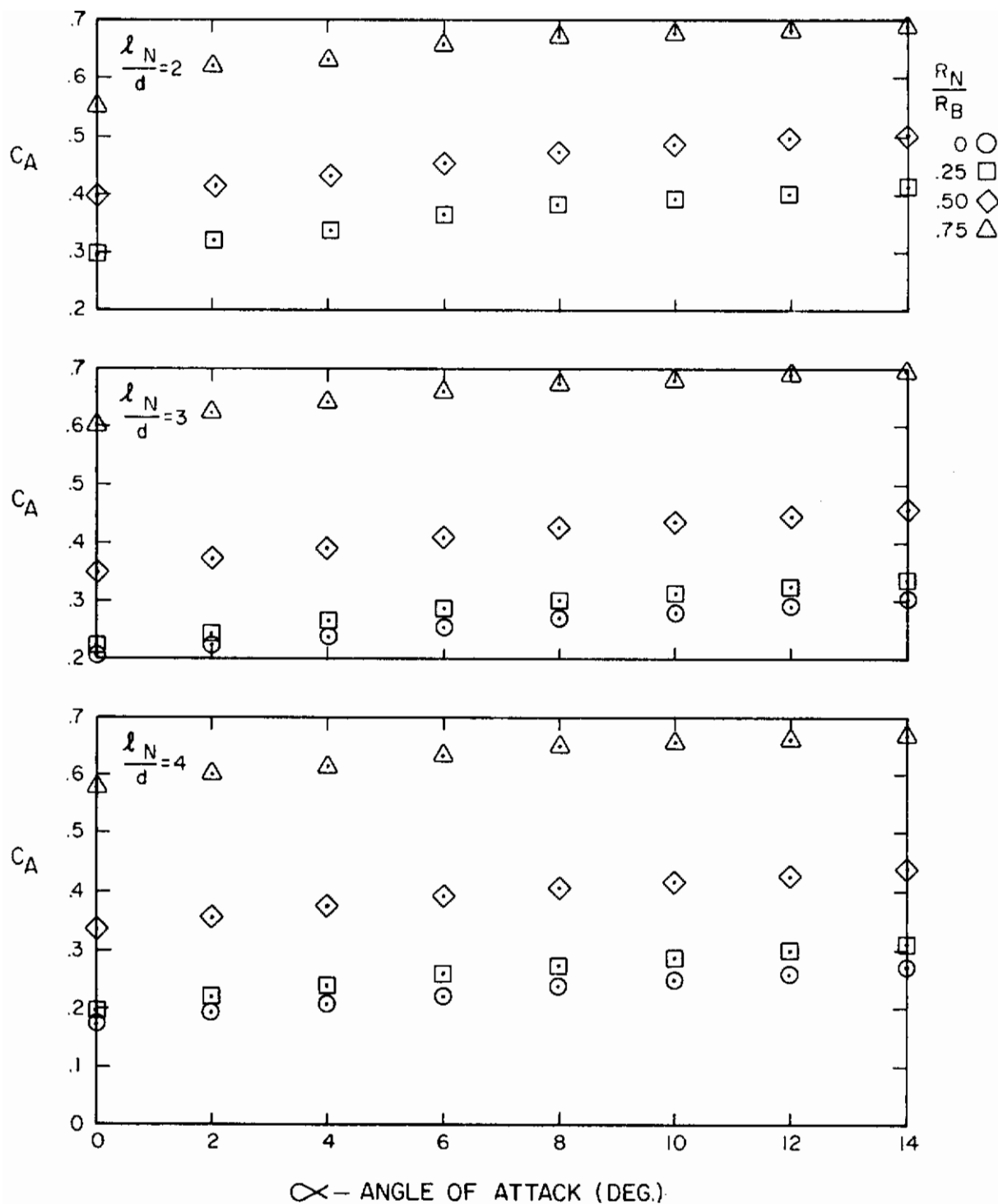


Figure A-17. Axial Force Coefficient Versus Angle of Attack for $l_A/d = 10$, $M = 3.0$

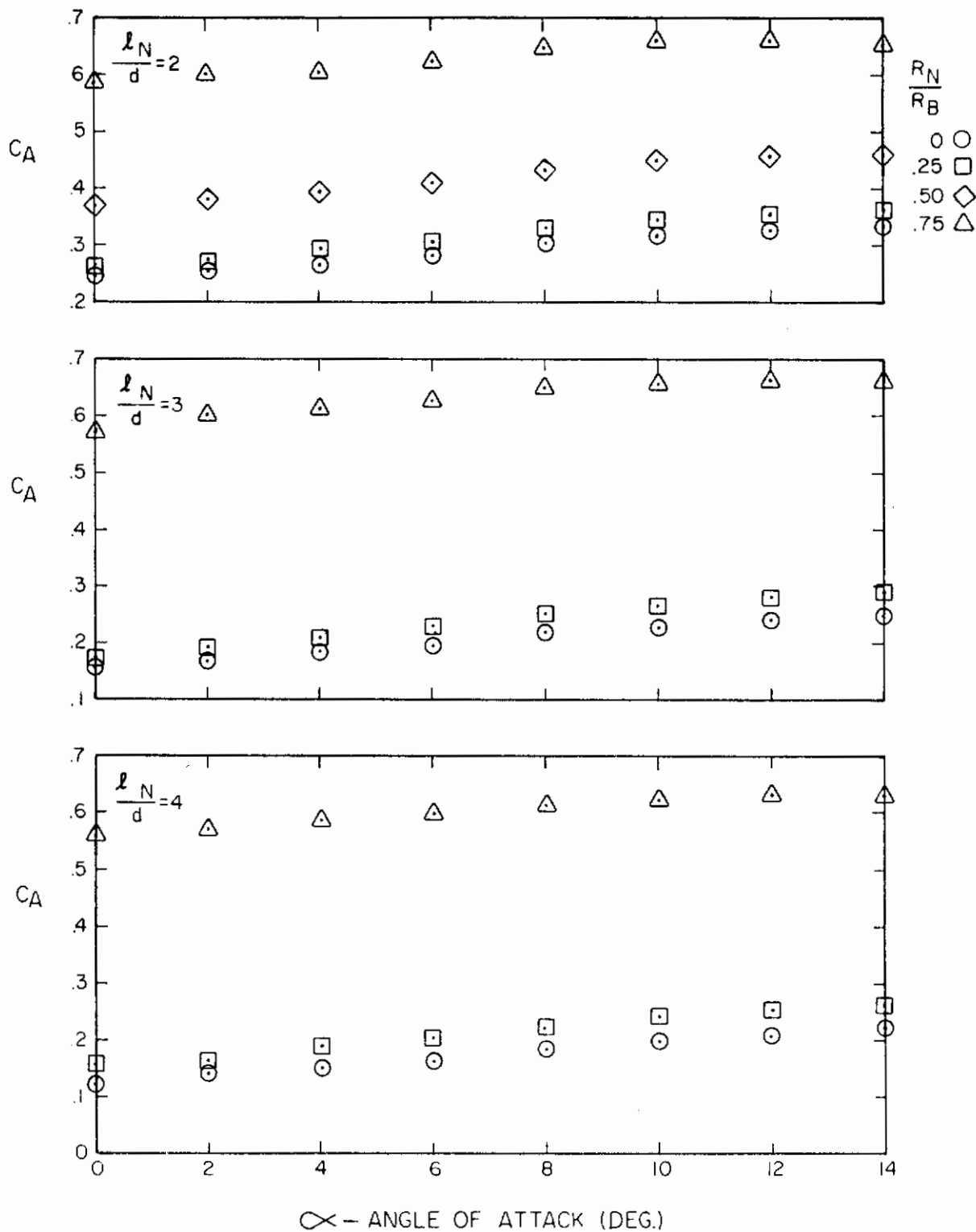


Figure A-18. Axial Force Coefficient Versus Angle of Attack for $\frac{l_A}{d} = 8$, $M = 4.0$

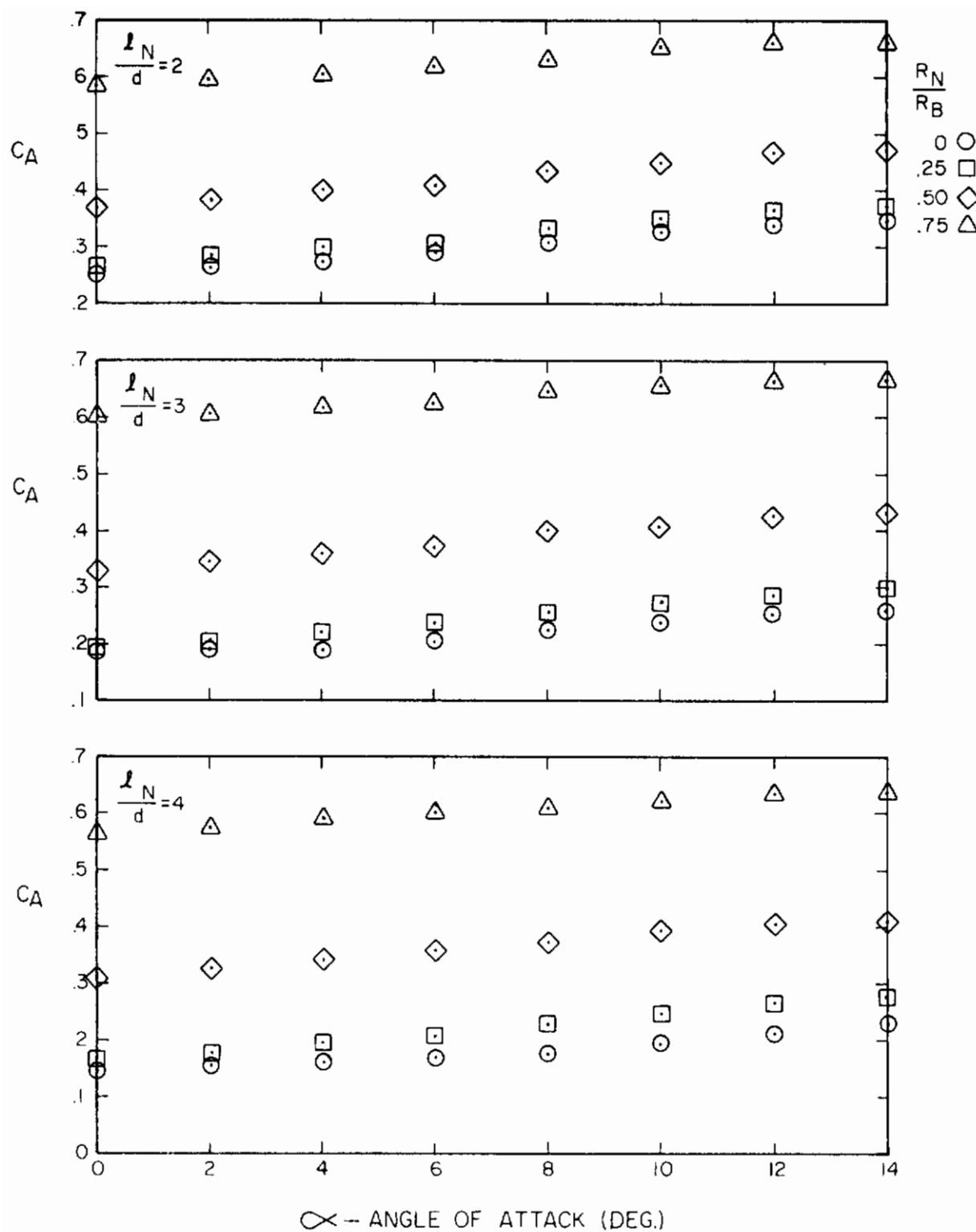


Figure 19. Axial Force Coefficient Versus Angle of Attack for $\frac{l_A}{d} = 10$, $M = 4.0$

Contrails

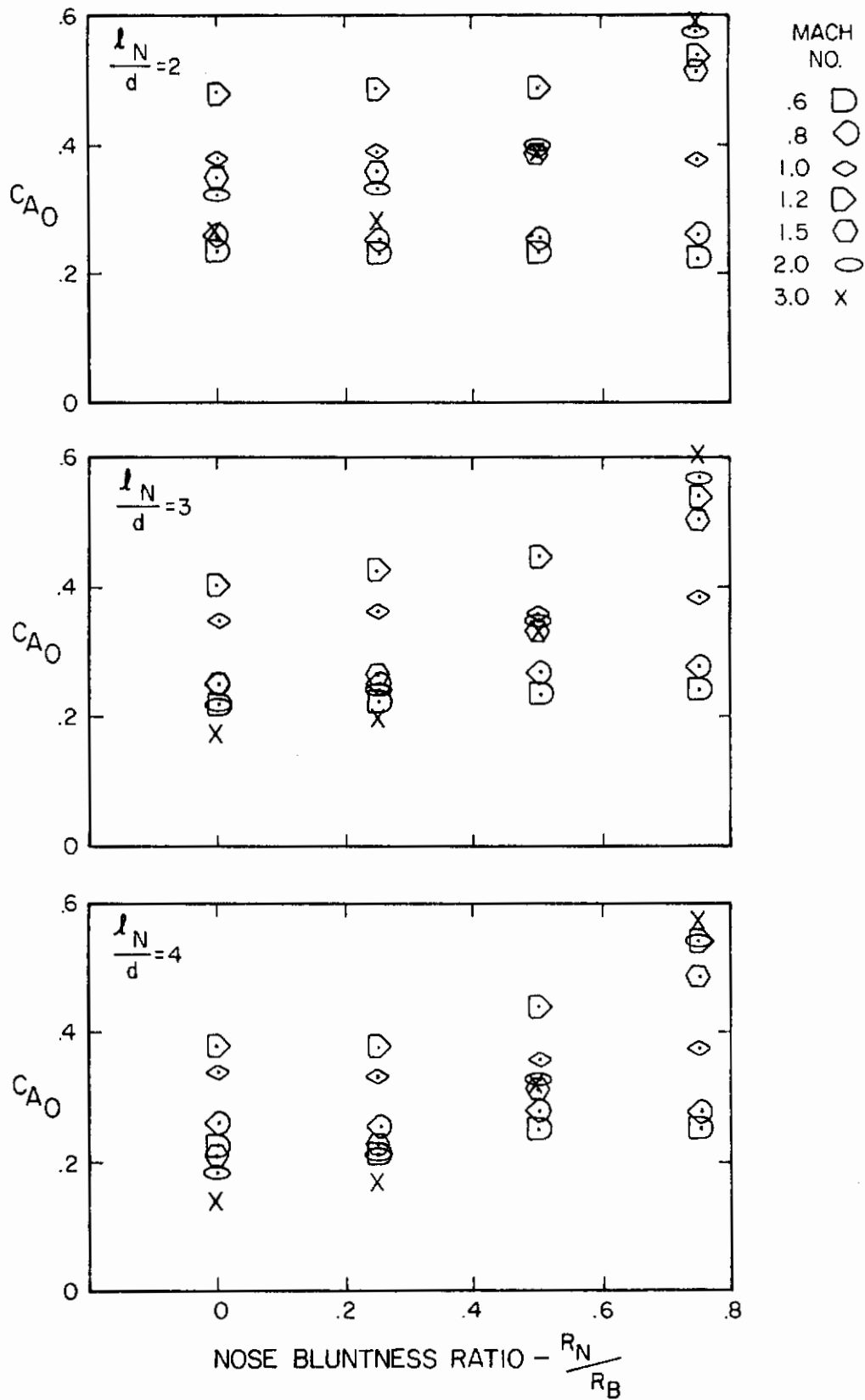


Figure A-20. Axial Force Coefficient Versus Nose Bluntness Ratio for $\frac{l_A}{d} = 6$

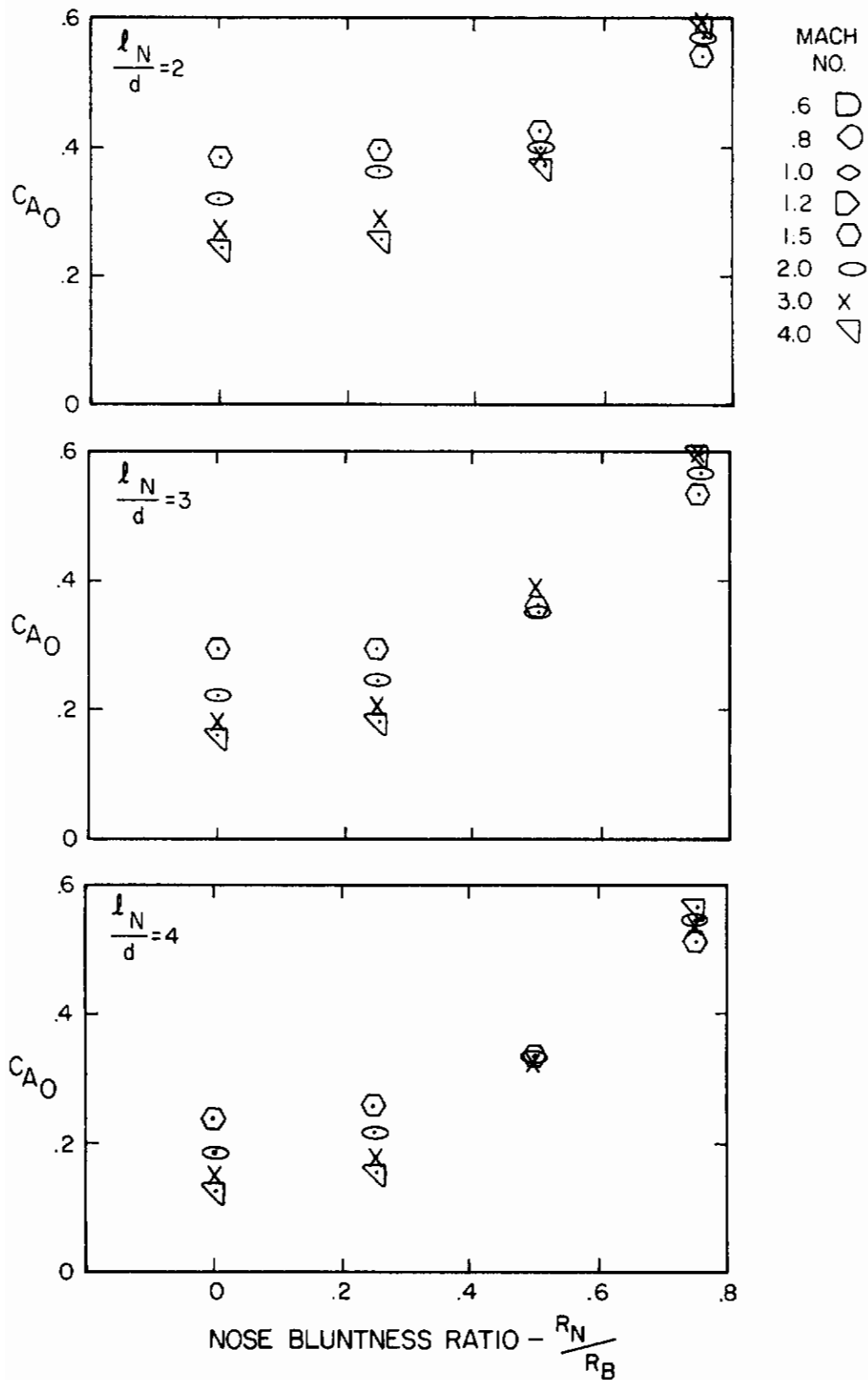


Figure A-21. Axial Force Coefficient Versus Nose Bluntness Ratio for $\frac{l_A}{d} = 8$

Contrails

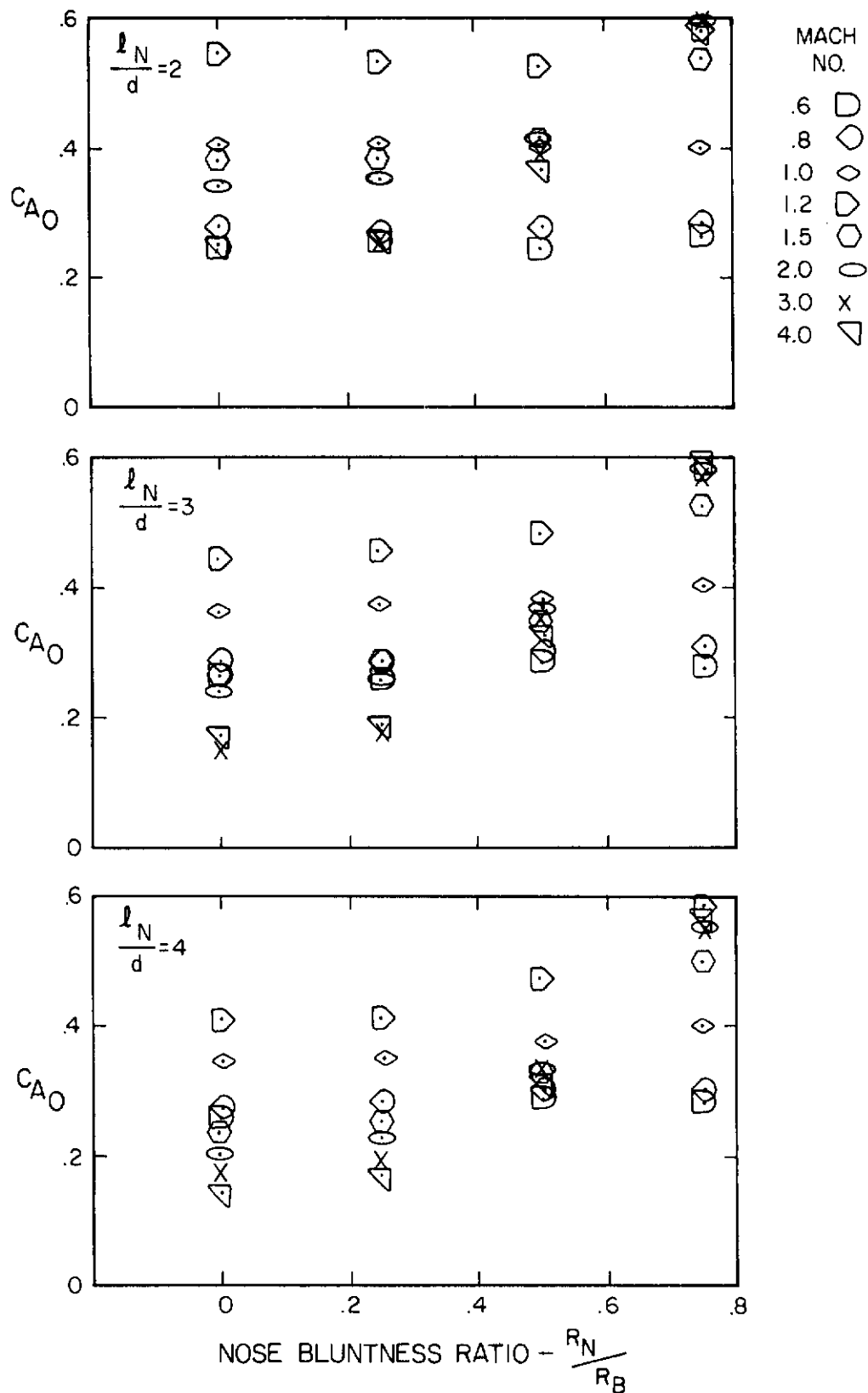


Figure A-22. Axial Force Coefficient Versus Nose Bluntness Ratio for $\frac{l_A}{d} = 10$

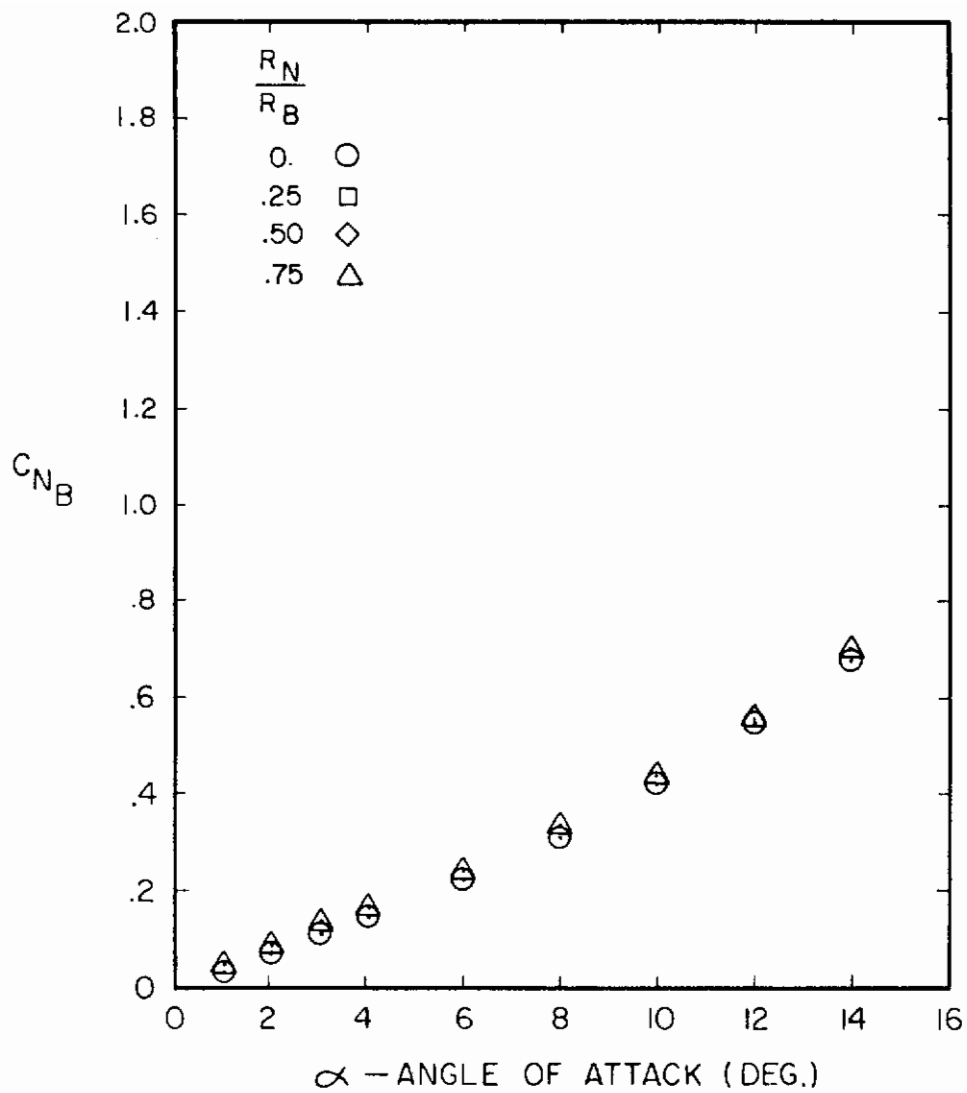


Figure A-23. Normal Force Coefficient Versus Angle of Attack for $l_N/d = 2$, $l_A/d = 6$, $M = 0.6$

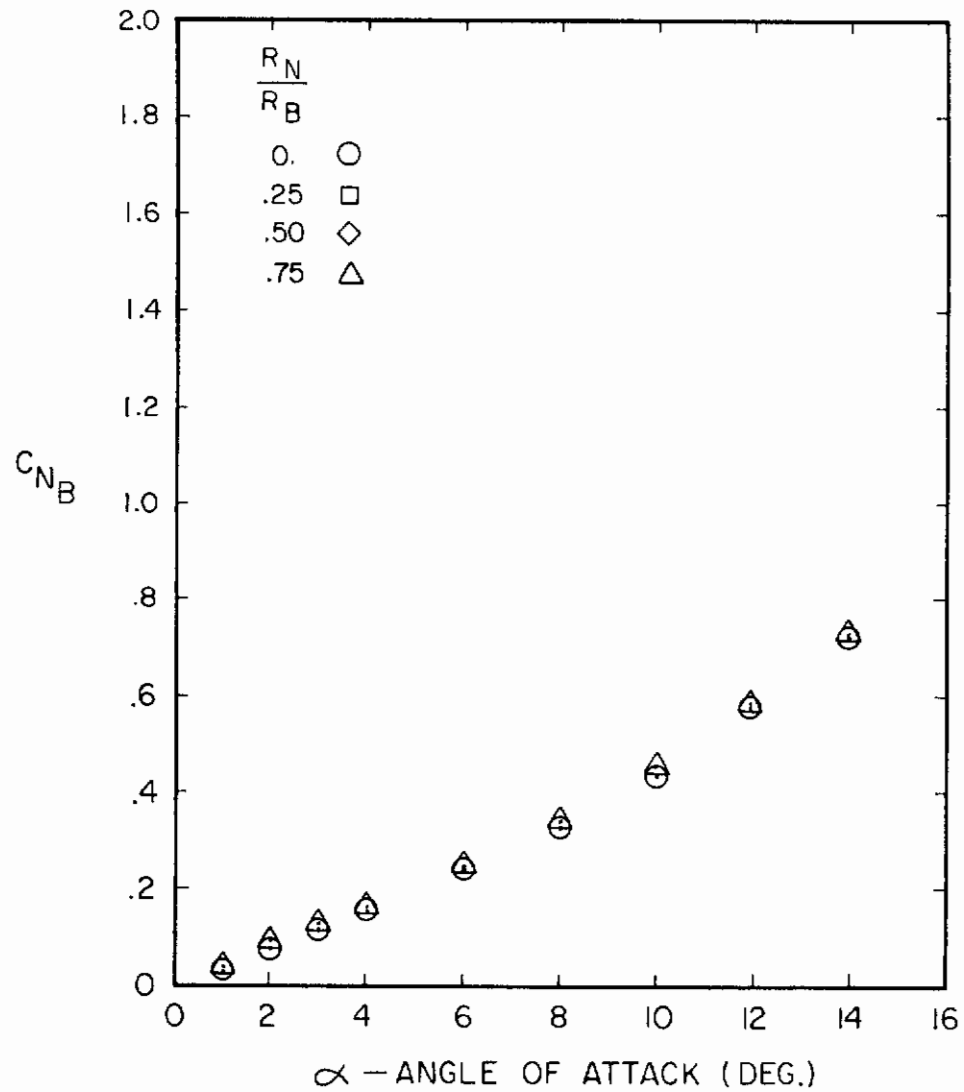


Figure A-24. Normal Force Coefficient Versus Angle of Attack for $l_N/d = 3$, $l_A = 6$, $M = 0.6$

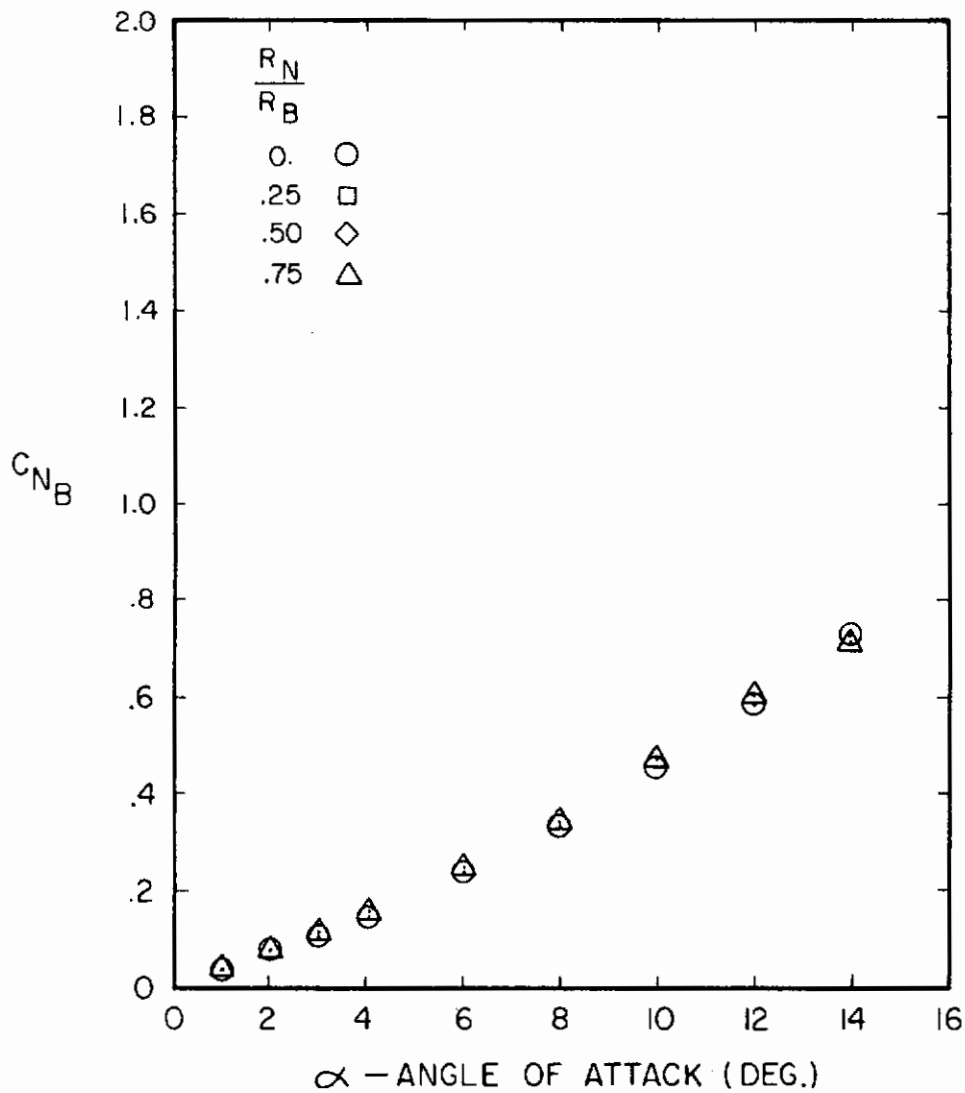


Figure A-25. Normal Force Coefficient Versus Angle of Attack for $l_N/d = 4$, $l_A/d = 6$, $M = 0.6$

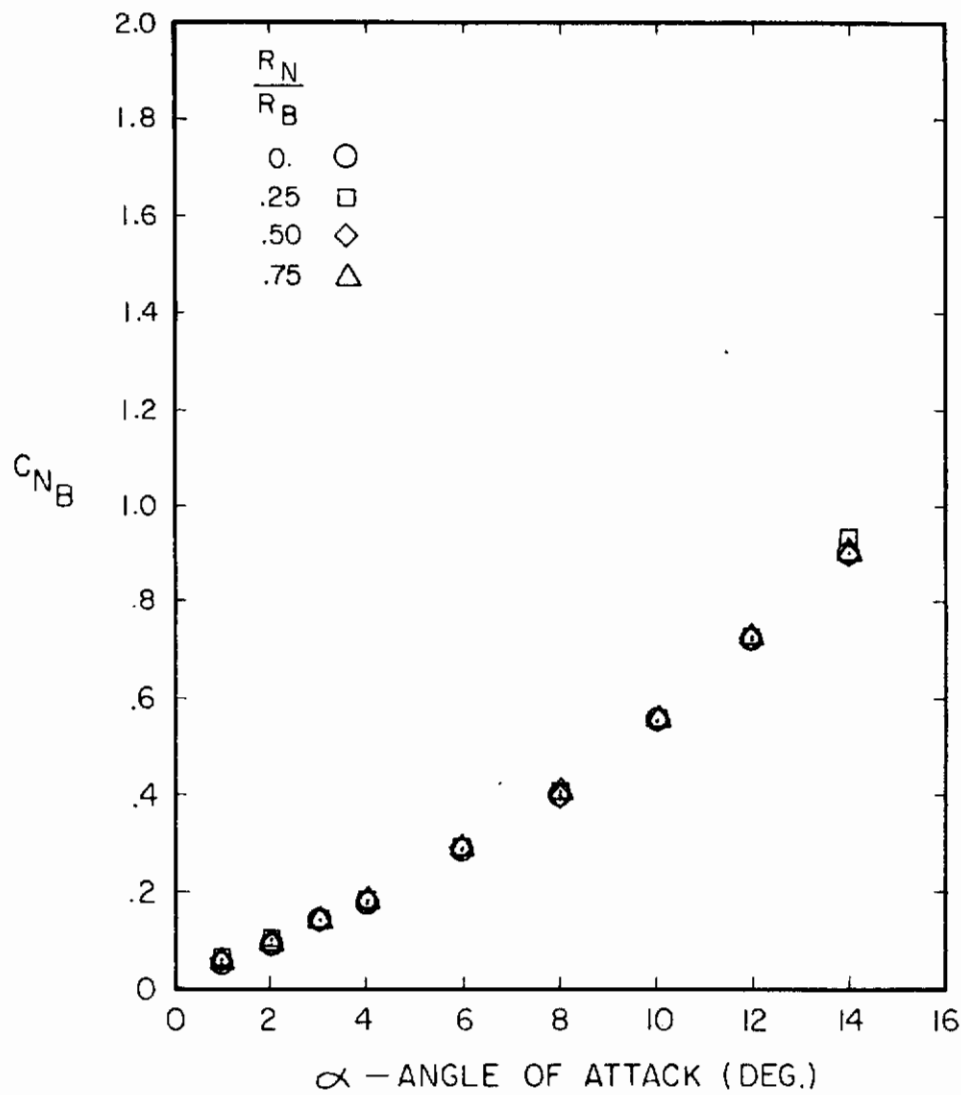


Figure A-26. Normal Force Coefficient Versus Angle of Attack for $\ell_N/d = 2$, $\ell_A/d = 10$, $M = 0.6$

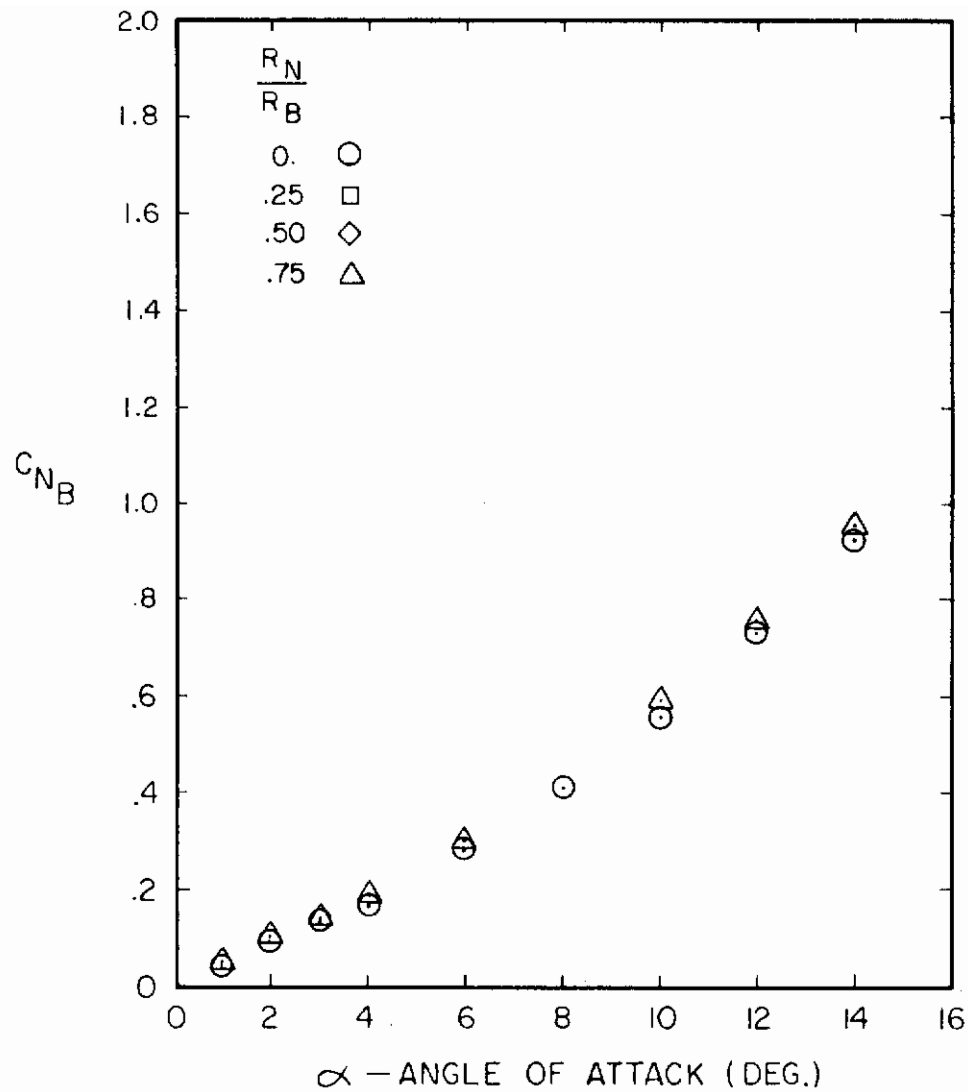


Figure A-27. Normal Force Coefficient Versus Angle of Attack for $\ell_N/d = 3$, $\ell_A/d = 10$, $M = 0.6$

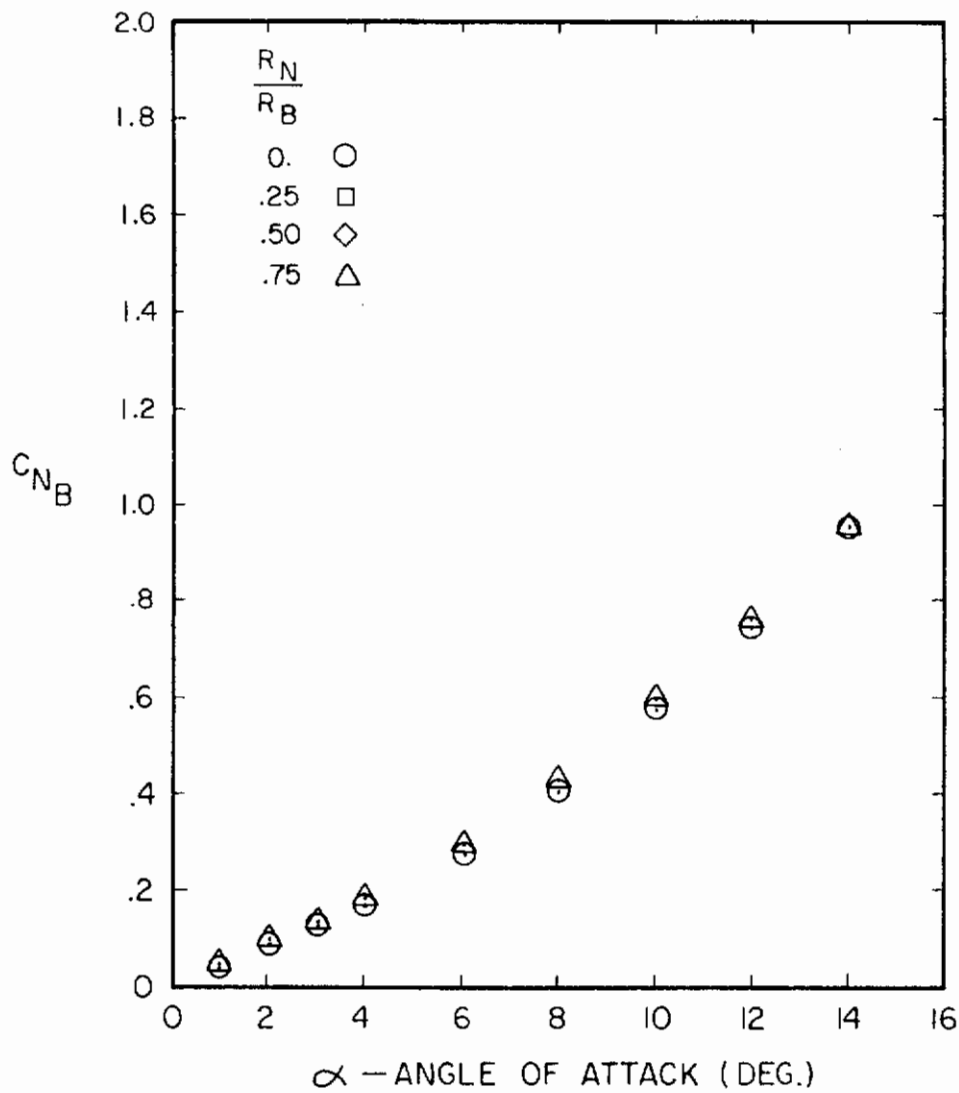


Figure A-28. Normal Force Coefficient Versus Angle of Attack for $l_N/d = 4$, $l_A/d = 10$, $M = 0.6$

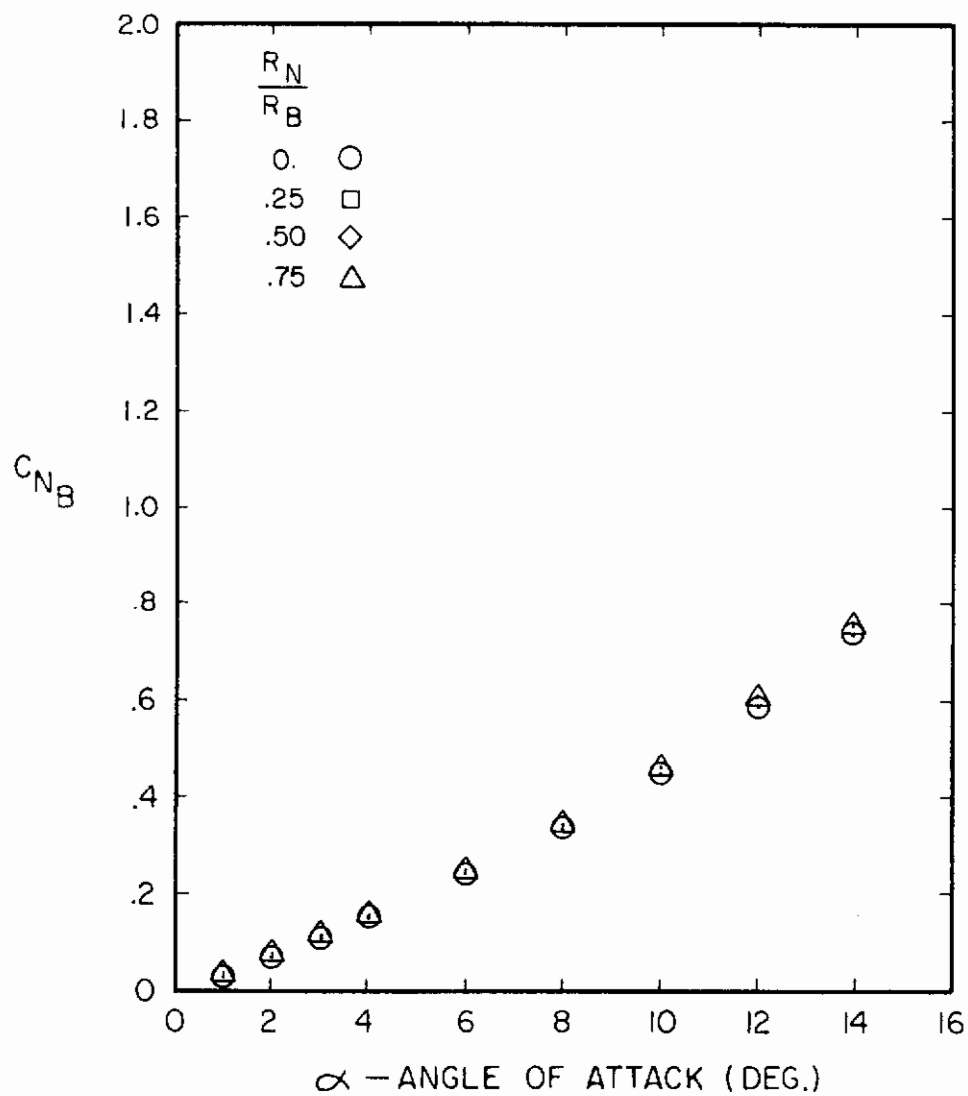


Figure A-29. Normal Force Coefficient Versus Angle of Attack for $l_N/d = 2$, $l_A/d = 6$, $M = 0.8$

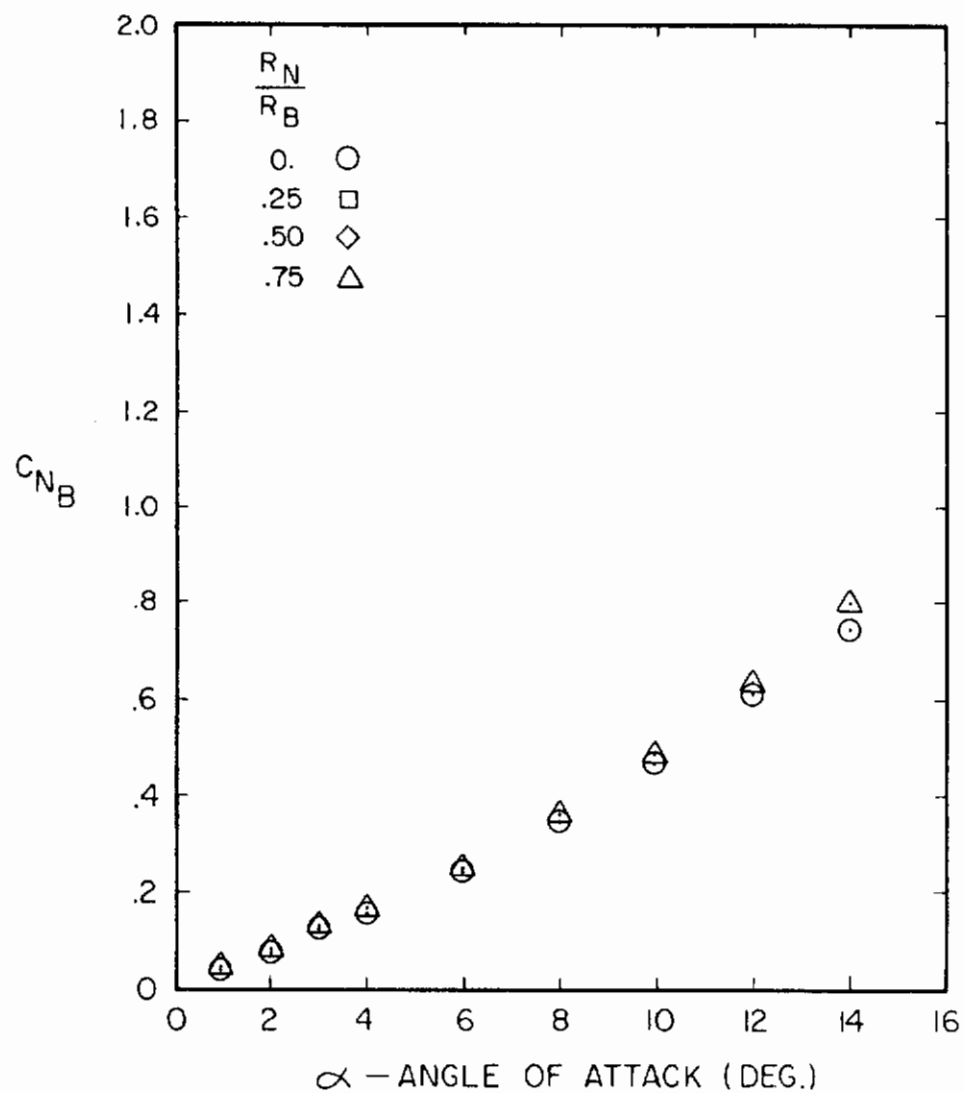


Figure 30. Normal Force Coefficient Versus Angle of Attack for $l_N/d = 3$, $l_A/d = 6$, $M = 0.8$

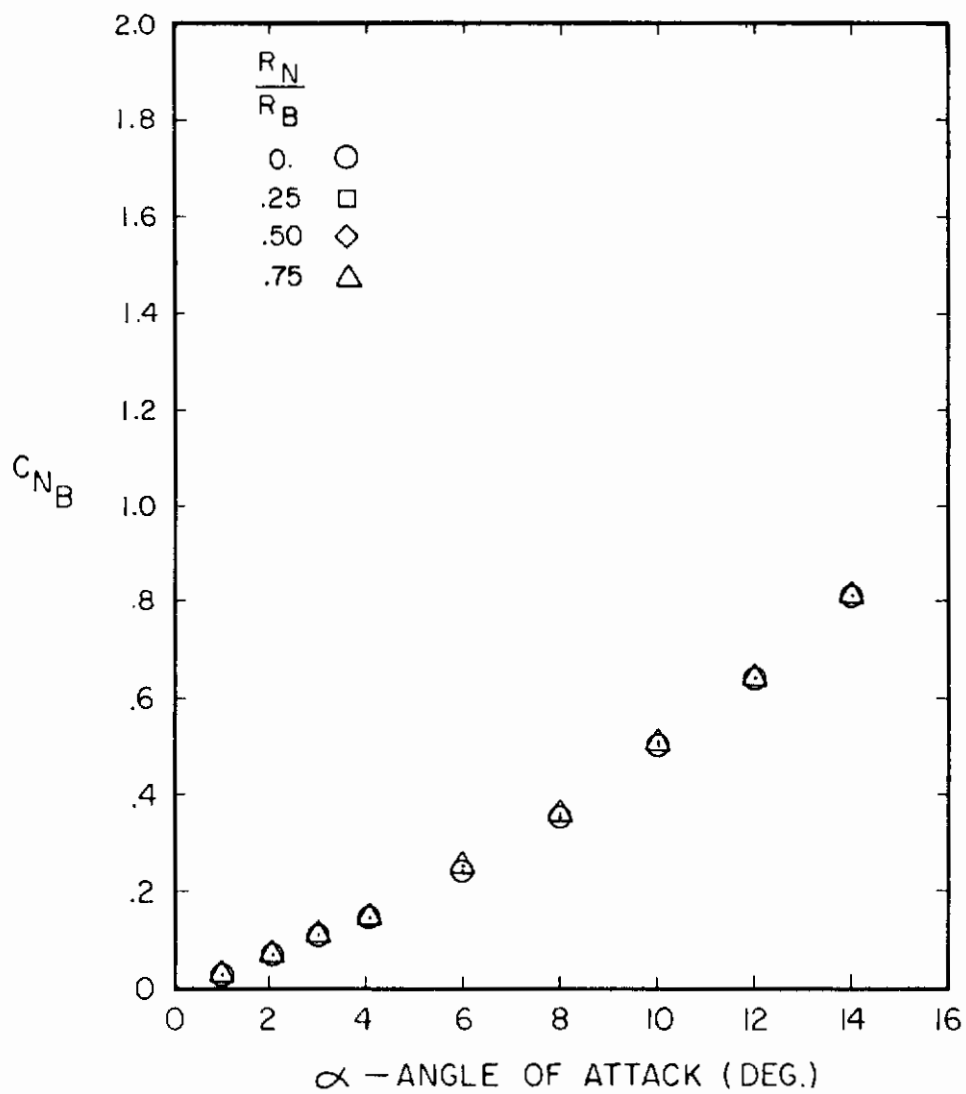


Figure A-31. Normal Force Coefficient Versus Angle of Attack for $l_N/d = 4$, $l_A/d = 6$, $M = 0.8$

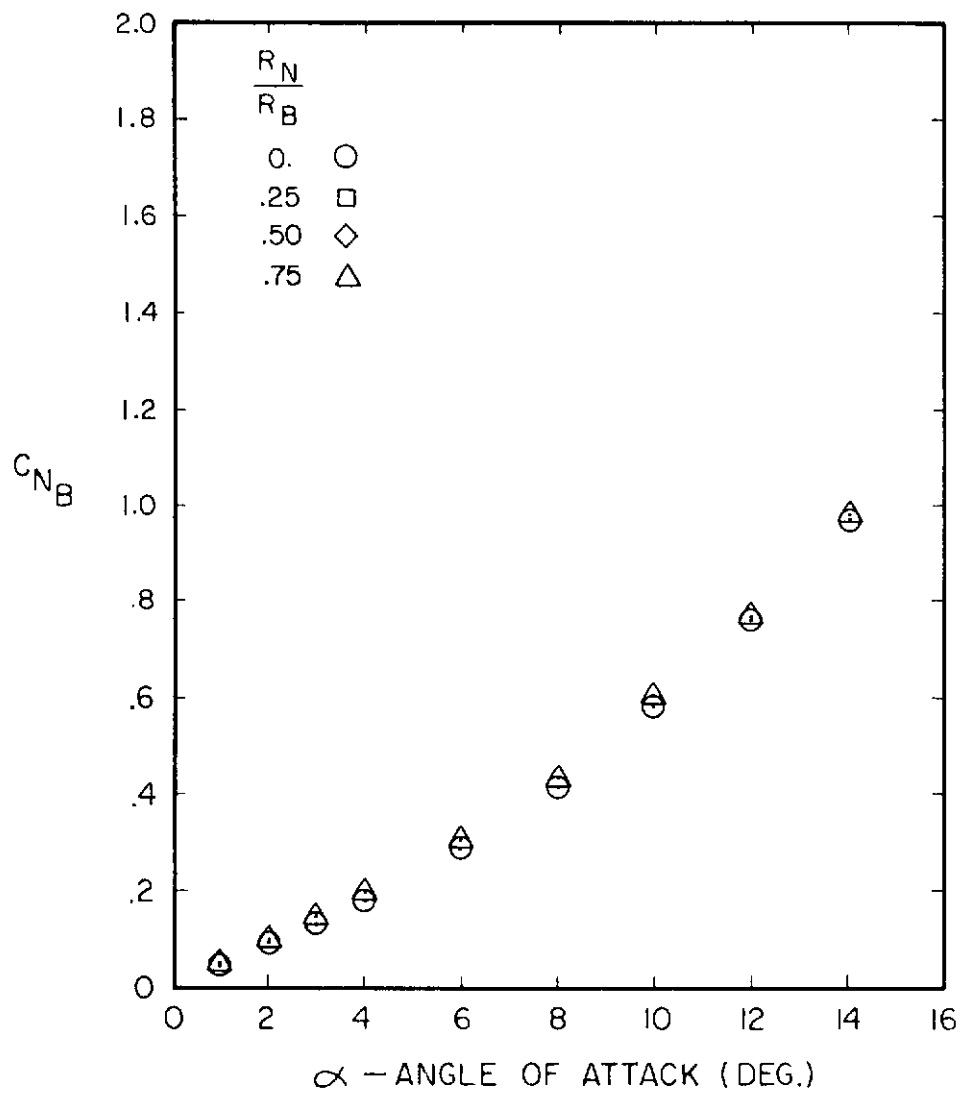


Figure A-32. Normal Force Coefficient Versus Angle of Attack for $l_N/d = 2$, $l_A/d = 10$, $M = 0.8$

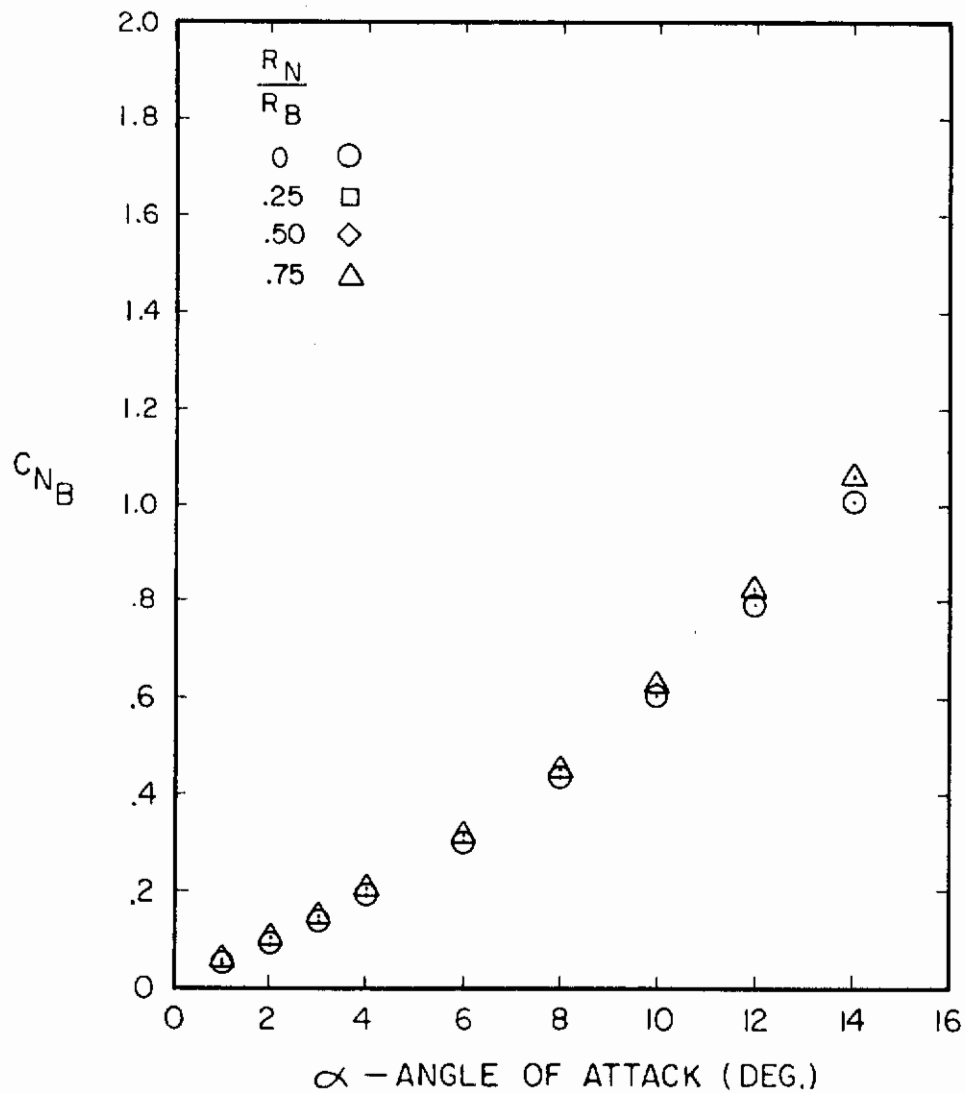


Figure A-33. Normal Force Coefficient Versus Angle of Attack for $\ell_N/d = 3$, $\ell_A/d = 10$, $M = 0.8$

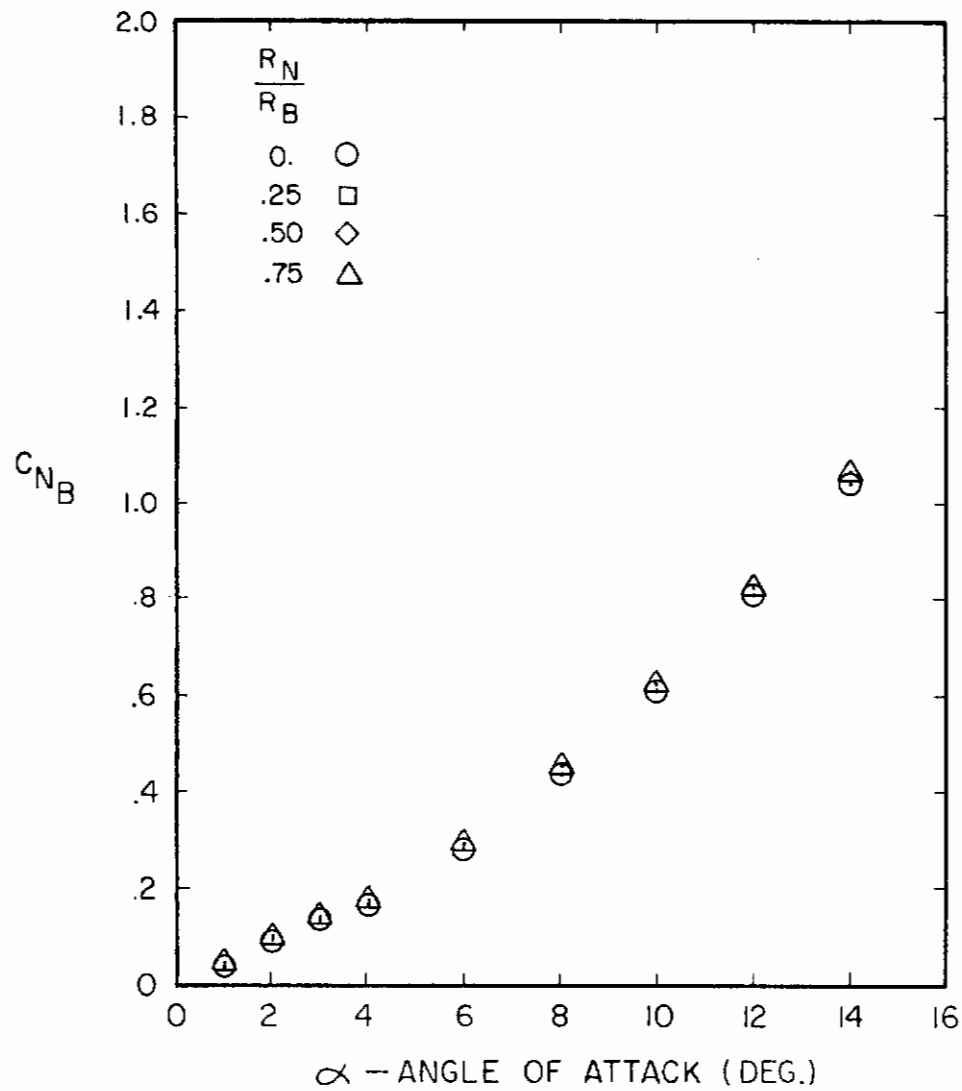


Figure A-34. Normal Force Coefficient Versus Angle of Attack for $l_N/d = 4$, $l_A/d = 10$, $M = 0.8$

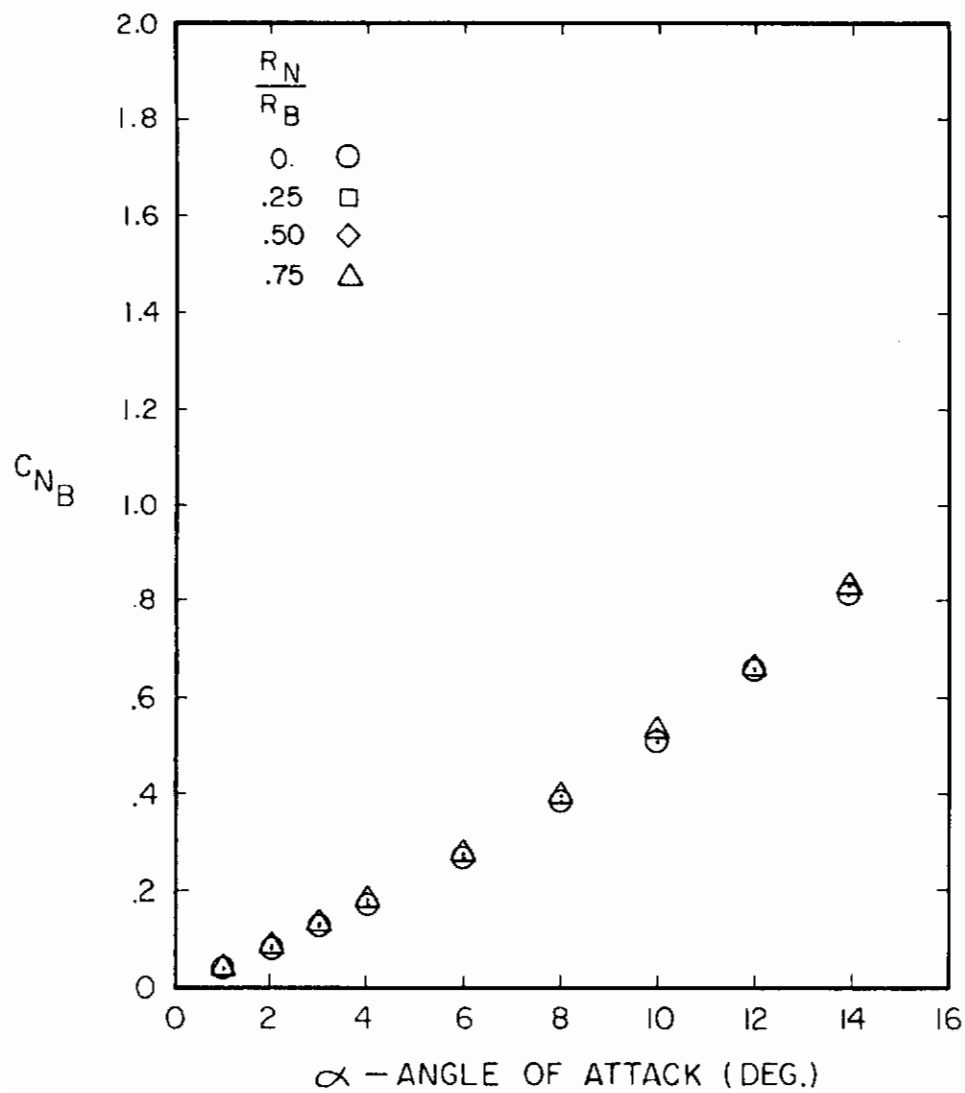


Figure A-35. Normal Force Coefficient Versus Angle of Attack for $l_N/d = 2$, $l_A/d = 6$, $M = 1.0$

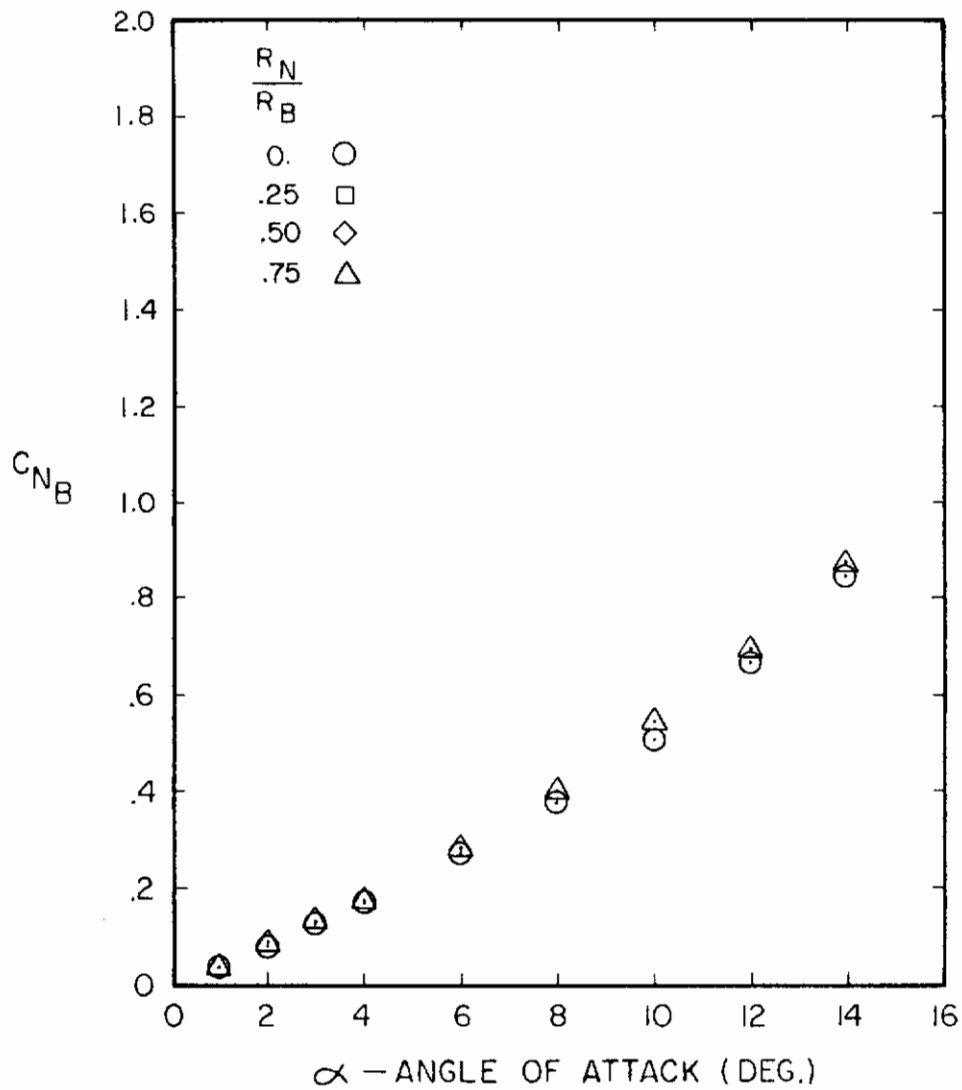


Figure A-36. Normal Force Coefficient Versus Angle of Attack for $l_N/d = 3$, $l_A/d = 6$, $M = 1.0$

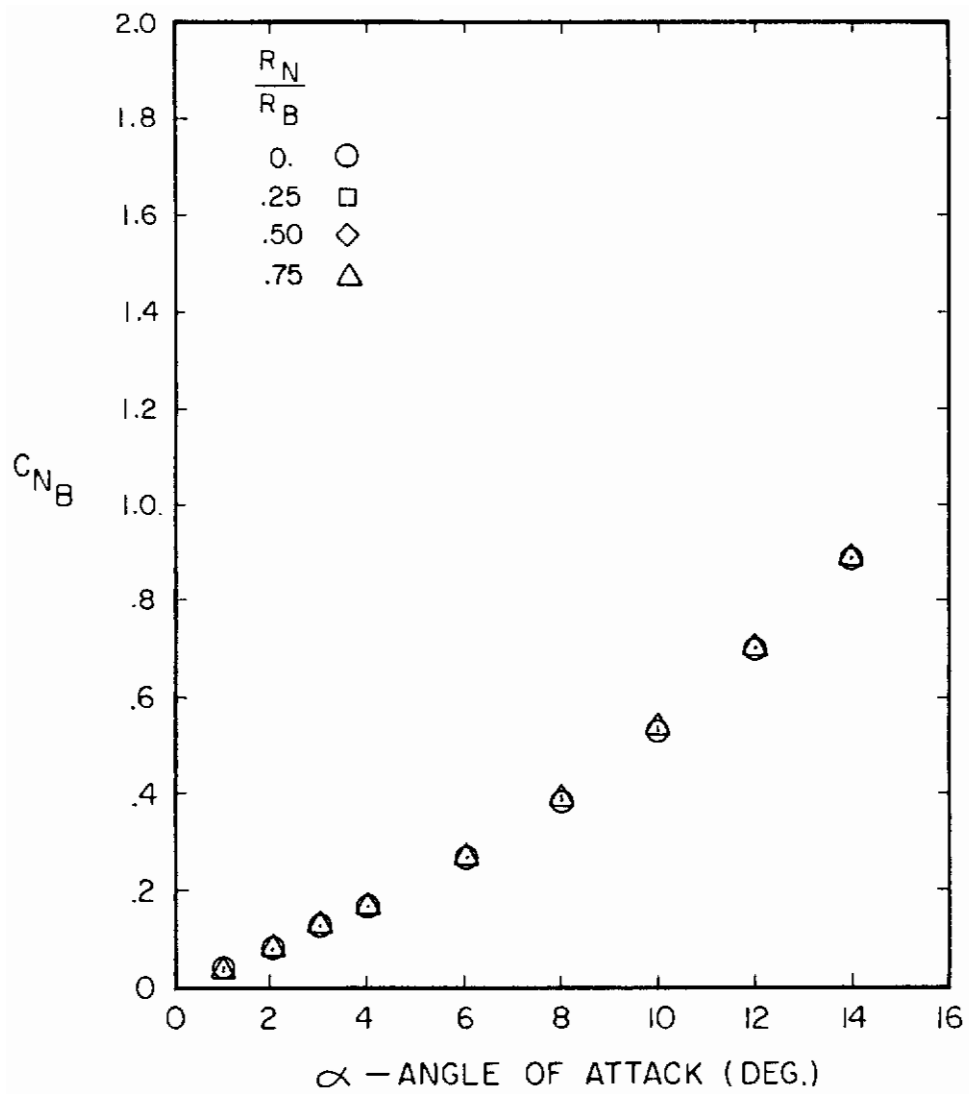


Figure A-37. Normal Force Coefficient Versus Angle of Attack for $l_N/d = 4$, $l_A/d = 6$, $M = 1.0$

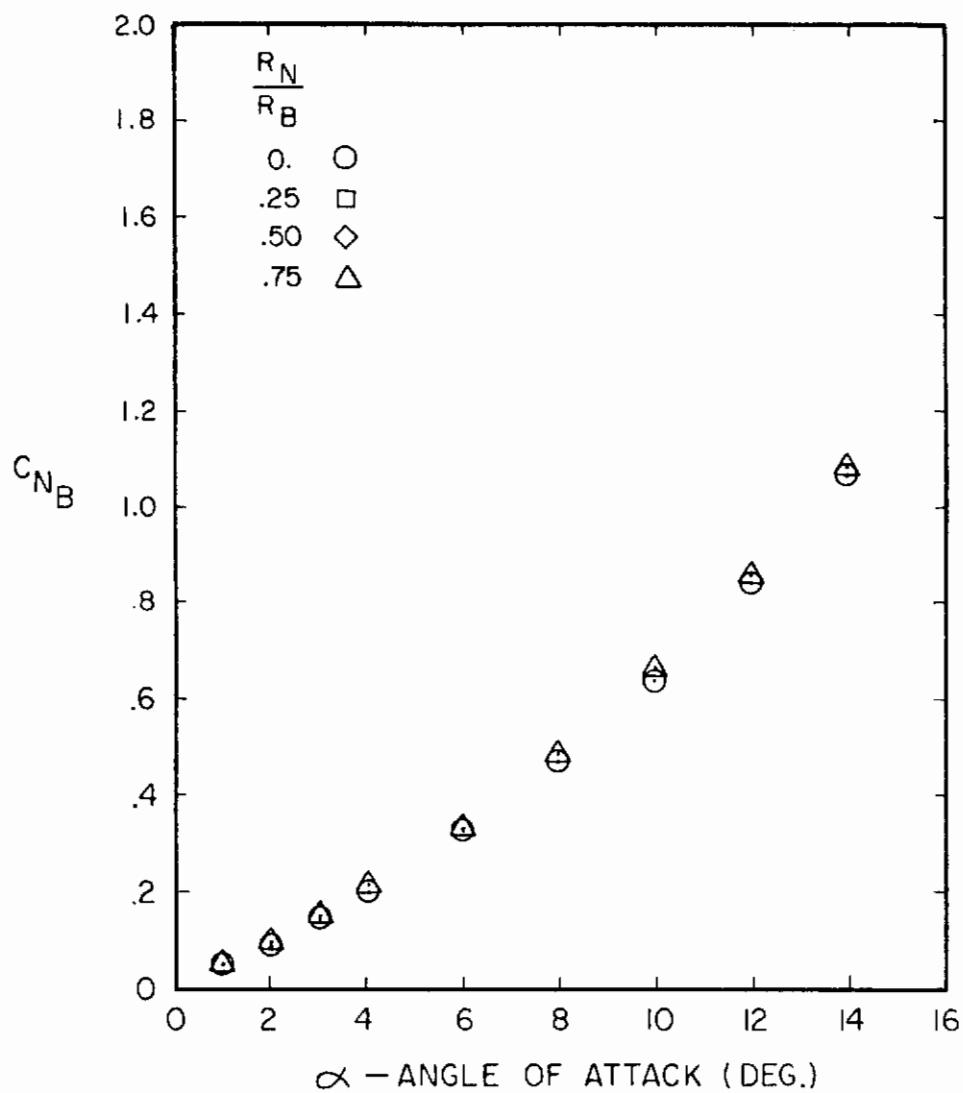


Figure A-38. Normal Force Coefficient Versus Angle of Attack for $l_N/d = 2$, $l_A/d = 10$, $M = 1.0$

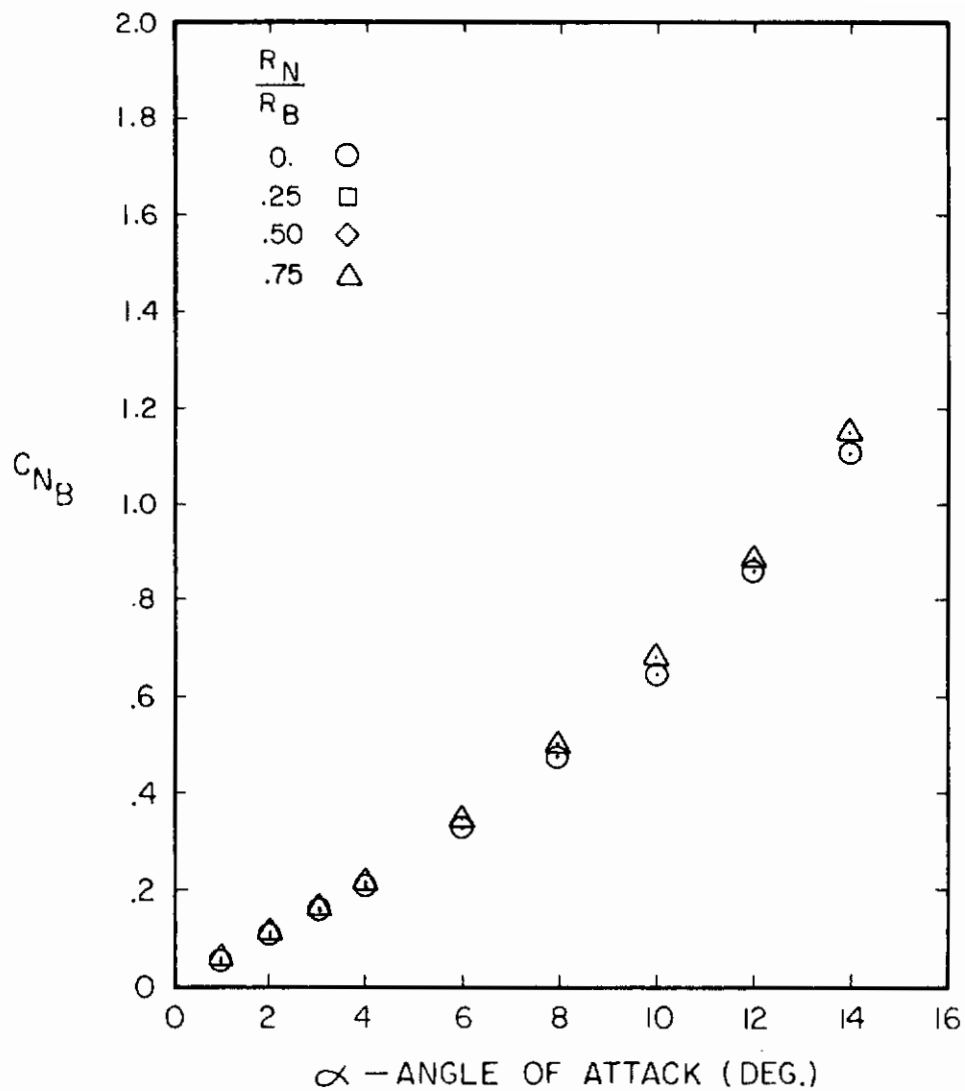


Figure A-39. Normal Force Coefficient Versus Angle of Attack for $l_N/d = 3$, $l_A/d = 10$, $M = 1.0$

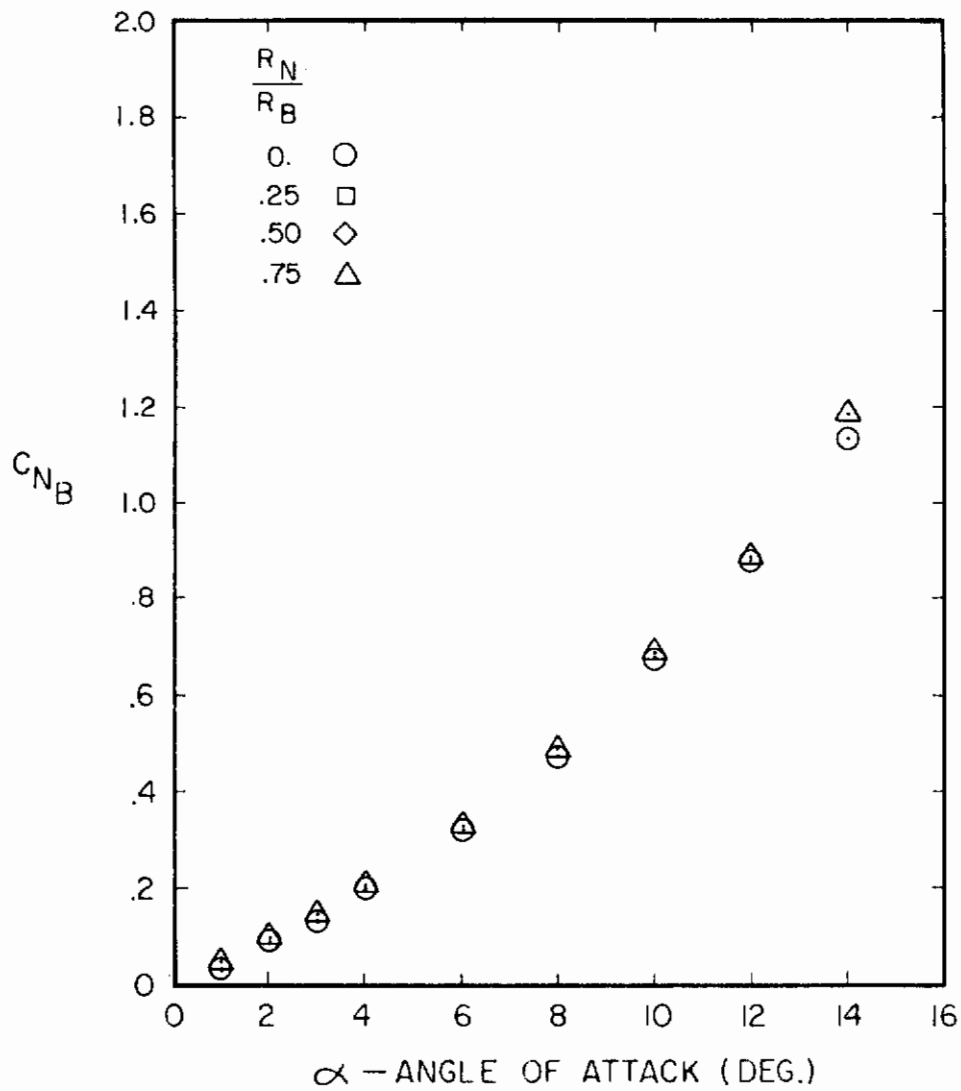


Figure A-40. Normal Force Coefficient Versus Angle of Attack for $l_N/d = 4$, $l_A/d = 10$, $M = 1.0$

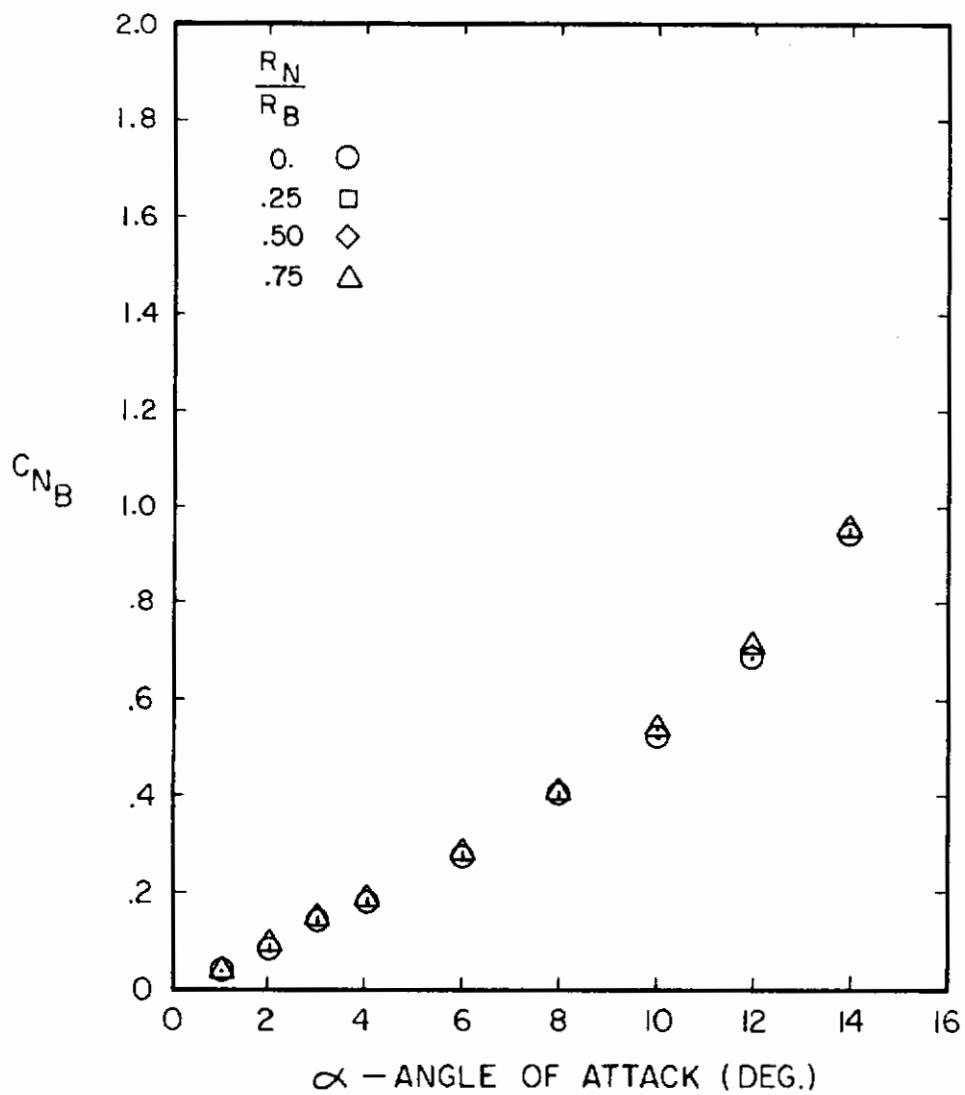


Figure A-41. Normal Force Coefficient Versus Angle of Attack for $\ell_N/d = 2$, $\ell_A/d = 6$, $M = 1.2$

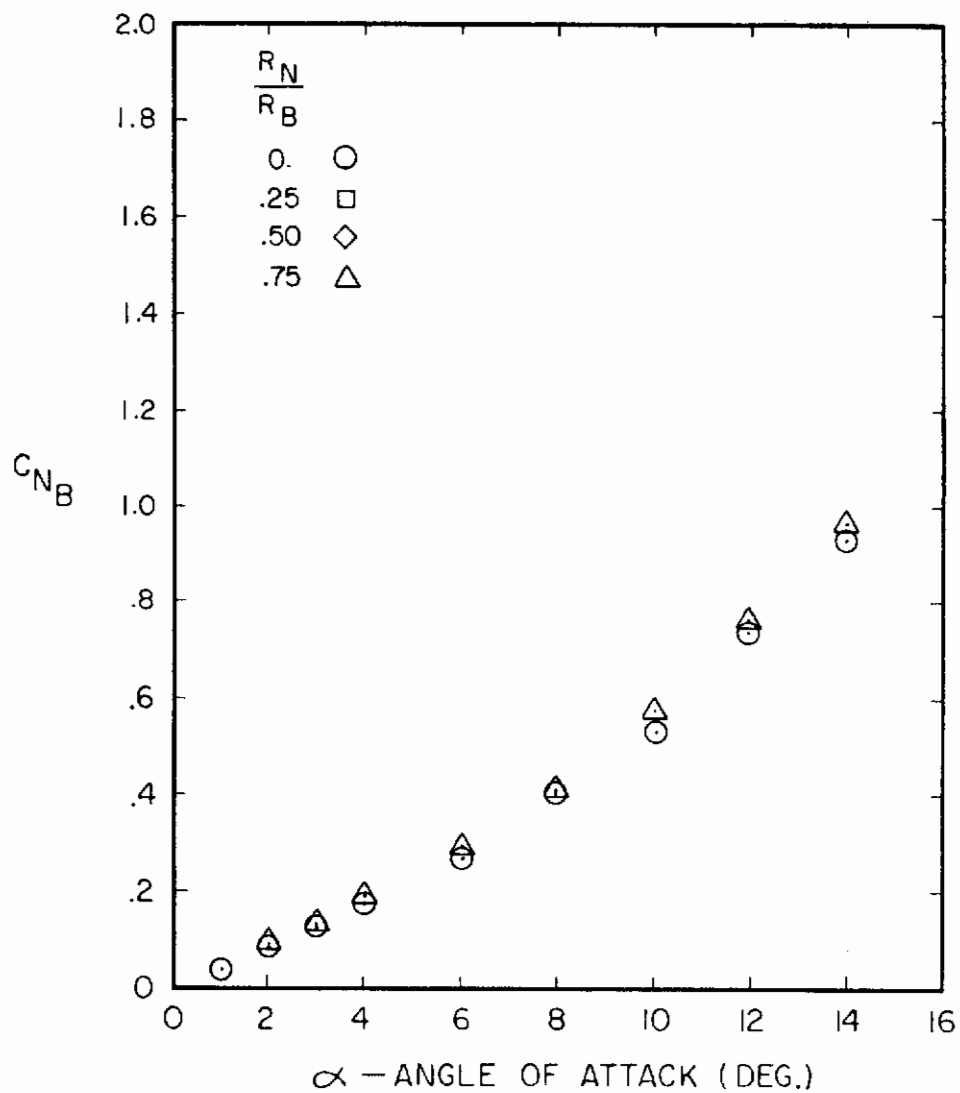


Figure A-42. Normal Force Coefficient Versus Angle of Attack for $\ell_N/d = 3$, $\ell_A/d = 6$, $M = 1.2$

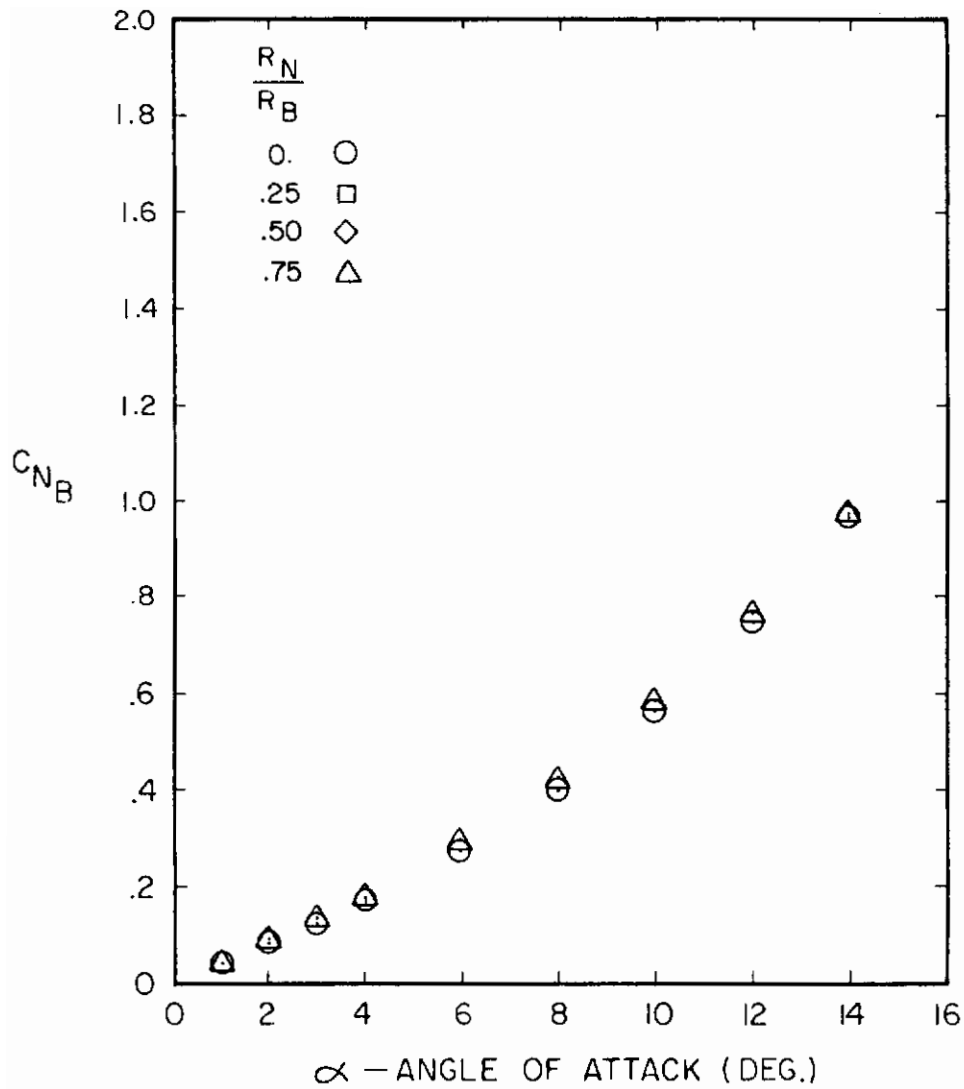


Figure A-43. Normal Force Coefficient Versus Angle of Attack for $\ell_N/d = 4$, $\ell_A/d = 6$, $M = 1.2$

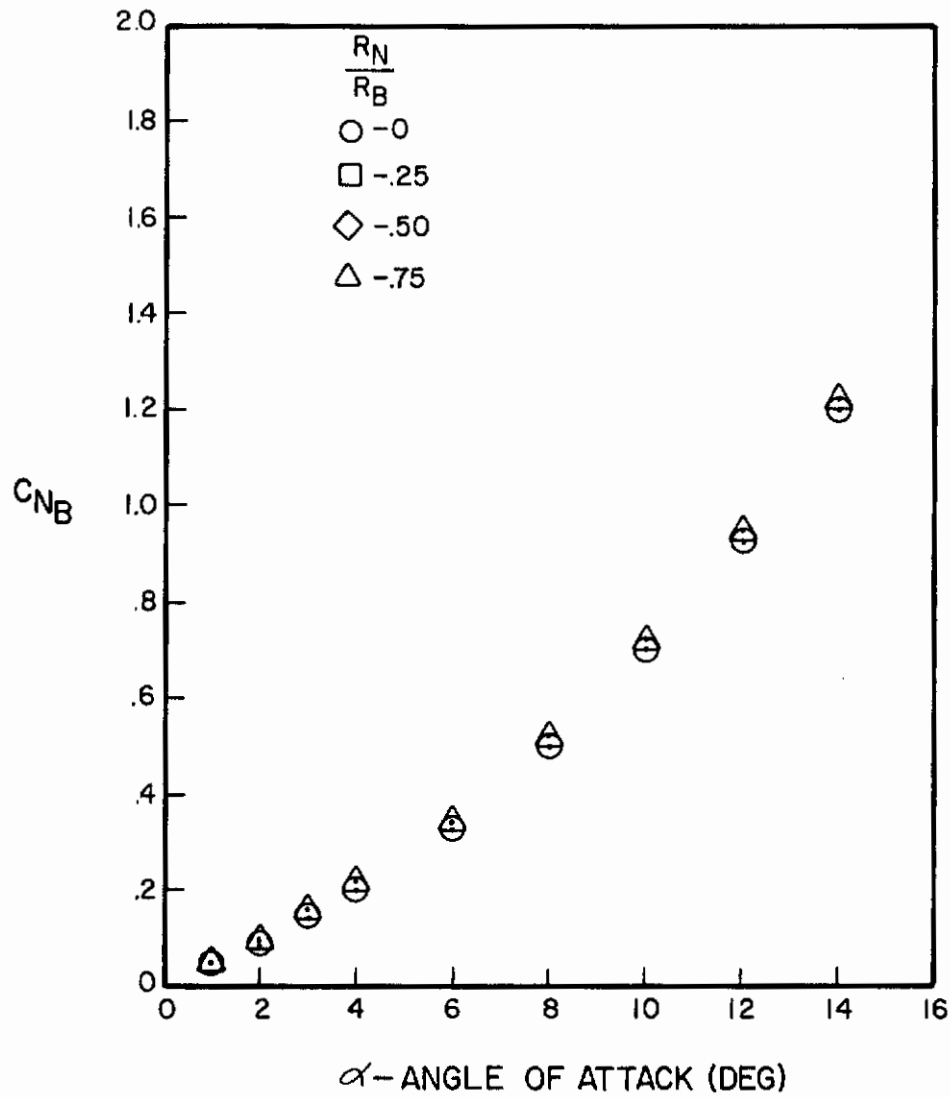


Figure A-44. Normal Force Coefficient Versus Angle of Attack for $l_N/d = 2$, $l_A/d = 10$, $M = 1.2$

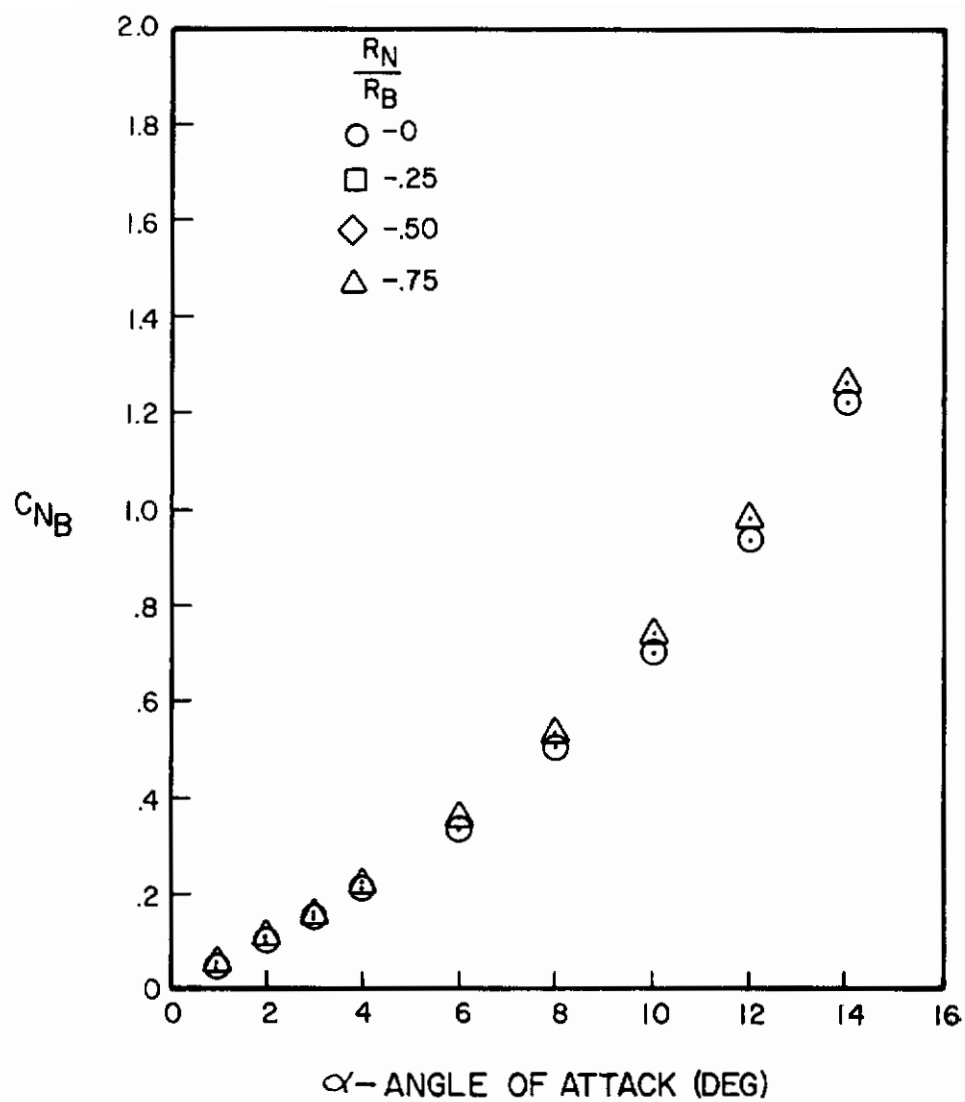


Figure A-45. Normal Force Coefficient Versus Angle of Attack for $l_N/d = 3$, $l_A/d = 10$, $M = 1.2$

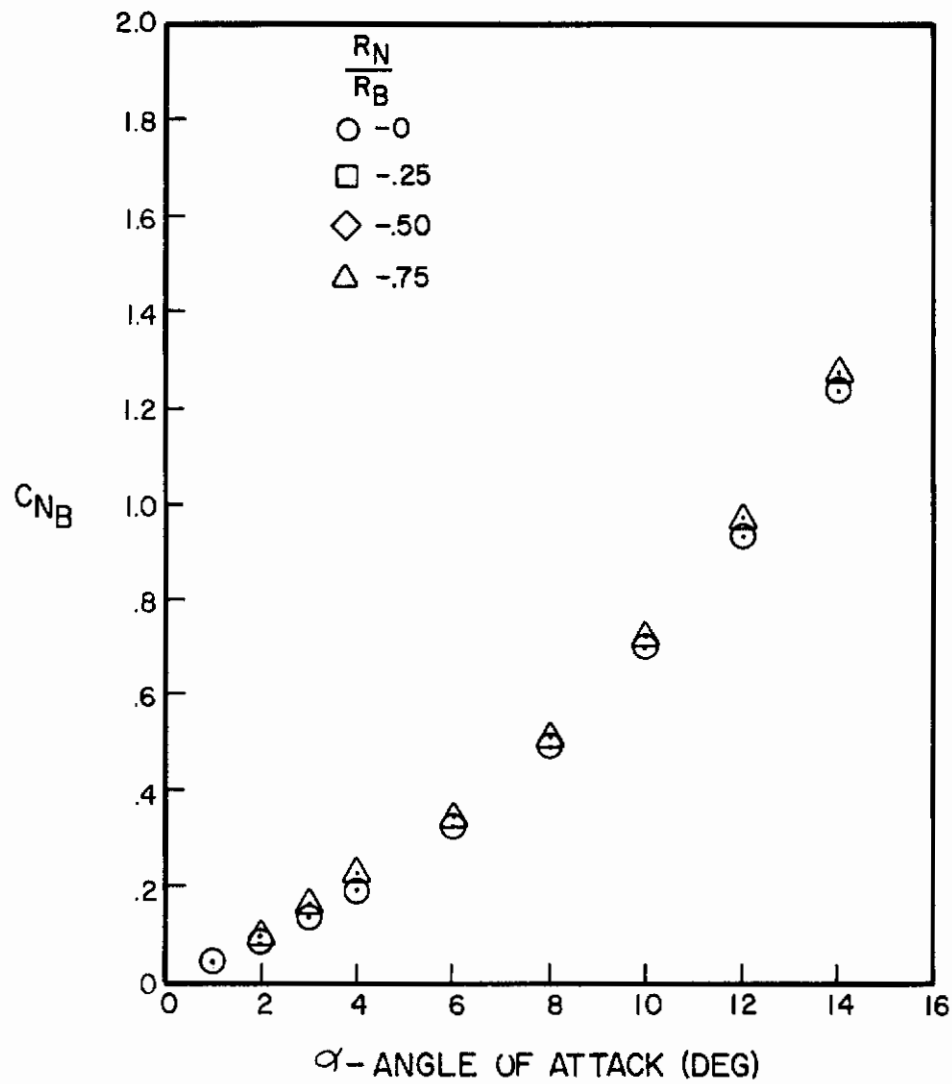


Figure A-46. Normal Force Coefficient Versus Angle of Attack for $l_N/d = 4$, $l_A/d = 10$, $M = 1.2$

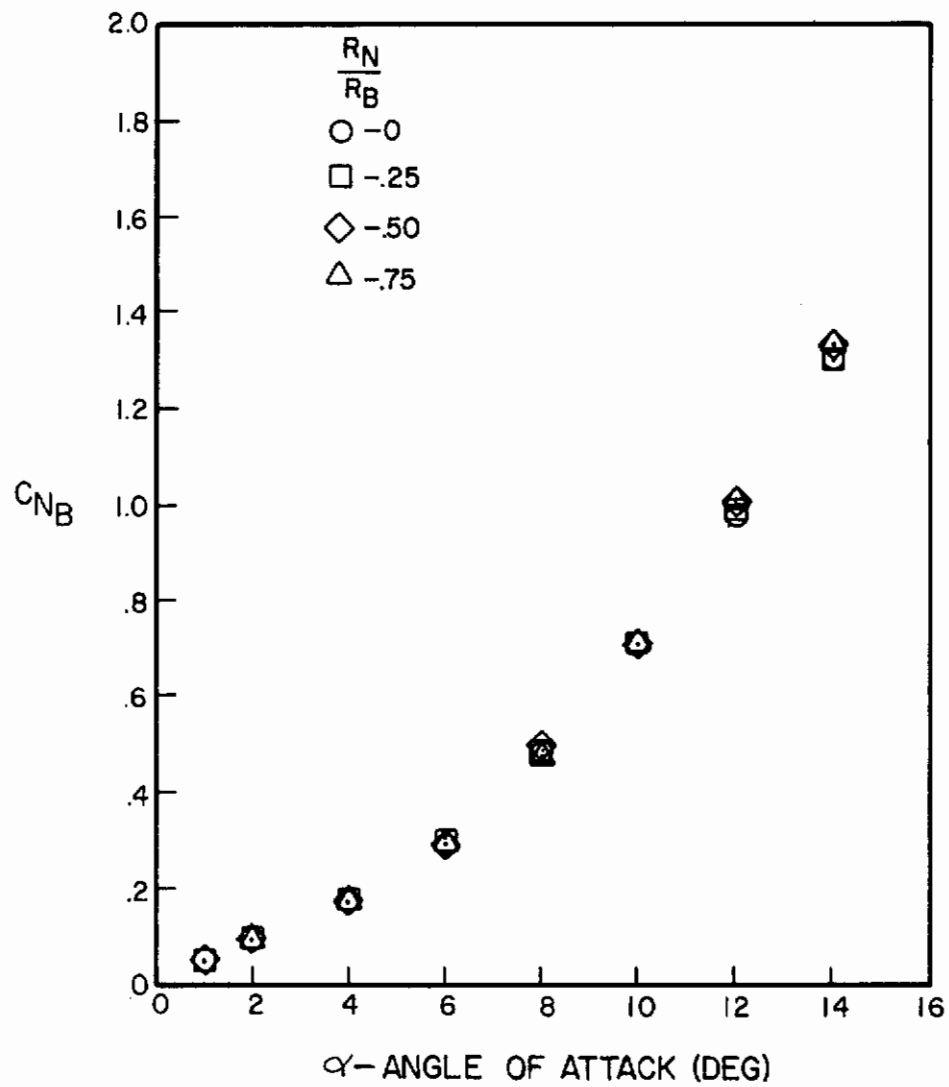


Figure A-47. Normal Force Coefficient Versus Angle of Attack for $l_N/d = 2$, $l_A/d = 6$, $M = 1.5$

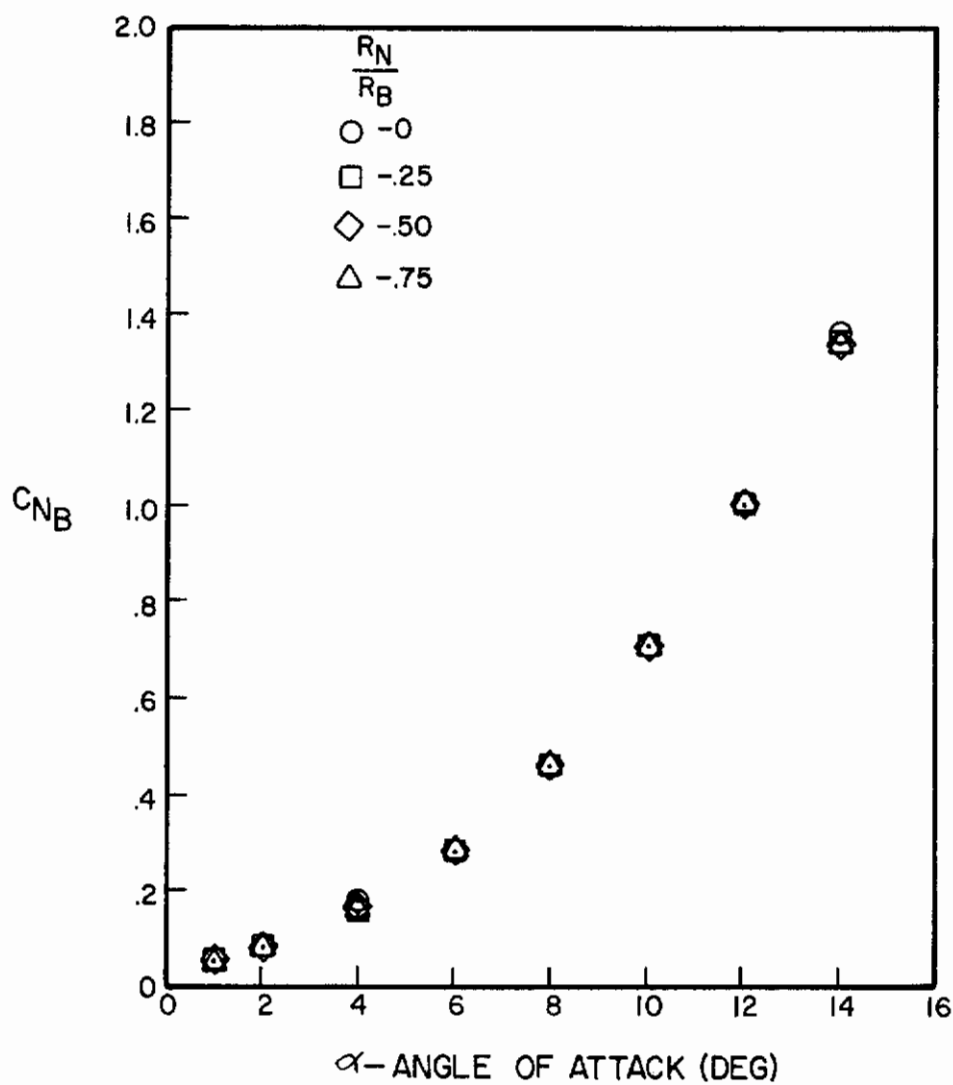


Figure A-48. Normal Force Coefficient Versus Angle of Attack for $l_N/d = 3$, $l_A/d = 6$, $M = 1.5$

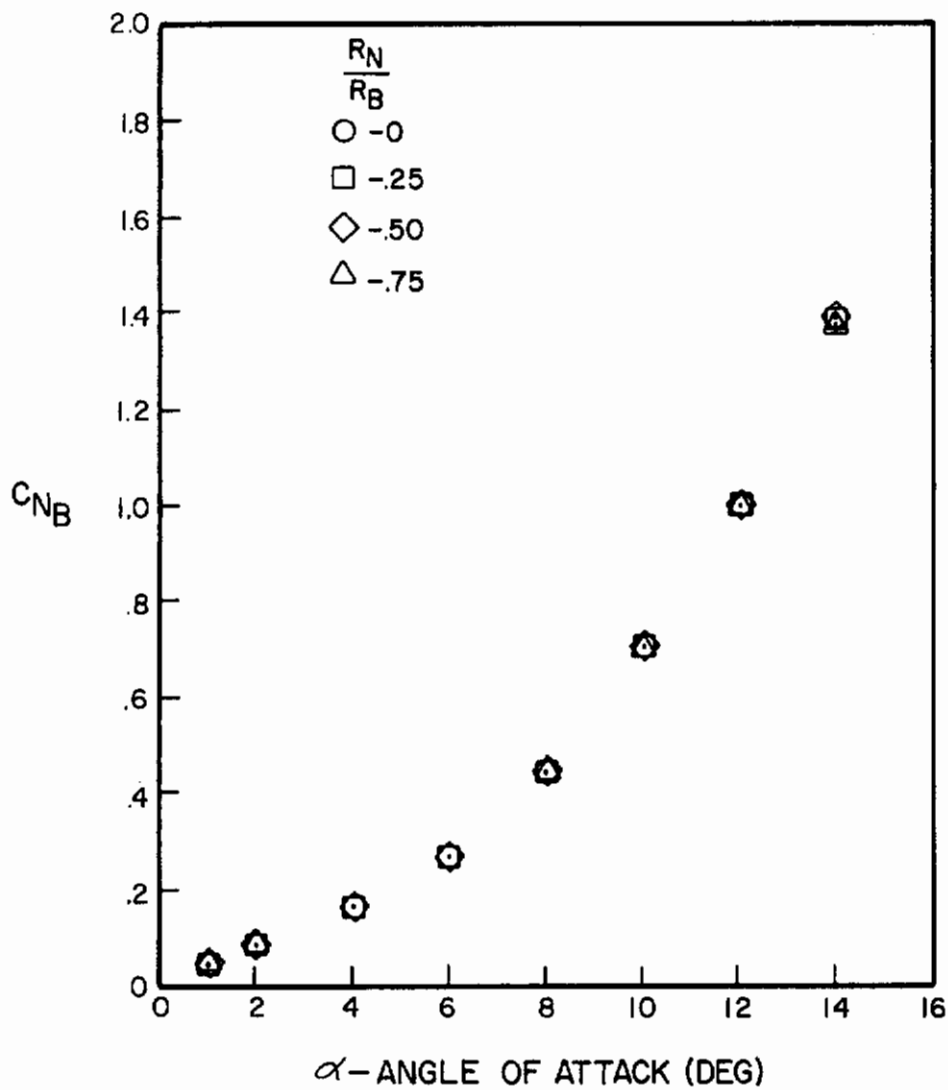


Figure A-49. Normal Force Coefficient Versus Angle of Attack for $\ell_N/d = 4$, $\ell_A/d = 6$, $M = 1.5$

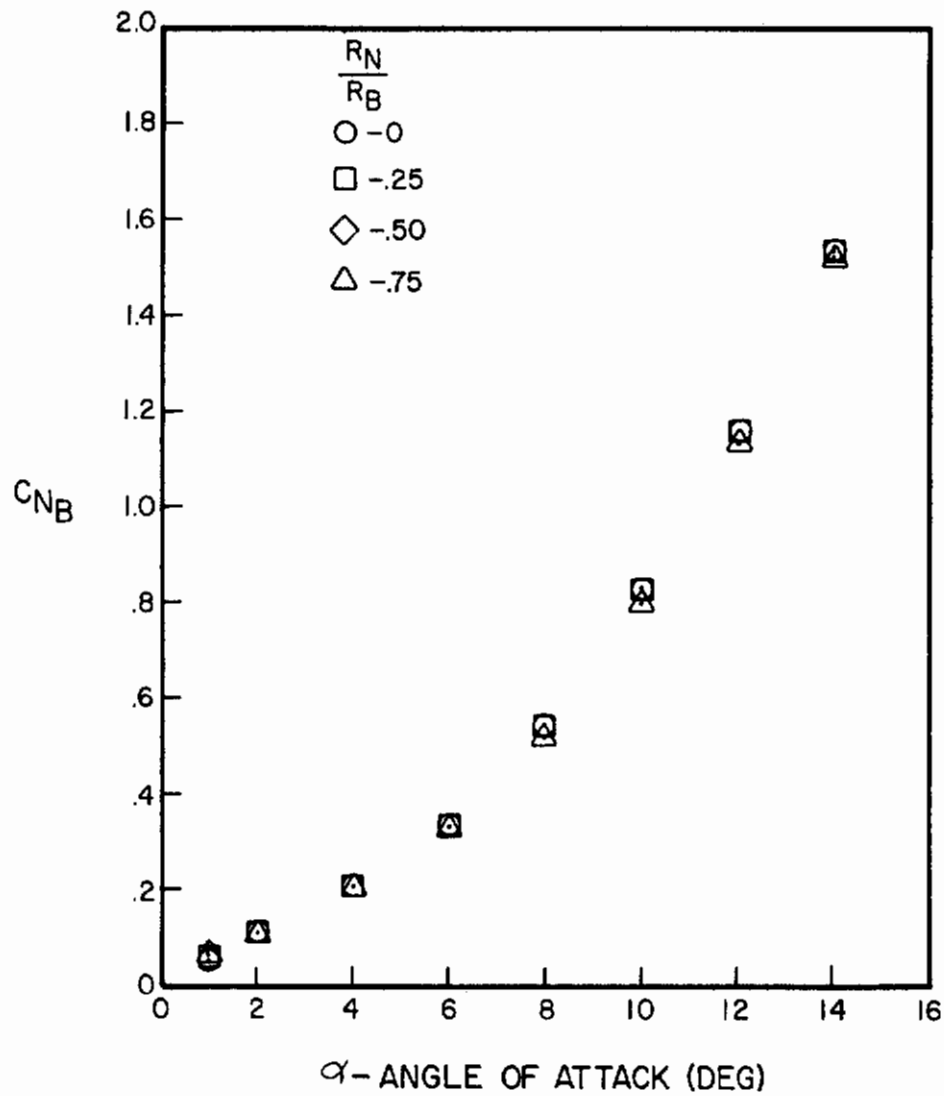


Figure A-50. Normal Force Coefficient Versus Angle of Attack for $l_N/d = 3$, $l_A/d = 8$, $M = 1.5$

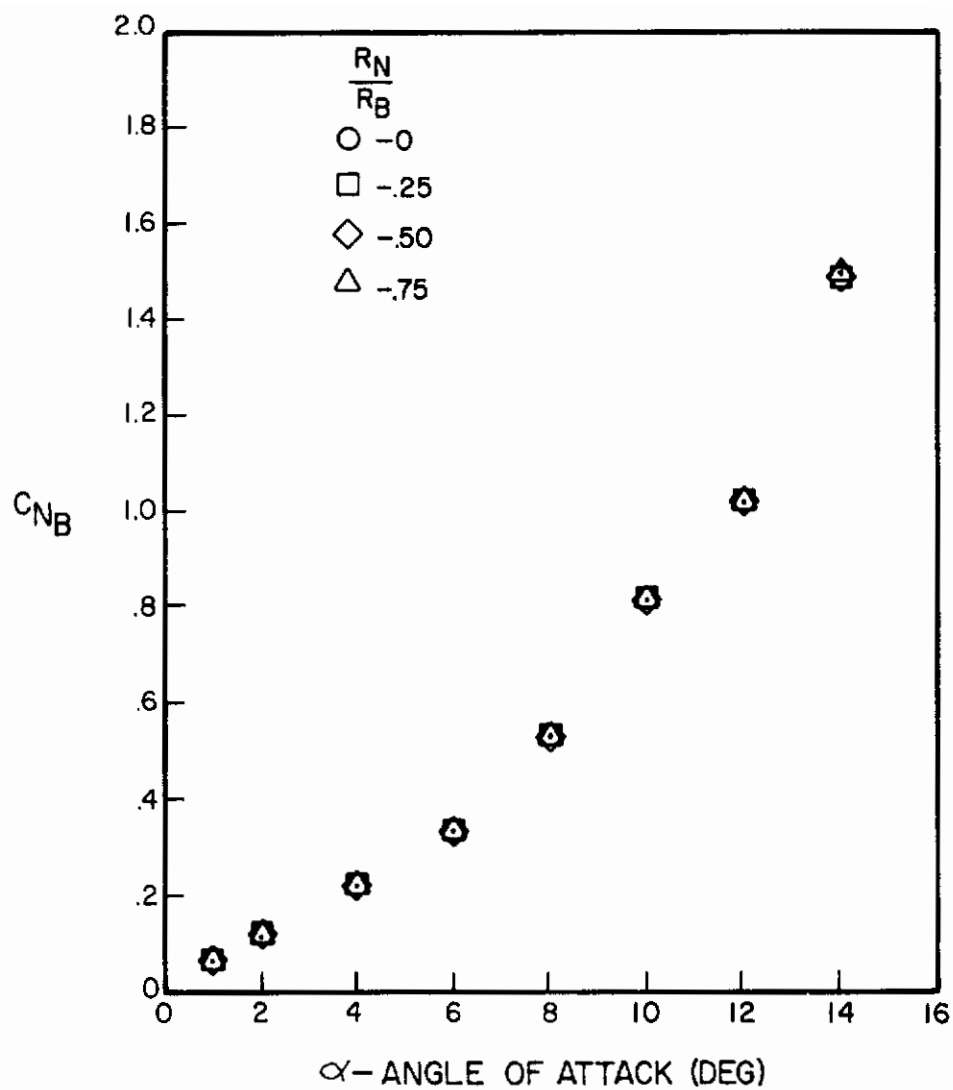


Figure A-51. Normal Force Coefficient Versus Angle of Attack for $l_N/d = 2$, $l_A/d = 8$, $M = 1.5$

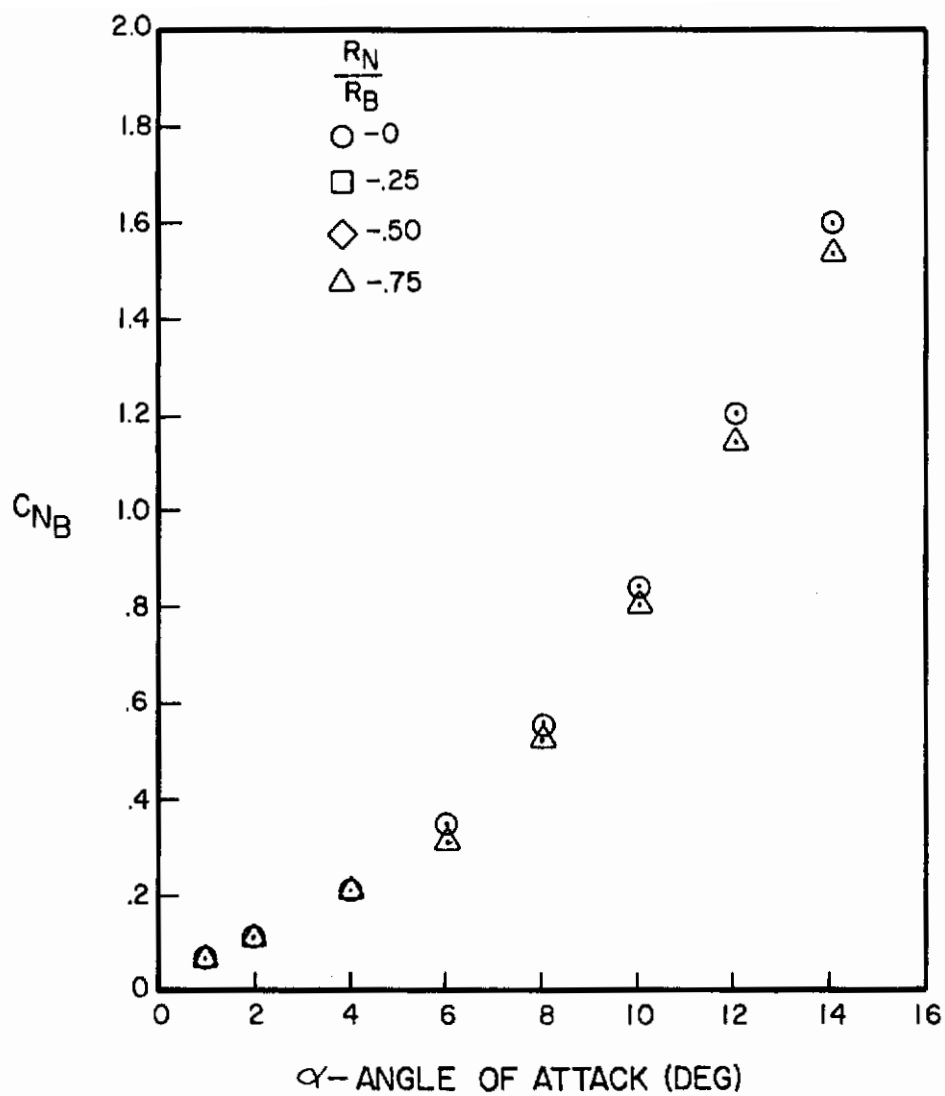


Figure A-52. Normal Force Coefficient Versus Angle of Attack for $\ell_N/d = 4$, $\ell_A/d = 8$, $M = 1.5$

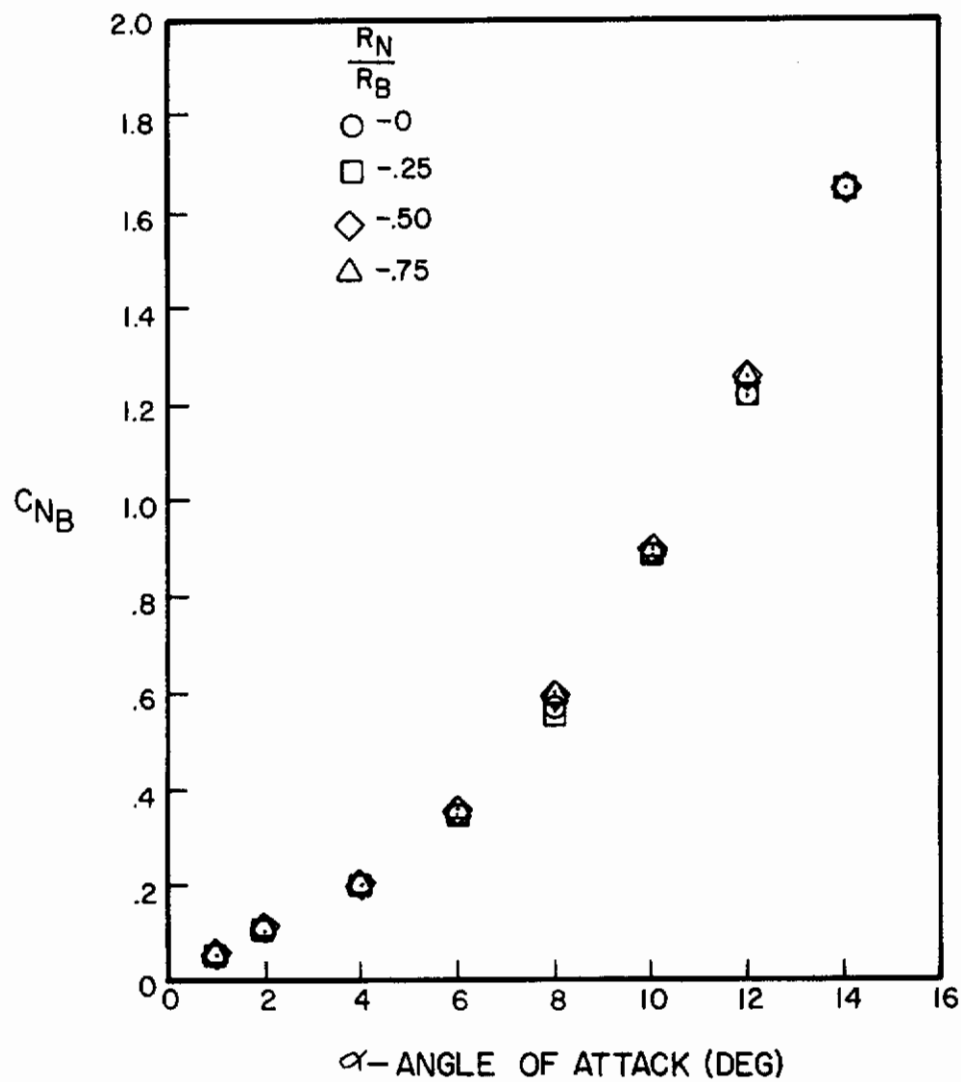


Figure A-53. Normal Force Coefficient Versus Angle of Attack for $l_N/d = 2$, $l_A/d = 10$, $M = 1.5$

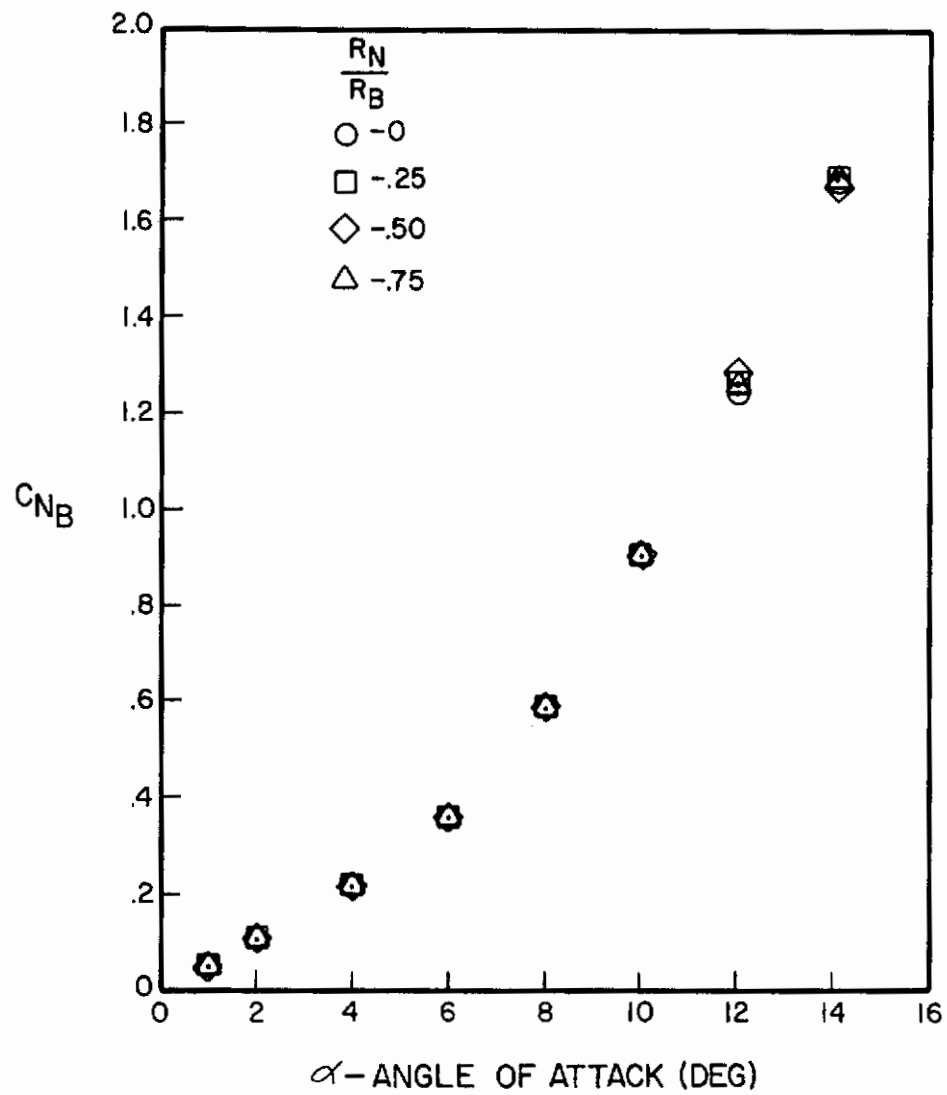


Figure A-54. Normal Force Coefficient Versus Angle of Attack for $l_N/d = 3$, $l_A/d = 10$, $M = 1.5$

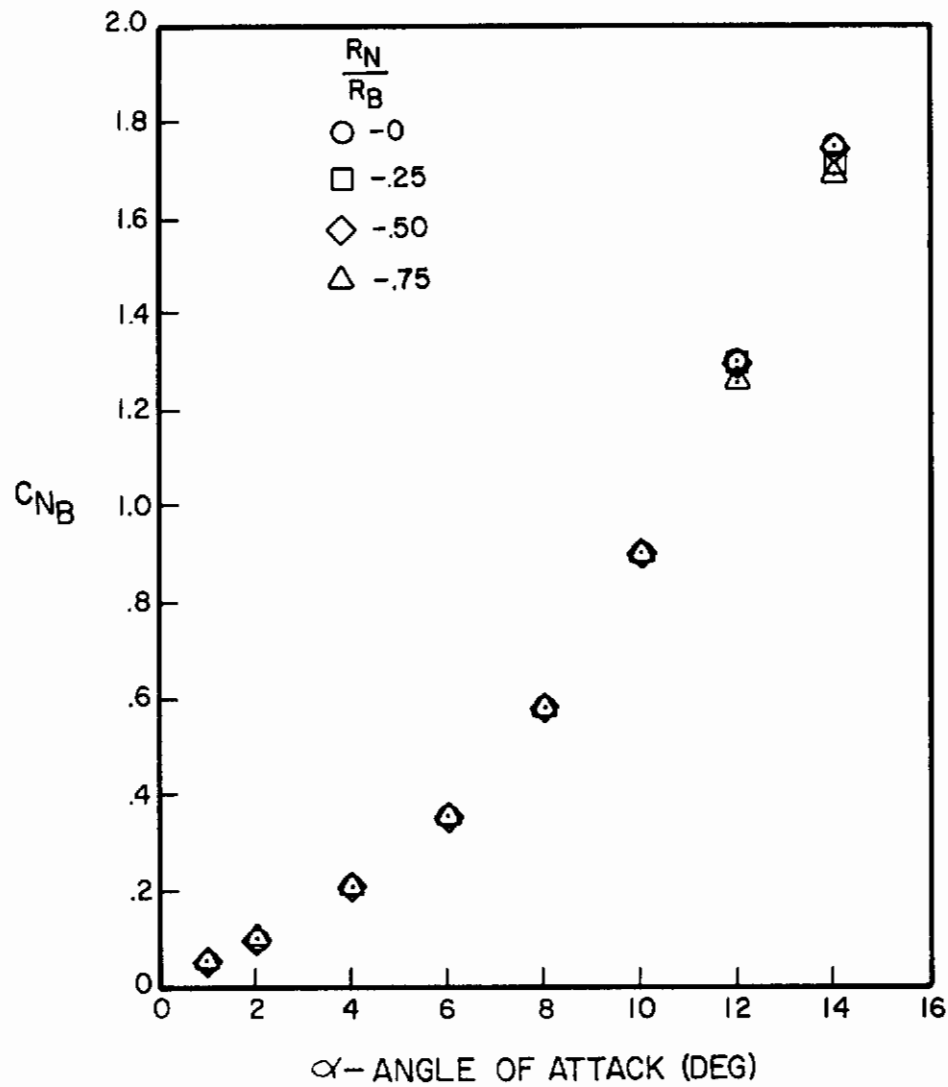


Figure A-55. Normal Force Coefficient Versus Angle of Attack for $\ell_N/d = 4$, $\ell_A/d = 10$, $M = 1.5$

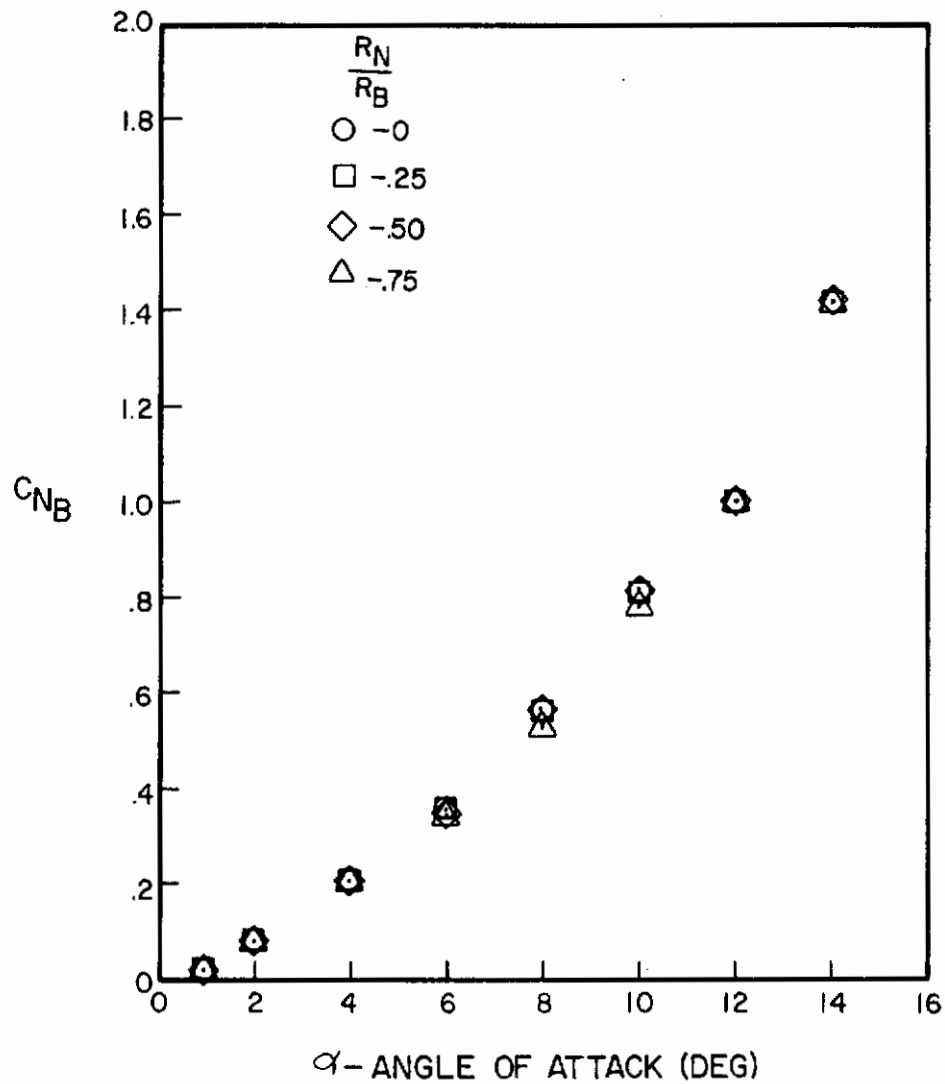


Figure A-56. Normal Force Coefficient Versus Angle of Attack for $l_N/d = 2$, $l_A/d = 6$, $M = 2.0$

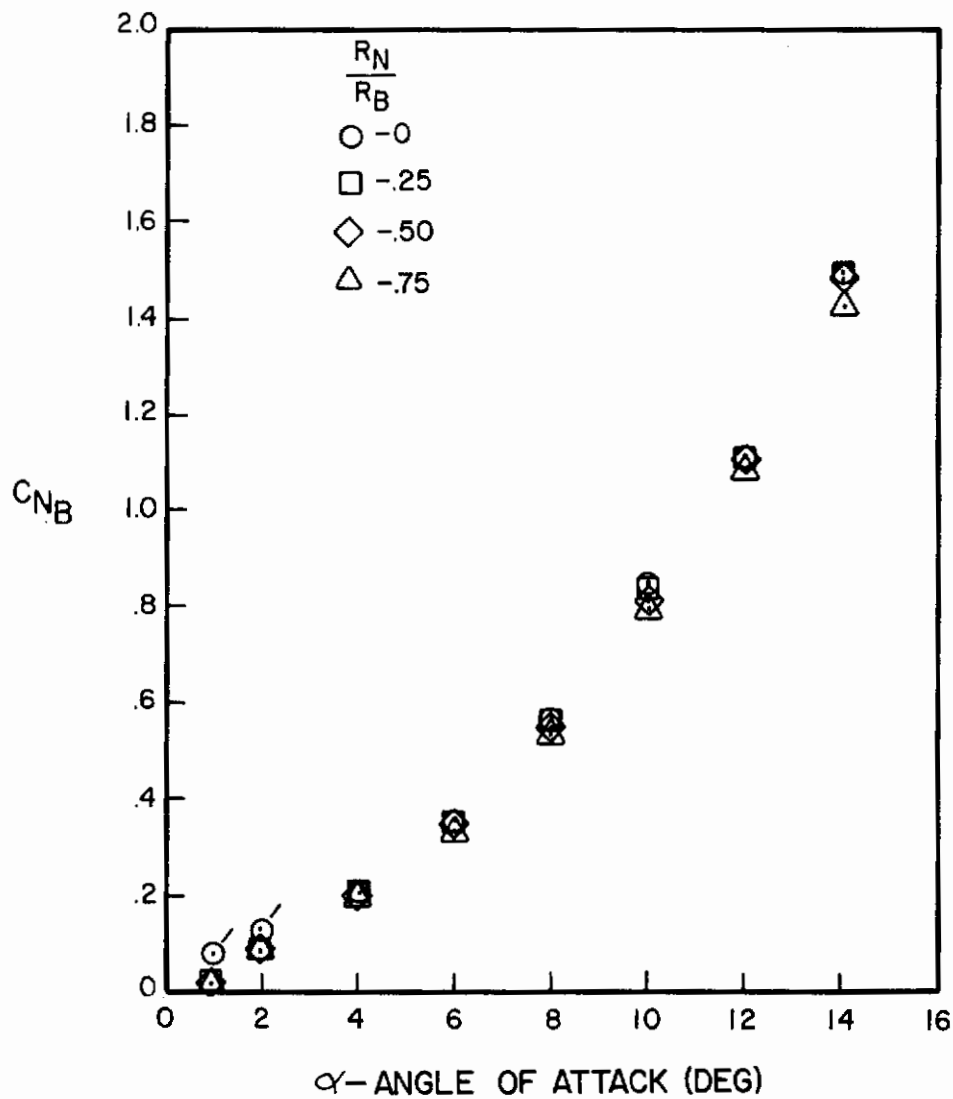


Figure A-57. Normal Force Coefficient Versus Angle of Attack for $l_N/d = 3$, $l_A/d = 6$, $M = 2.0$

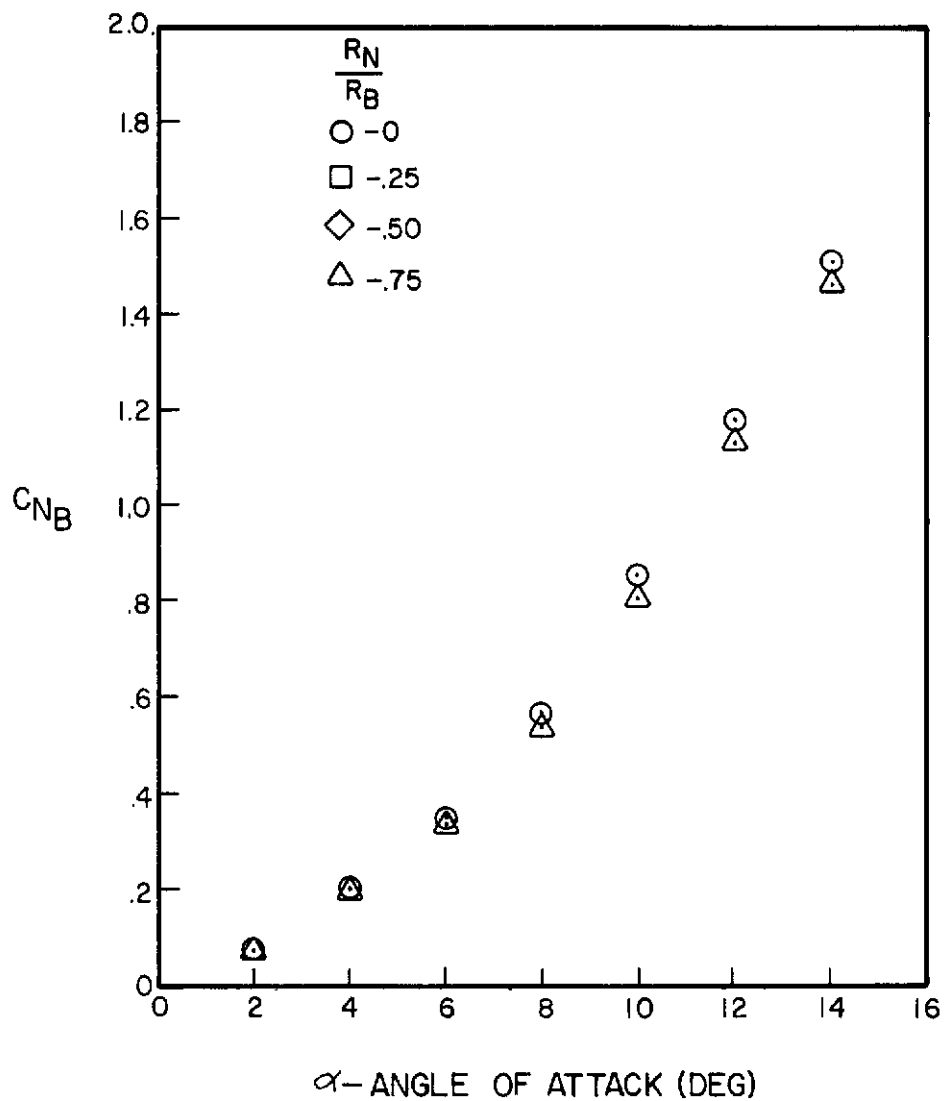


Figure A-58. Normal Force Coefficient Versus Angle of Attack for $l_N/d = 4$, $l_A/d = 6$, $M = 2.0$

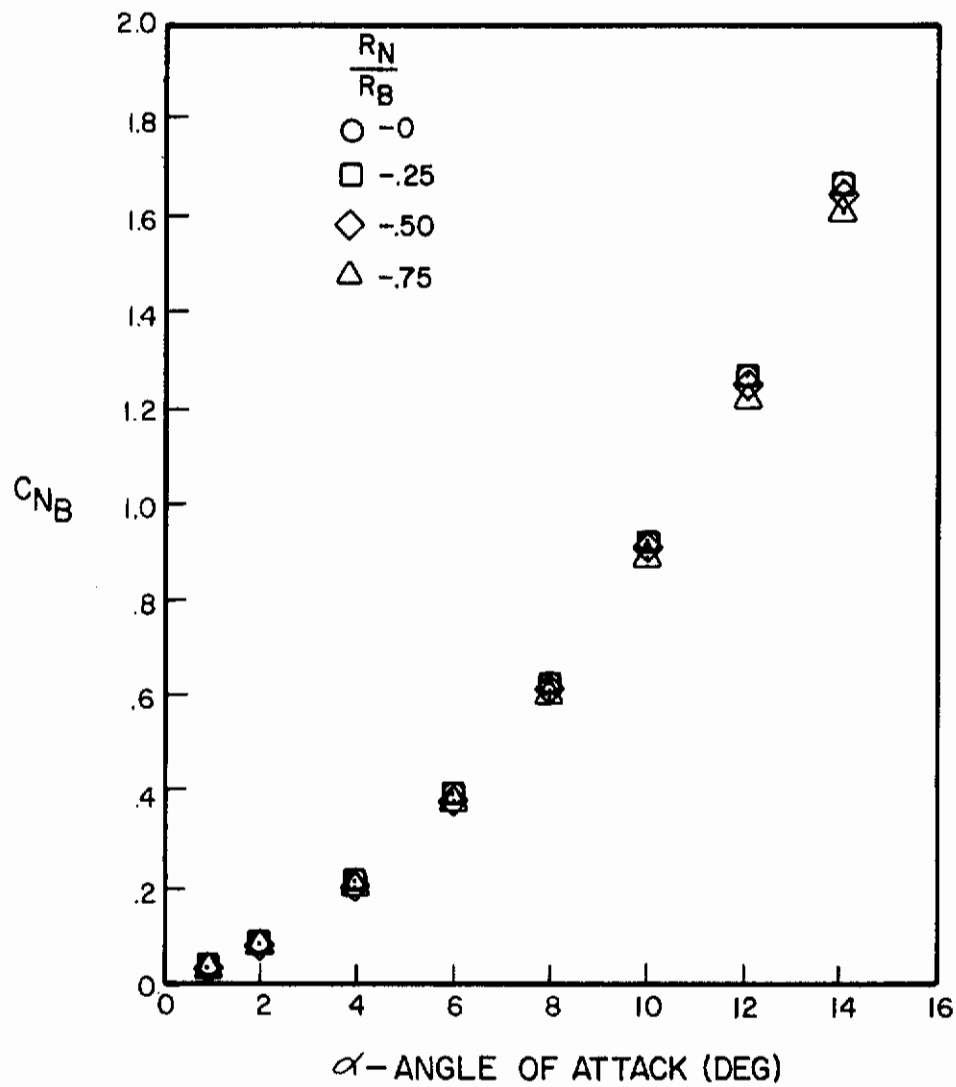


Figure A-59. Normal Force Coefficient Versus Angle of Attack for $l_N/d = 2$, $l_A/d = 8$, $M = 2.0$

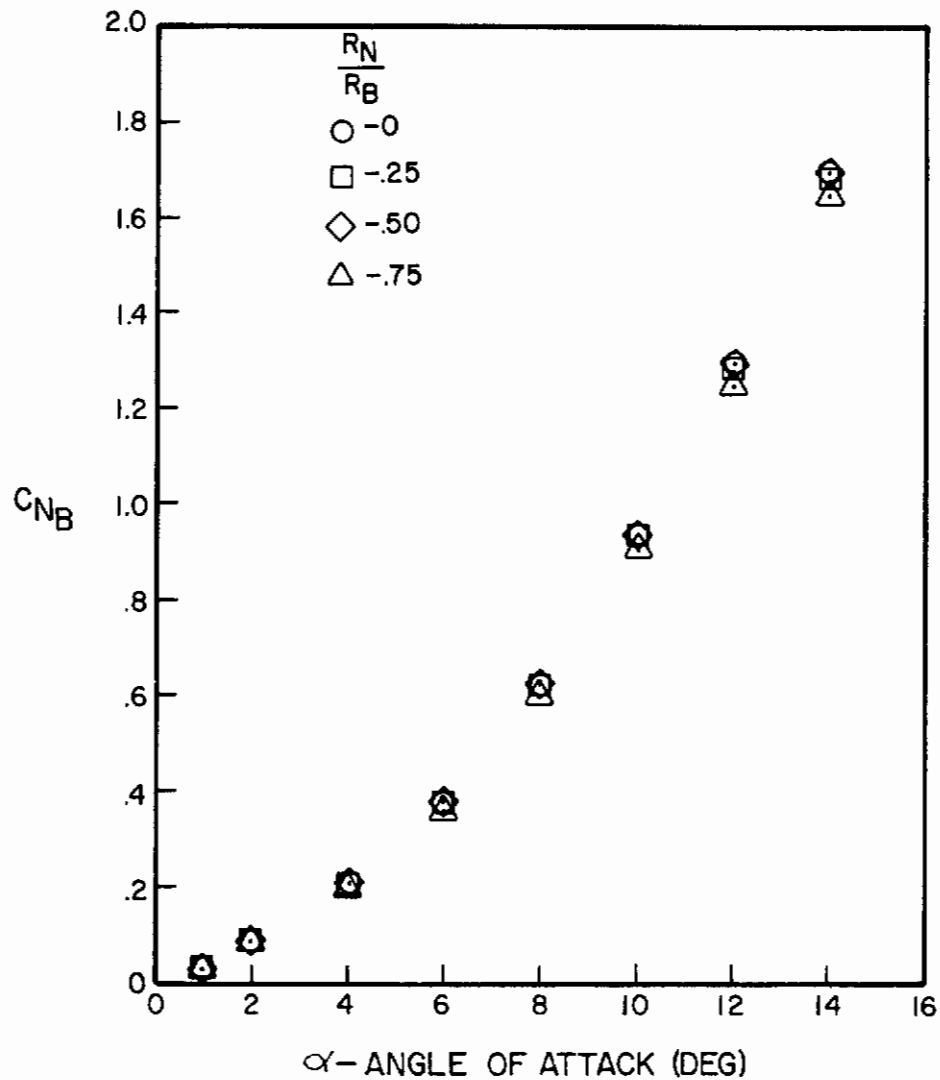


Figure A-60. Normal Force Coefficient Versus Angle of Attack for $l_N/d = 3$, $l_A/d = 8$, $M = 2.0$

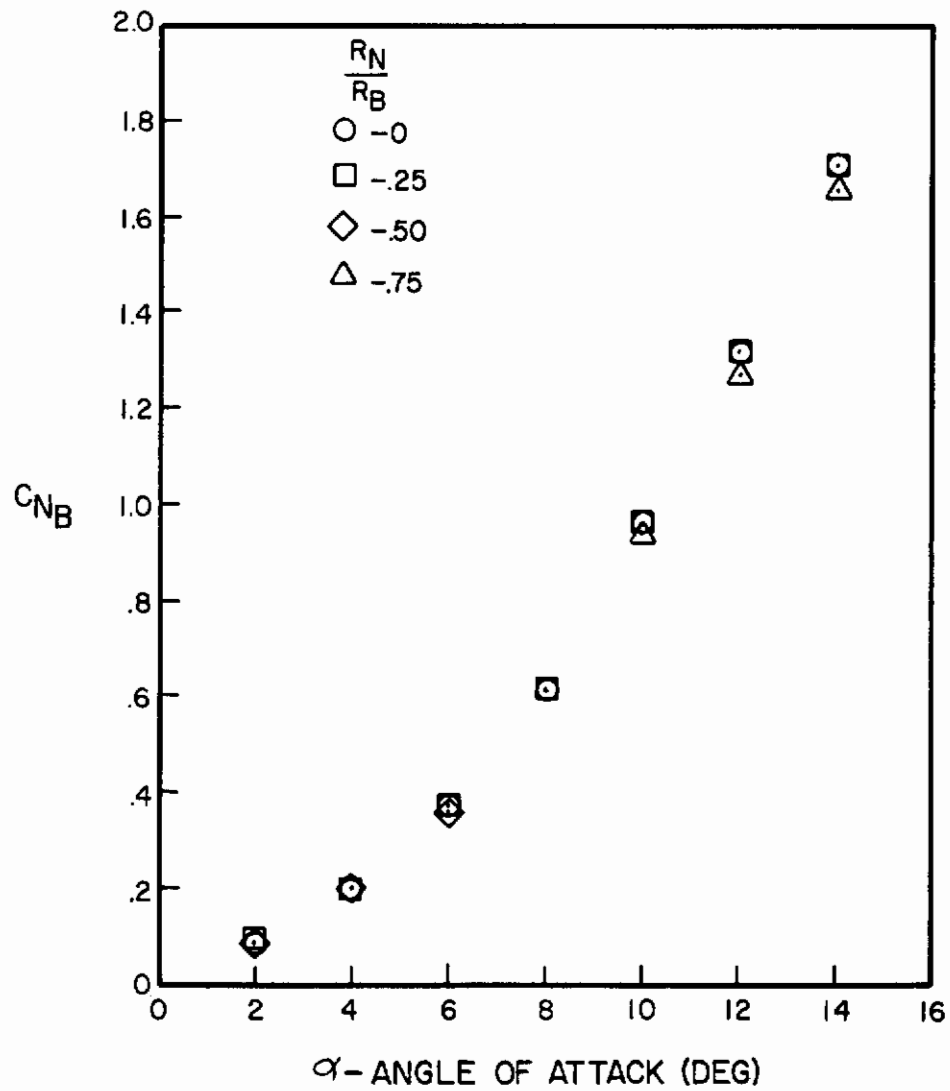


Figure A-61. Normal Force Coefficient Versus Angle of Attack for $\ell_N/d = 4$, $\ell_A/d = 8$, $M = 2.0$

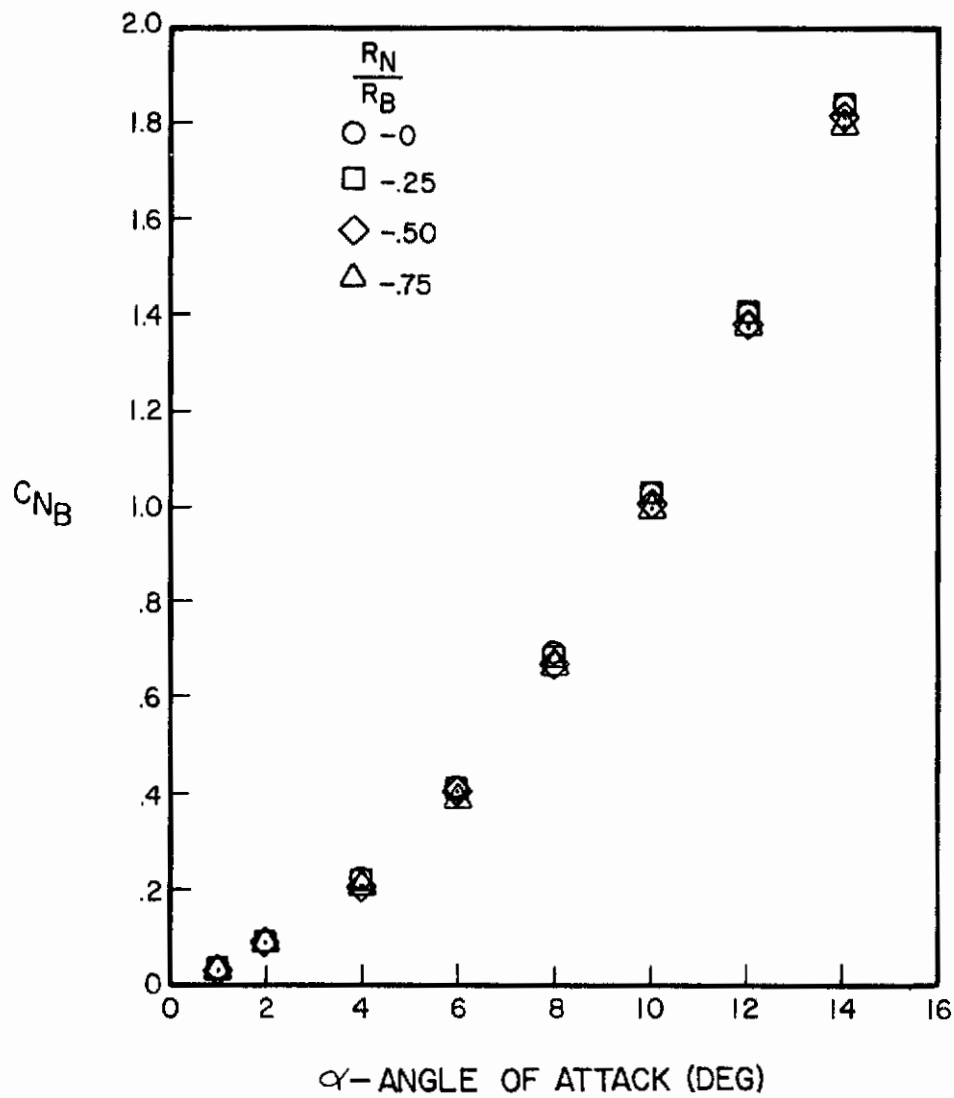


Figure A-62. Normal Force Coefficient Versus Angle of Attack for $l_N/d = 2$, $l_A/d = 10$, $M = 2.0$

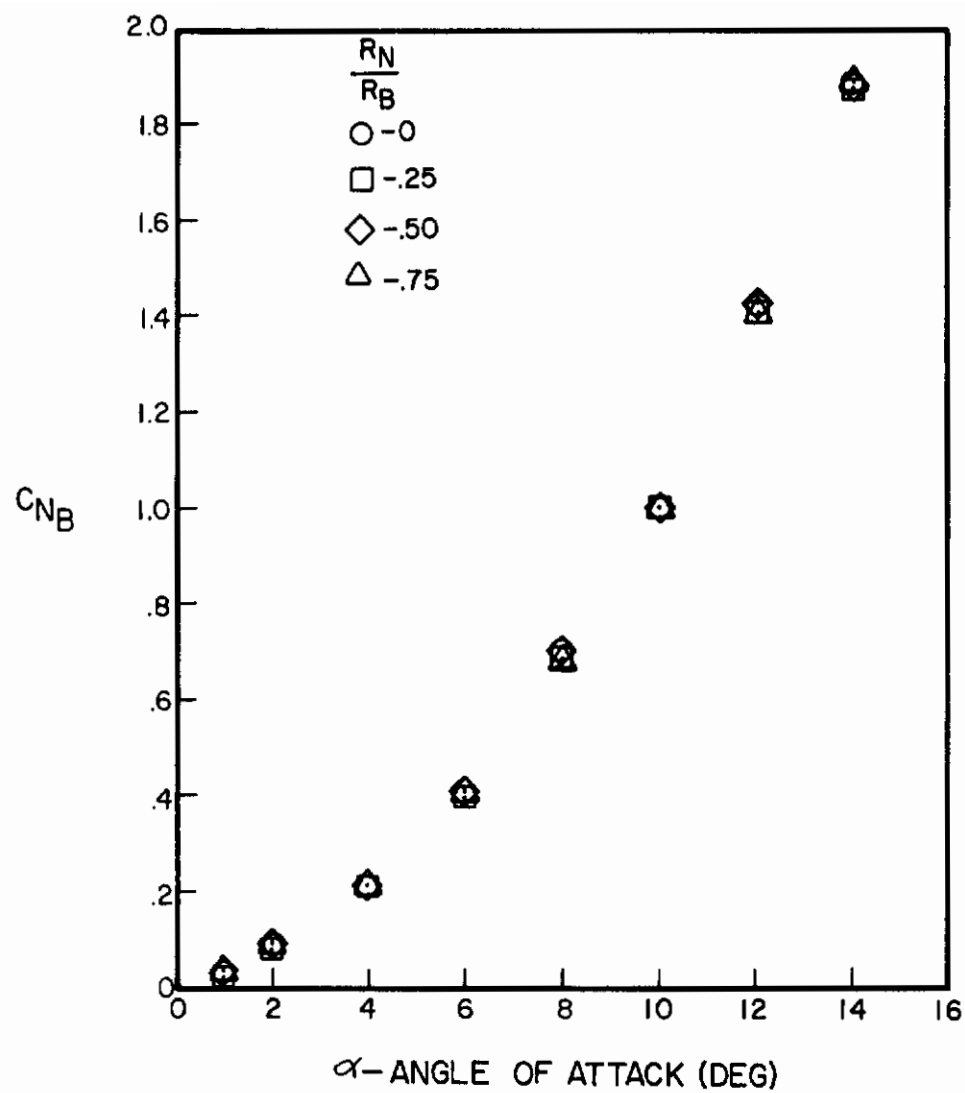


Figure A-63. Normal Force Coefficient Versus Angle of Attack for $l_N/d = 3$, $l_A/d = 10$, $M = 2.0$

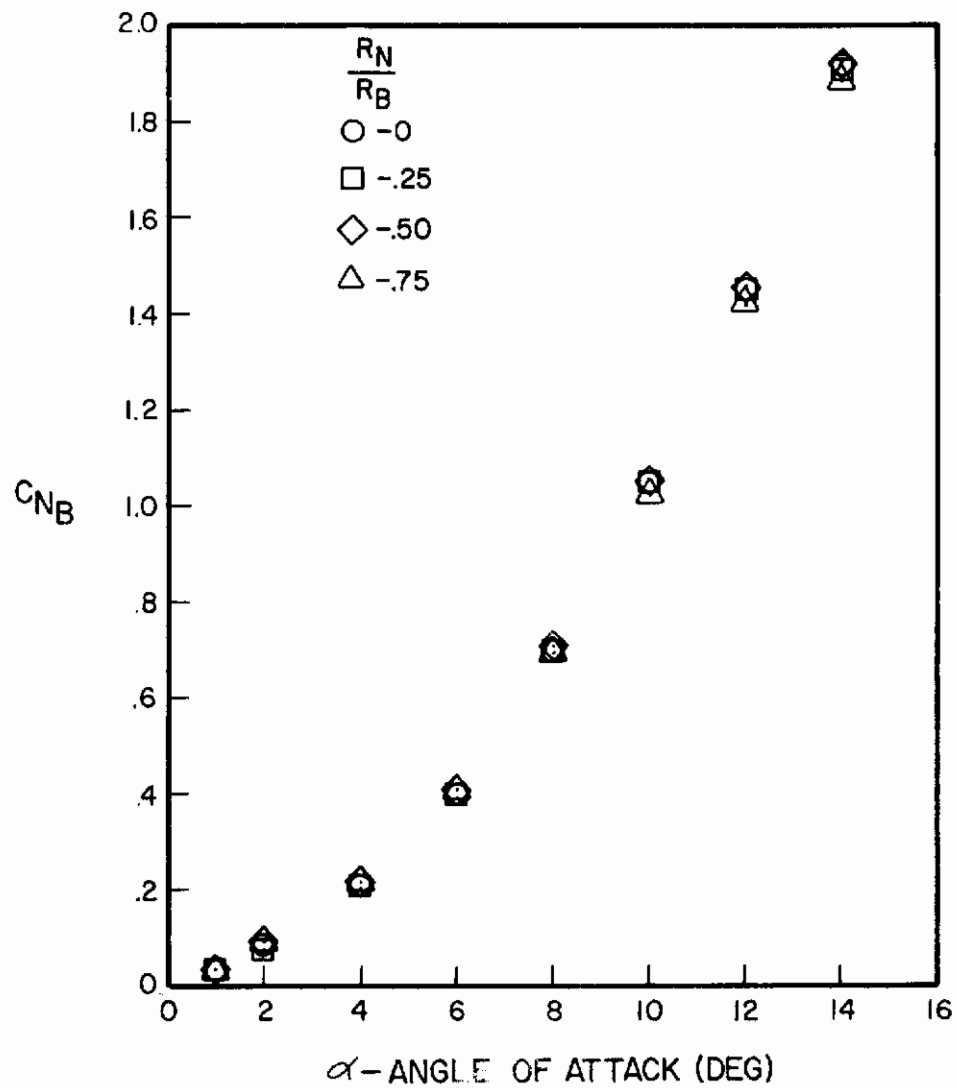


Figure A-64. Normal Force Coefficient Versus Angle of Attack for $\ell_N/d = 4$, $\ell_A/d = 10$, $M = 2.0$

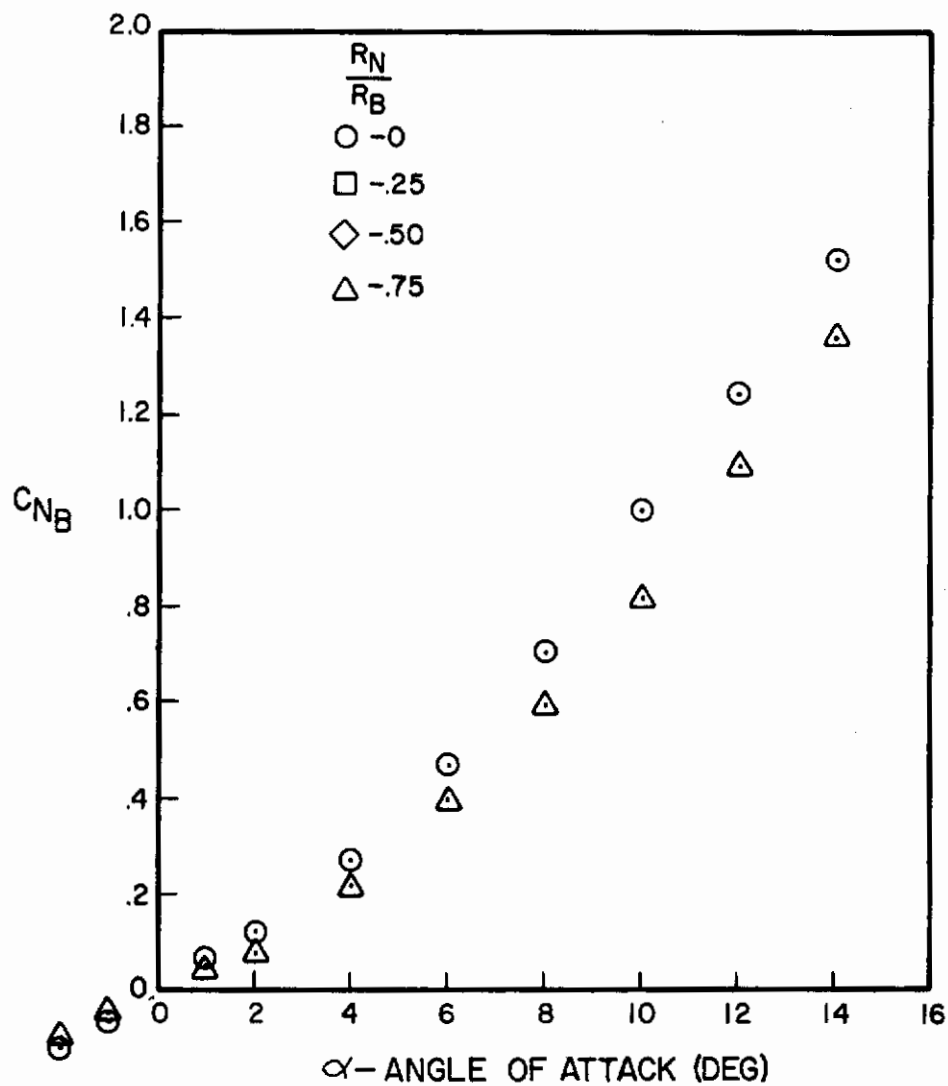


Figure A-65. Normal Force Coefficient Versus Angle of Attack for $\ell_N/d = 2$, $\ell_A/d = 6$, $M = 3.0$

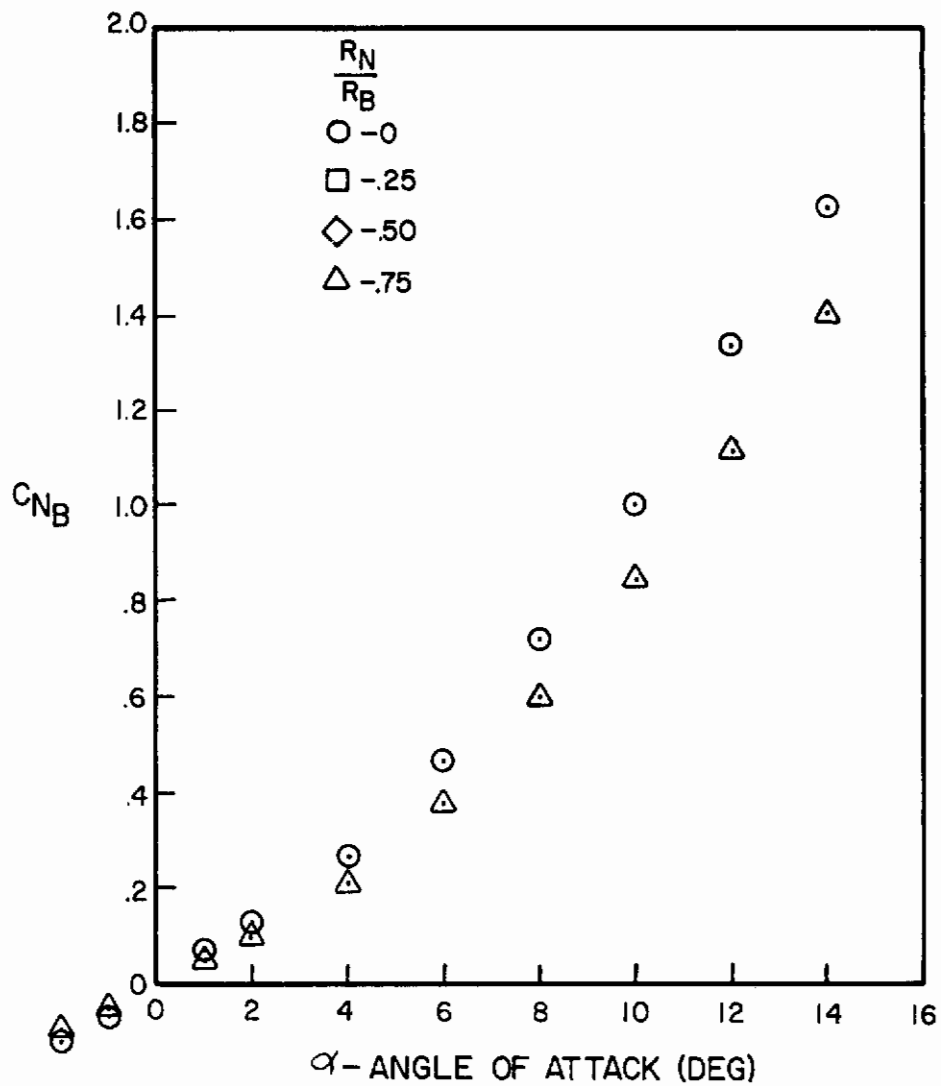


Figure A-66. Normal Force Coefficient Versus Angle of Attack for $l_N/d = 3$, $l_A/d = 6$, $M = 3.0$

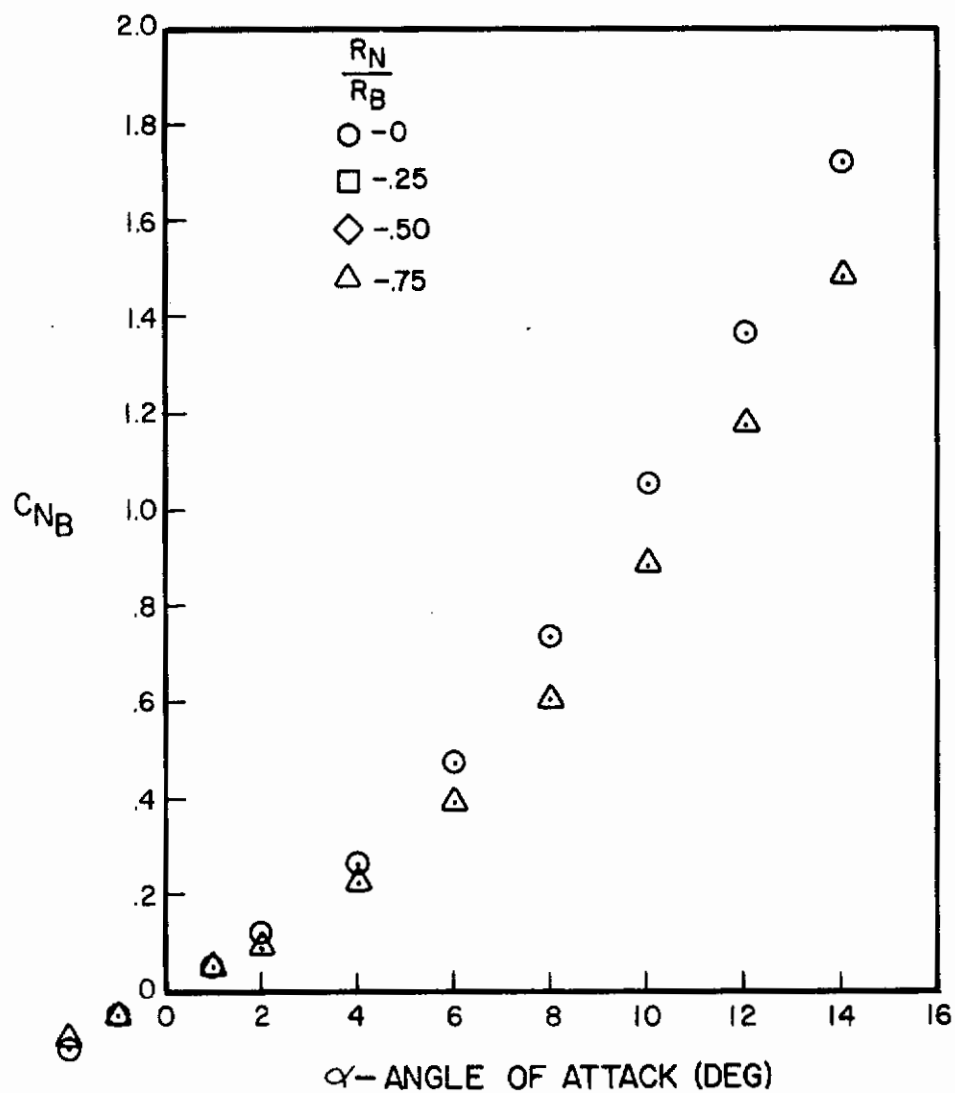


Figure A-67. Normal Force Coefficient Versus Angle of Attack for $l_N/d = 4$, $l_A/d = 6$, $M = 3.0$

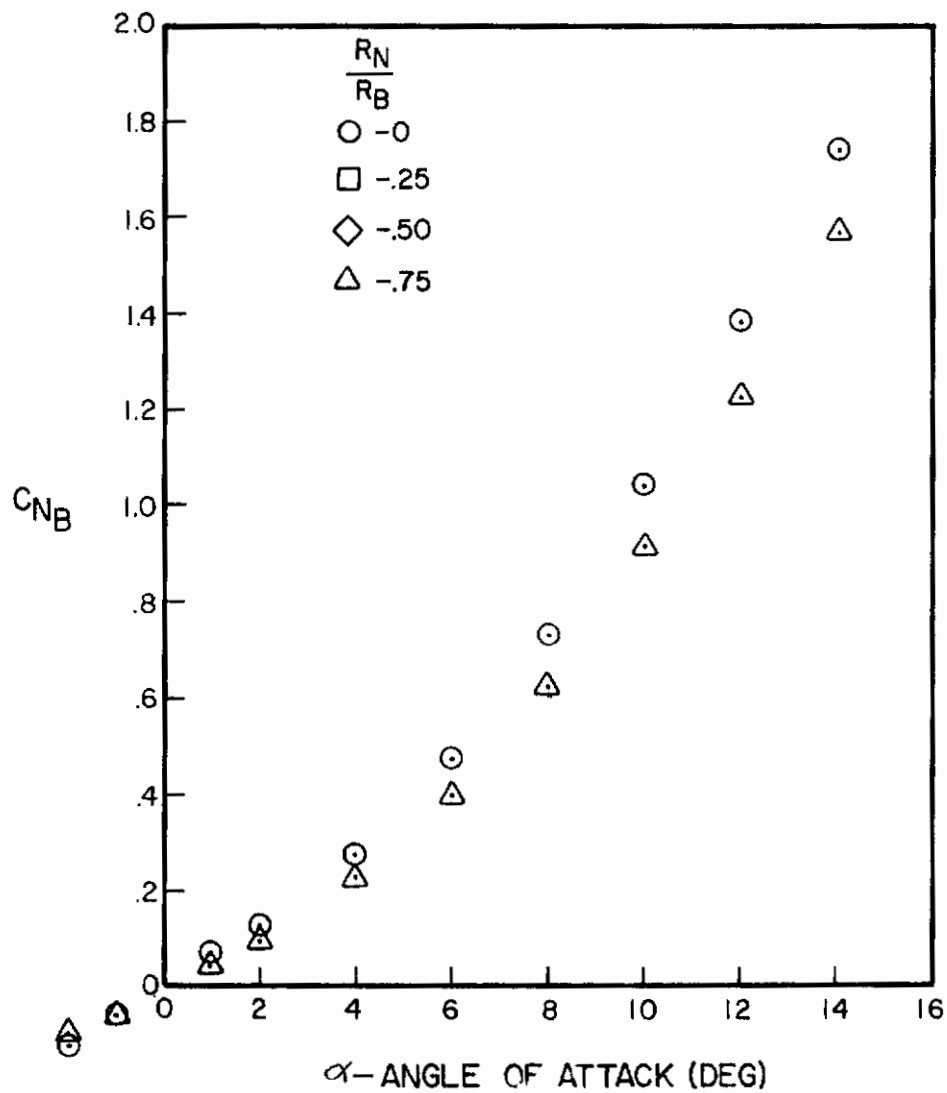


Figure A-68. Normal Force Coefficient Versus Angle of Attack for $\ell_N/d = 2$, $\ell_A/d = 8$, $M = 3.0$

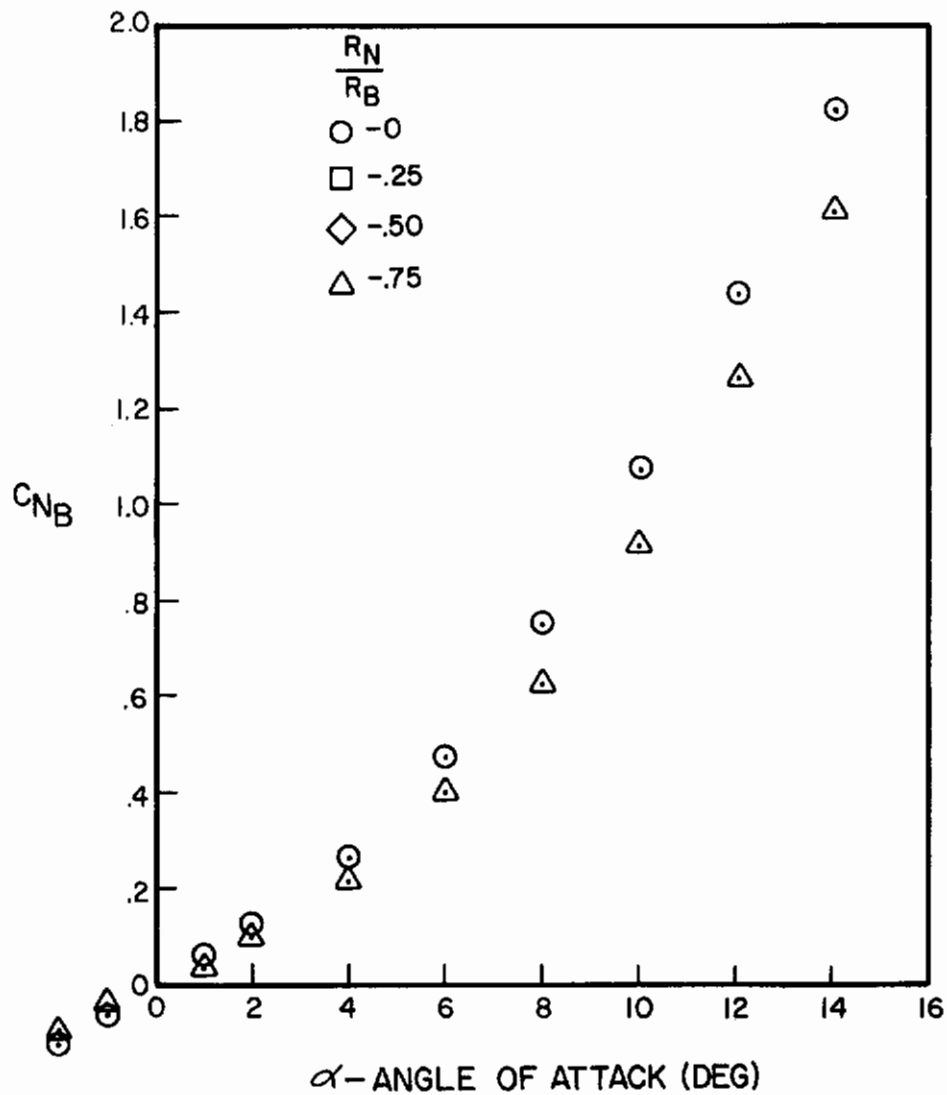


Figure A-69. Normal Force Coefficient Versus Angle of Attack for $\ell_N/d = 3$, $\ell_A/d = 8$, $M = 3.0$

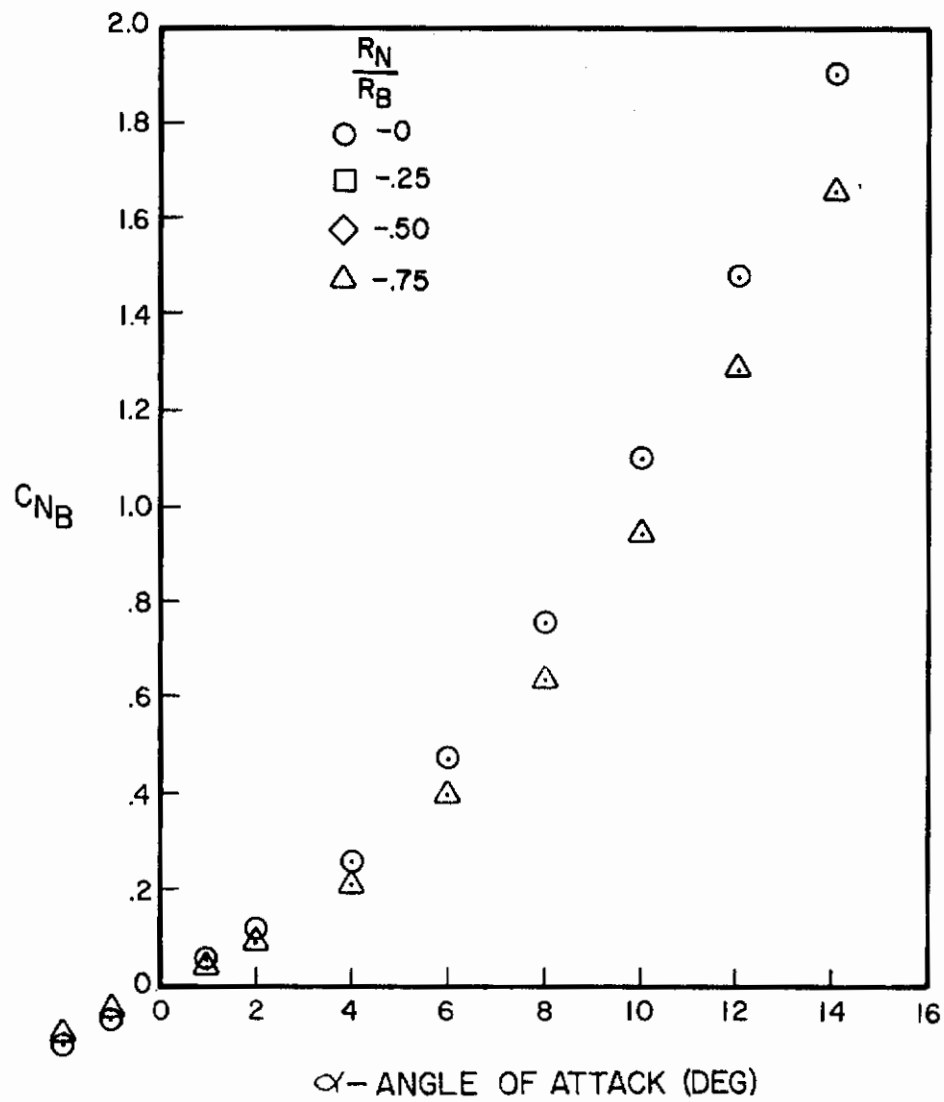


Figure A-70. Normal Force Coefficient Versus Angle of Attack for $l_N/d = 4$, $l_A/d = 8$, $M = 3.0$

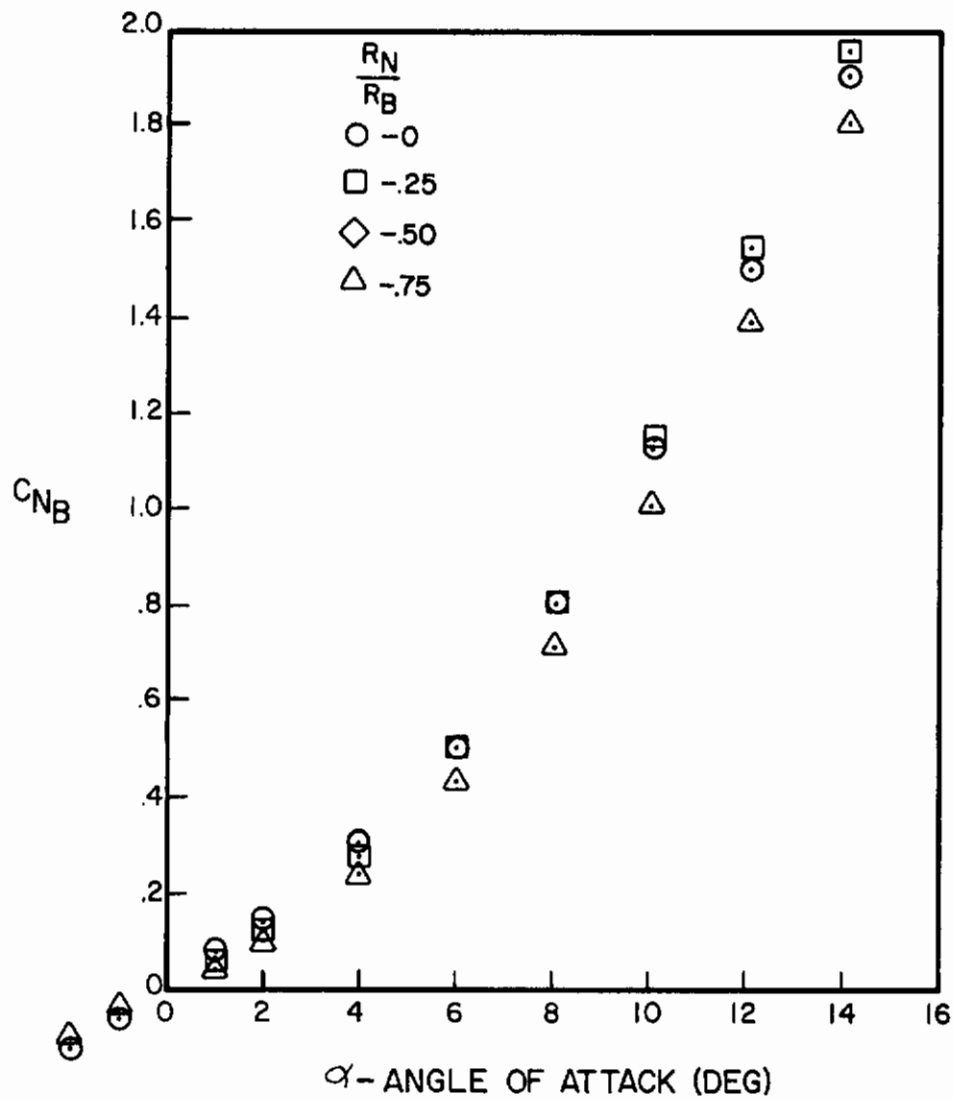


Figure A-71. Normal Force Coefficient Versus Angle of Attack for $\ell_N/d = 2$, $\ell_A/d = 10$, $M = 3.0$

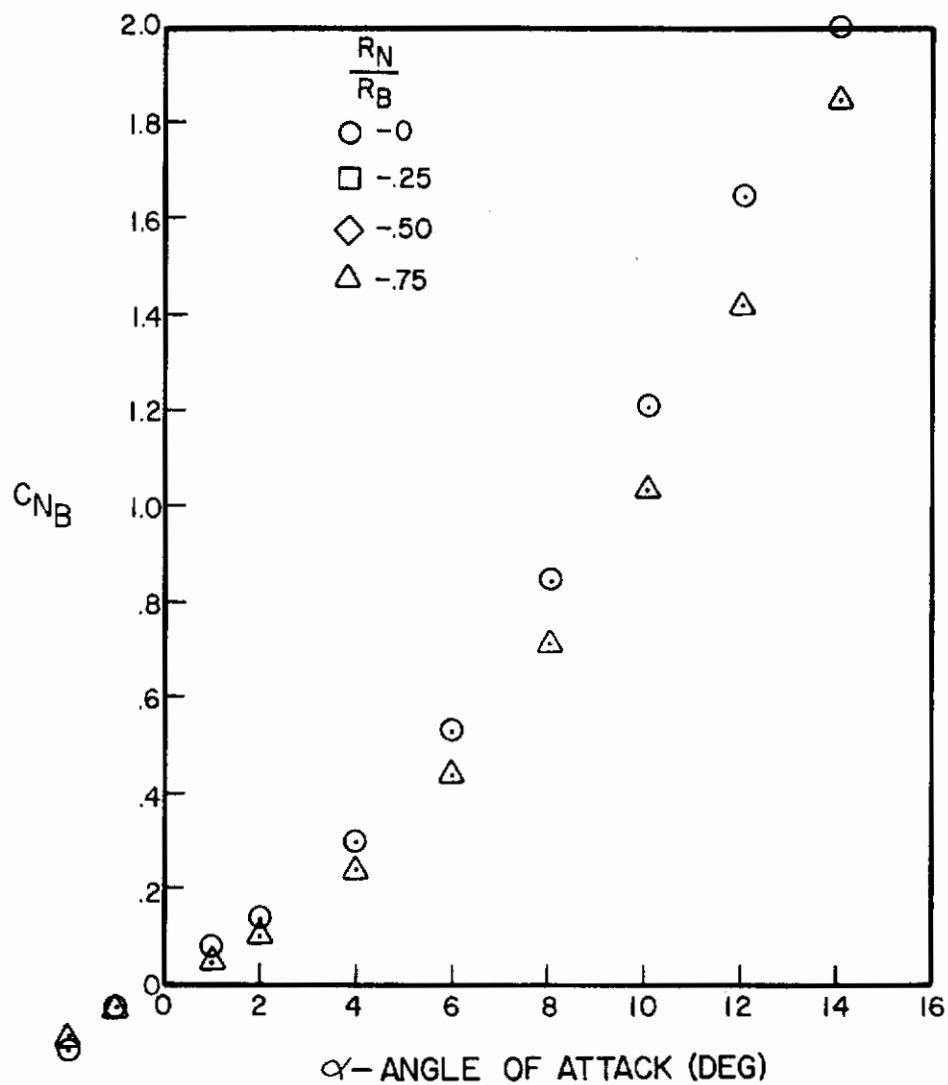


Figure A-72. Normal Force Coefficient Versus Angle of Attack for $l_N/d = 3$, $l_A/d = 10$, $M = 3.0$

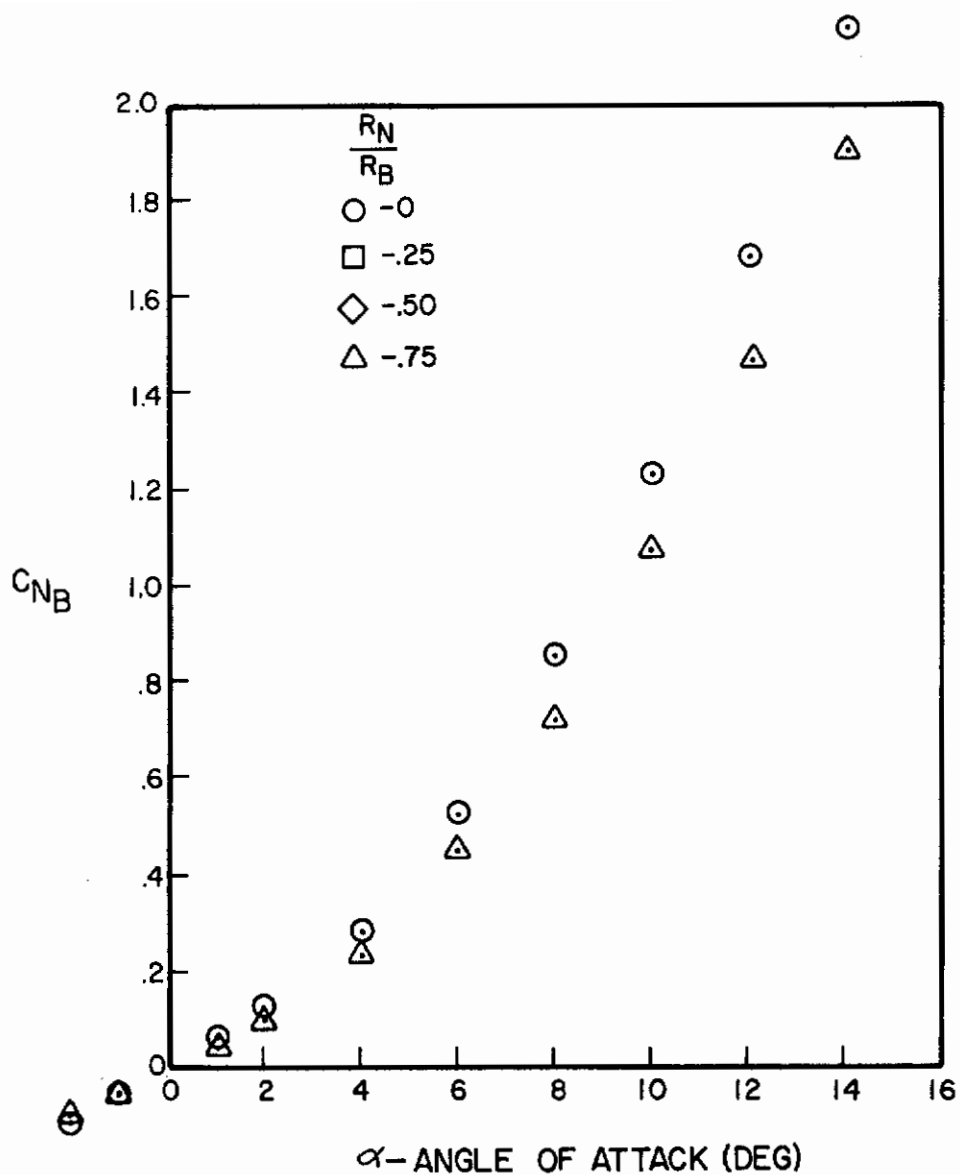


Figure A-73. Normal Force Coefficient Versus Angle of Attack for $\ell_N/d = 4$, $\ell_A/d = 10$, $M = 3.0$

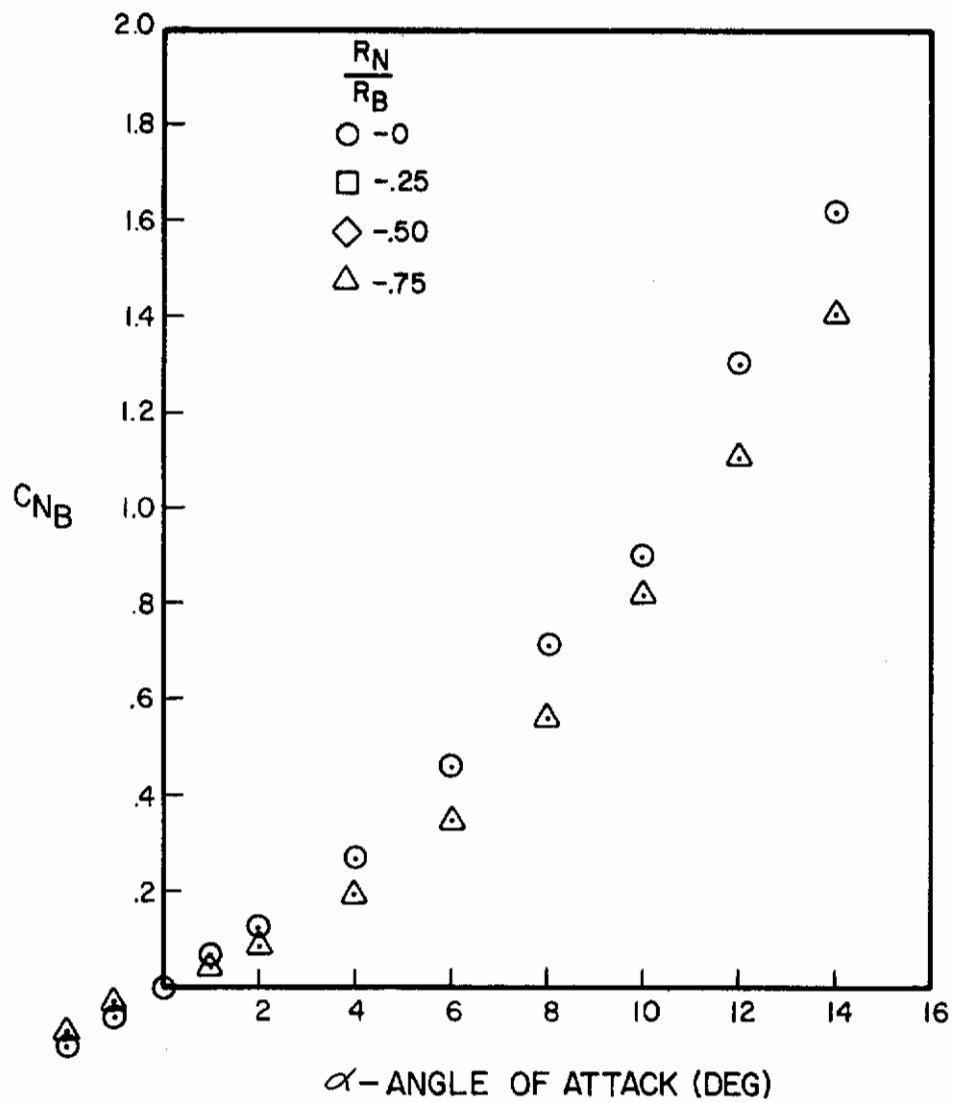


Figure A-74. Normal Force Coefficient Versus Angle of Attack for $l_N/d = 2$, $l_A/d = 8$, $M = 4.0$

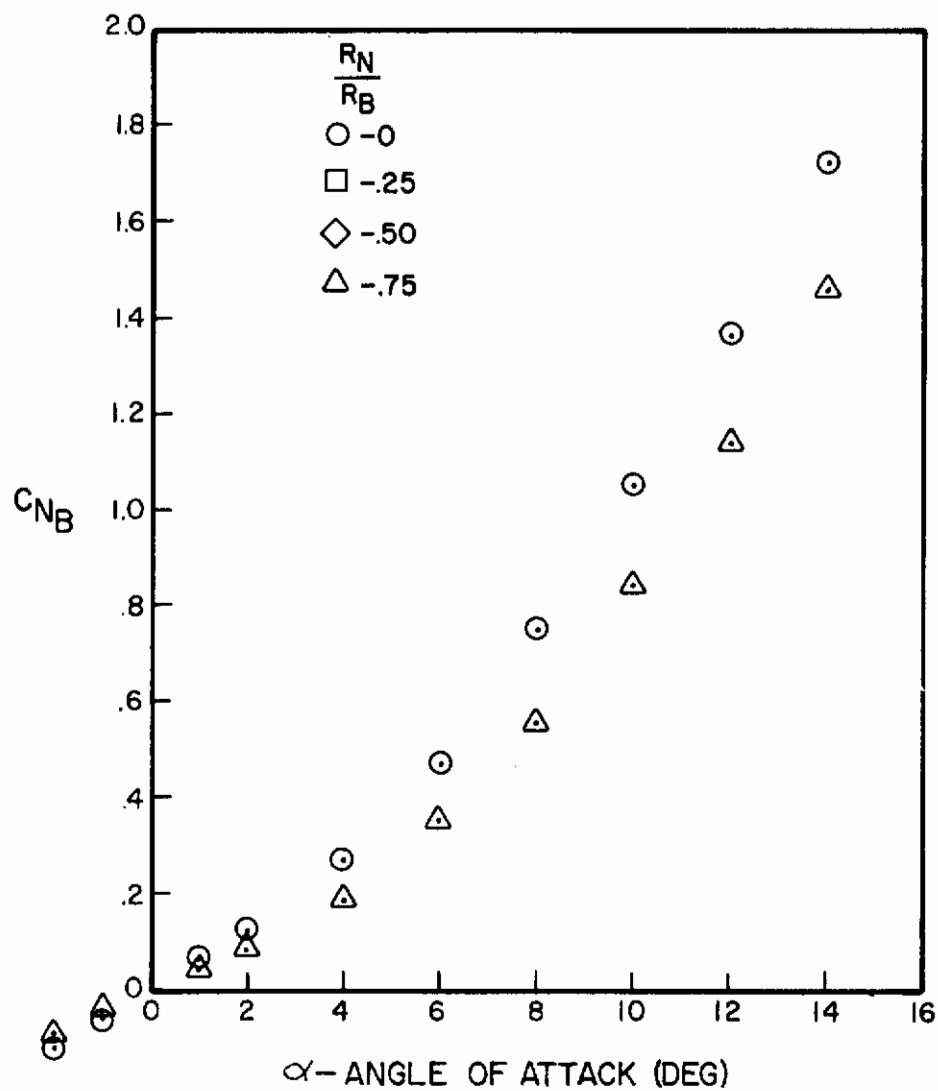


Figure A-75. Normal Force Coefficient Versus Angle of Attack for $l_N/d = 3$, $l_A/d = 8$, $M = 4.0$

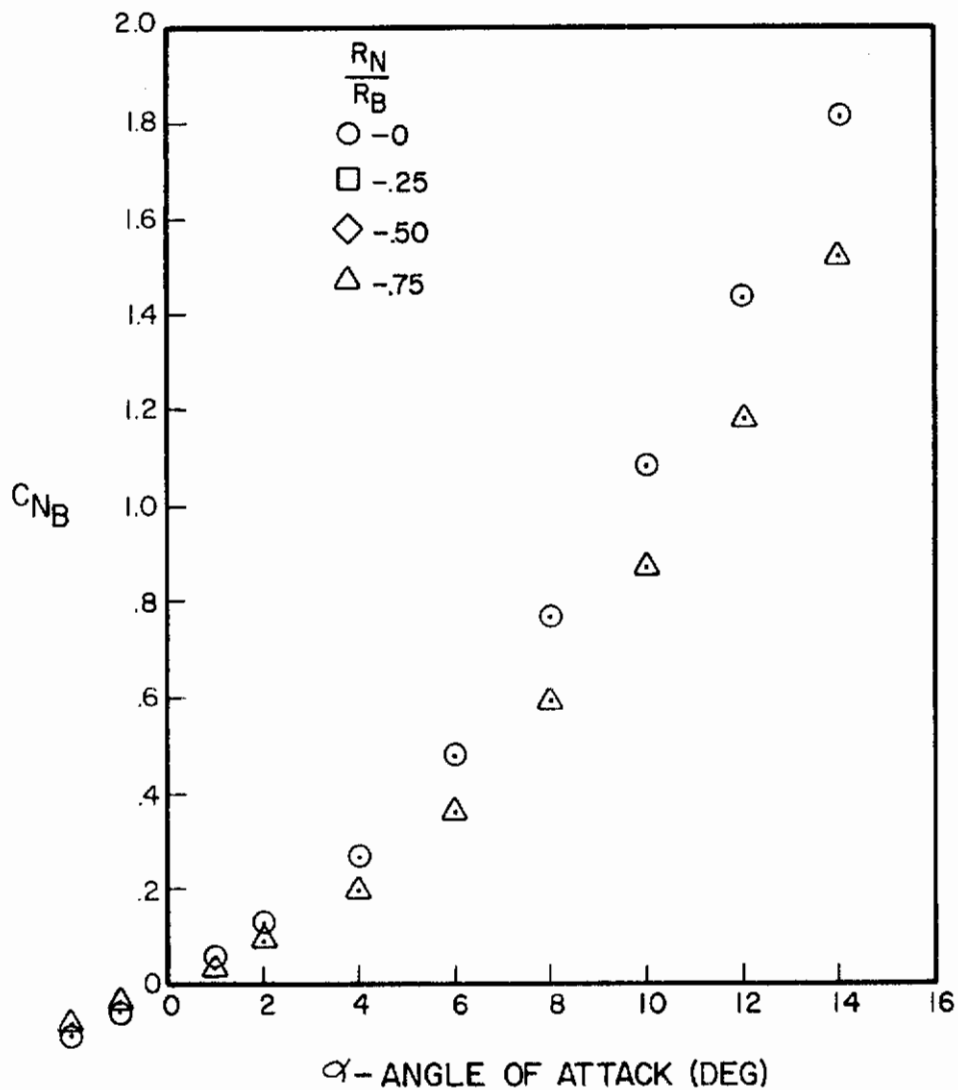


Figure A-76. Normal Force Coefficient Versus Angle of Attack for $\ell_N/d = 4$, $\ell_A/d = 8$, $M = 4.0$

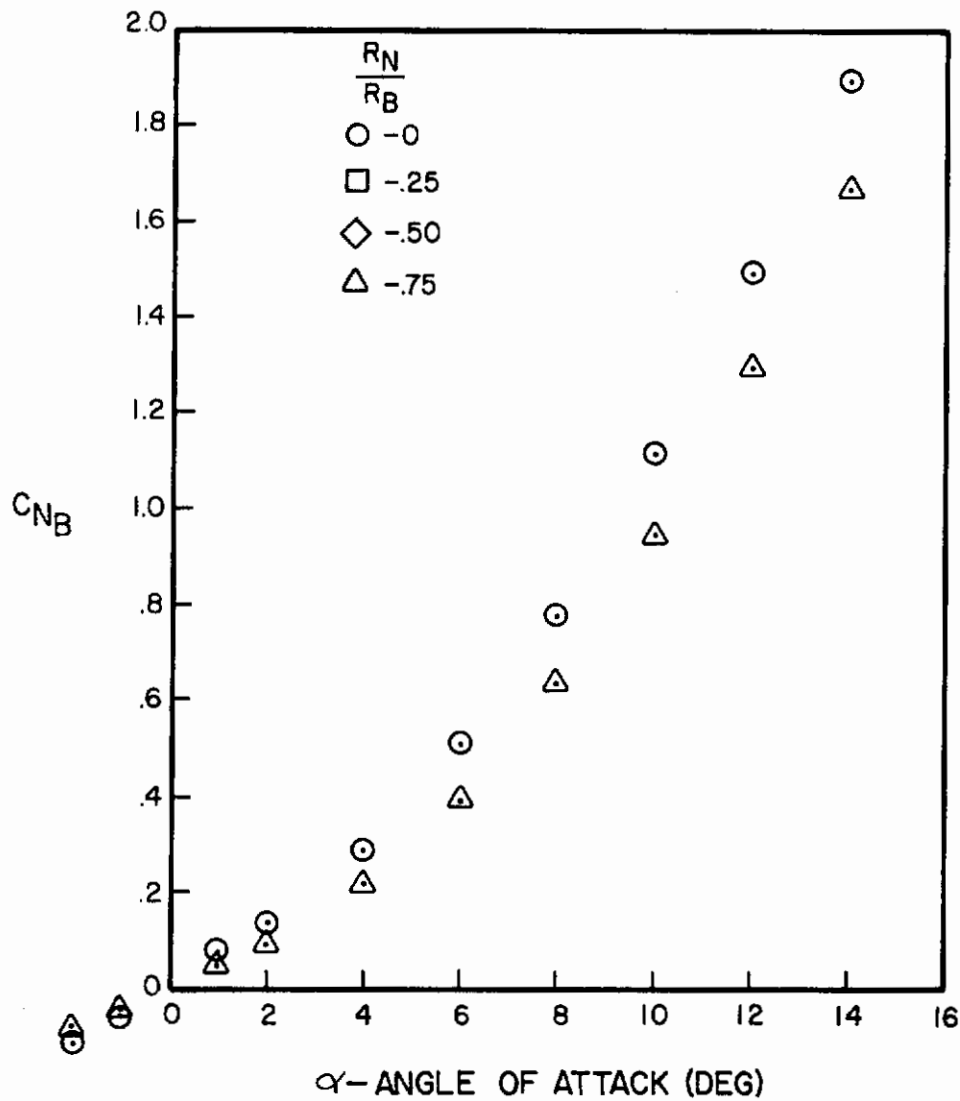


Figure A-77. Normal Force Coefficient Versus Angle of Attack for $l_N/d = 2$, $l_A/d = 10$, $M = 4.0$

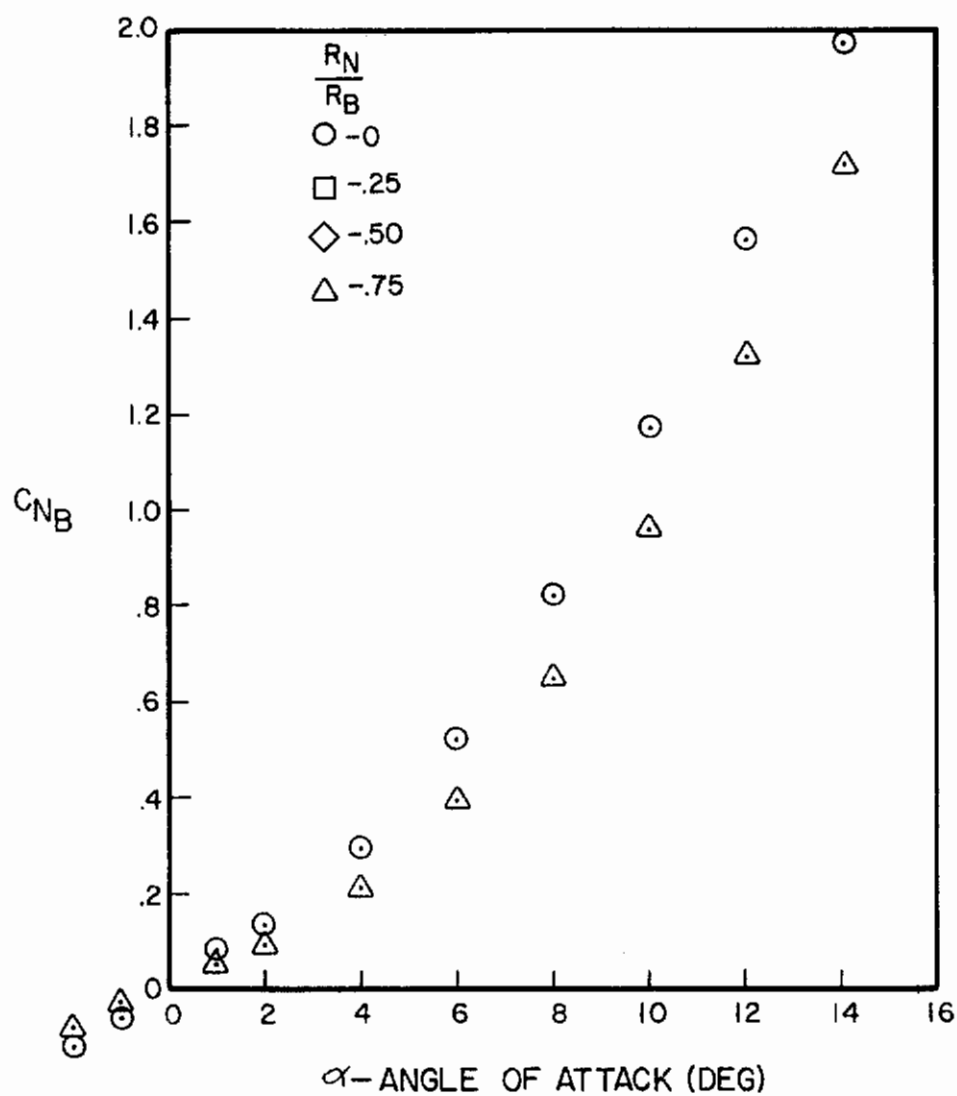


Figure A-78. Normal Force Coefficient Versus Angle of Attack for $l_N/d = 3$, $l_A/d = 10$, $M = 4.0$

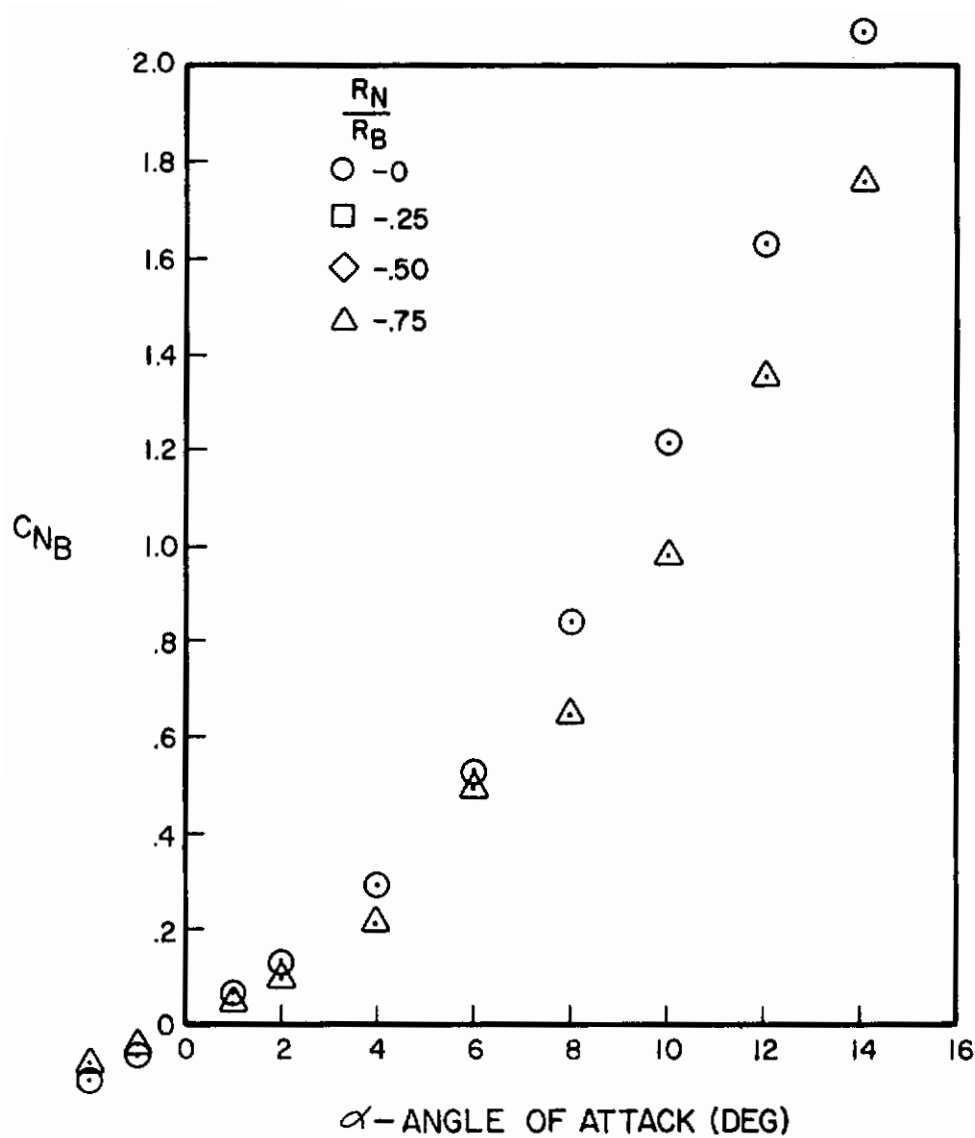


Figure A-79. Normal Force Coefficient Versus Angle of Attack for $l_N/d = 4$, $l_A/d = 10$, $M = 4.0$

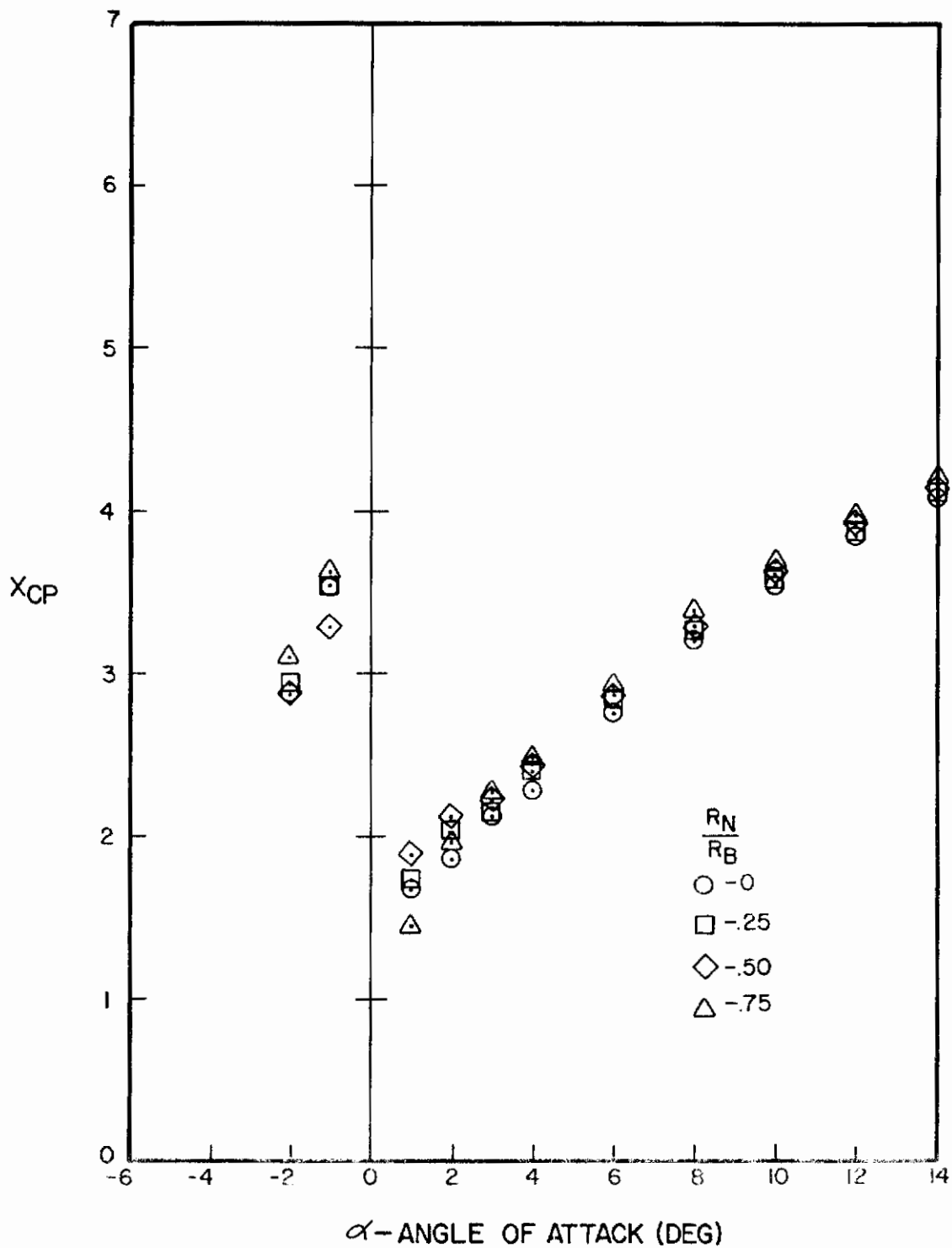


Figure A-80. Center of Pressure Versus Angle of Attack for $l_N/d = 2$, $l_A/d = 6$, $M = 0.6$

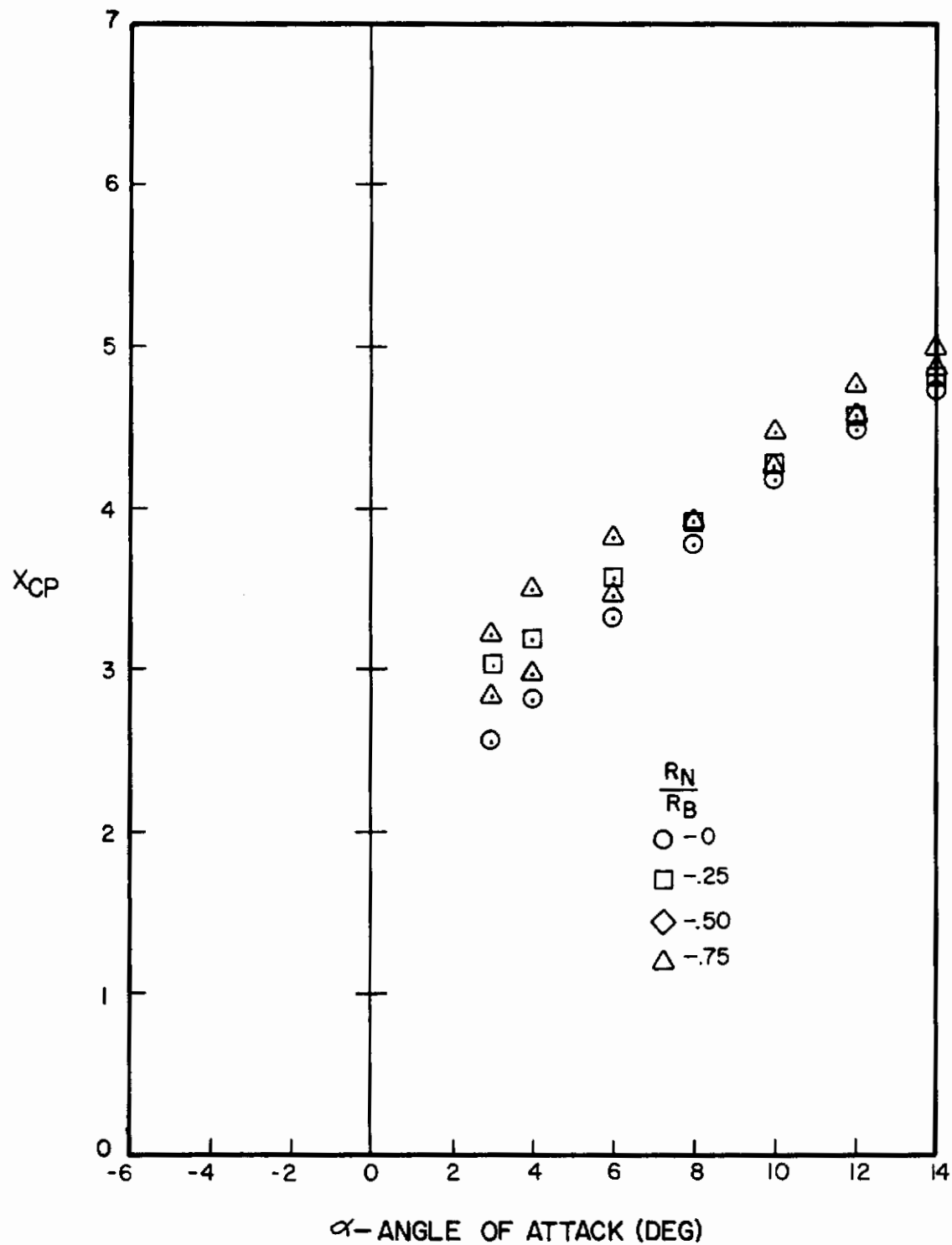


Figure A-81. Center of Pressure Versus Angle of Attack for $l_N/d = 3$, $l_A/d = 6$, $M = 0.6$

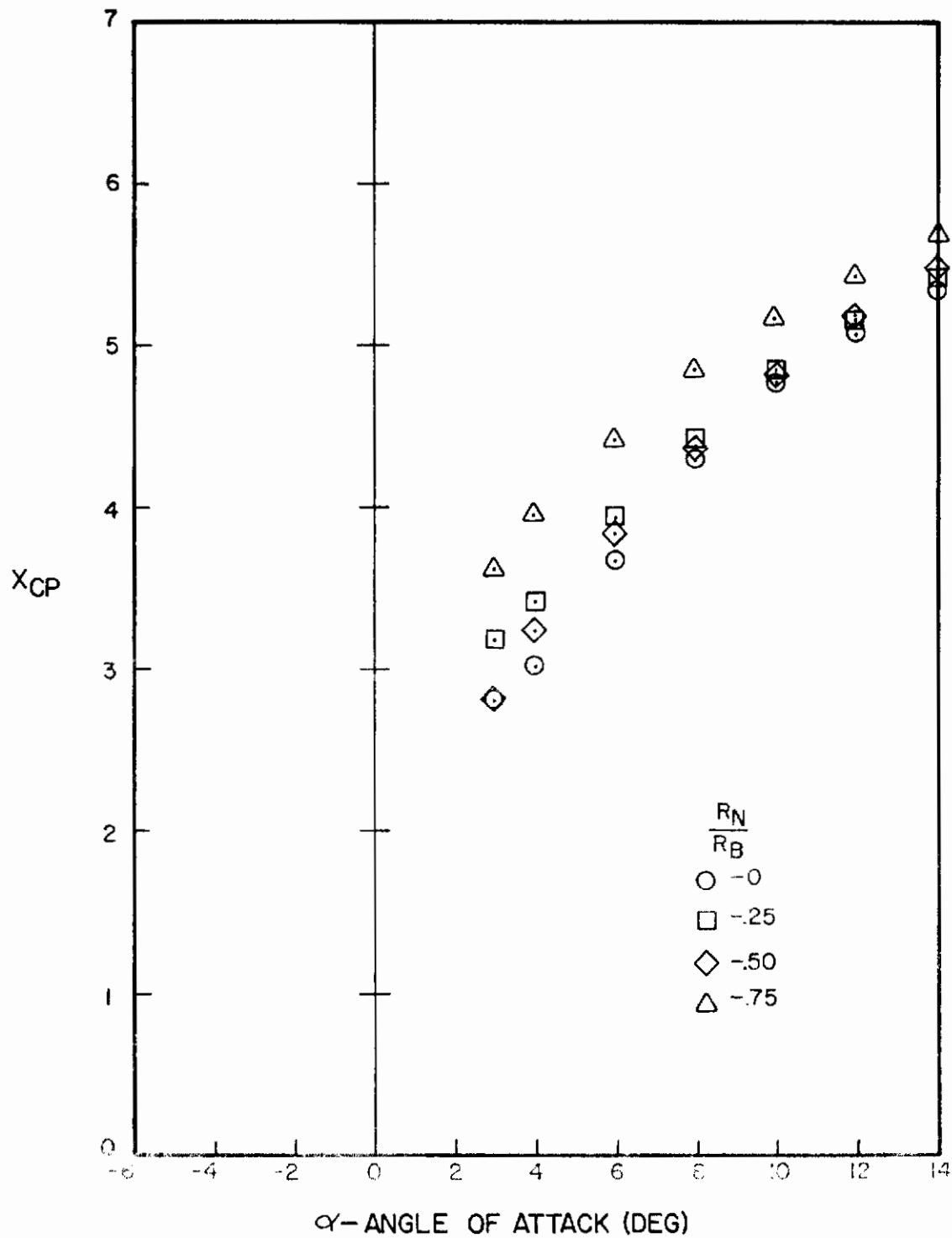


Figure A-82. Center of Pressure Versus Angle of Attack for $l_N/d = 4$, $l_A/d = 6$, $M = 0.6$

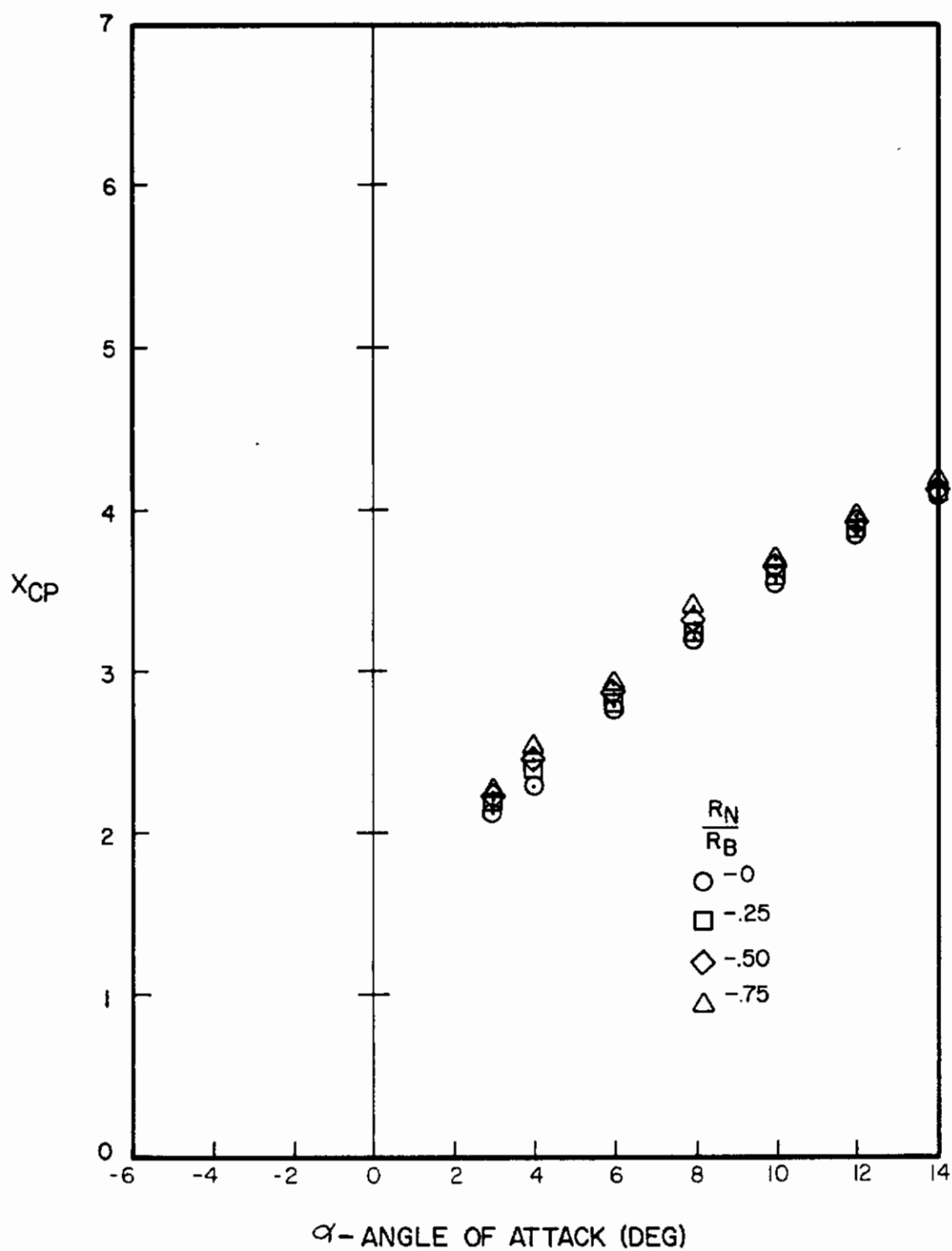


Figure A-83. Center of Pressure Versus Angle of Attack for $l_N/d = 2$, $l_A/d = 10$, $M = 0.6$

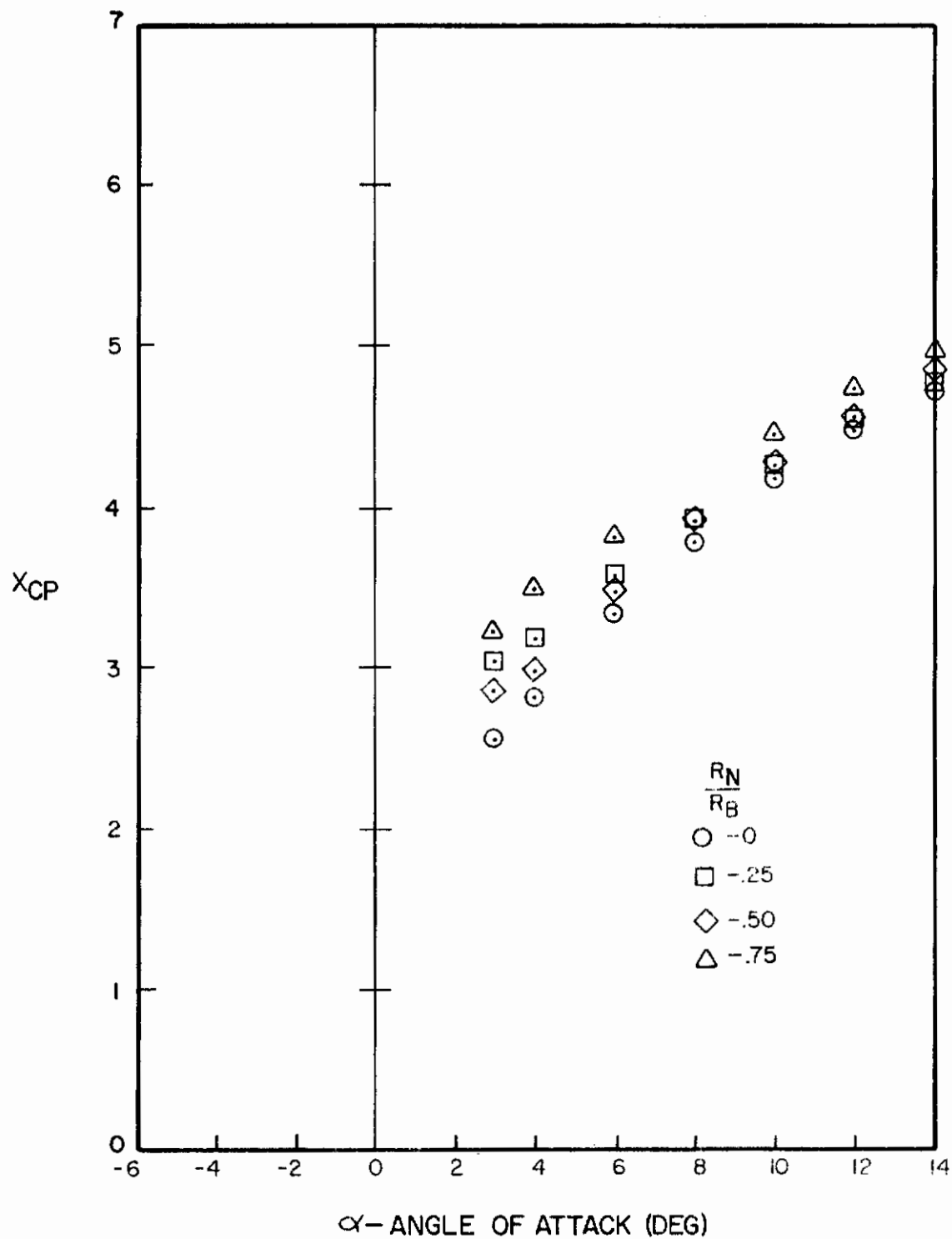


Figure A-84. Center of Pressure Versus Angle of Attack for $l_N/d = 3$, $l_A/d = 10$, $M = 0.6$

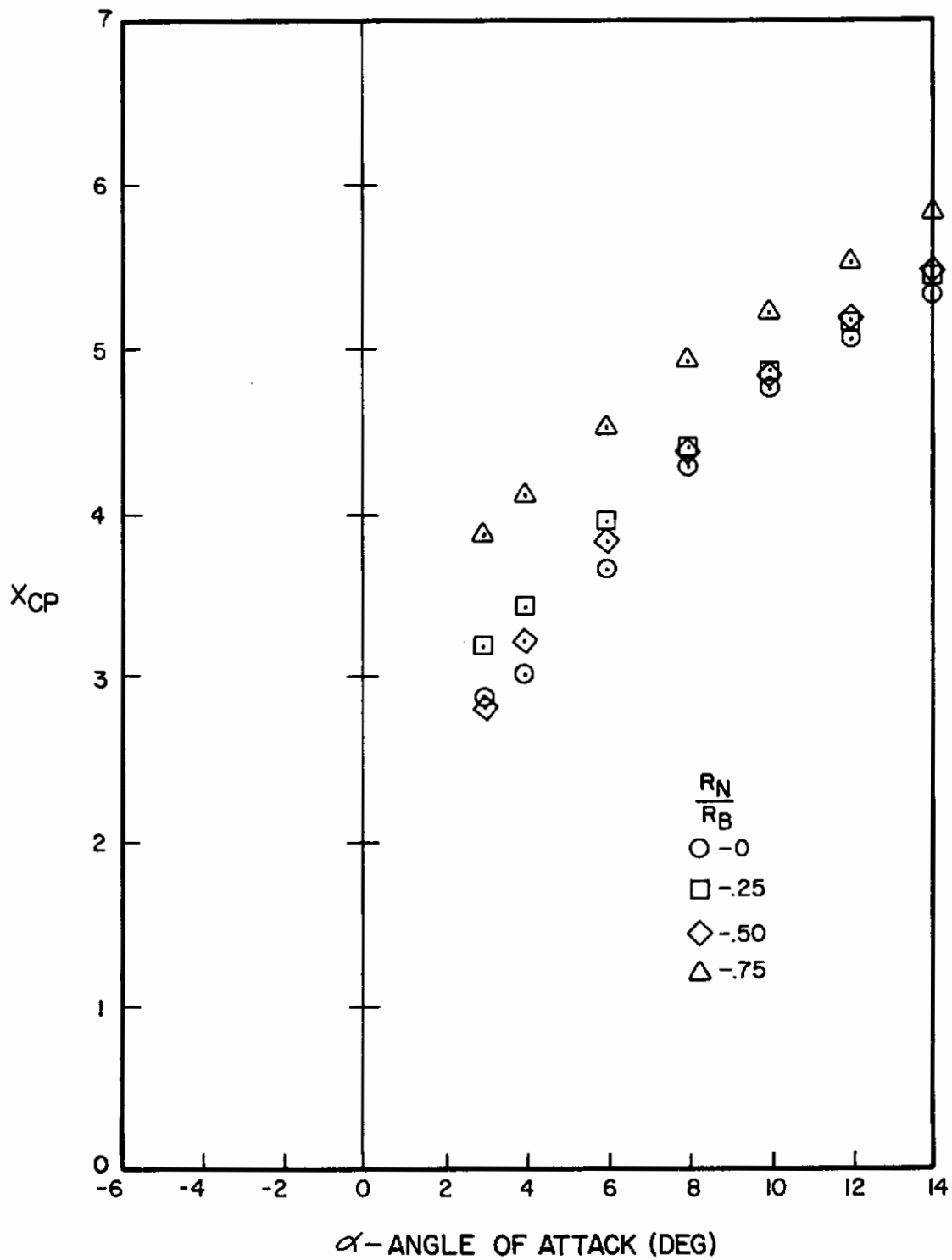


Figure A-85. Center of Pressure Versus Angle of Attack for $l_N/d = 4$, $l_A/d = 10$, $M = 0.6$

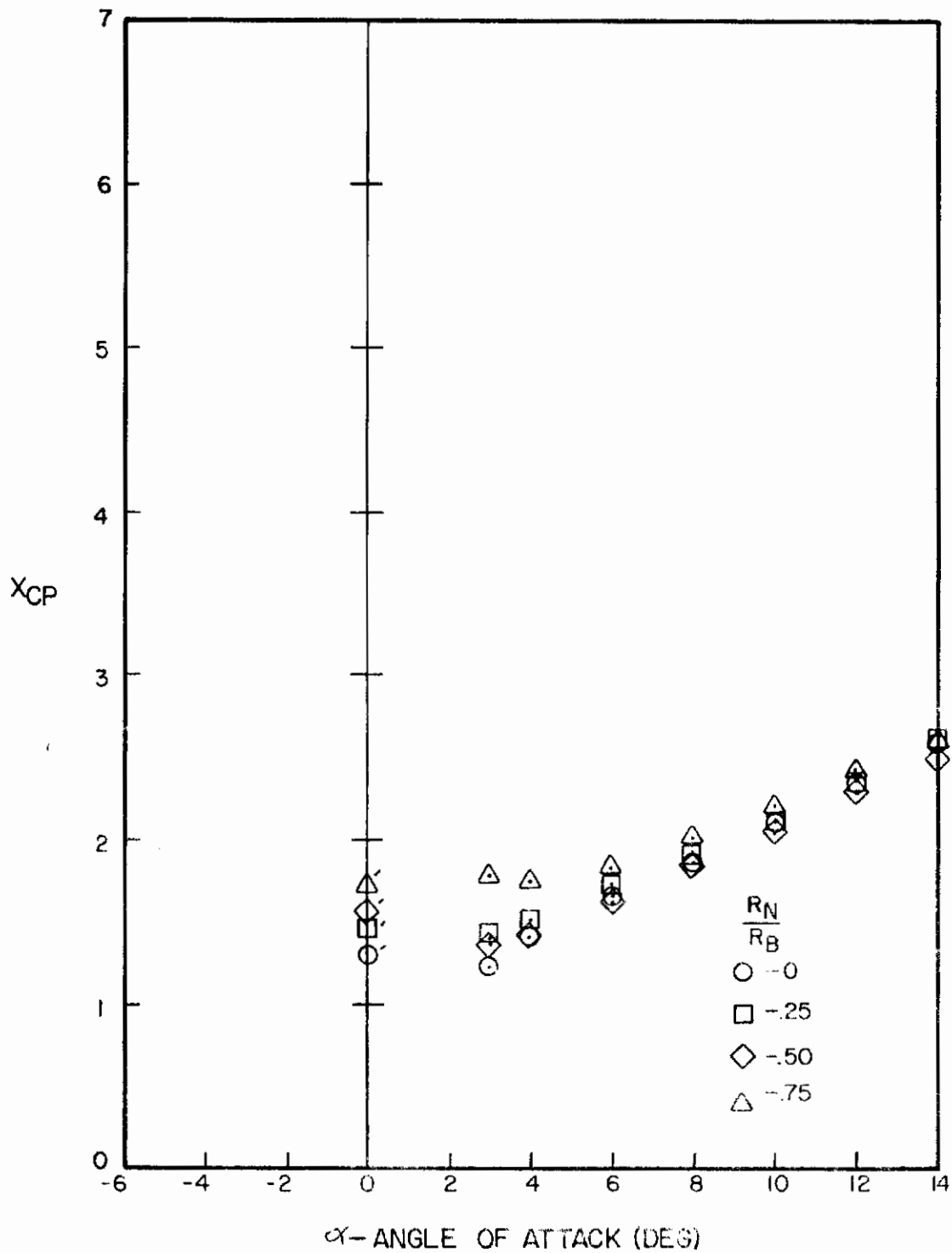


Figure A-86. Center of Pressure Versus Angle of Attack for $l_N/d = 2$, $l_A/d = 6$, $M = 0.8$

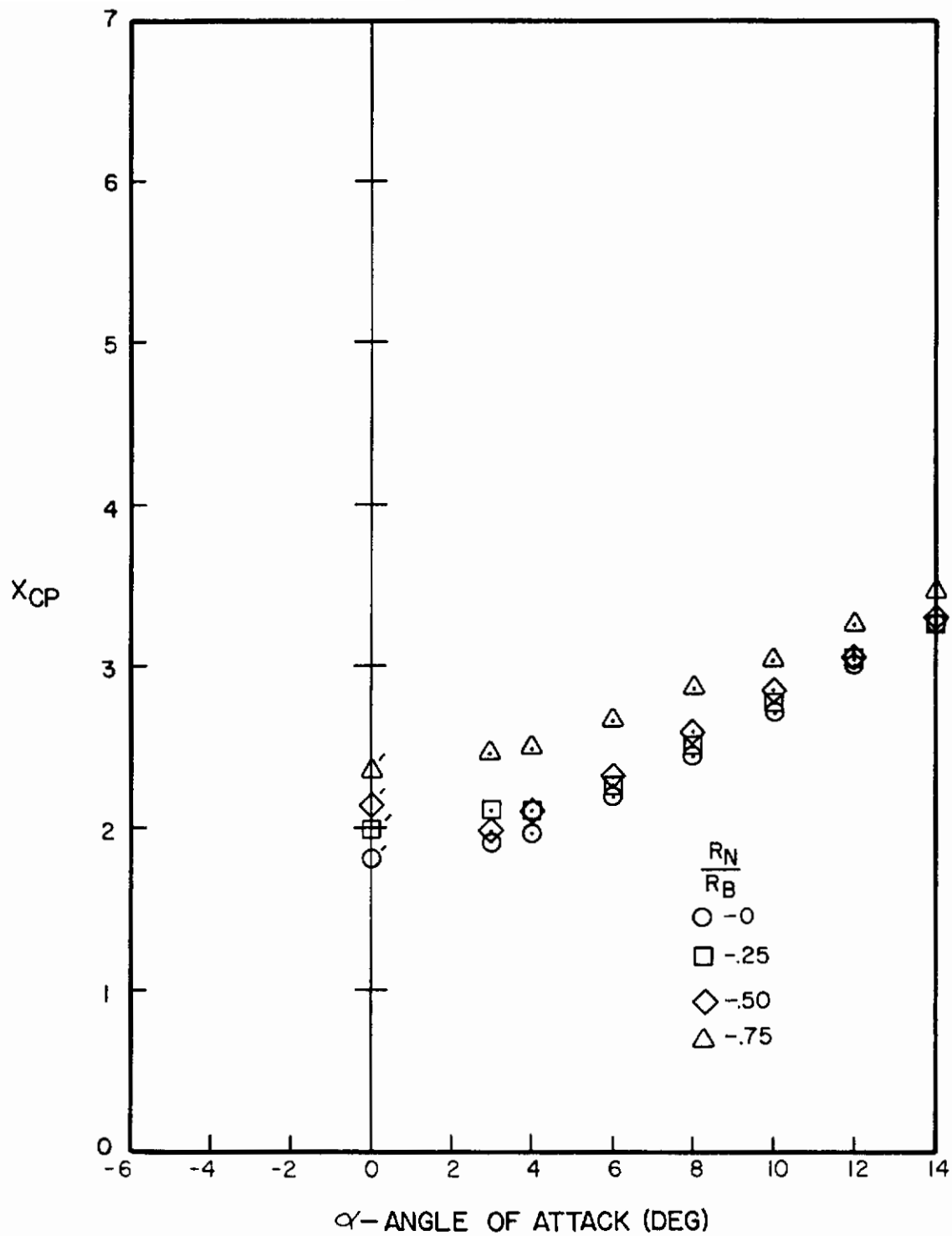


Figure A-87. Center of Pressure Versus Angle of Attack for $l_N/d = 3$, $l_A/d = 6$, $M = 0.8$

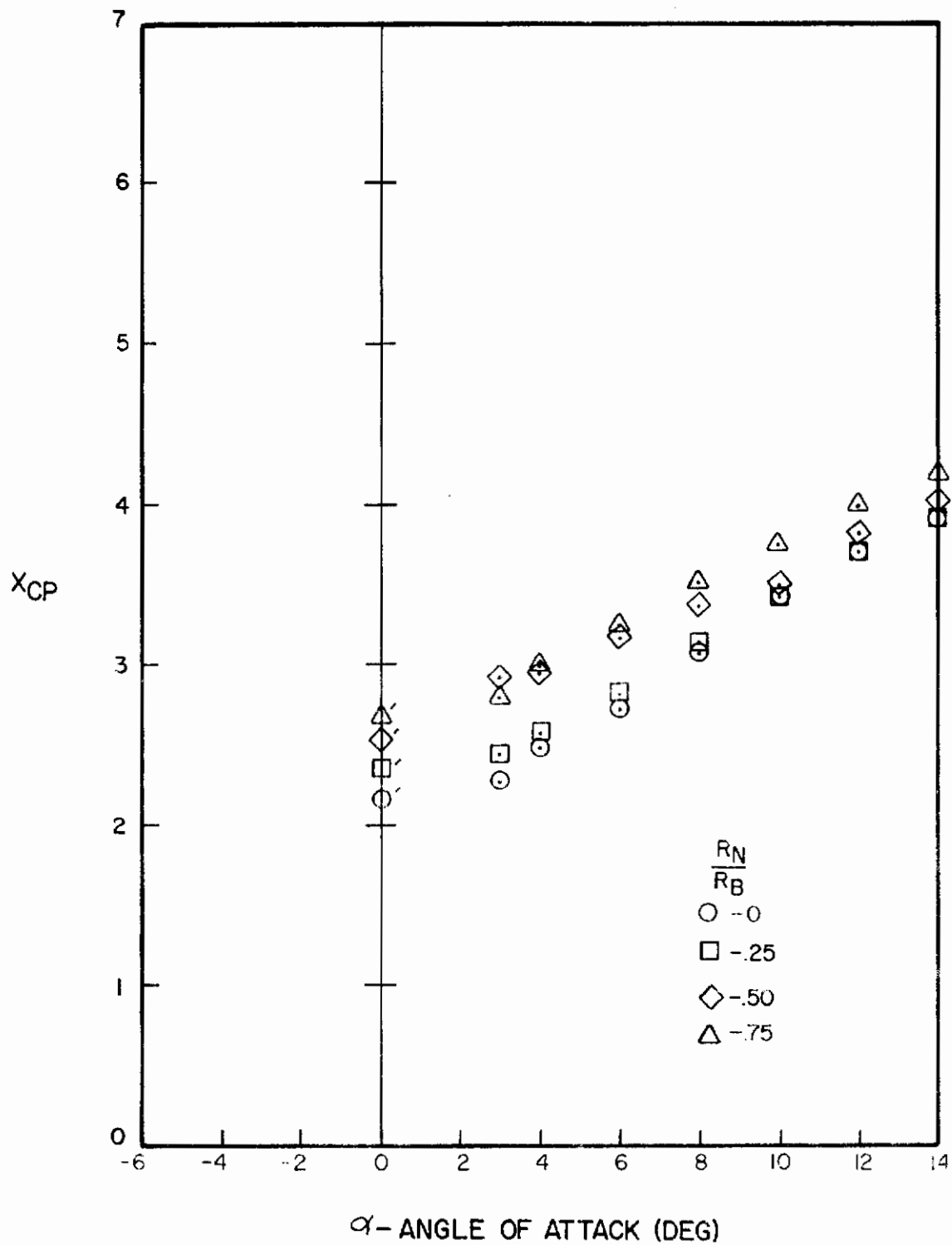


Figure A-88. Center of Pressure Versus Angle of Attack for $l_N/d = 4$, $l_A/d = 6$, $M = 0.8$

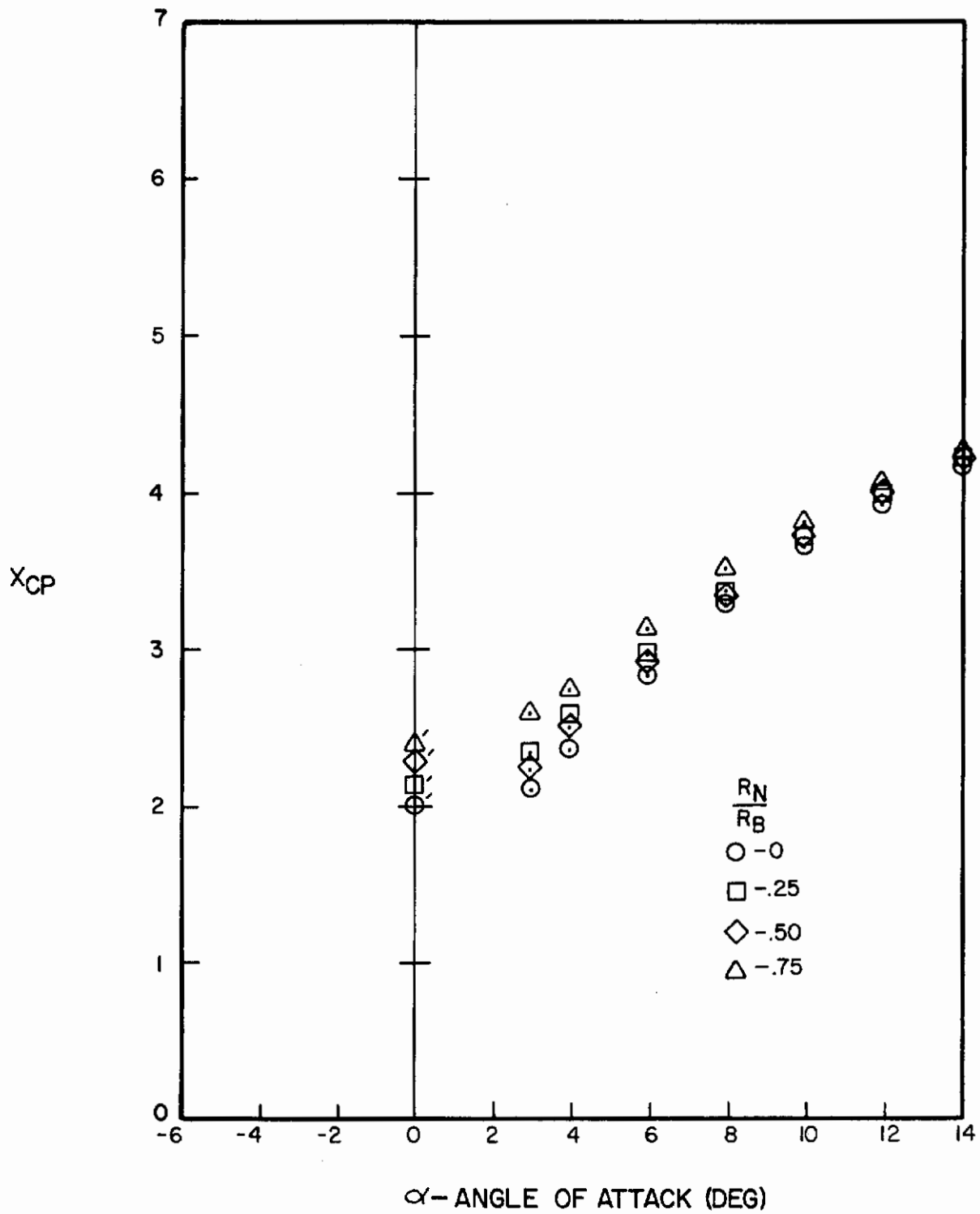


Figure A-89. Center of Pressure Versus Angle of Attack for $l_N/d = 2$, $l_A/d = 10$, $M = 0.8$

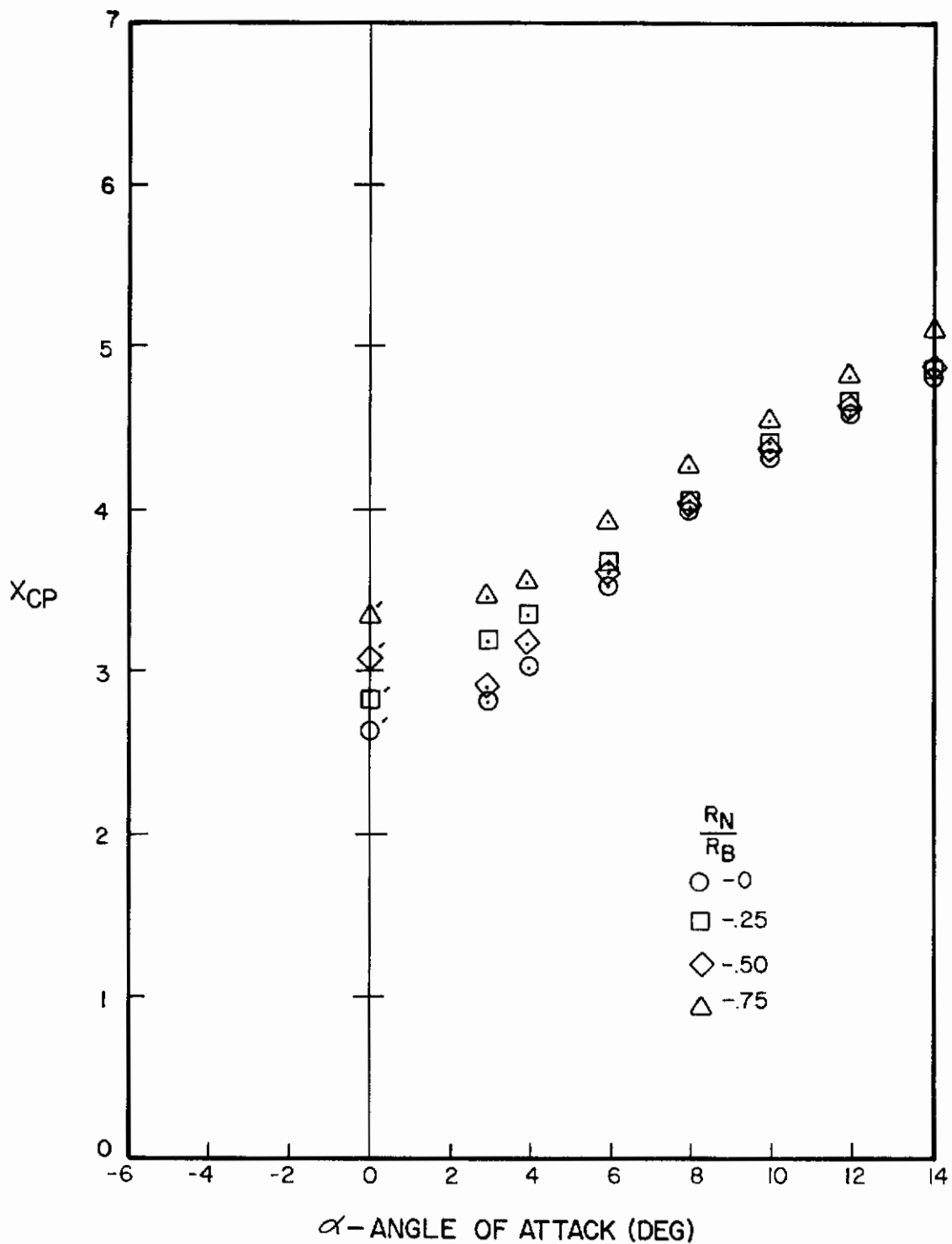


Figure A-90. Center of Pressure Versus Angle of Attack for $l_N/d = 3$, $l_A/d = 10$, $M = 0.8$

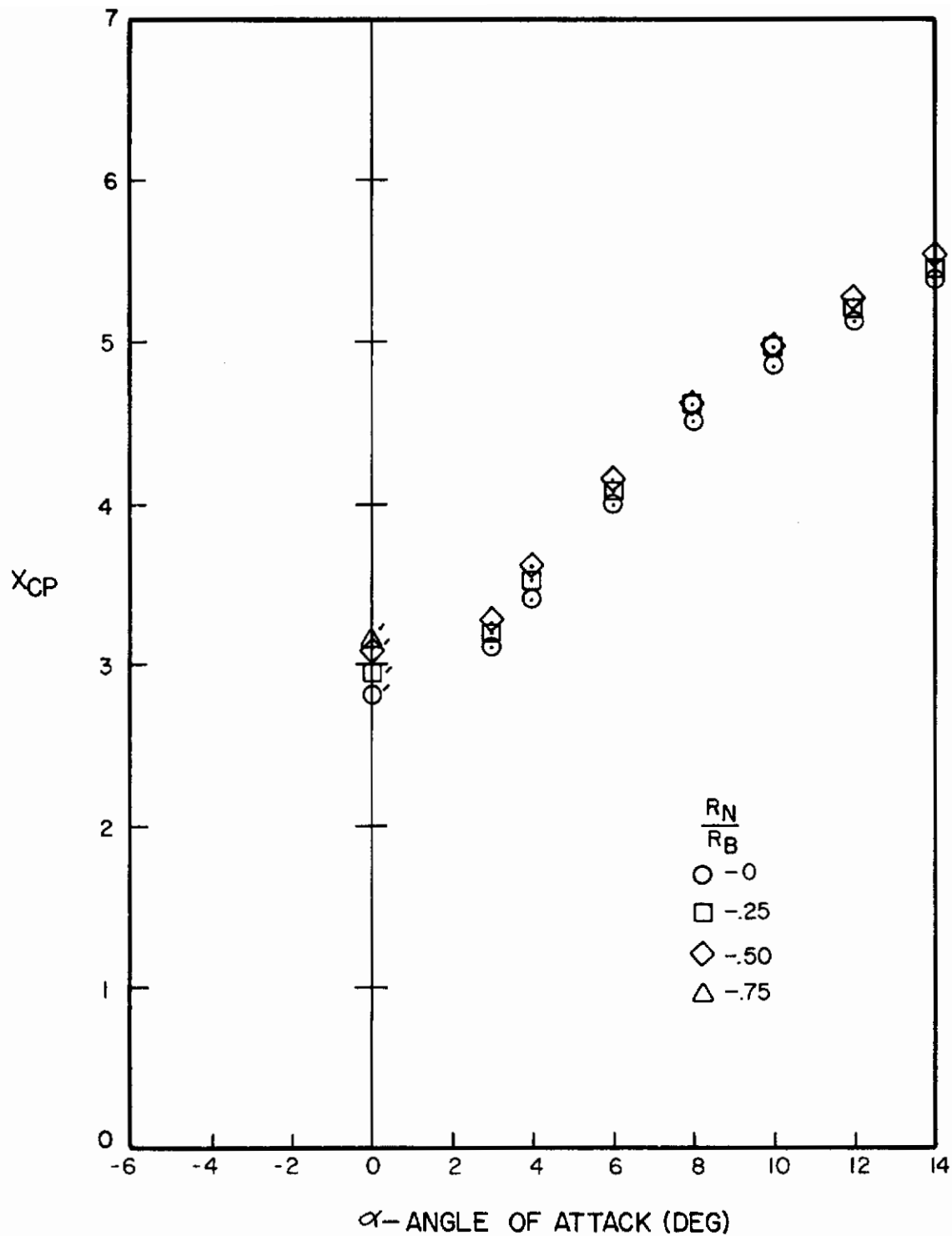


Figure A-91. Center of Pressure Versus Angle of Attack for $l_N/d = 4$, $l_A/d = 10$, $M = 0.8$

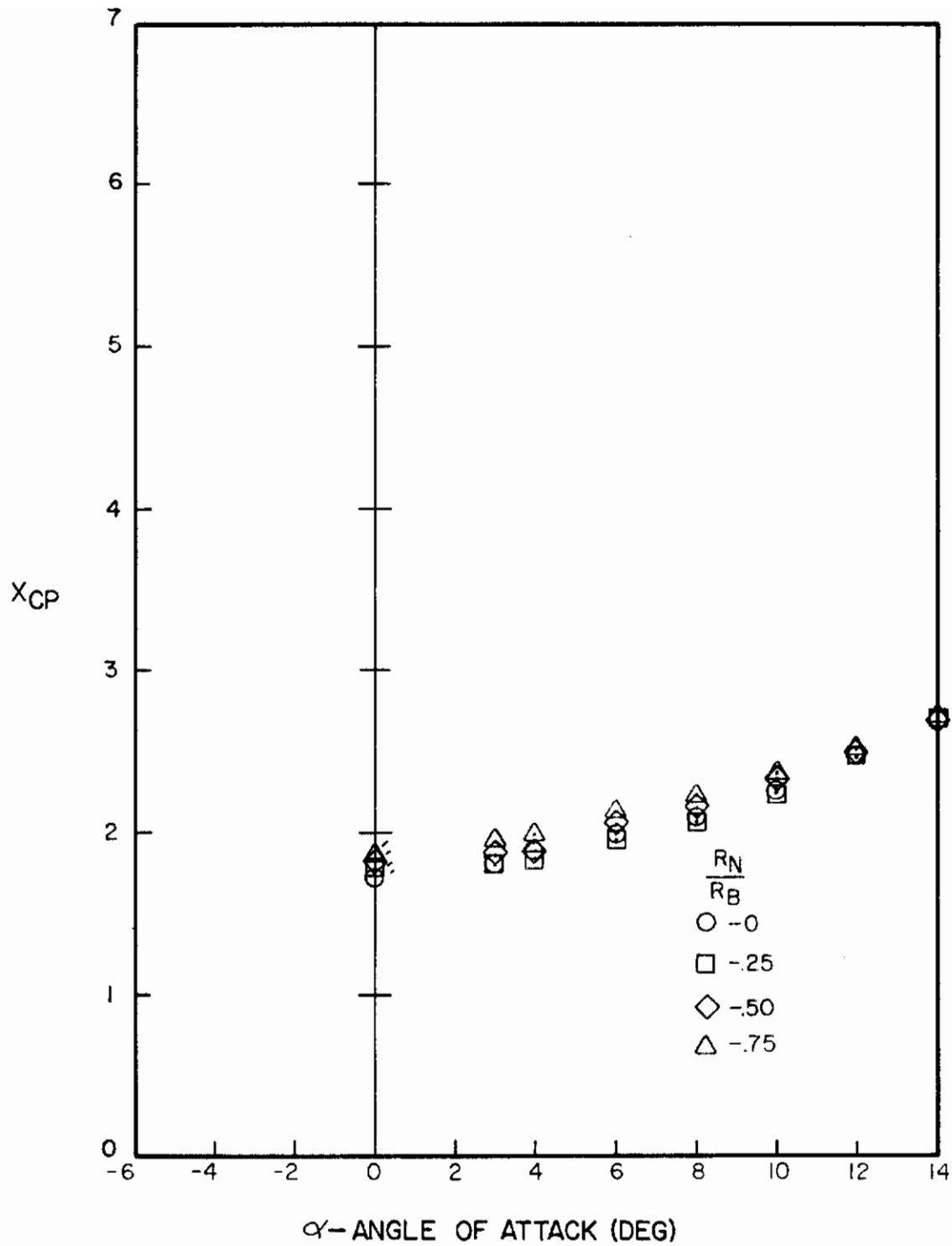


Figure A-92. Center of Pressure Versus Angle of Attack for $l_N/d = 2$, $l_A/d = 6$, $M = 1.0$

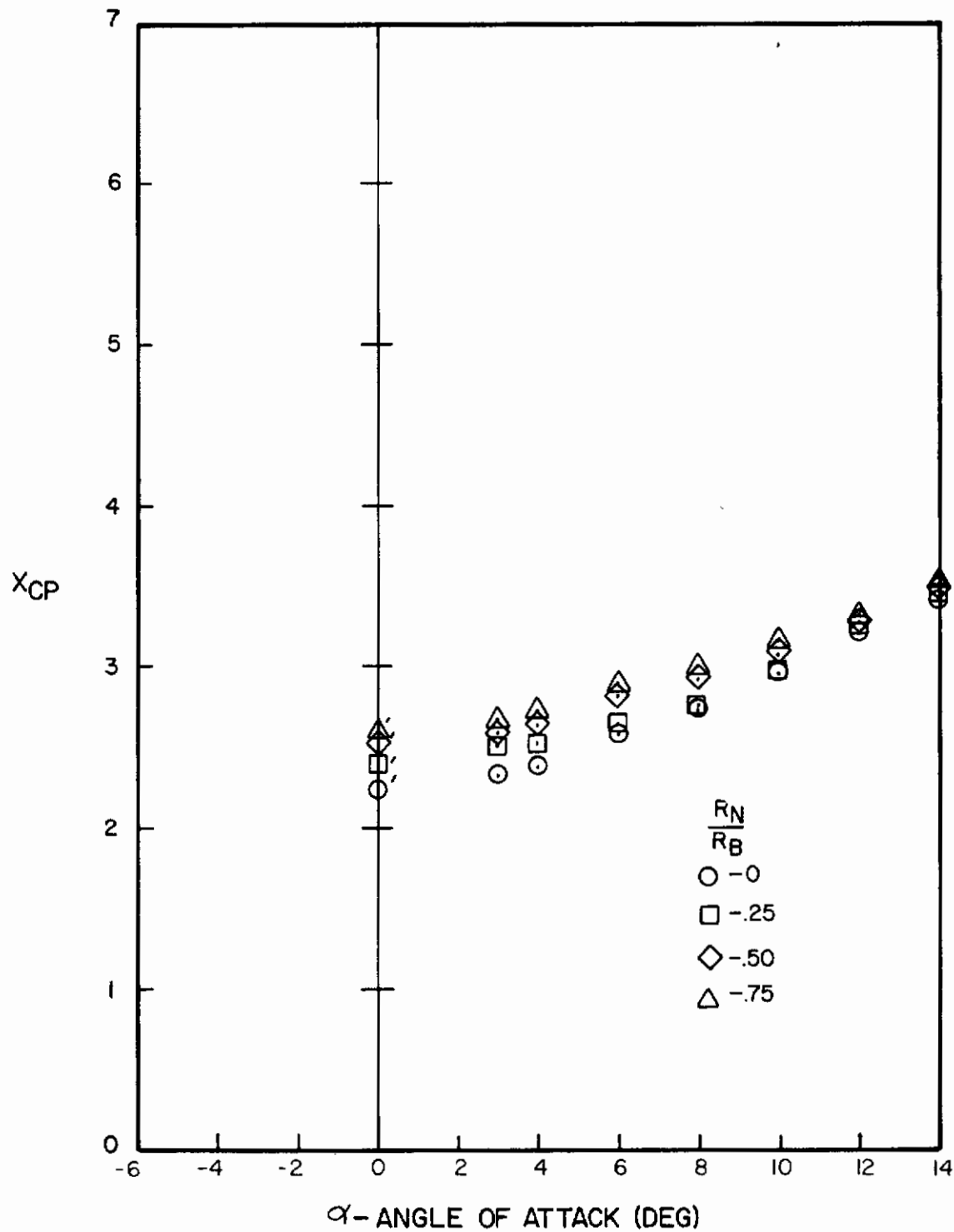


Figure A-93. Center of Pressure Versus Angle of Attack for $l_N/d = 3$, $l_A/d = 6$, $M = 1.0$

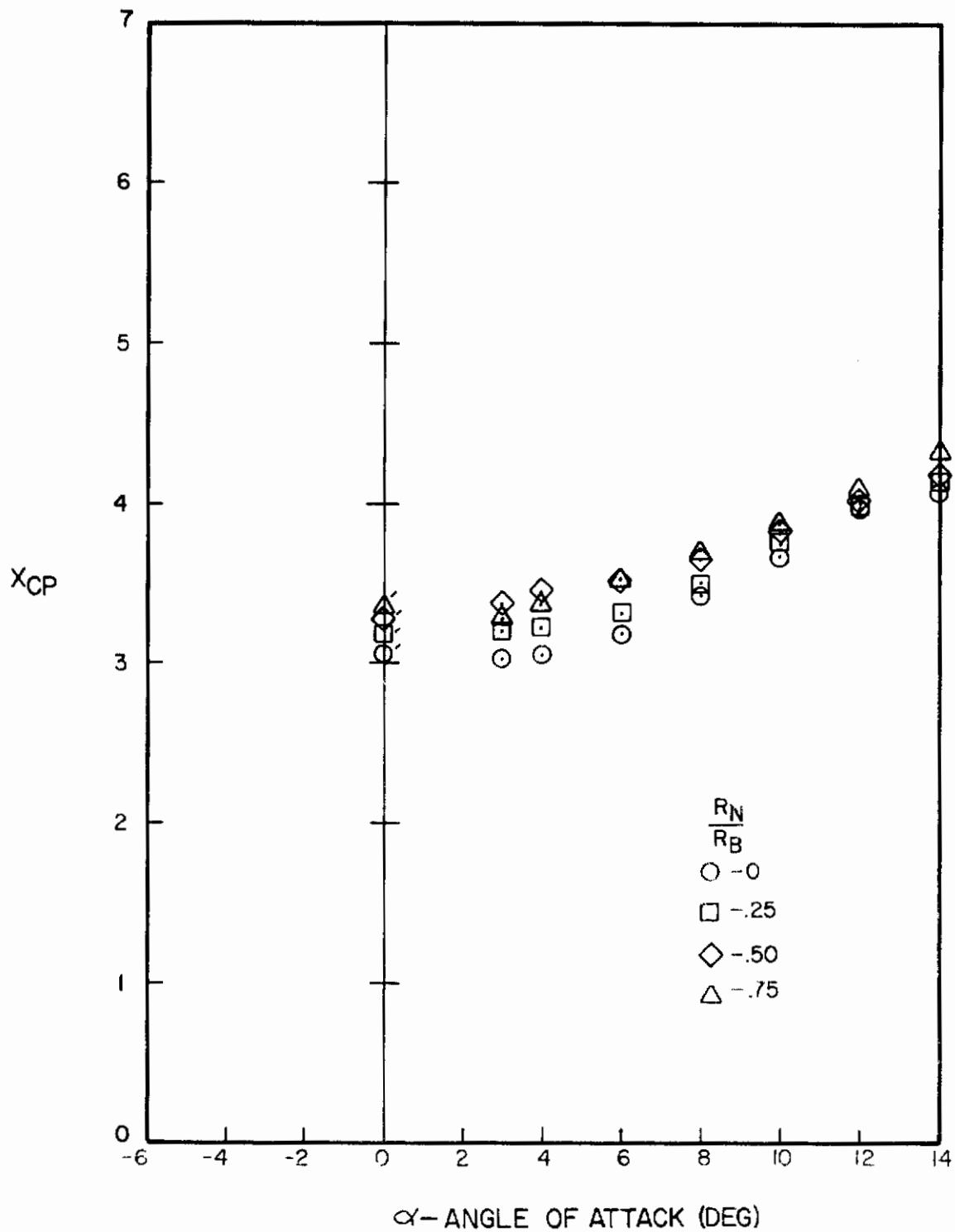


Figure A-94. Center of Pressure Versus Angle of Attack for $l_N/d = 4$, $l_A/d = 6$, $M = 1.0$

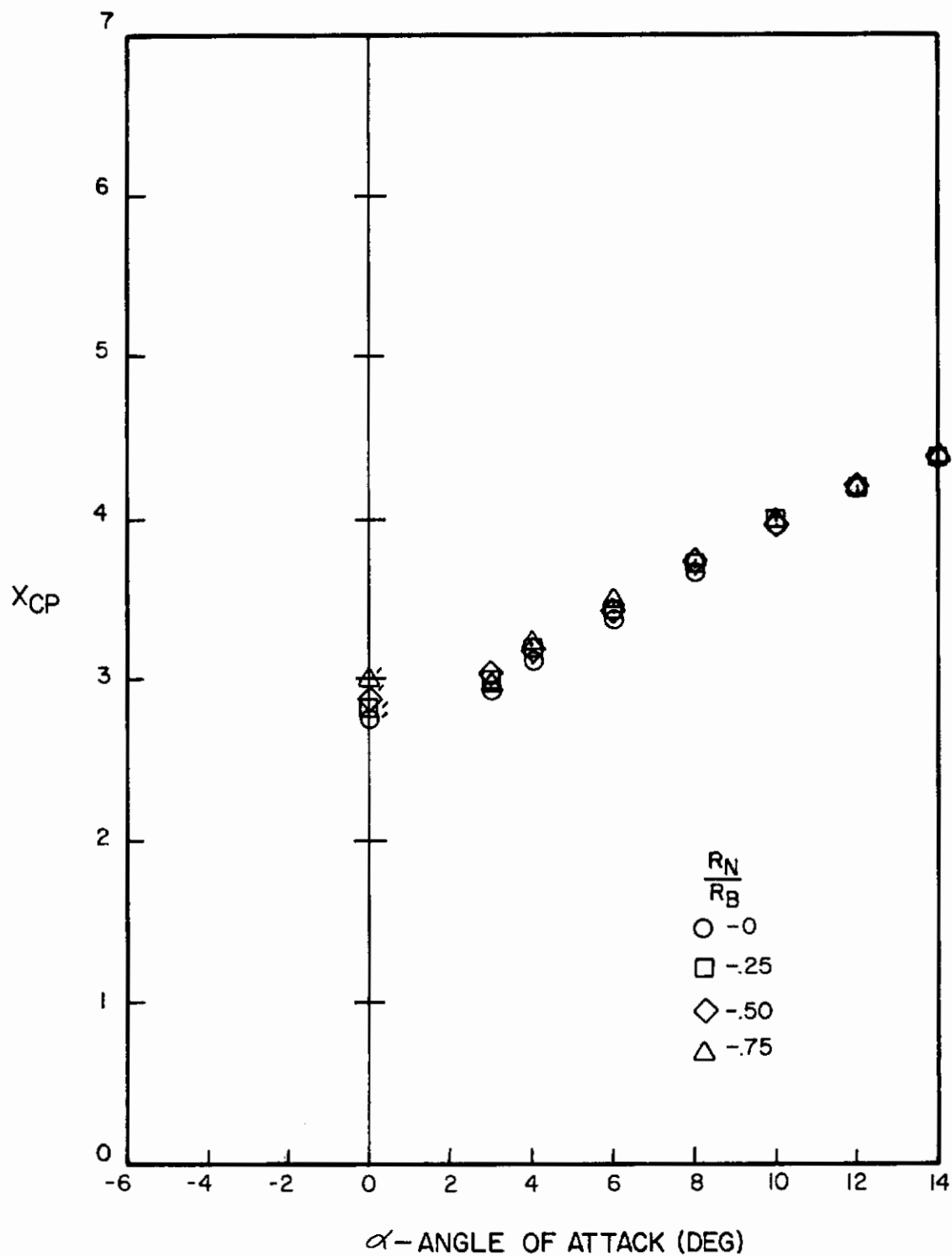


Figure A-95. Center of Pressure Versus Angle of Attack for $l_N/d = 2$, $l_A/d = 10$, $M = 1.0$

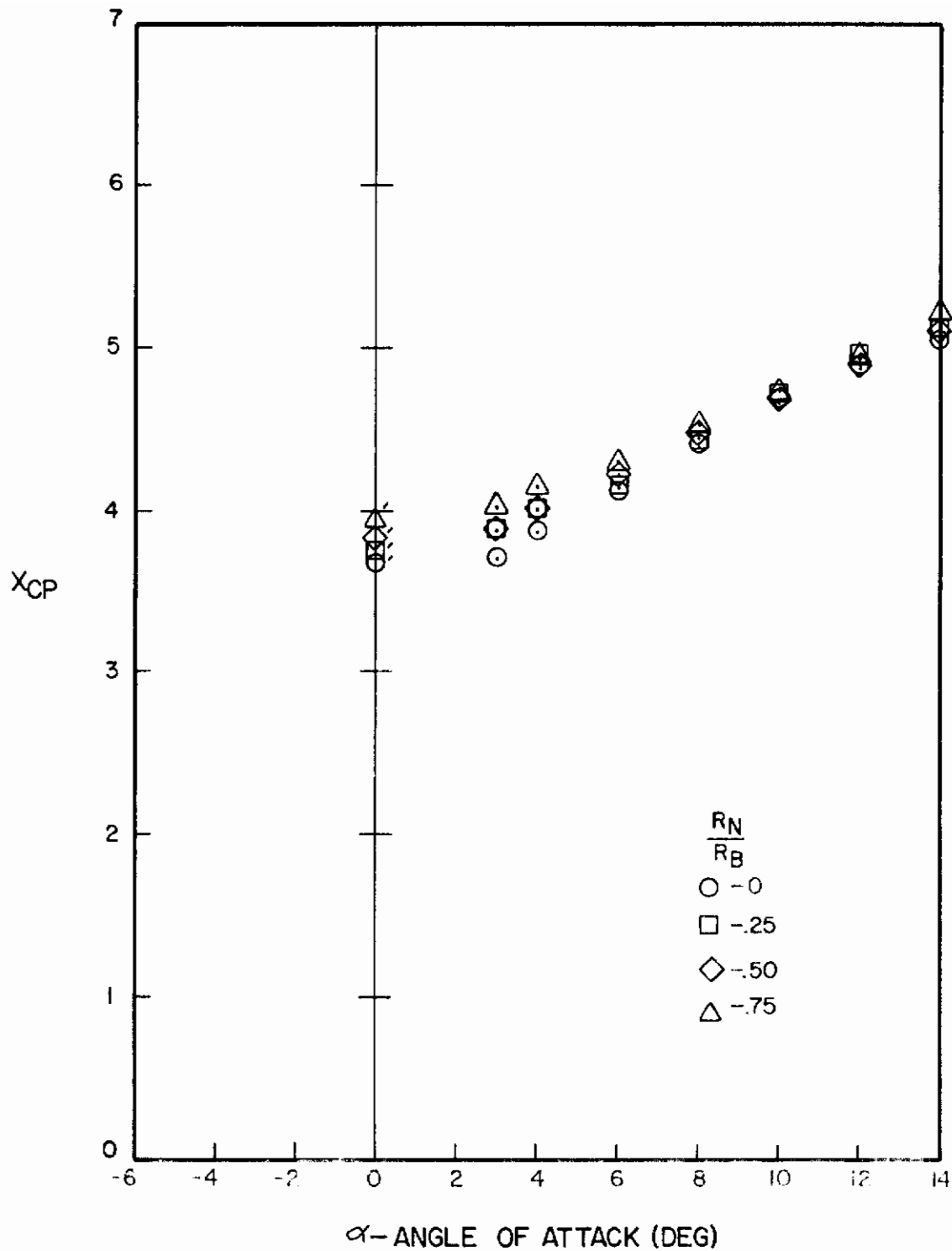


Figure A-96. Center of Pressure Versus Angle of Attack for $l_N/d = 3$, $l_A/d = 10$, $M = 1.0$

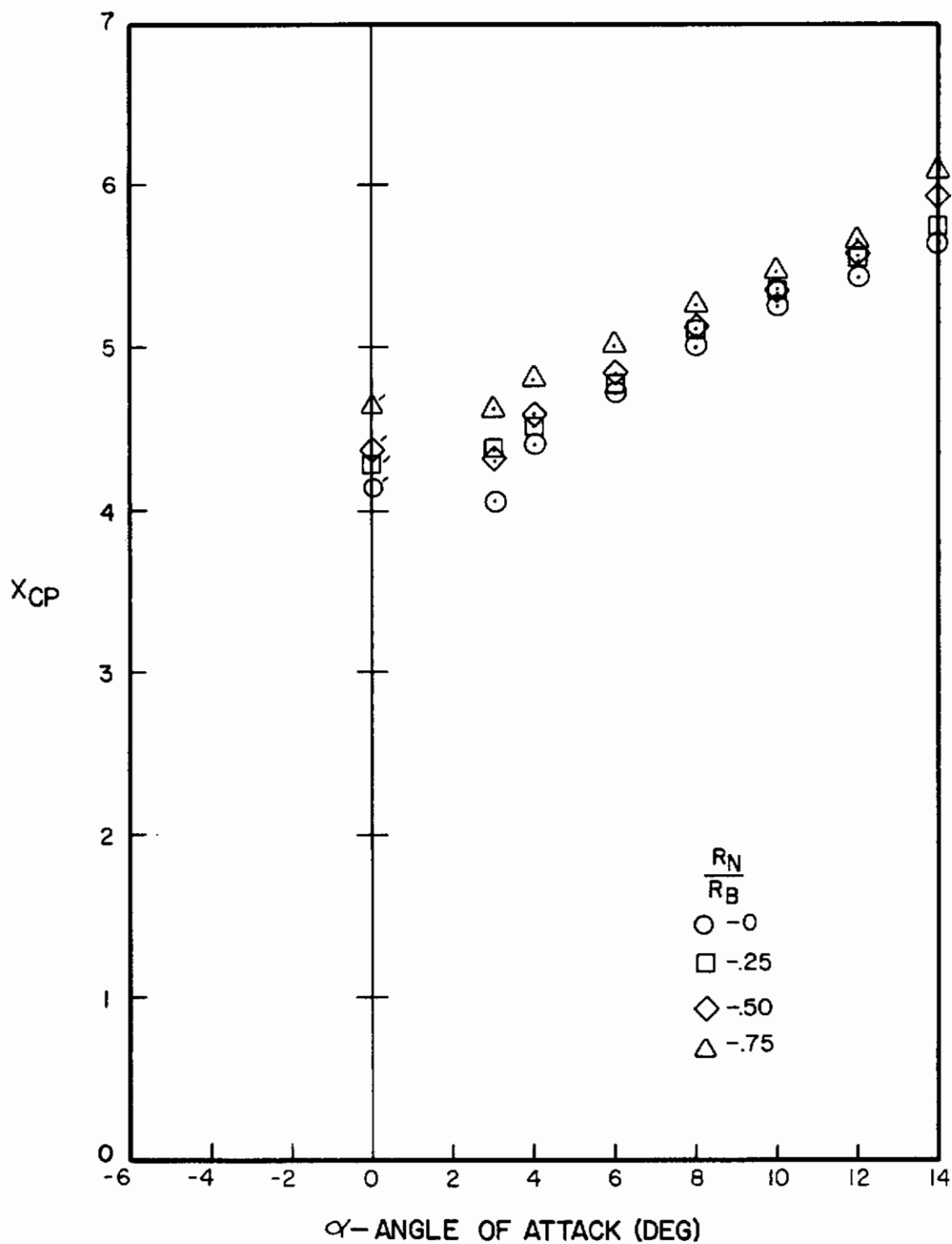


Figure A-97. Center of Pressure Versus Angle of Attack for $l_N/d = 4$, $l_A/d = 10$, $M = 1.0$

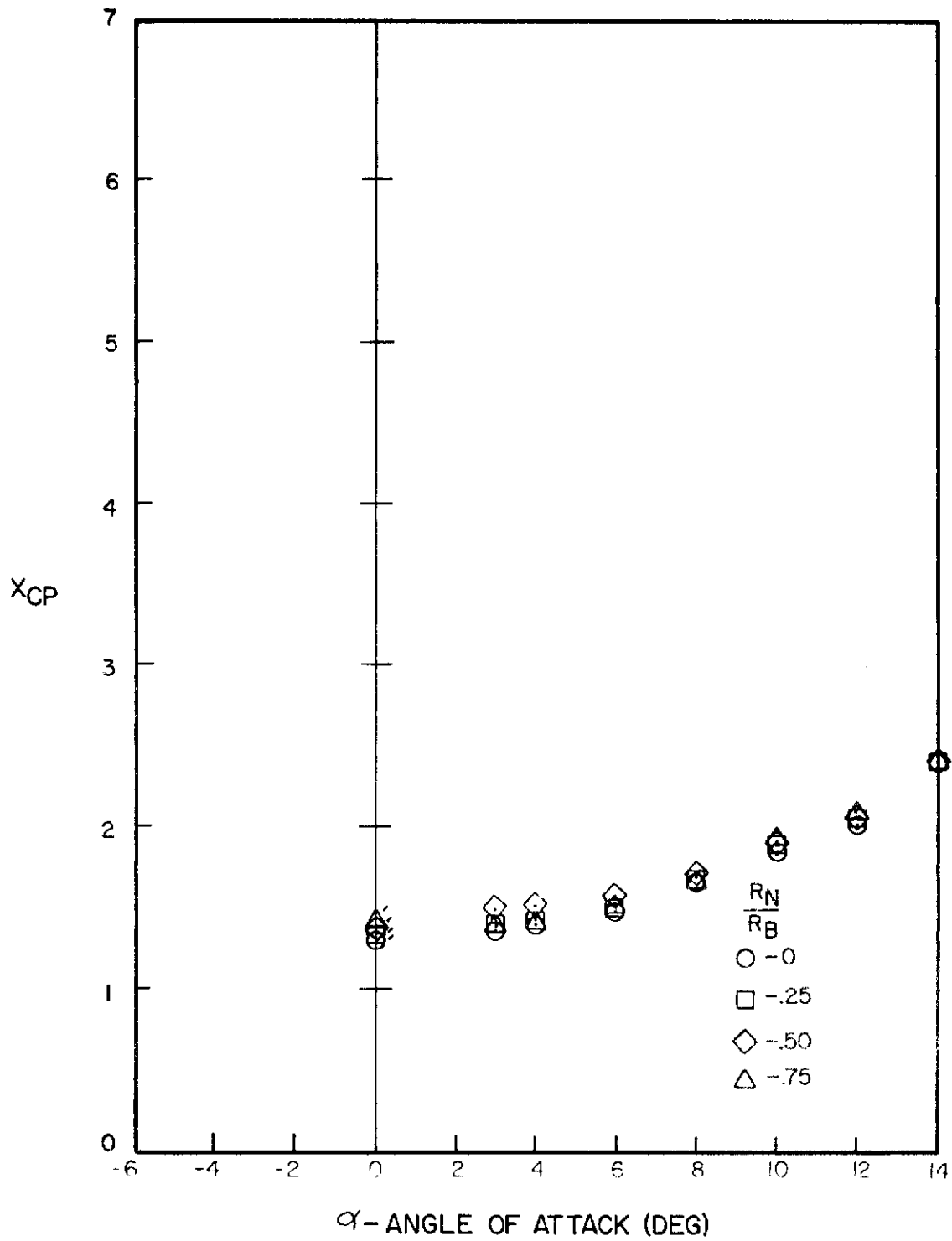


Figure A-98. Center of Pressure Versus Angle of Attack for $l_N/d = 2$, $l_A/d = 6$, $M = 1.2$

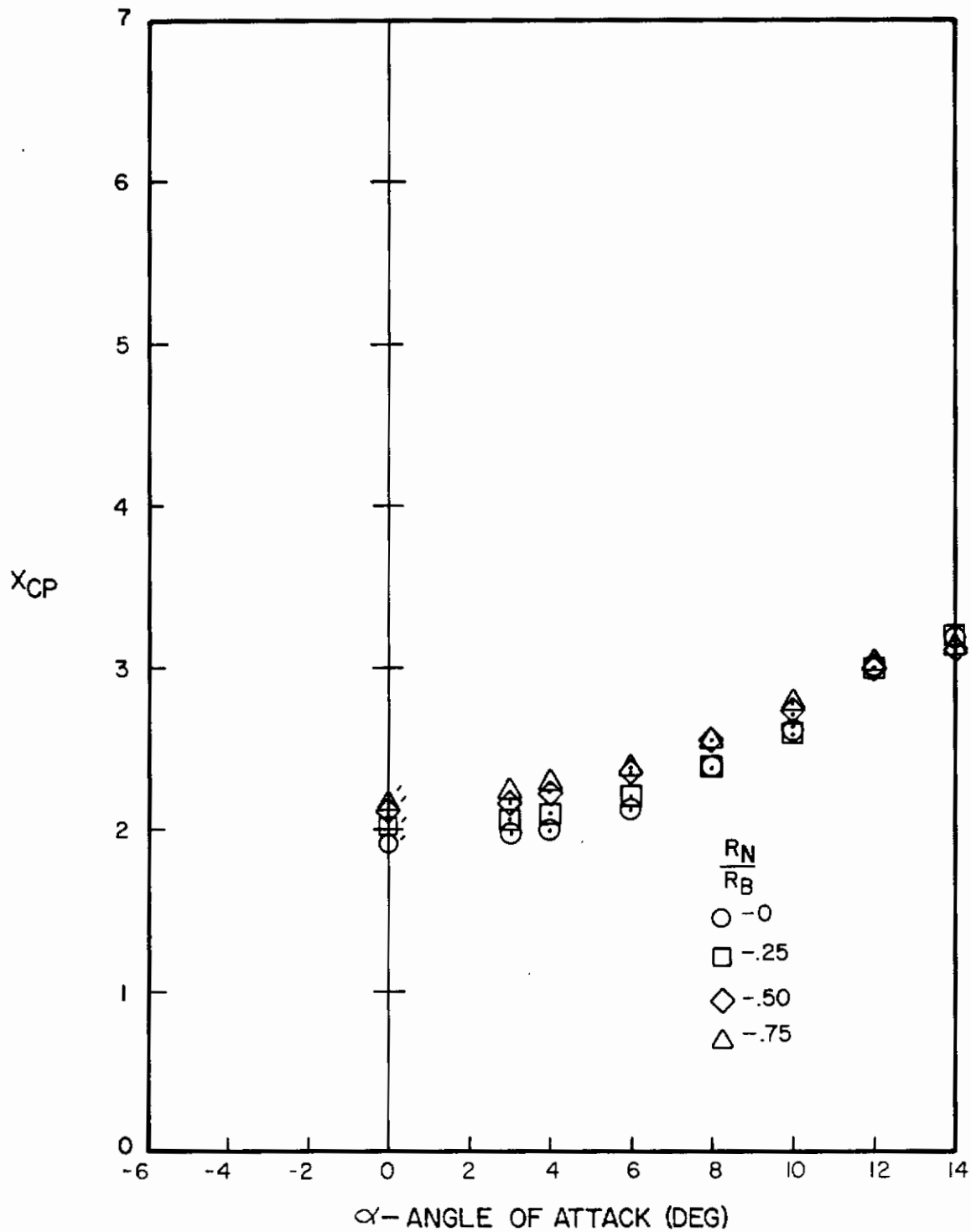


Figure A-99. Center of Pressure Versus Angle of Attack for $l_N/d = 3$, $l_A/d = 6$, $M = 1.2$

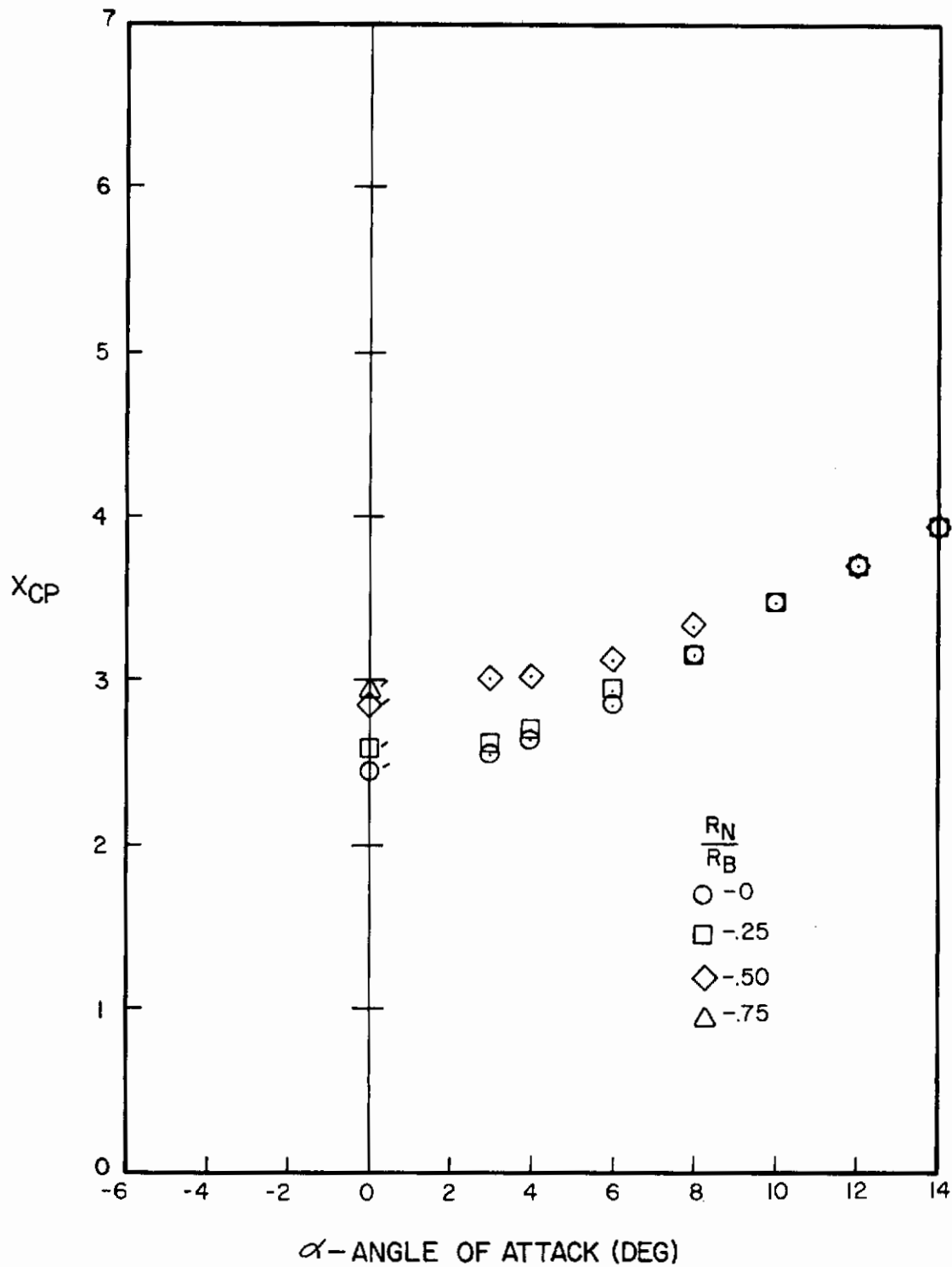


Figure A-100. Center of Pressure Versus Angle of Attack for $l_N/d = 4$, $l_A/d = 6$, $M = 1.2$

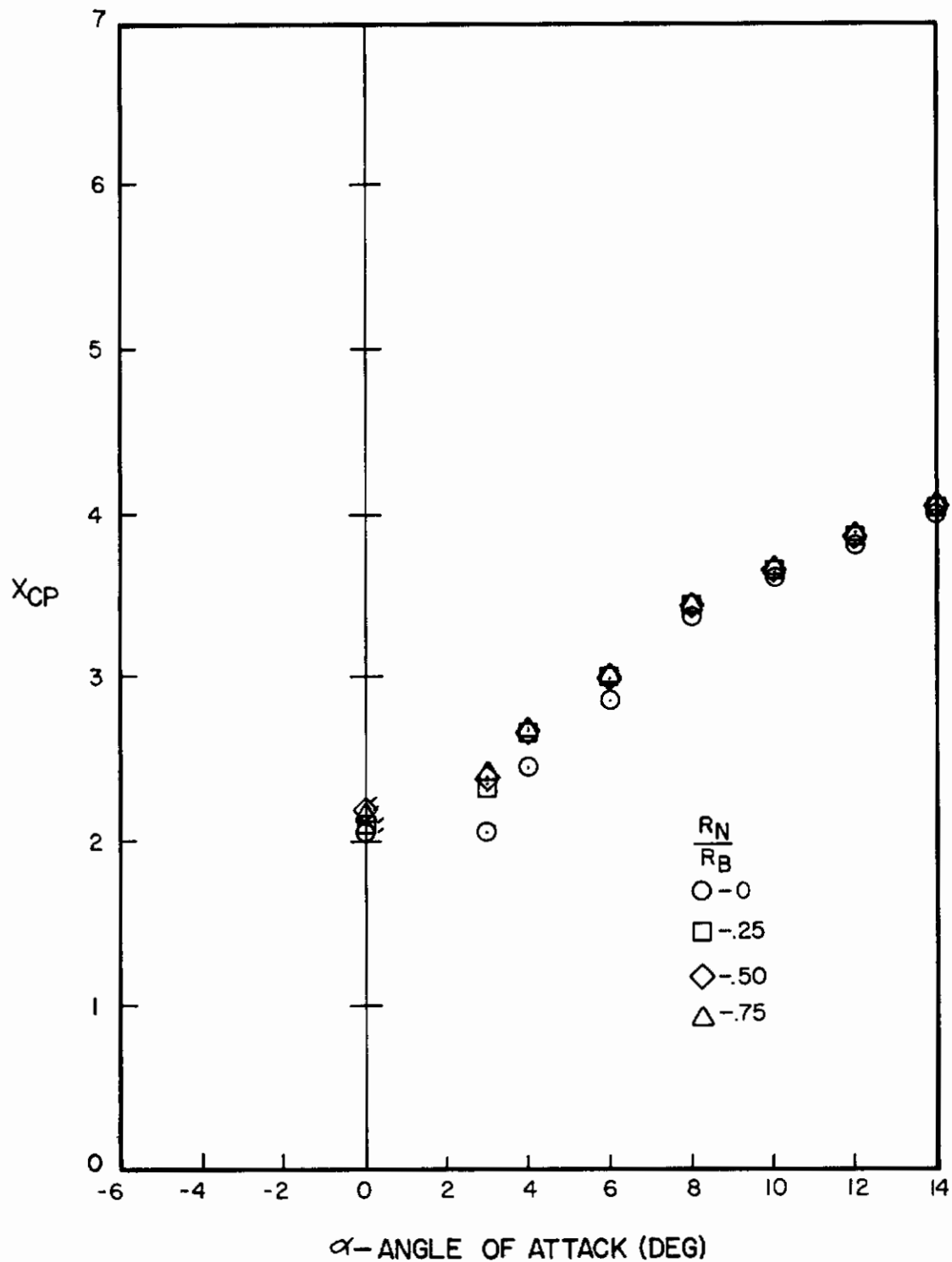


Figure A-101. Center of Pressure Versus Angle of Attack for $l_N/d = 2$, $l_A/d = 10$, $M = 1.2$

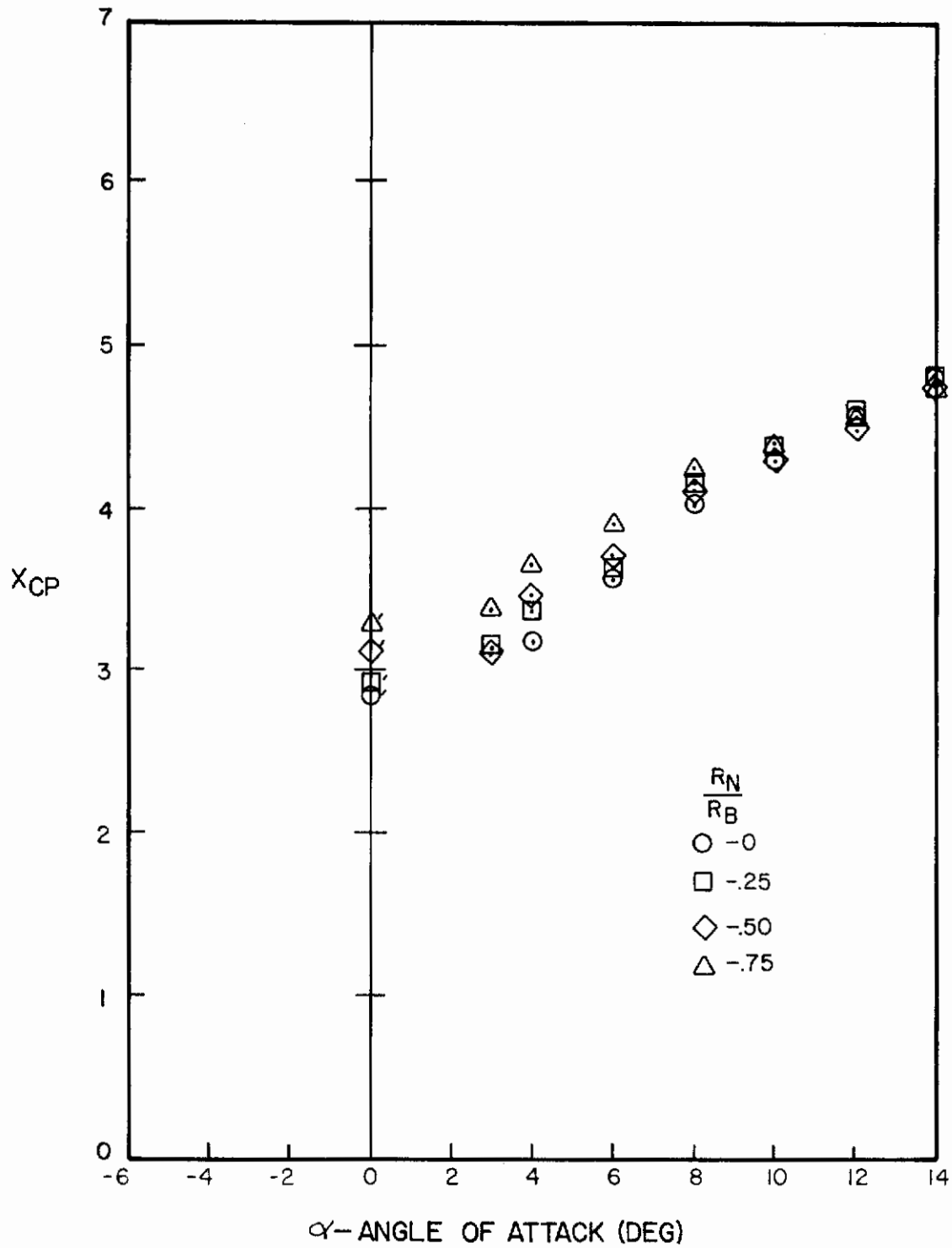


Figure A-102. Center of Pressure Versus Angle of Attack for $l_N/d = 3$, $l_A/d = 10$, $M = 1.2$

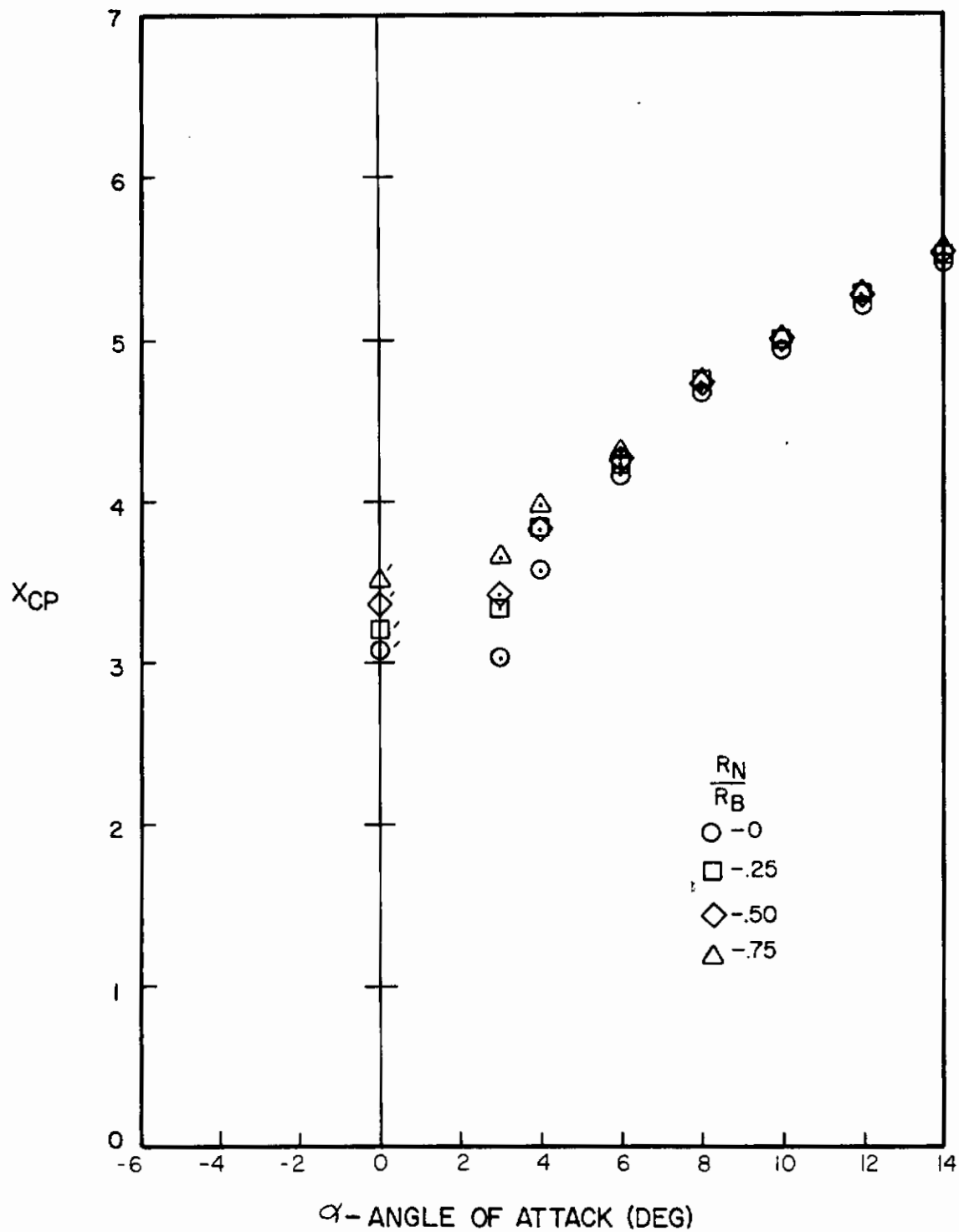


Figure A-103. Center of Pressure Versus Angle of Attack for $l_N/d = 4$, $l_A/d = 10$, $M = 1.2$

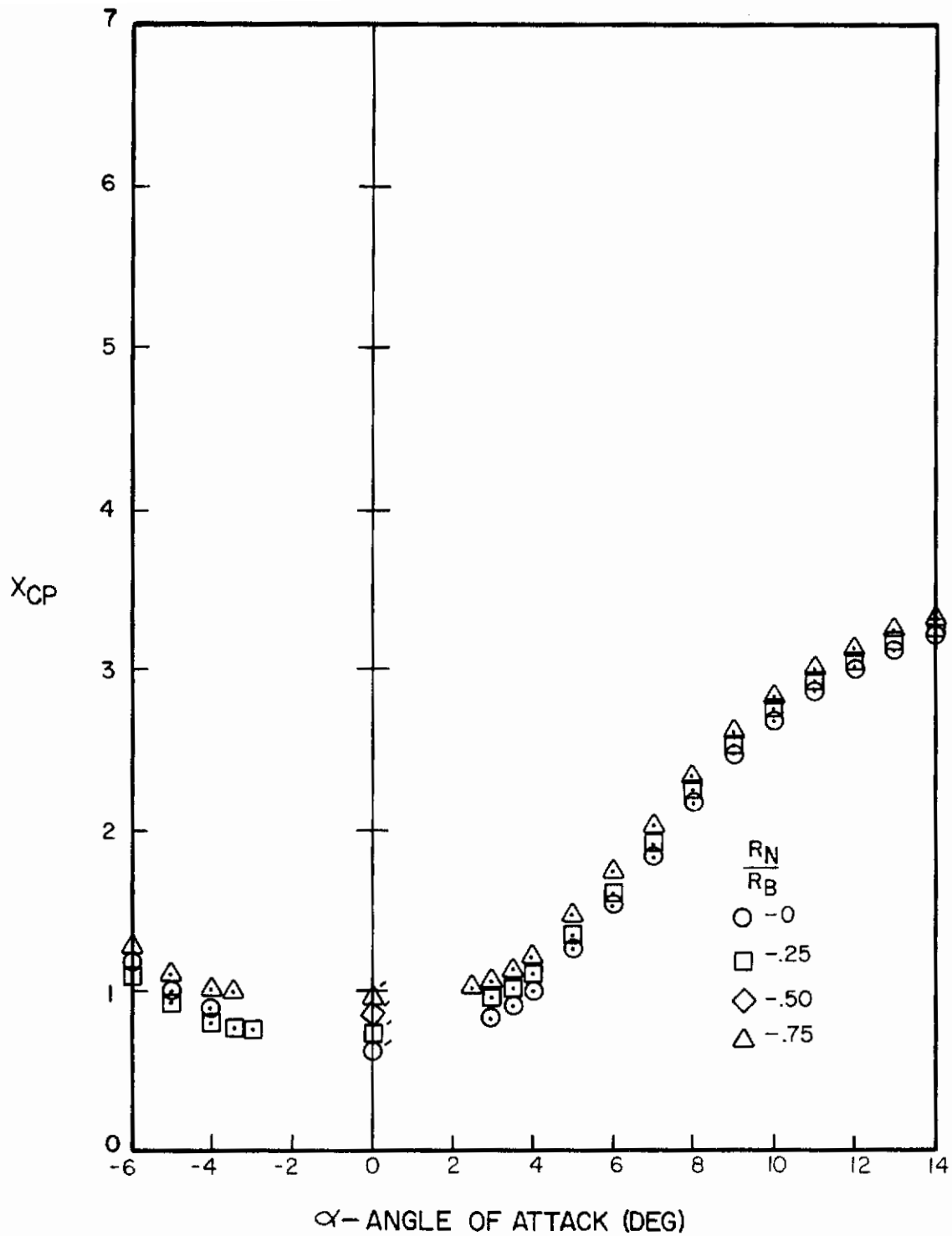


Figure A-104. Center of Pressure Versus Angle of Attack for $l_N/d = 2$, $l_A/d = 6$, $M = 1.5$

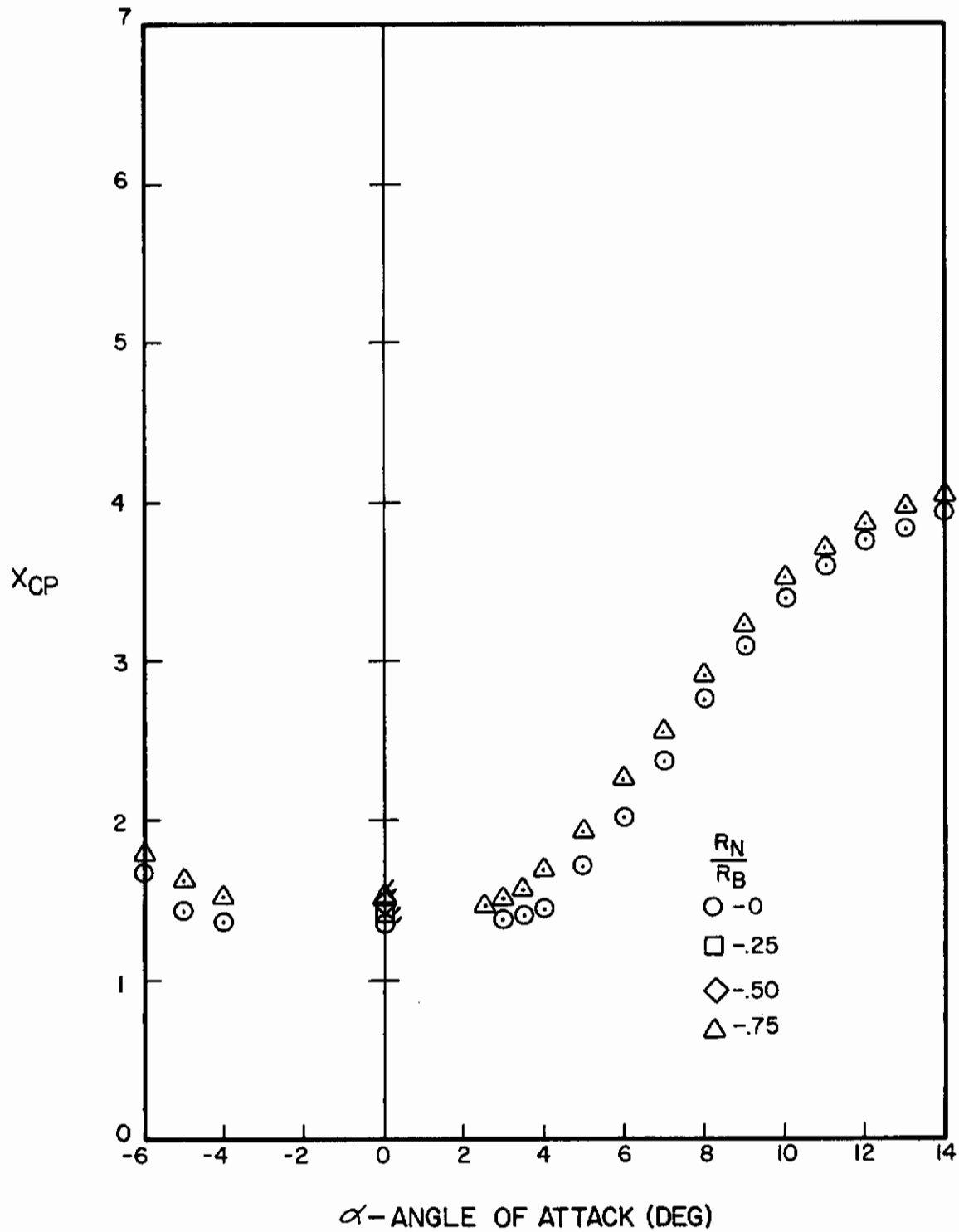


Figure A-105. Center of Pressure Versus Angle of Attack for $l_N/d = 3$, $l_A/d = 6$, $M = 1.5$

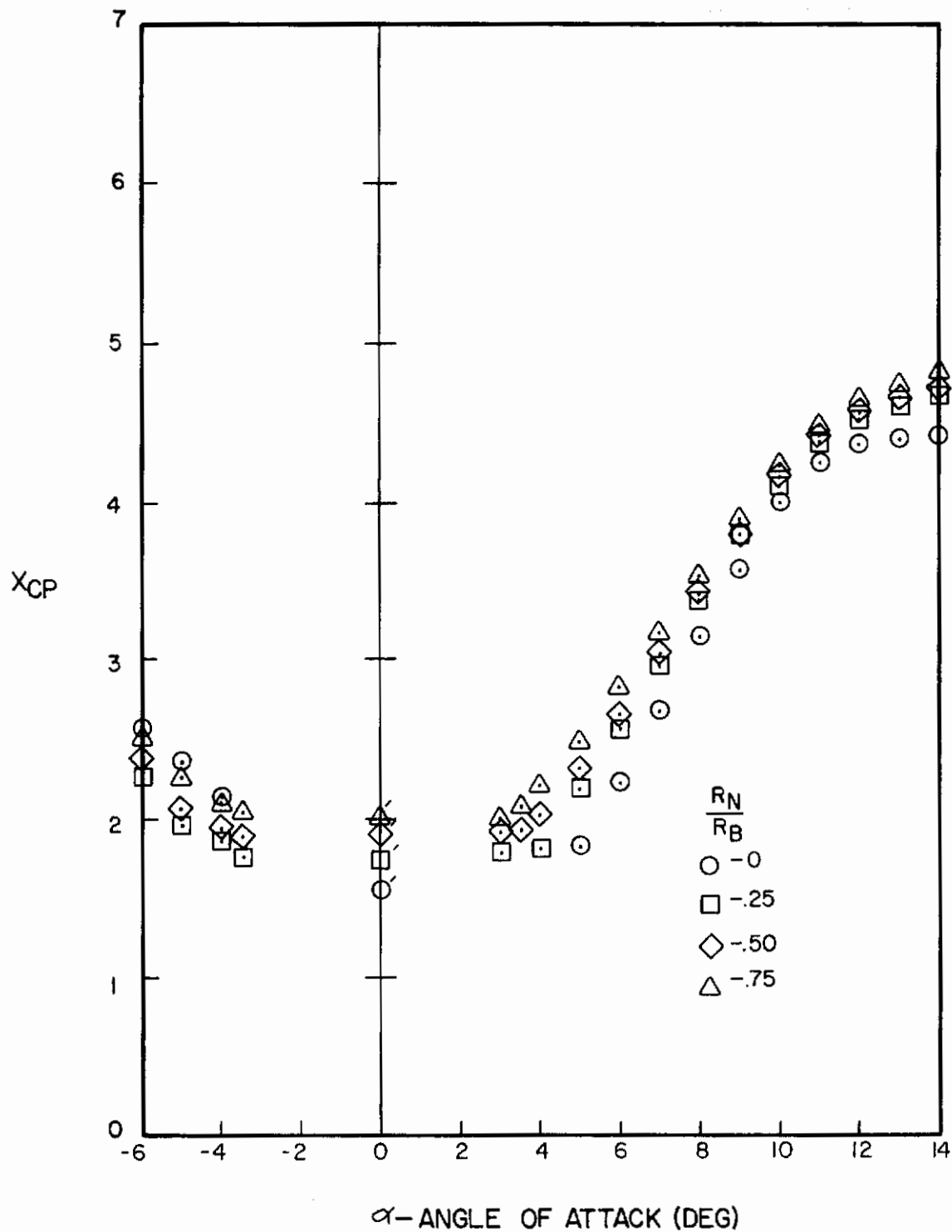


Figure A-106. Center of Pressure Versus Angle of Attack for $l_N/d = 4$, $l_A/d = 6$, $M = 1.5$

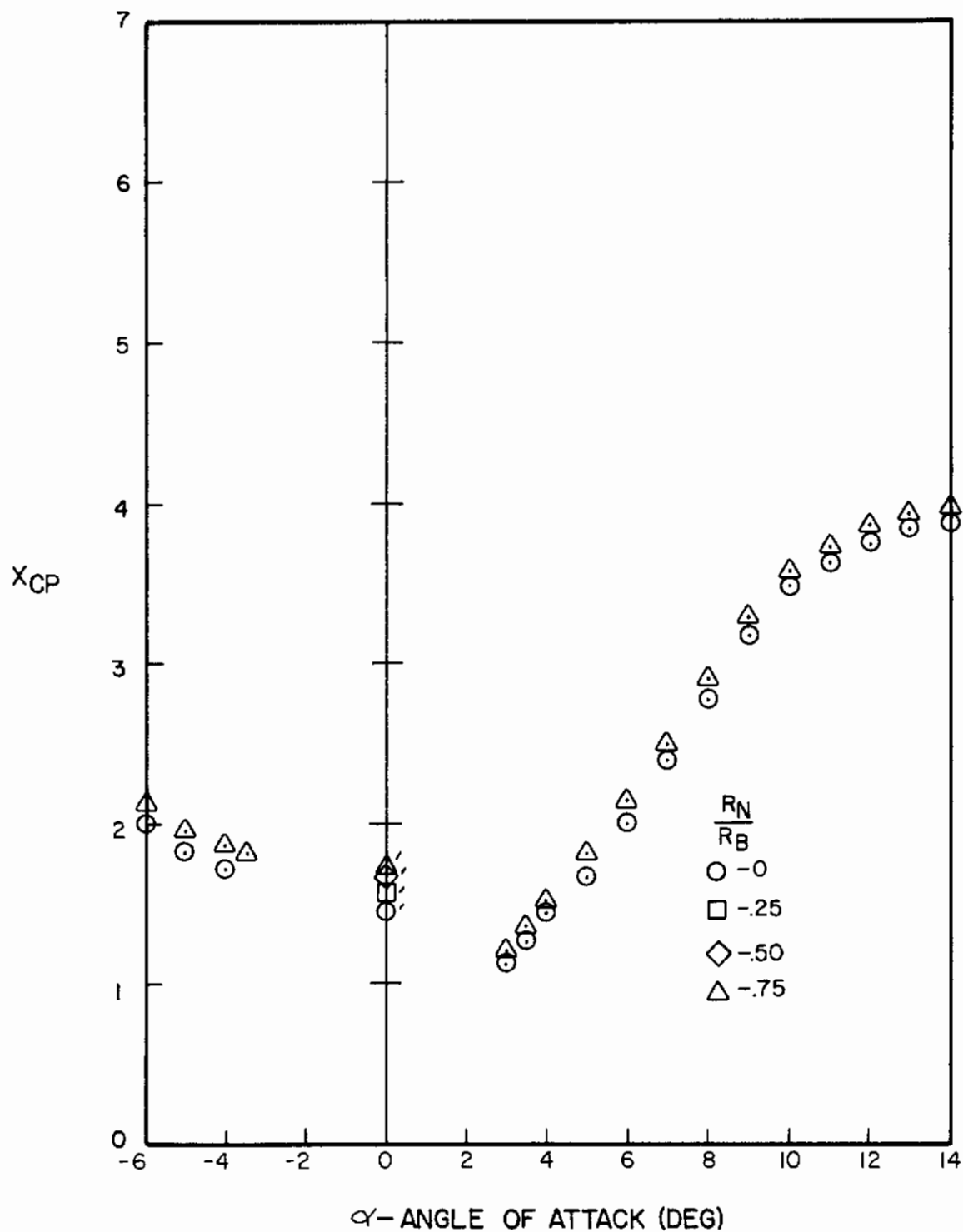


Figure A-107. Center of Pressure Versus Angle of Attack for $l_N/d = 2$, $l_A/d = 8$, $M = 1.5$

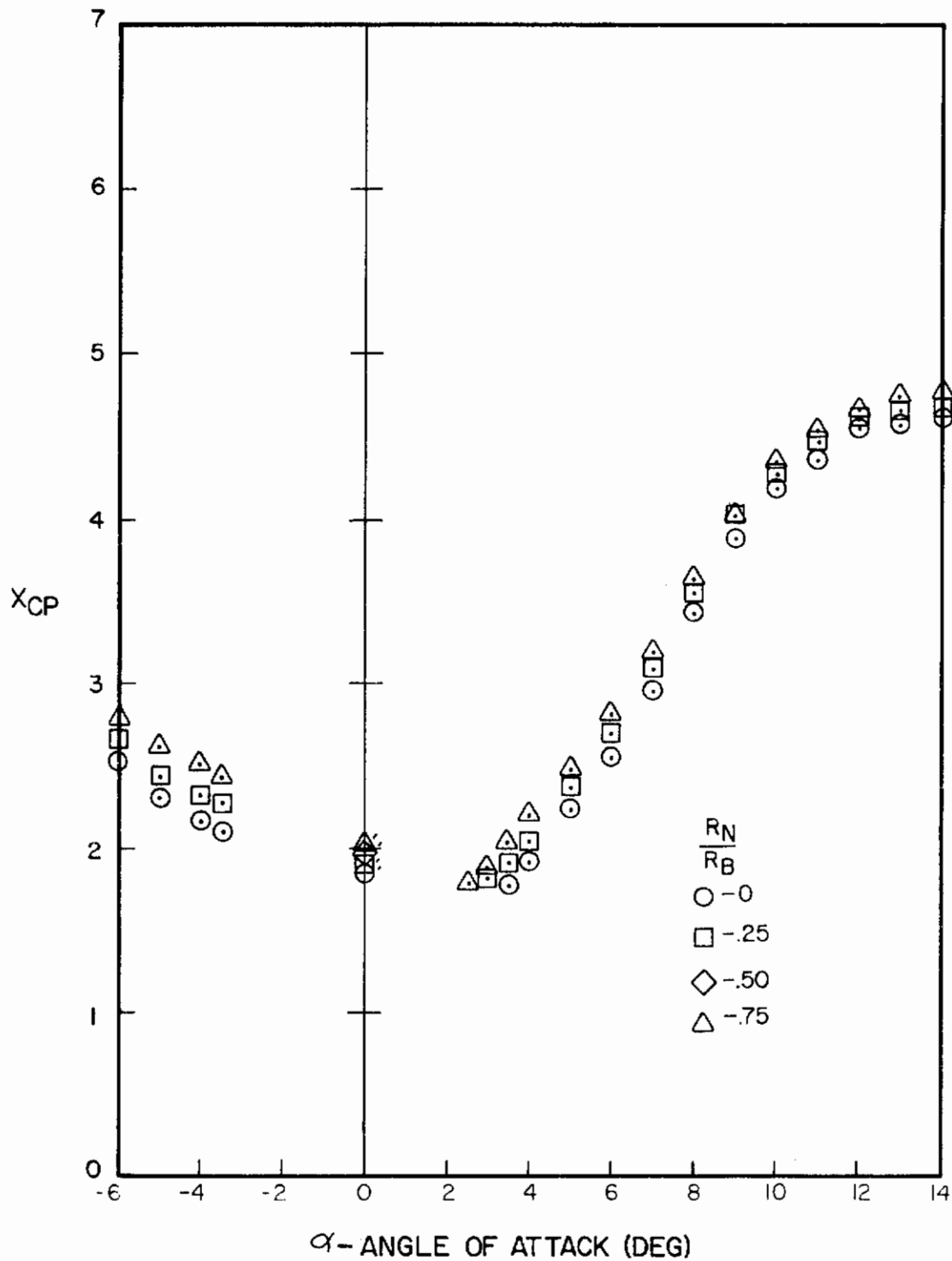


Figure A-108. Center of Pressure Versus Angle of Attack for $l_N/d = 3$, $l_A/d = 8$, $M = 1.5$

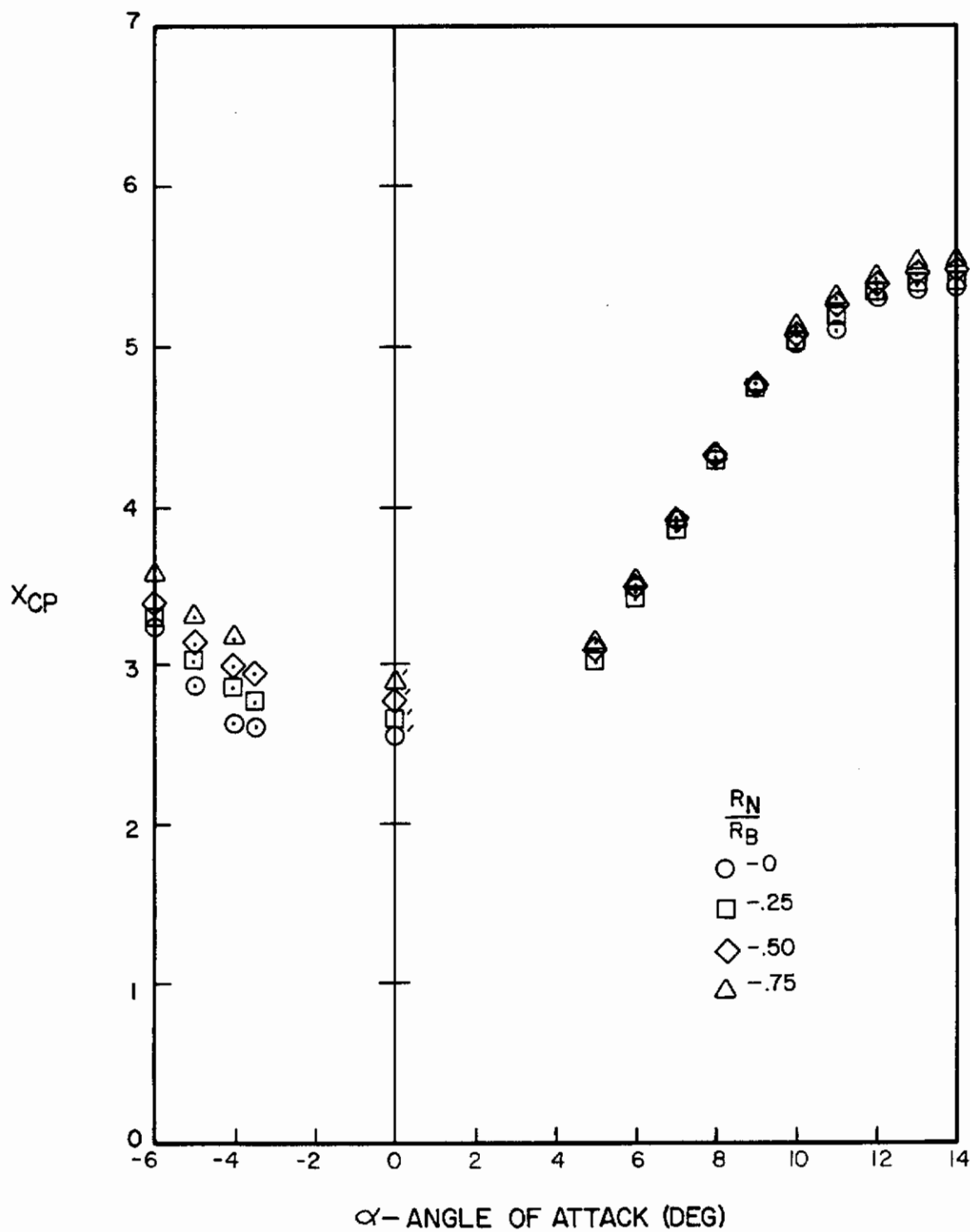


Figure A-109. Center of Pressure Versus Angle of Attack for $l_N/d = 4$, $l_A/d = 8$, $M = 1.5$

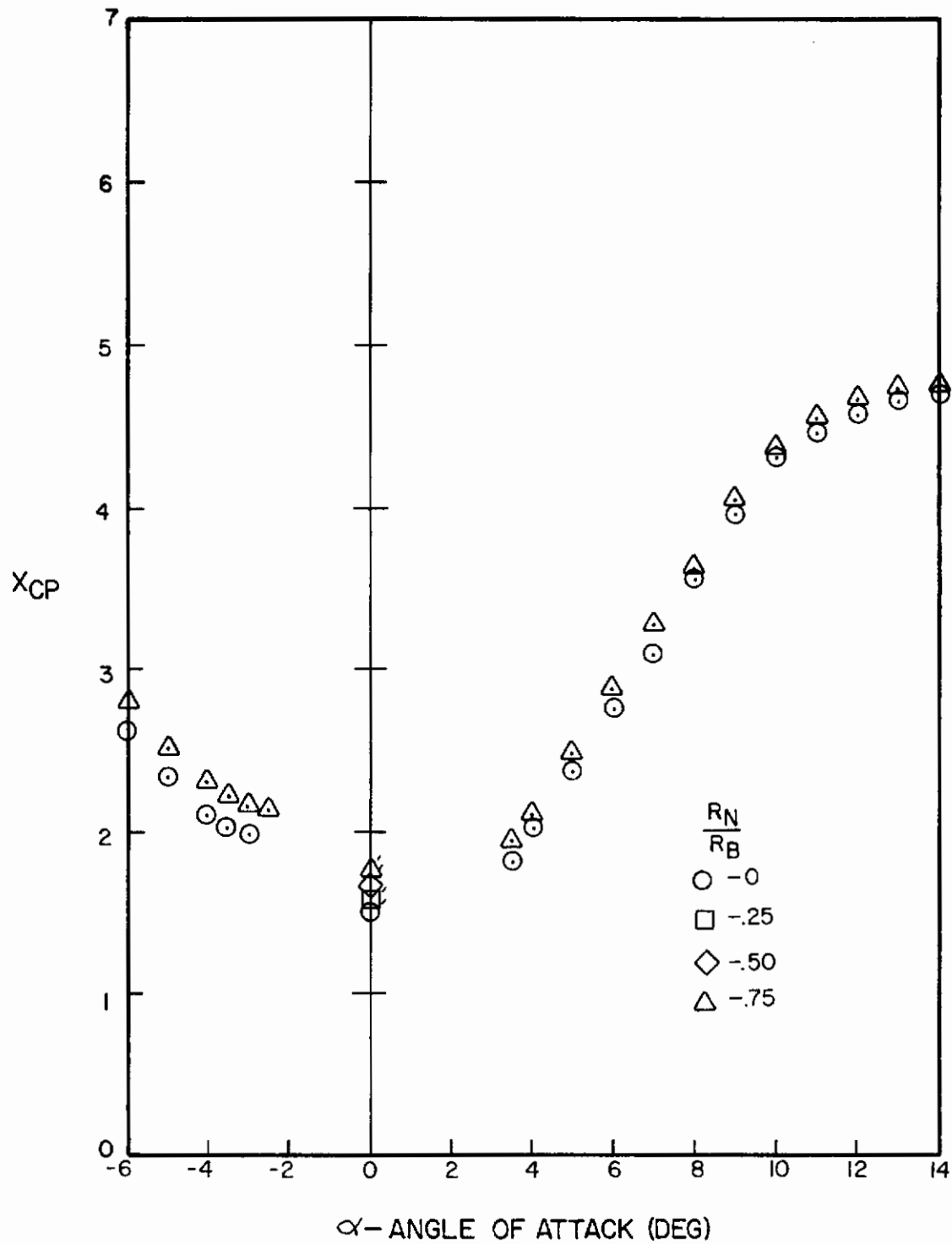


Figure A-110. Center of Pressure Versus Angle of Attack for $l_N/d = 2$, $l_A/d = 10$, $M = 1.5$

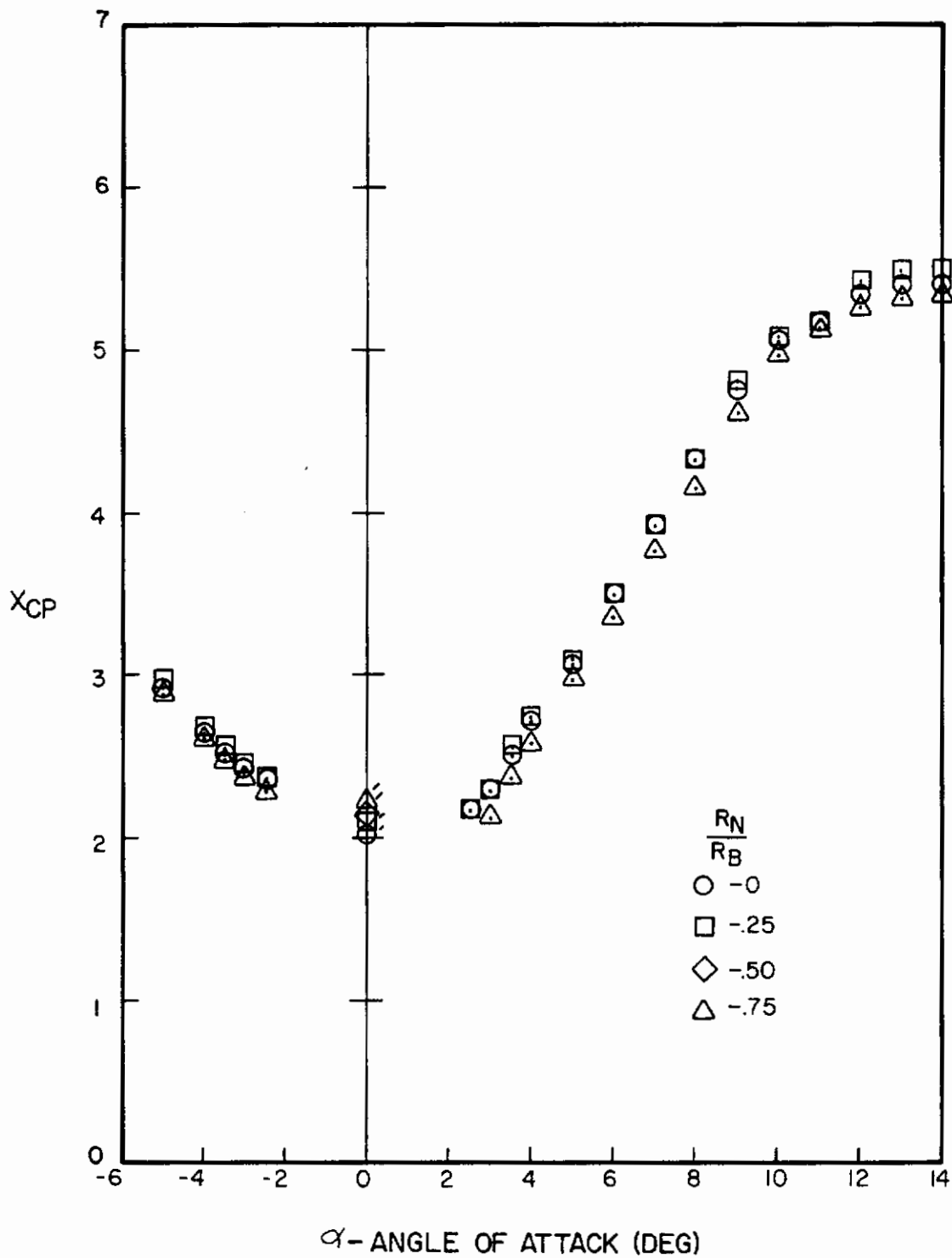


Figure A-111. Center of Pressure Versus Angle of Attack for $l_N/d = 3$, $l_A/d = 10$, $M = 1.5$

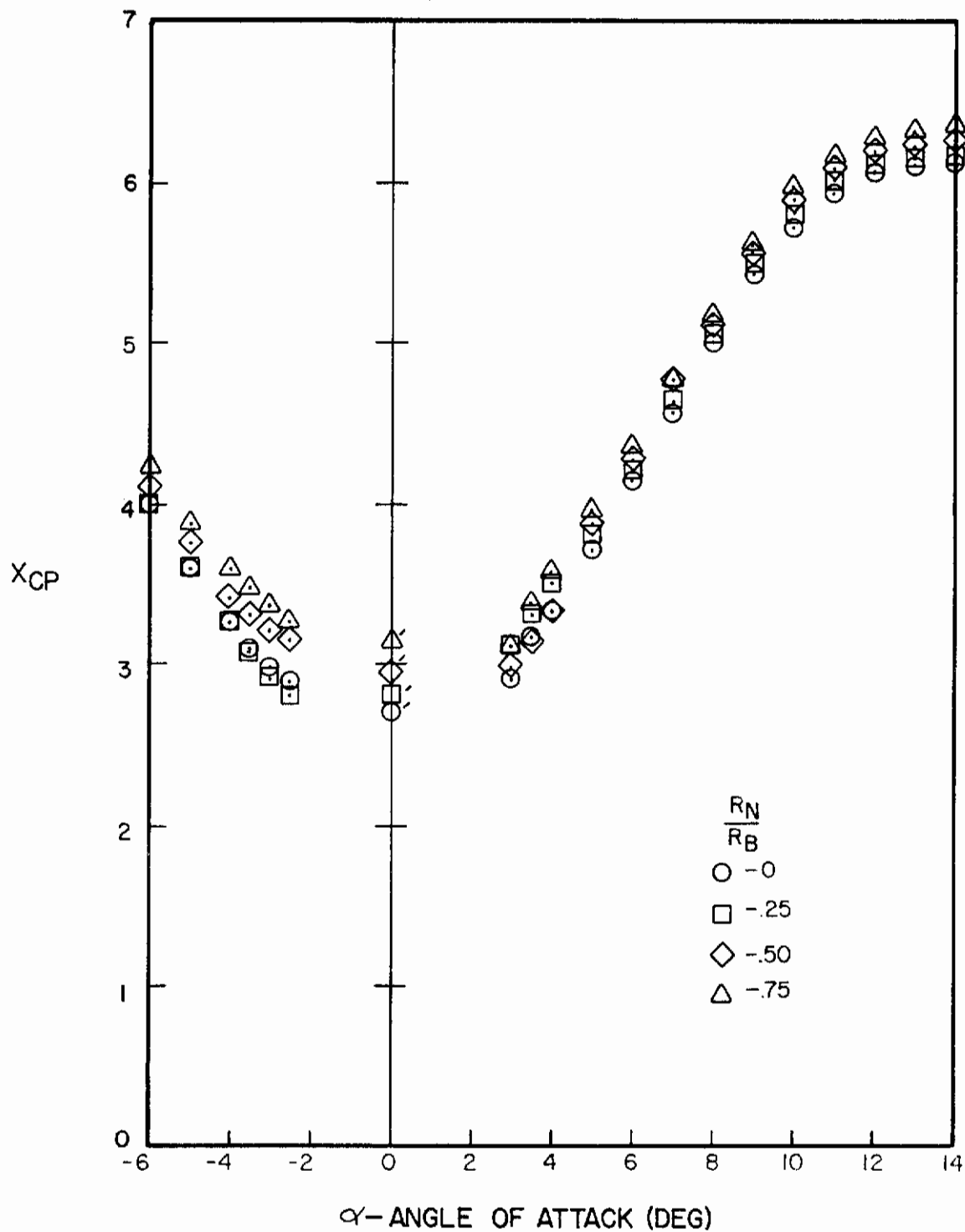


Figure A-112. Center of Pressure Versus Angle of Attack for $l_N/d = 4$, $l_A/d = 10$, $M = 1.5$

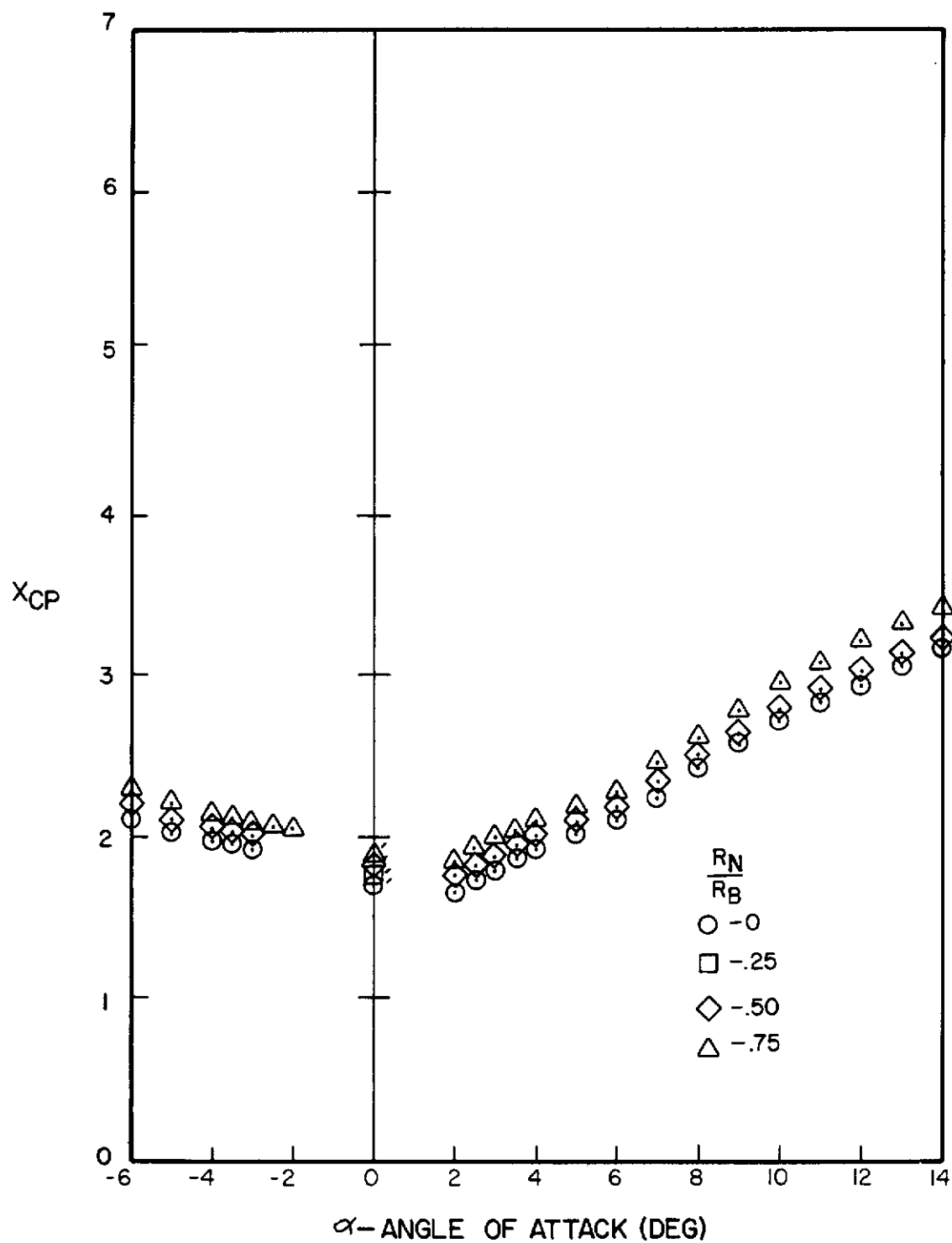


Figure A-113. Center of Pressure Versus Angle of Attack for $l_N/d = 2$, $l_A/d = 6$, $M = 2.0$

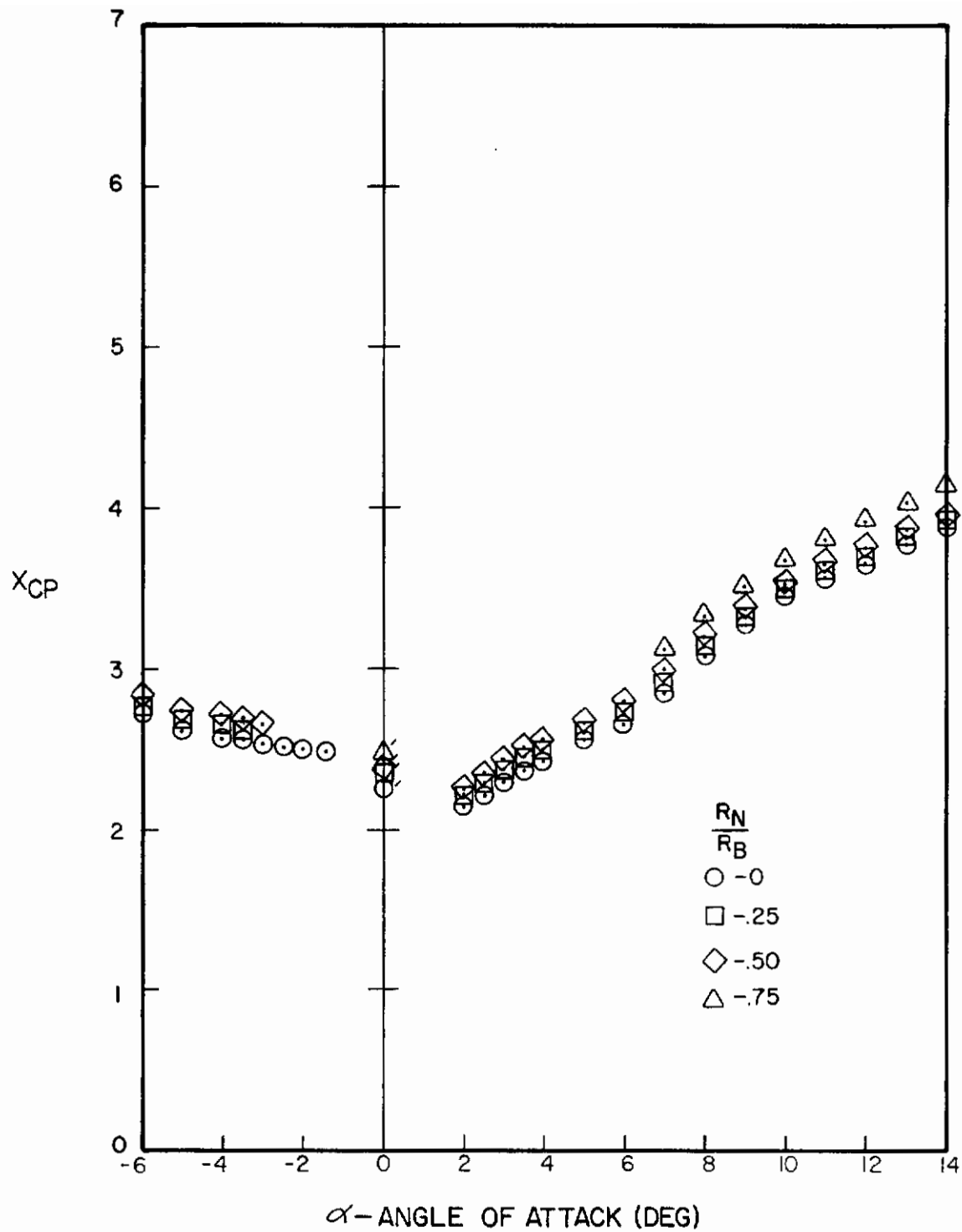


Figure A-114. Center of Pressure Versus Angle of Attack for $l_N/d = 3$, $l_A/d = 6$, $M = 2.0$

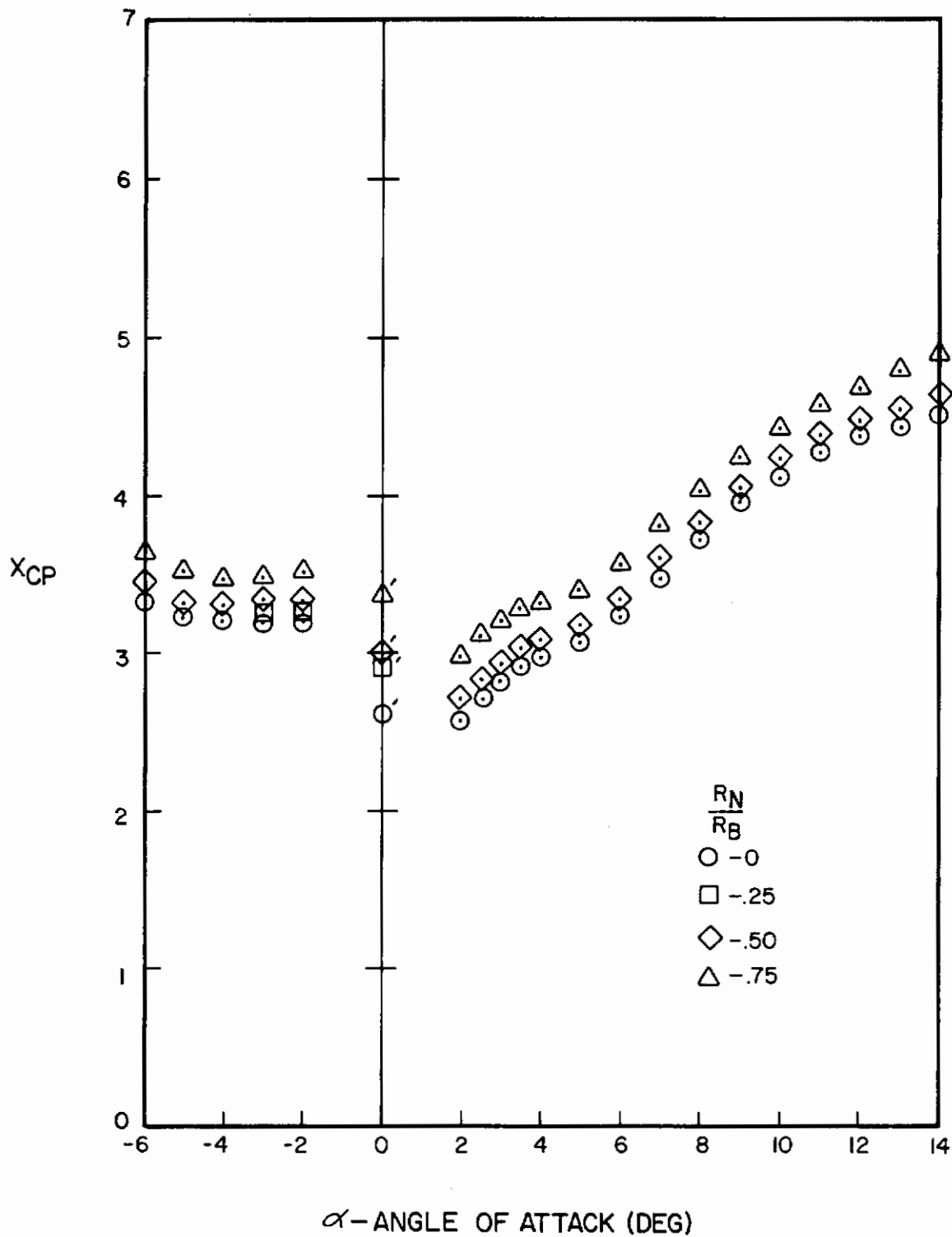


Figure A-115. Center of Pressure Versus Angle of Attack for $l_N/d = 4$, $l_A/d = 6$, $M = 2.0$

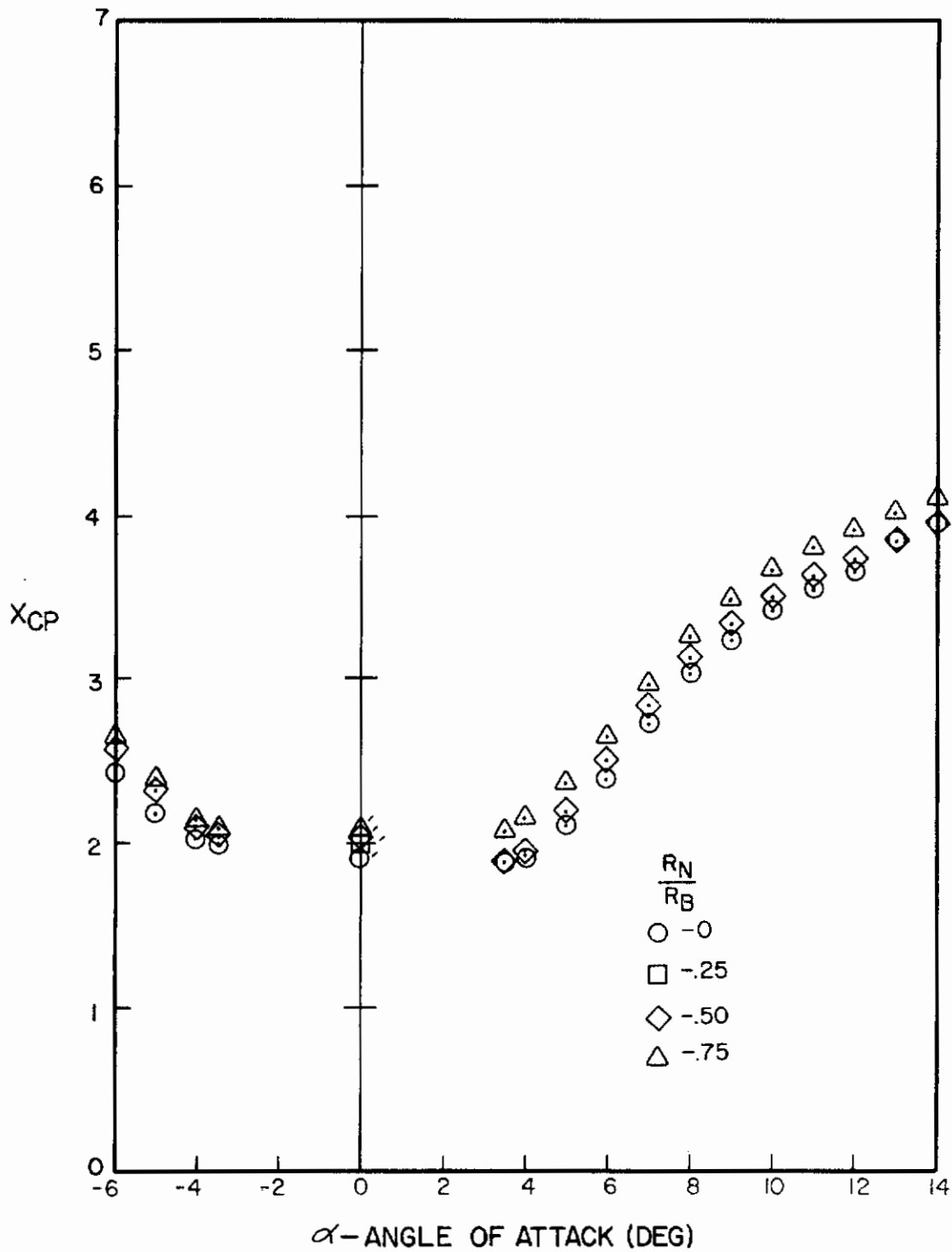


Figure A-116. Center of Pressure Versus Angle of Attack for $l_N/d = 2$, $l_A/d = 8$, $M = 2.0$

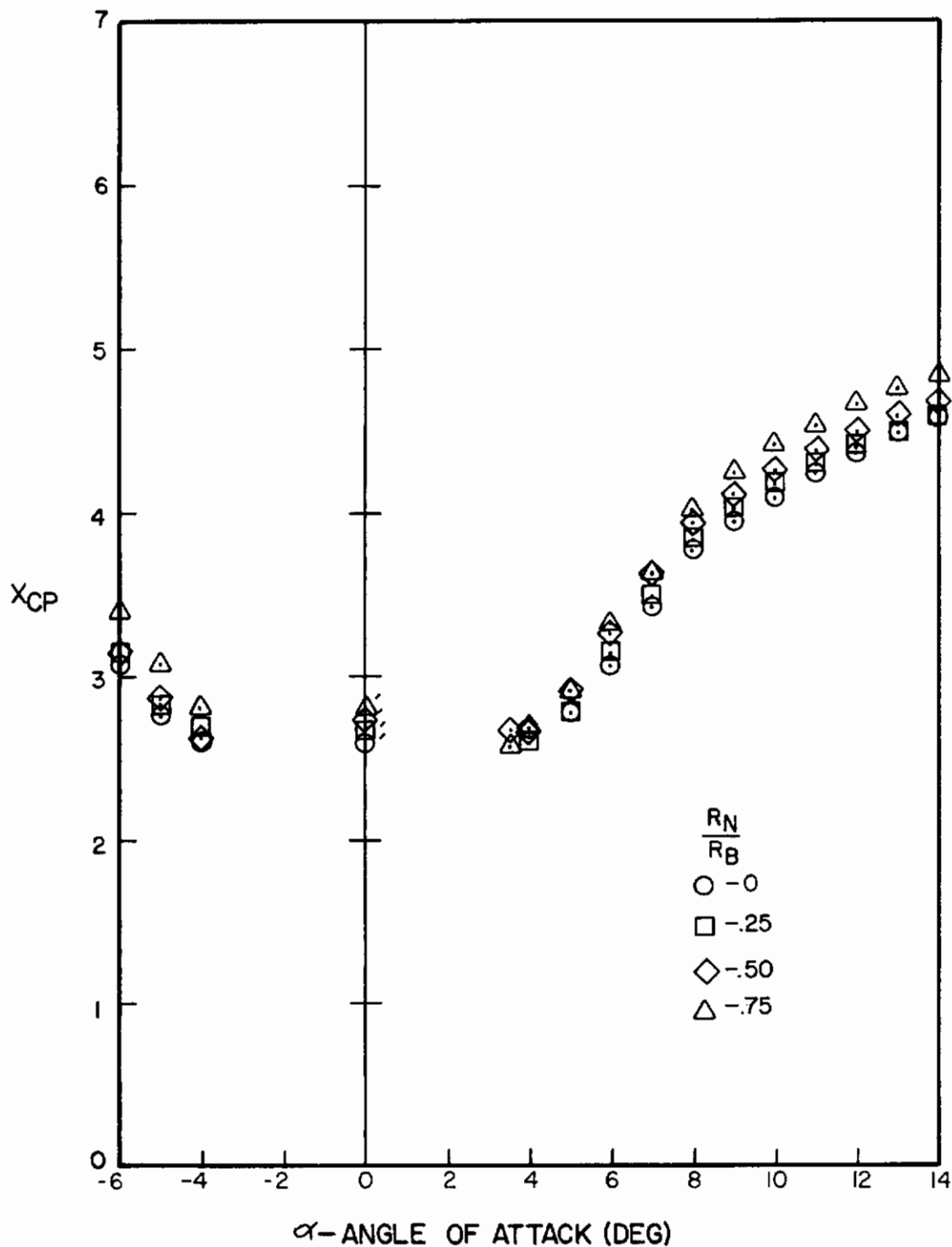


Figure A-117. Center of Pressure Versus Angle of Attack for $l_N/d = 3$, $l_A/d = 8$, $M = 2.0$

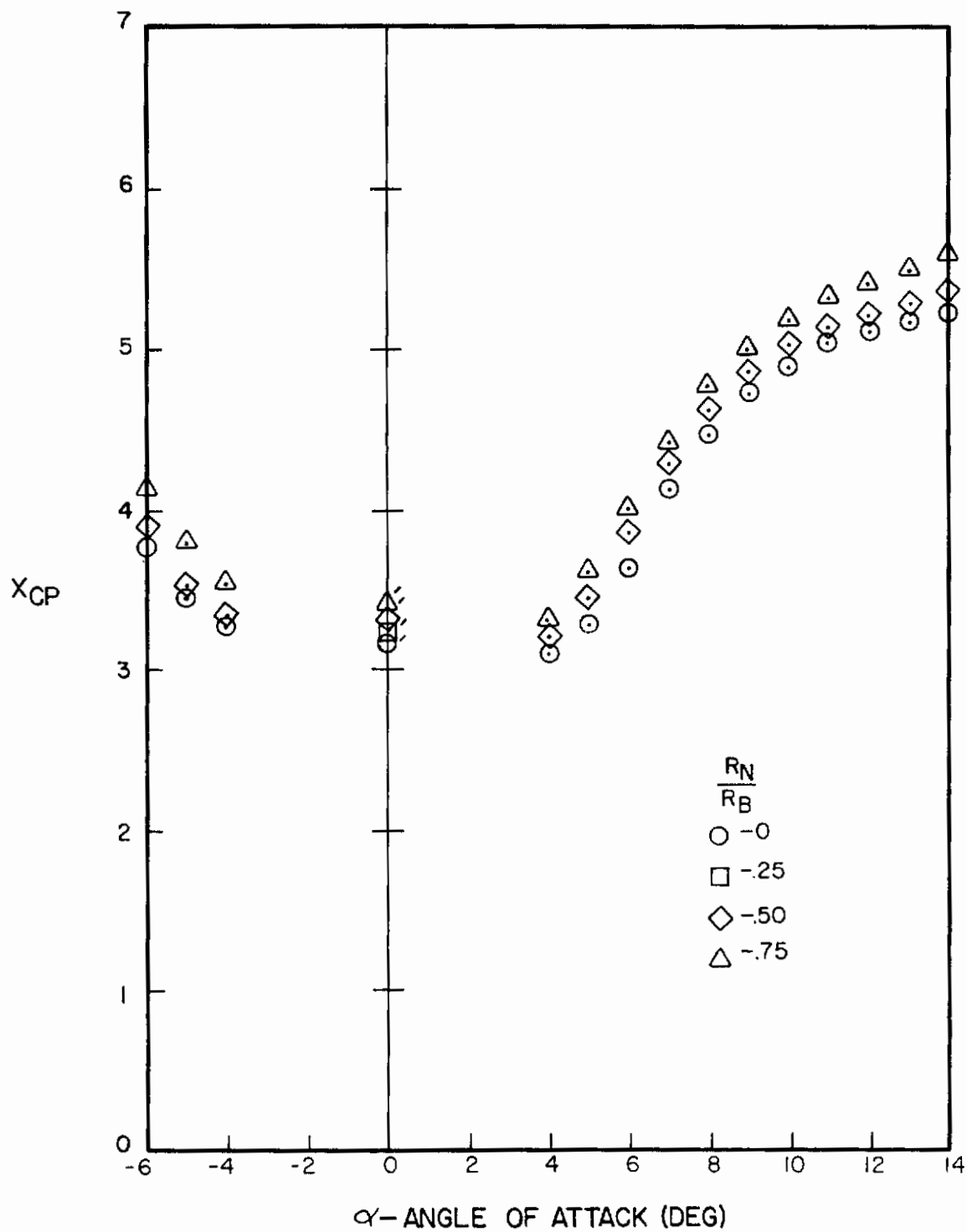


Figure A-118. Center of Pressure Versus Angle of Attack for $l_N/d = 4$, $l_A/d = 8$, $M = 2.0$

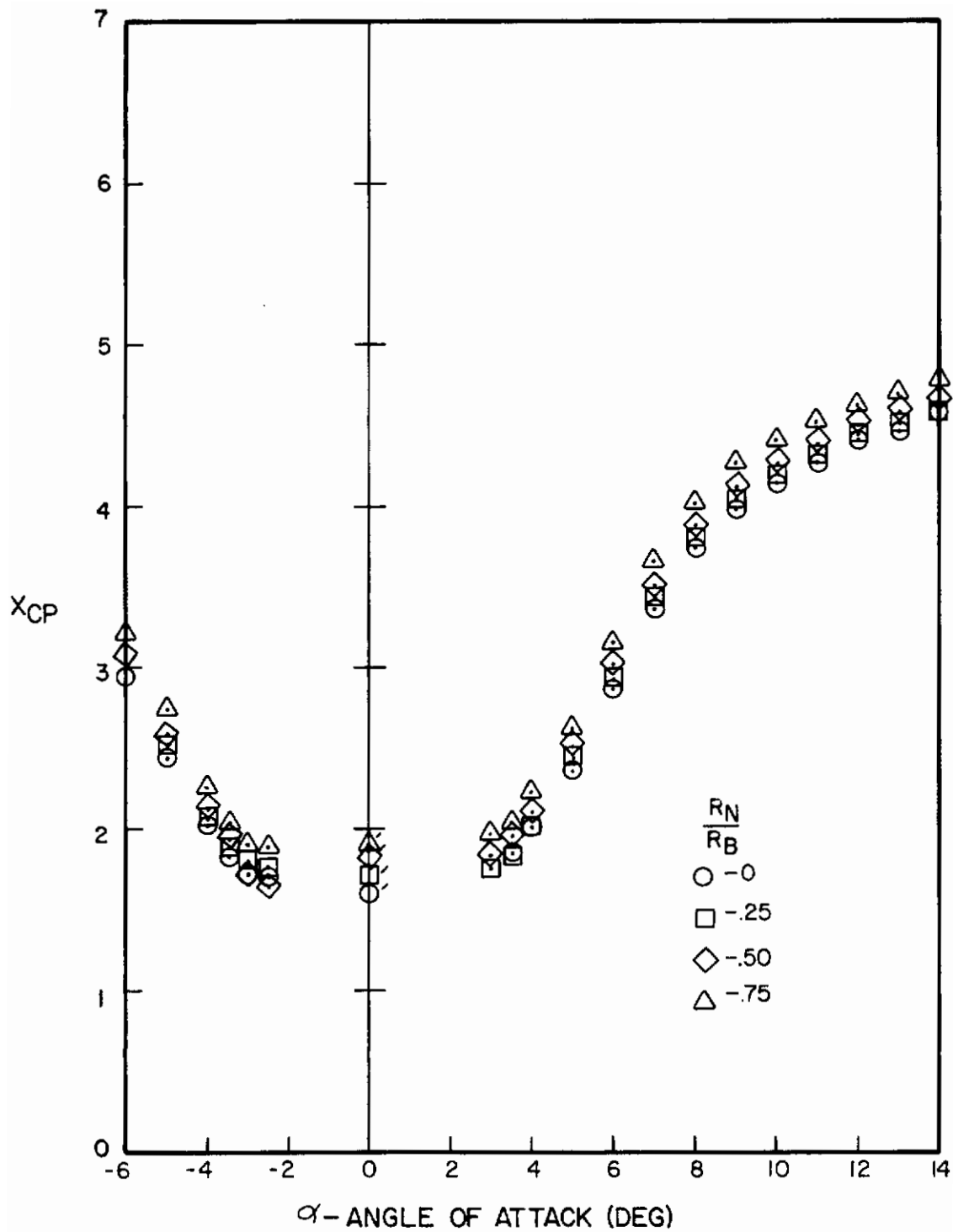


Figure A-119. Center of Pressure Versus Angle of Attack for $l_N/d = 2$, $l_A/d = 10$, $M = 2.0$

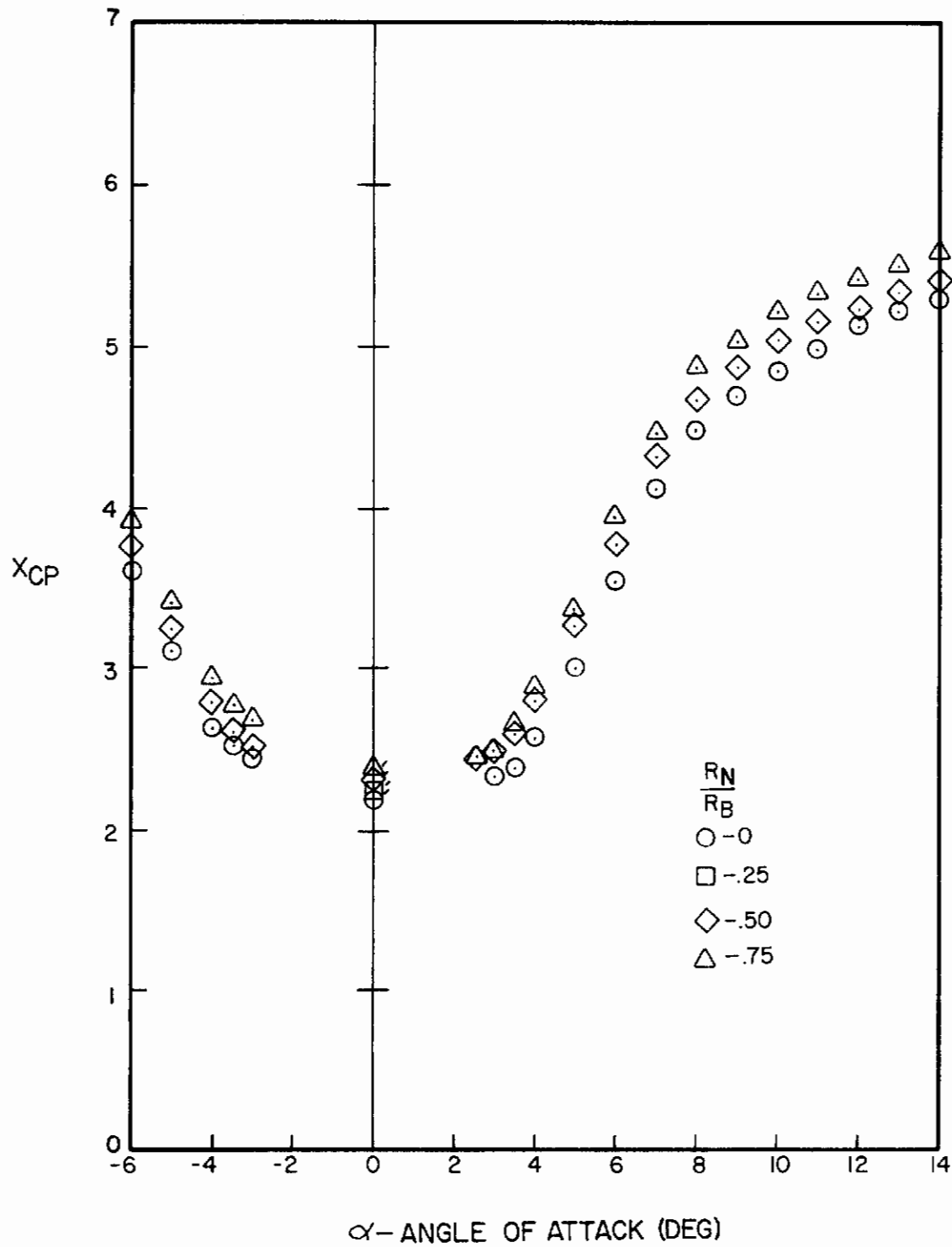


Figure A-120. Center of Pressure Versus Angle of Attack for $l_N/d = 3$, $l_A/d = 10$, $M = 2.0$

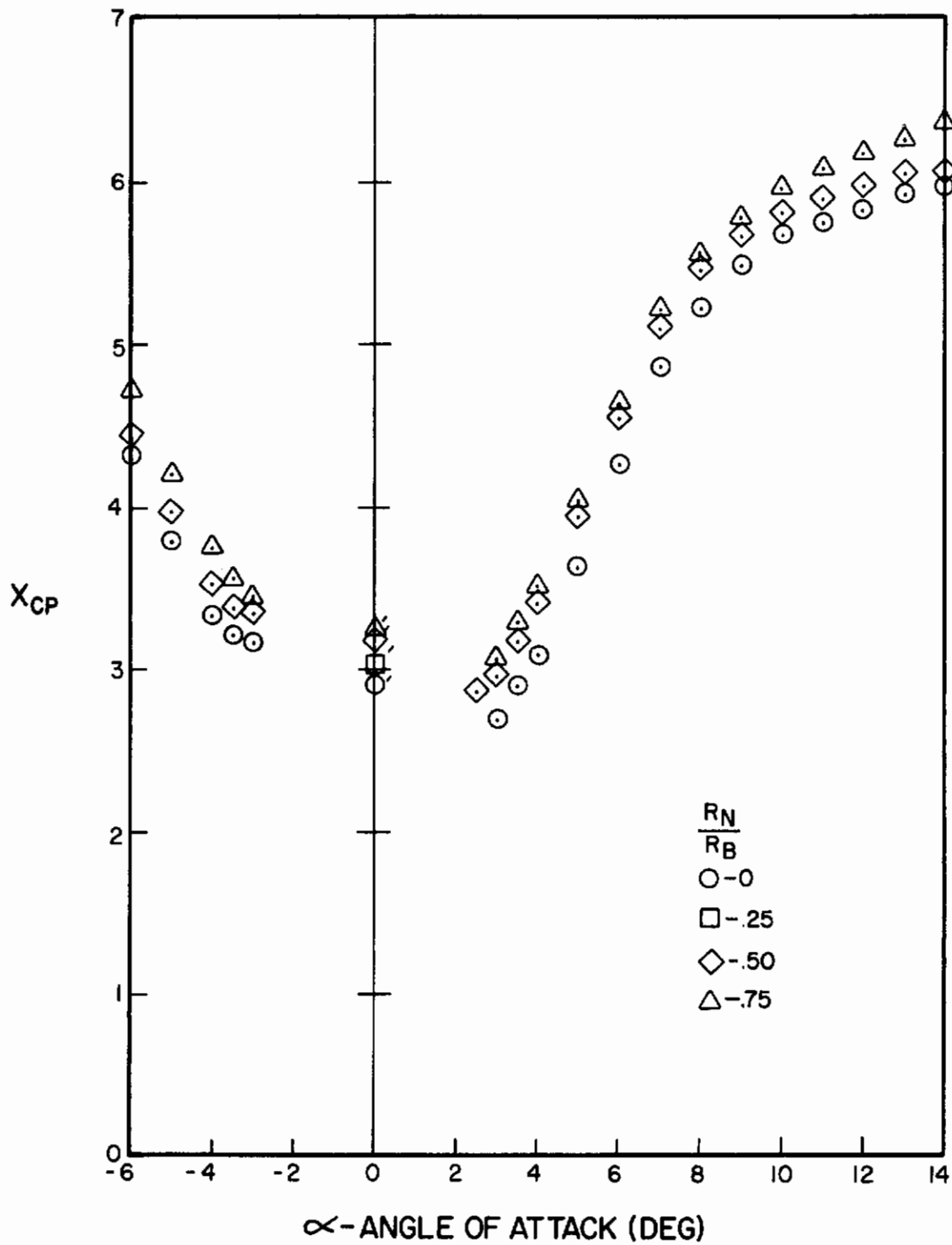


Figure A-121. Center of Pressure Versus Angle of Attack for $l_N/d = 4$, $l_A/d = 10$, $M = 2.0$

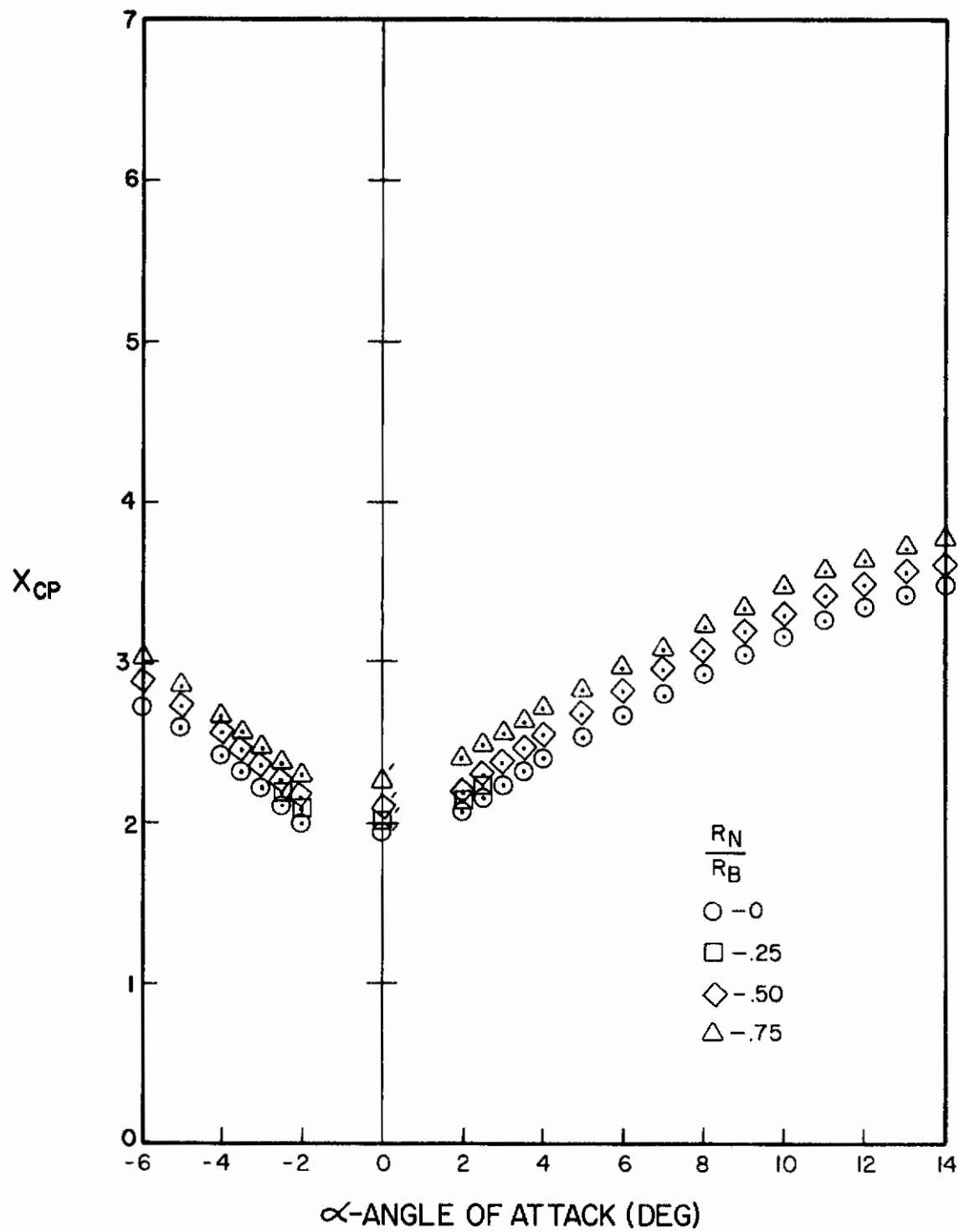


Figure A-122. Center of Pressure Versus Angle of Attack for $l_N/d = 2$, $l_A/d = 6$, $M = 3.0$

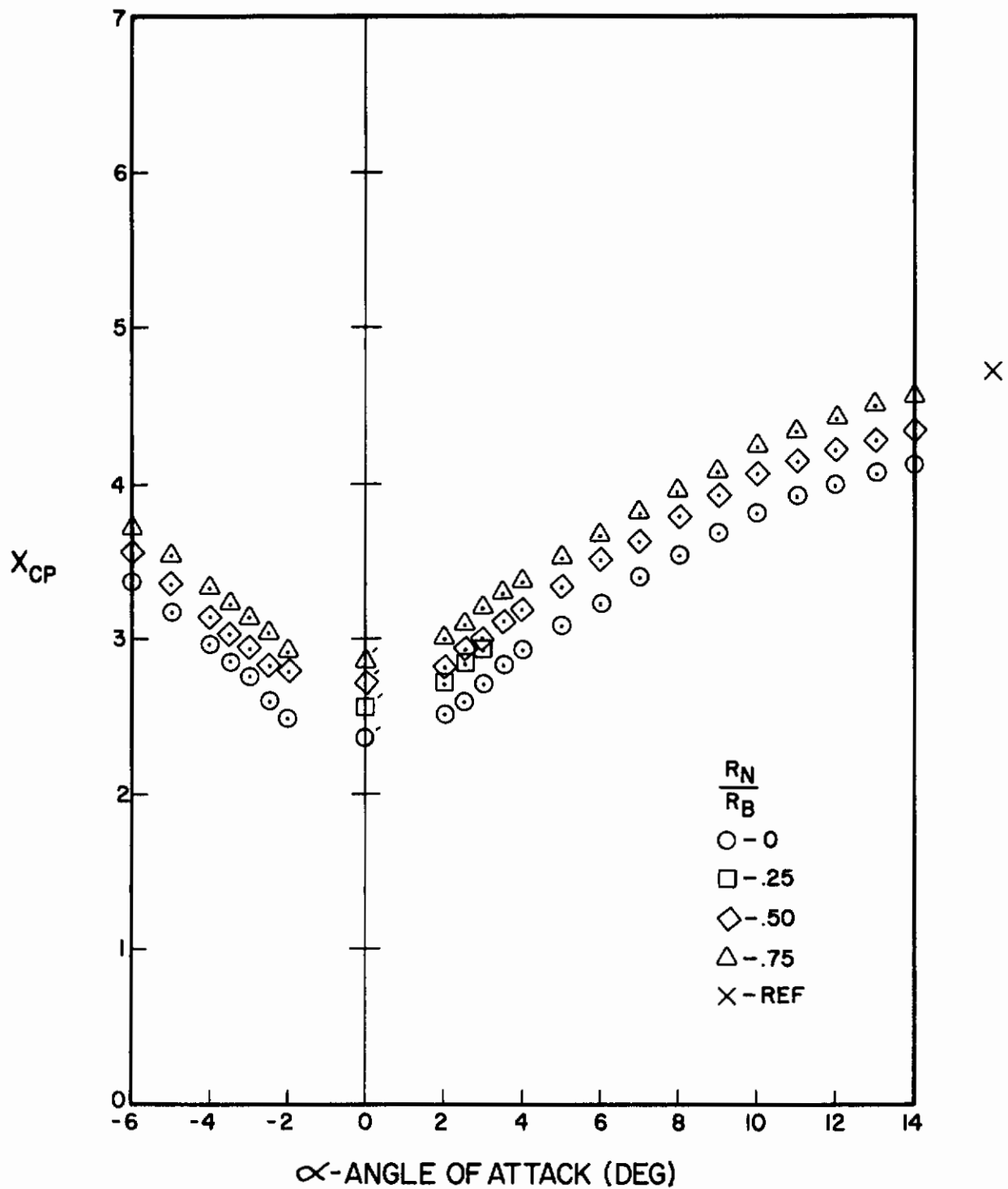


Figure A-123. Center of Pressure Versus Angle of Attack for $l_N/d = 3$, $l_A/d = 6$, $M = 3.0$

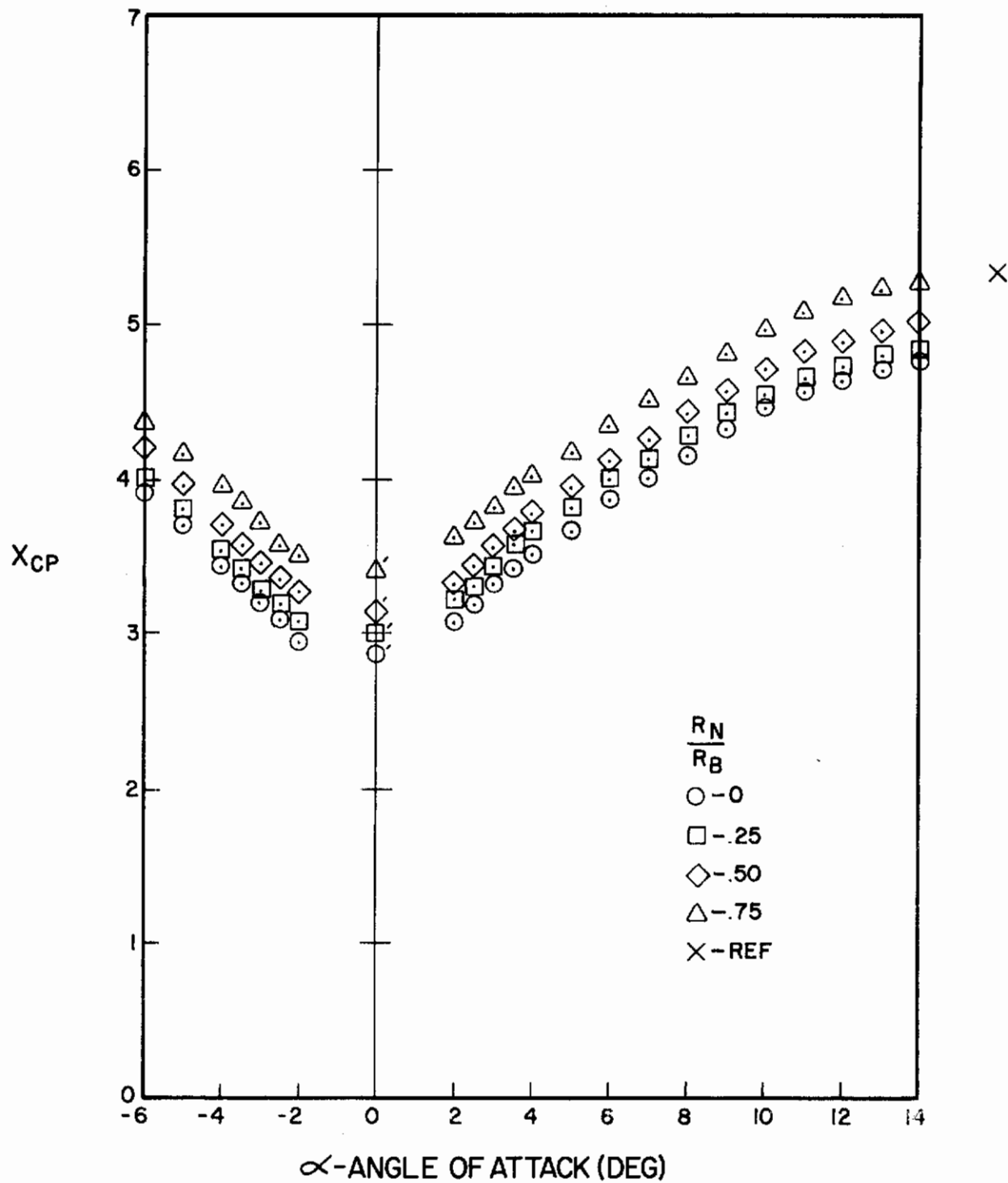


Figure A-124. Center of Pressure Versus Angle of Attack for $l_N/d = 4$, $l_A/d = 6$, $M = 3.0$

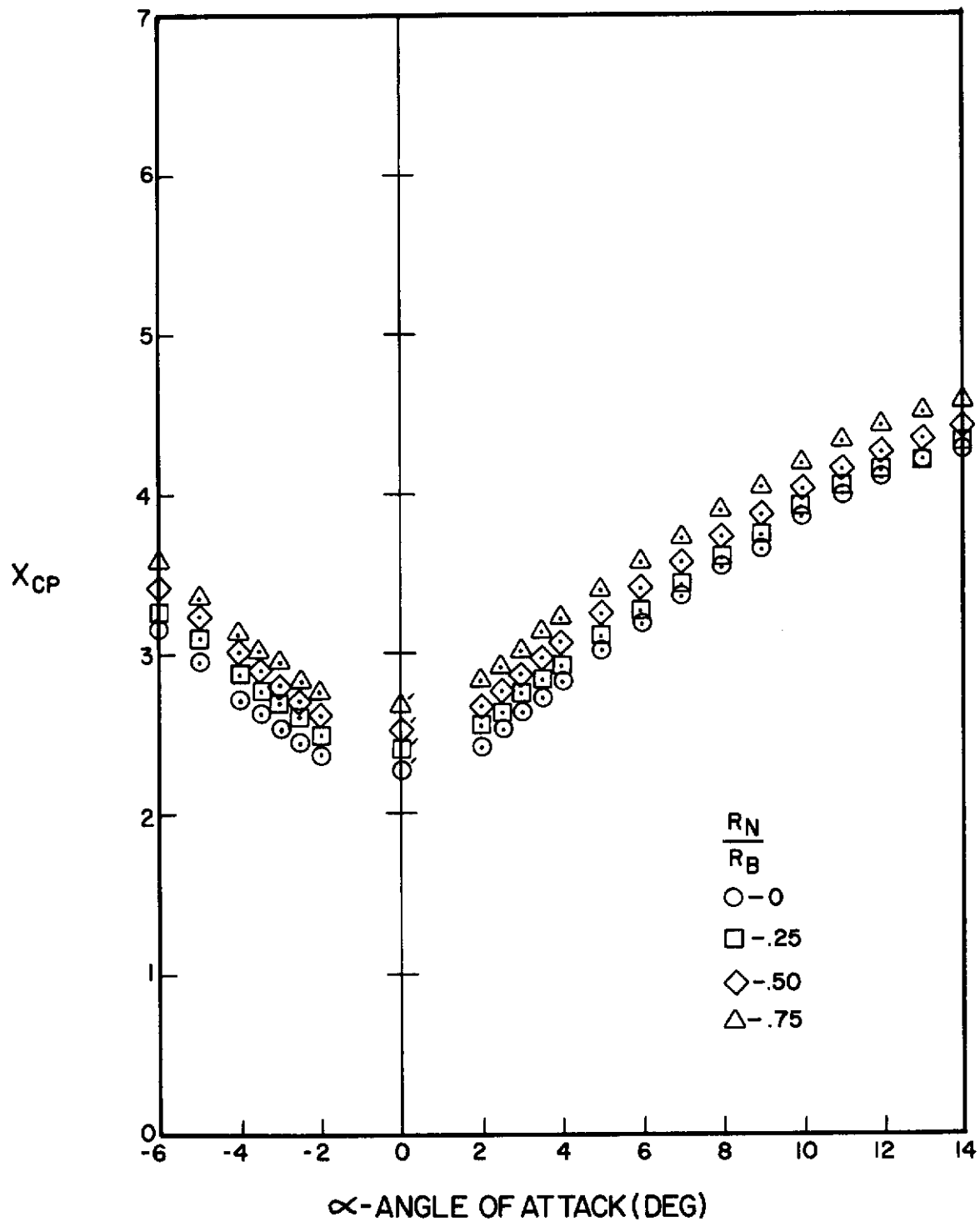


Figure A-125. Center of Pressure Versus Angle of Attack
for $l_N/d = 2$, $l_A/d = 8$, $M = 3.0$

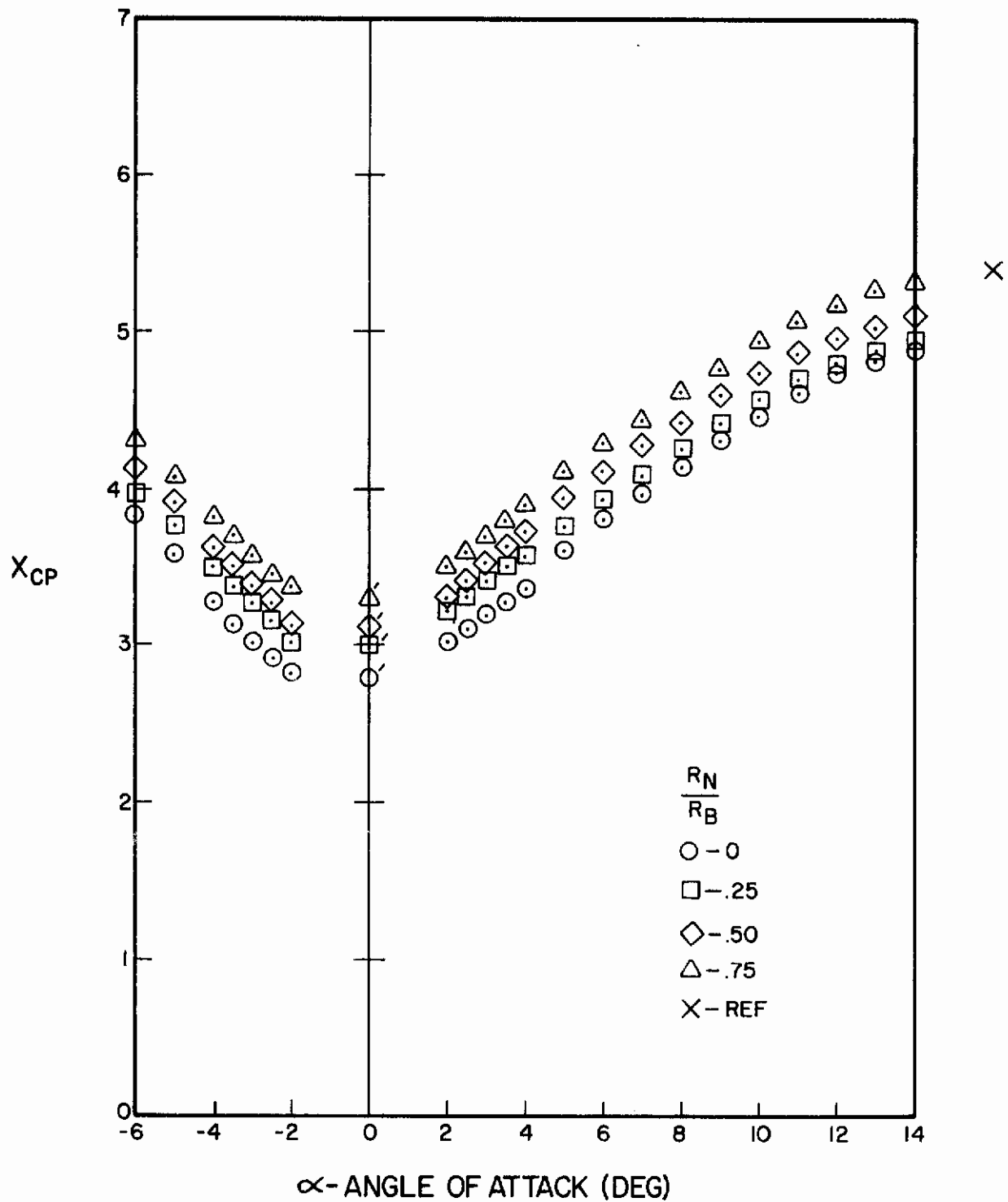


Figure A-126. Center of Pressure Versus Angle of Attack for $l_N/d = 3$, $l_A/d = 8$, $M = 3.0$

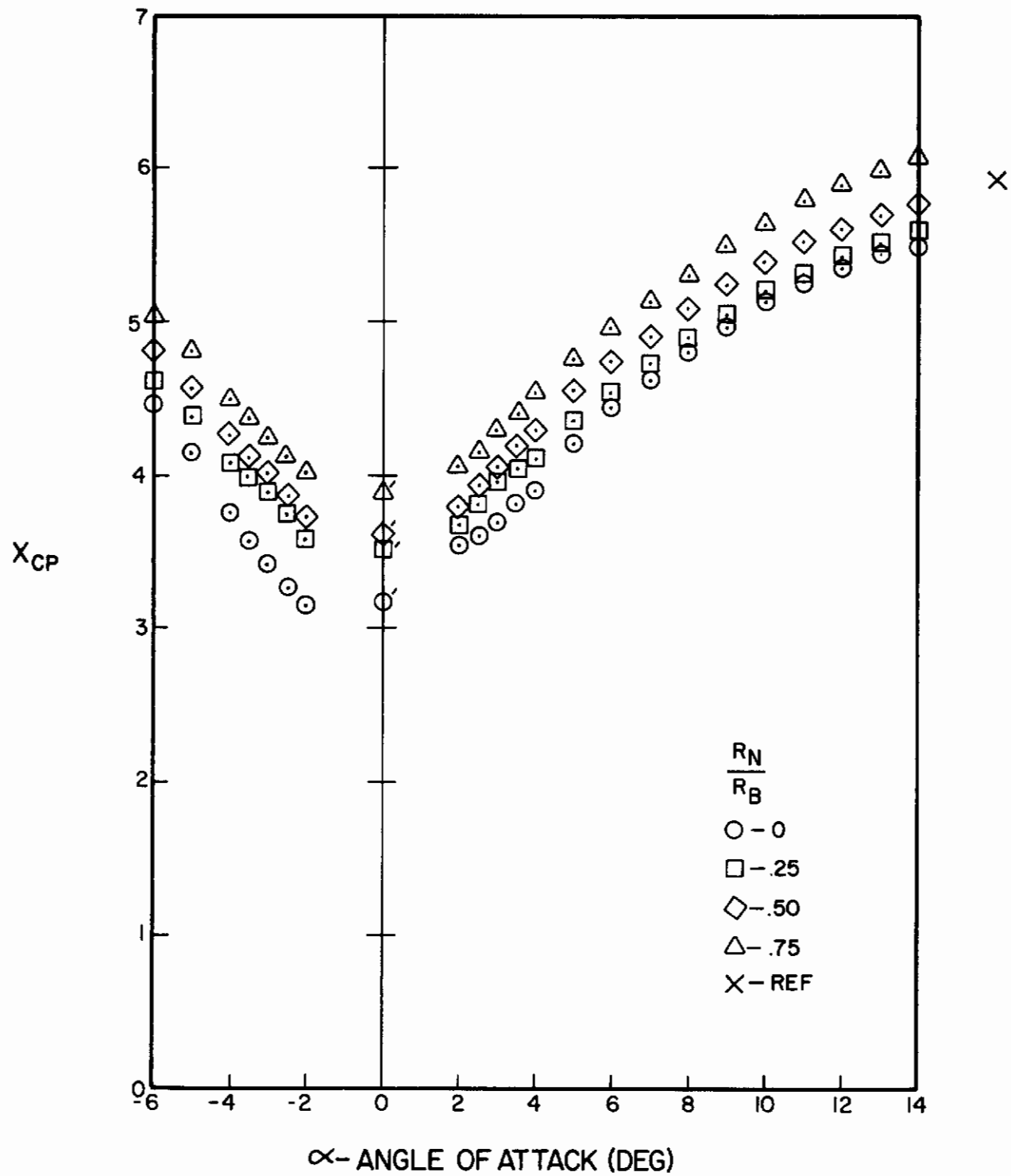


Figure A-127. Center of Pressure Versus Angle of Attack for $l_N/d = 4$, $l_A/d = 8$, $M = 3.0$

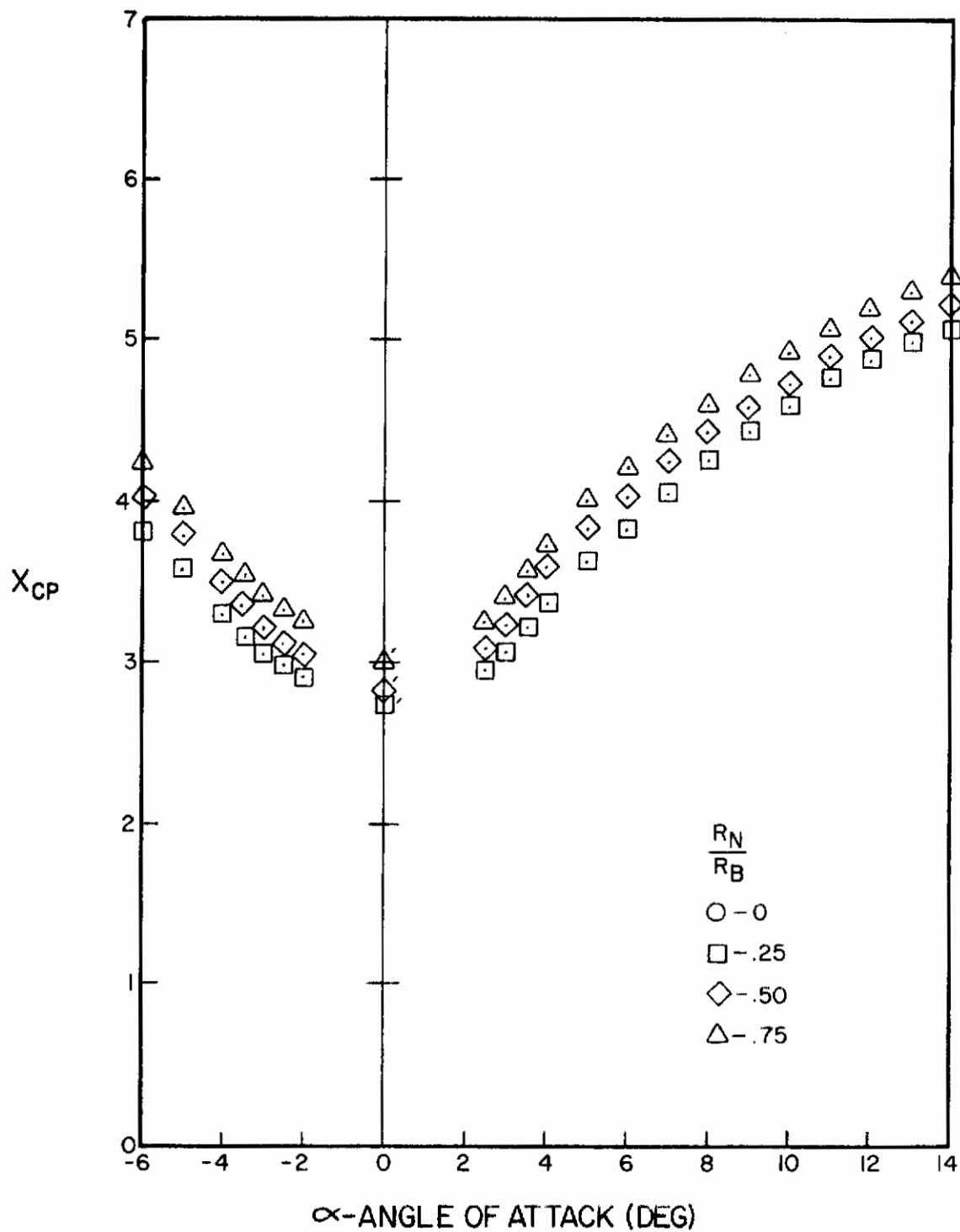


Figure A-128. Center of Pressure Versus Angle of Attack for $l_N/d = 2$, $l_A/d = 10$, $M = 3.0$

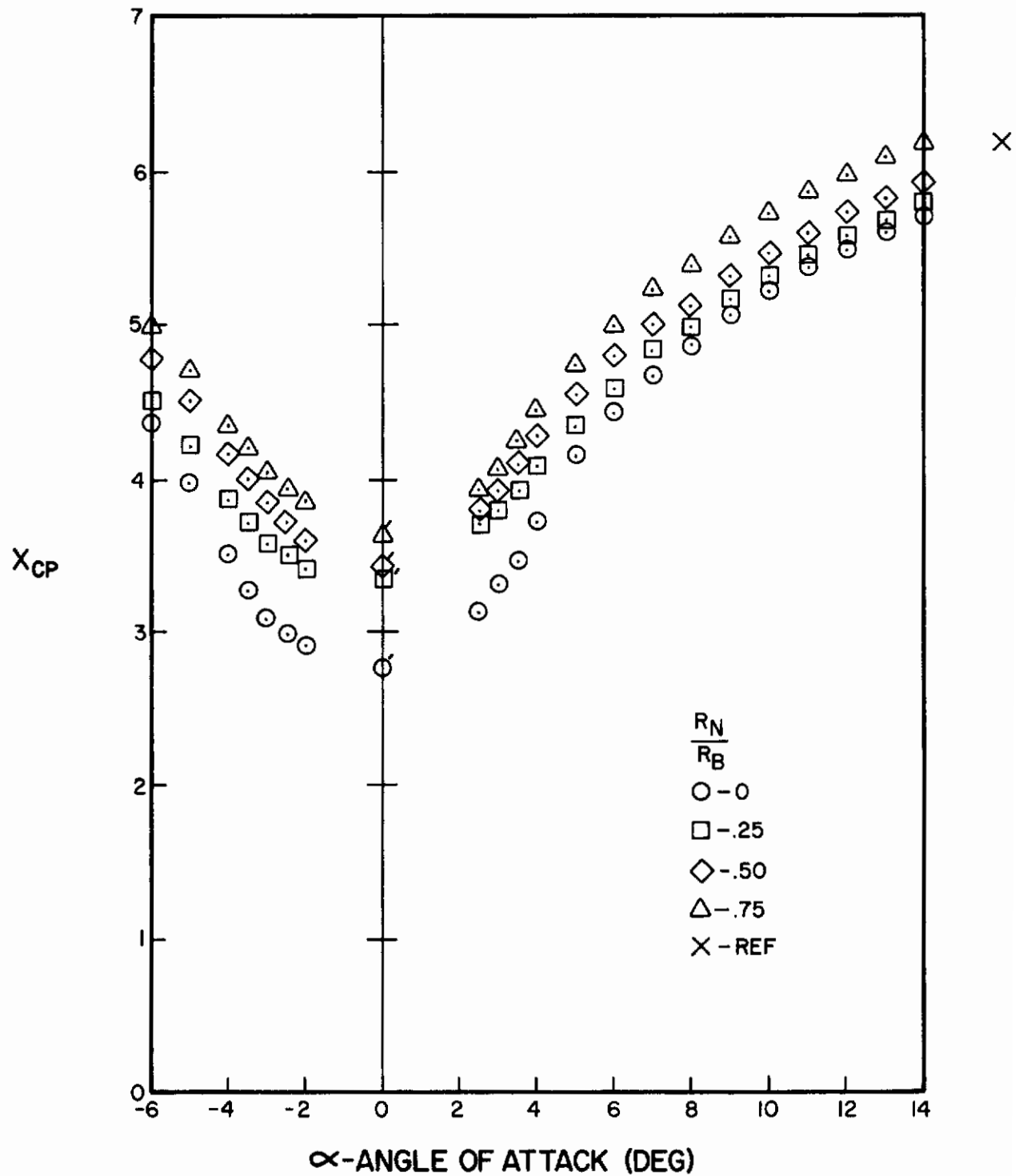


Figure A-129. Center of Pressure Versus Angle of Attack for $l_N/d = 3$, $l_A/d = 10$, $M = 3.0$

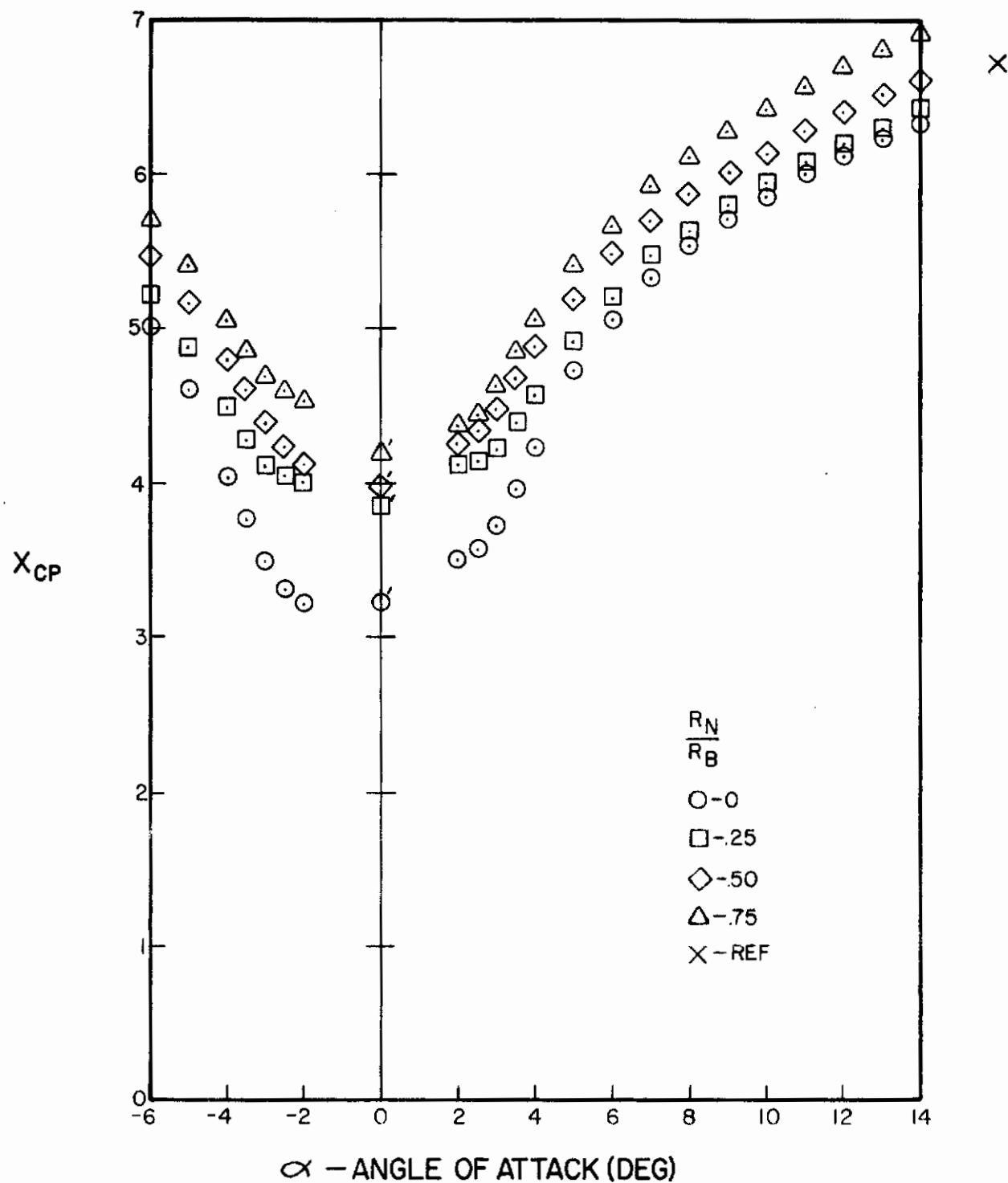


Figure A-130. Center of Pressure Versus Angle of Attack
for $l_N/d = 4$, $l_A/d = 10$, $M = 3.0$

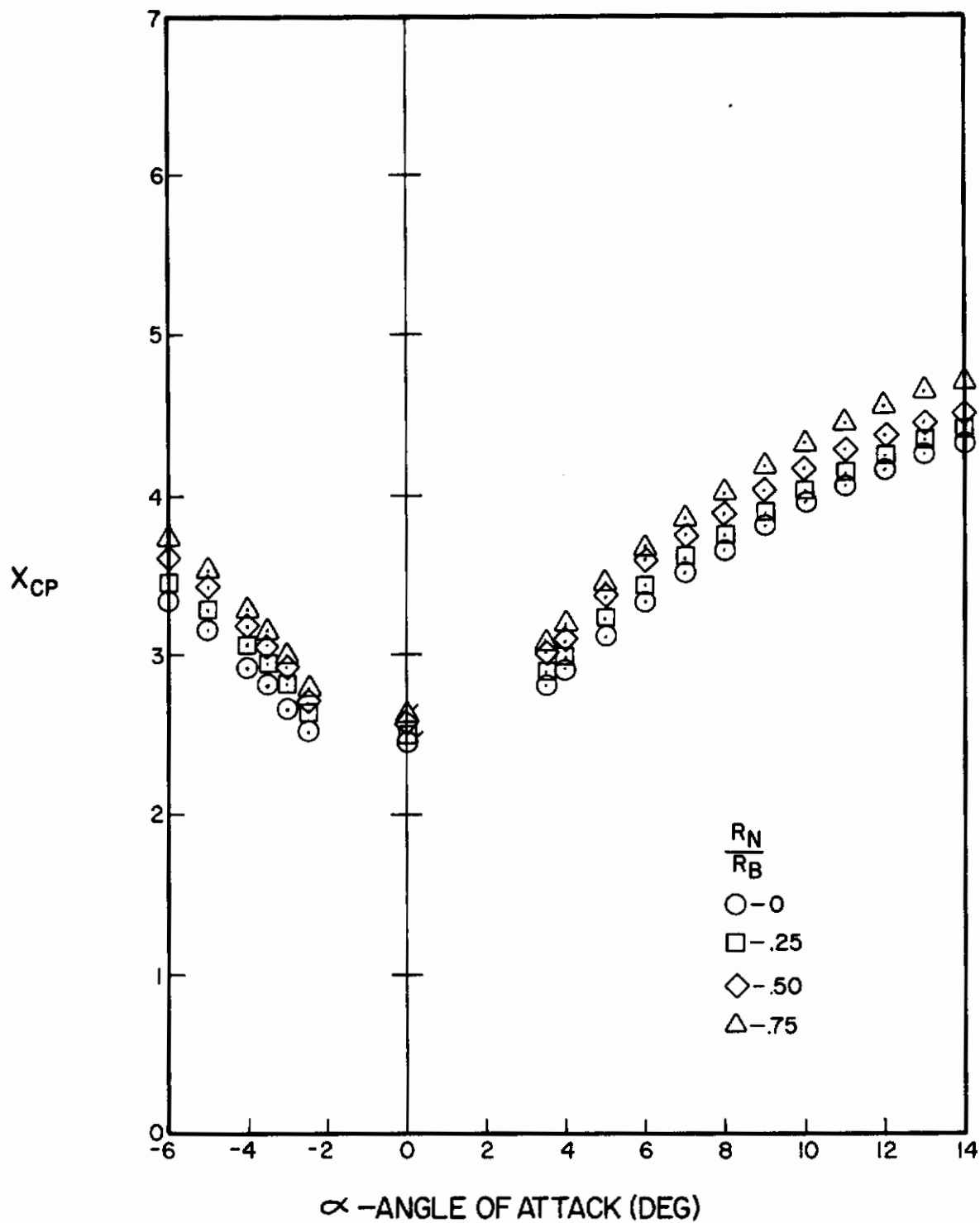


Figure A-131. Center of Pressure Versus Angle of Attack for $l_N/d = 2$, $l_A/d = 8$, $M = 4.0$

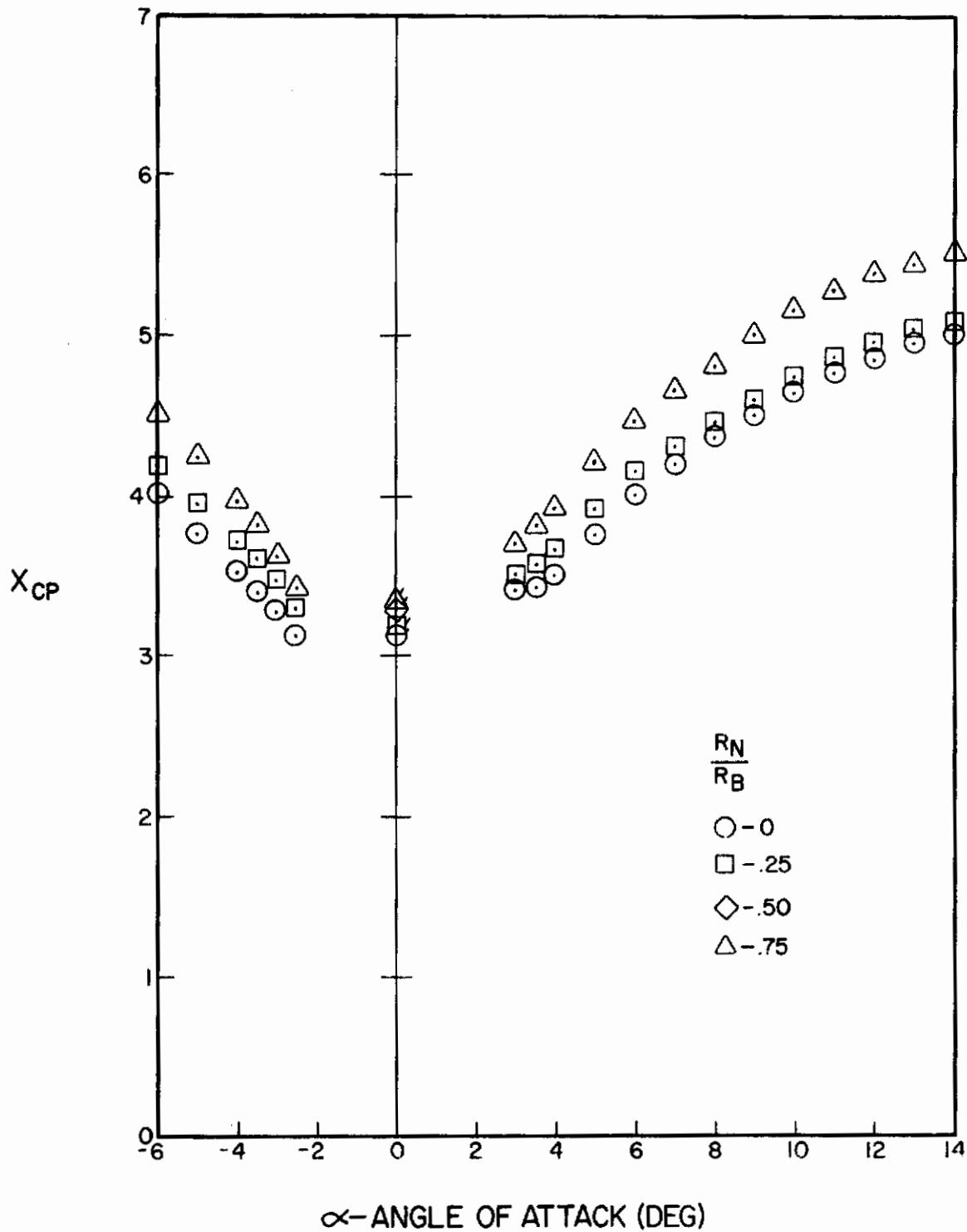


Figure A-132. Center of Pressure Versus Angle of Attack for $l_N/d = 3$, $l_A/d = 8$, $M = 4.0$

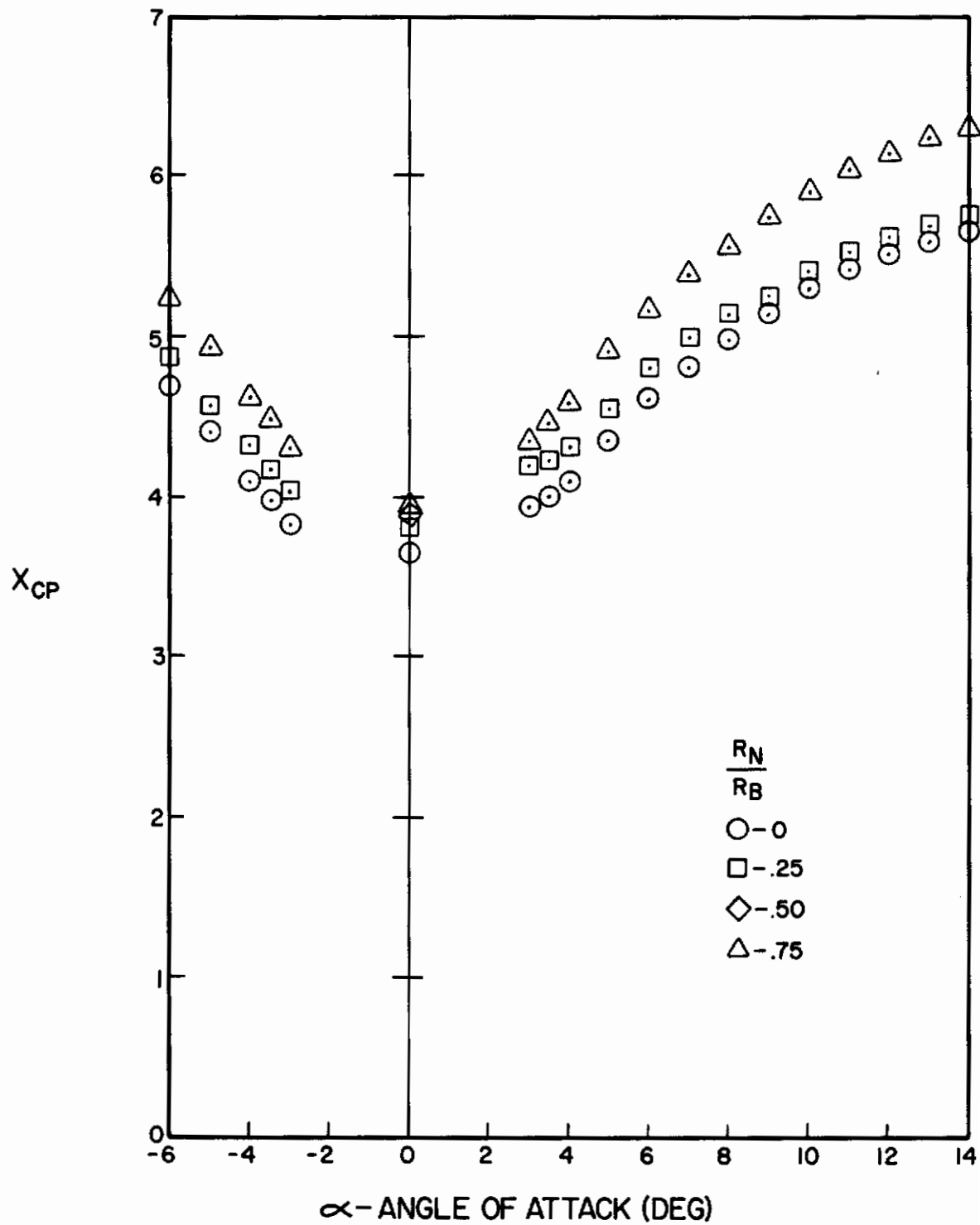


Figure A-133. Center of Pressure Versus Angle of Attack for $l_N/d = 4$, $l_A/d = 8$, $M = 4.0$

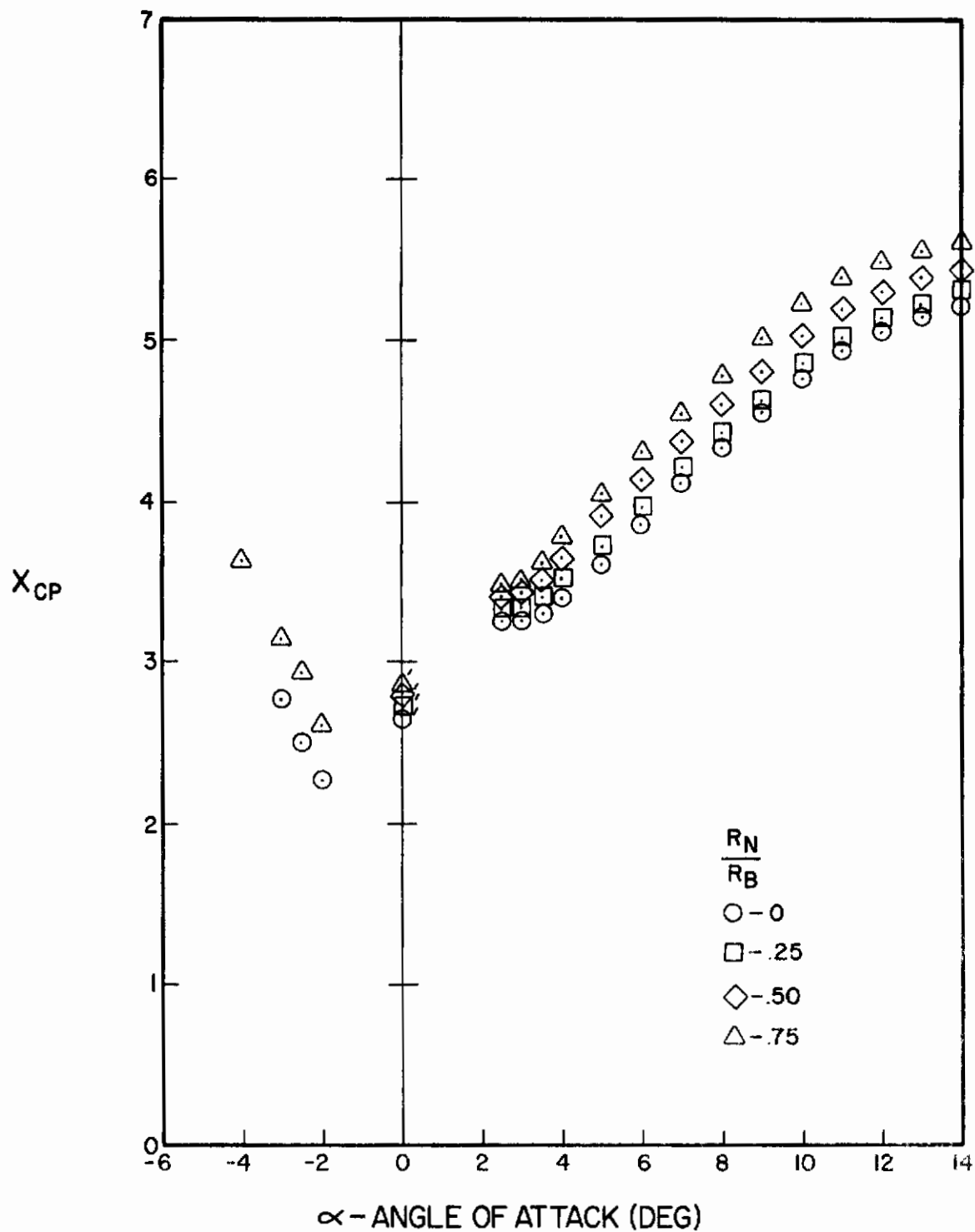


Figure A-134. Center of Pressure Versus Angle of Attack for $l_N/d = 2$, $l_A/d = 10$, $M = 4.0$

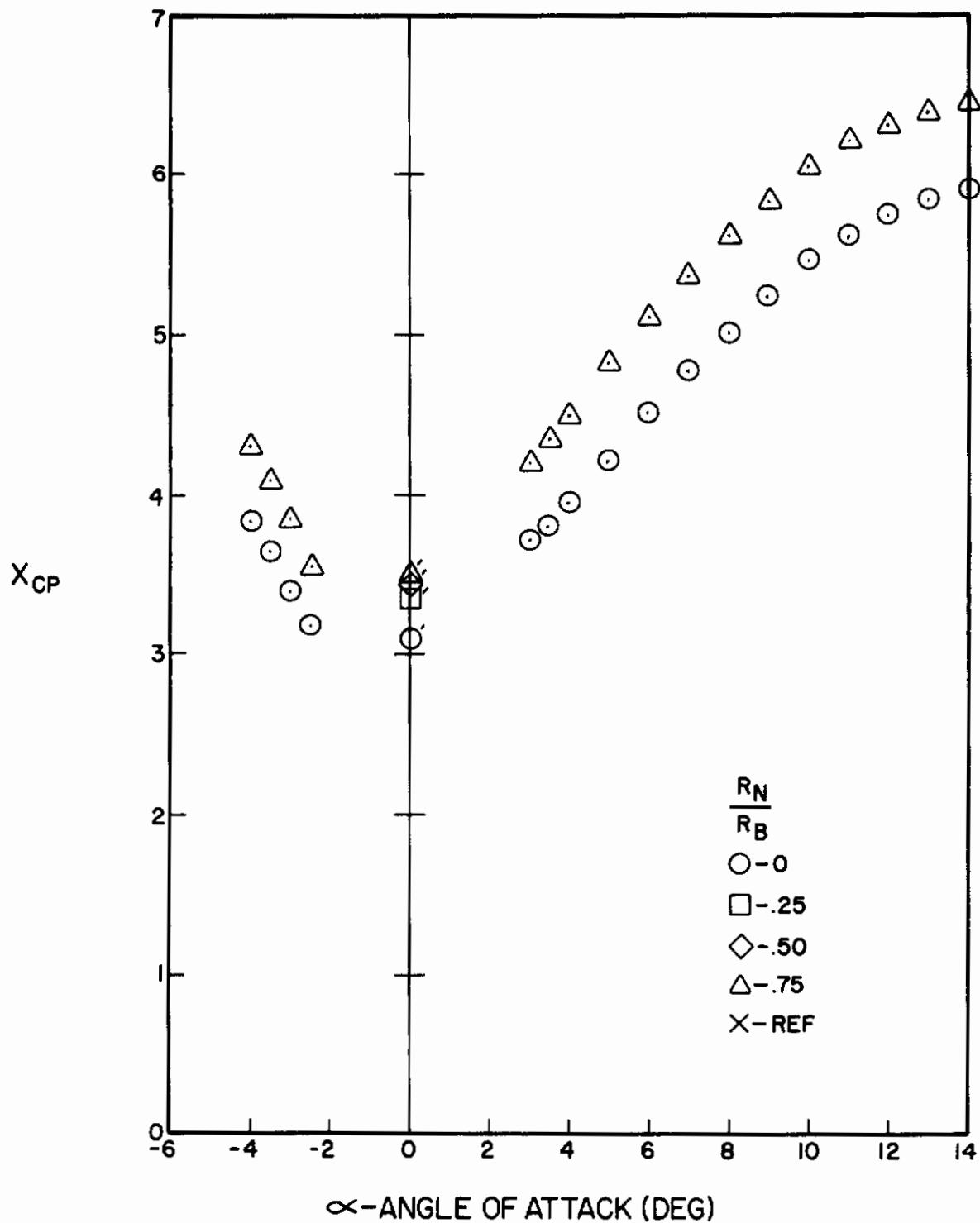


Figure A-135. Center of Pressure Versus Angle of Attack for $l_N/d = 3$, $l_A/d = 10$, $M = 4.0$

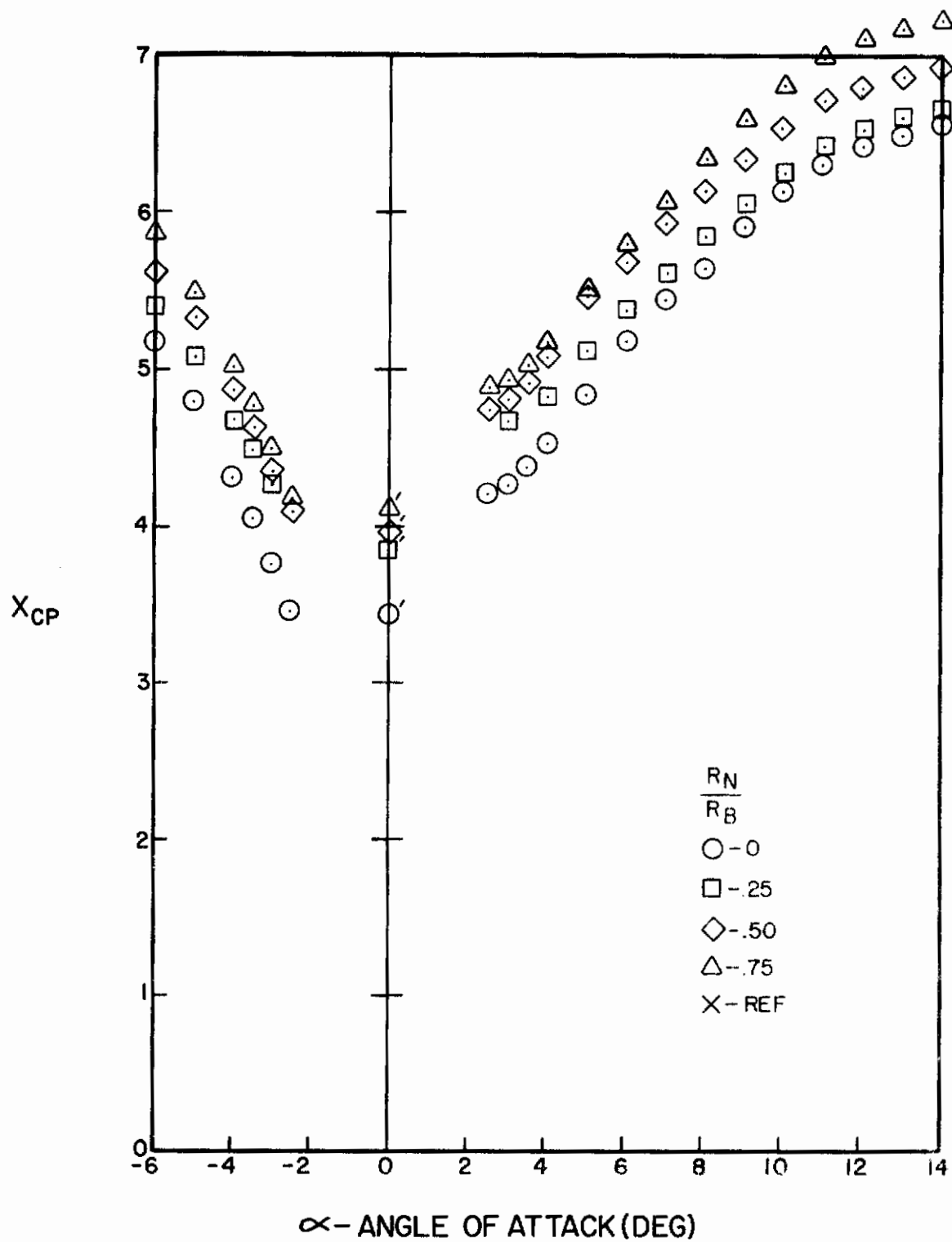


Figure A-136. Center of Pressure Versus Angle of Attack for $\ell_N/d = 4$, $\ell_A/d = 10$, $M = 4.0$

REFERENCES

1. Aiello, G. F. and Bateman, M. C., Aerodynamic Stability Technology for Technology for Maneuverable Missiles, AFFDL-TR-76-55, 1976.
2. Butler, C. B., Sears, E., and Pallas, S. G., Aerodynamic Characteristics of 2, 3, and 4 Caliber Tangent-Ogive Cylinders with Nose Bluntness Ratios of 0.0, 0.25, 0.50, and 0.75 at Mach Numbers from 0.6 - 24.0, AFATL-TR-77-8, Jan 1977.
3. Jernell, L. S., Effects of Nose Bluntness of Aerodynamic Characteristics of Cruciform-Finned Missile Configuration at Mach 1.50 to 2.86, NASA TM X-2031, 1970.
4. Stallings, R. L., Experimentally Determined Local Flow Properties and Drag Coefficients for a Family of Blunt Bodies of Mach Numbers from 2.49 to 4.63, NASA TR R-274, 1967.
5. Jernell, L. S., Aerodynamic Characteristics of Bodies of Revolution at Mach Numbers from 1.50 to 2.86 and Angles of Attack to 180°, NASA TM X-1658, 1968.
6. Jorgensen, L. H., Prediction of Static Aerodynamic Characteristics for Space-Shuttle-Like and Other Bodies at Angles of Attack from 0° to 180°, NASA, TN D-6996, NASA, 1972.
7. Baker, W., Static Aerodynamic Characteristics of a Series of Generalized Slender Bodies with and without Fins at Mach Numbers from 0.6 to 3.0 and Angles of Attack from 0.6 to 3.0 and Angles of Attack from 0 to 180 Degrees, AEDC-TR-75-124, 1976.
8. The USAF Stability and Control Datcom, AFFDL/FGC, October 1960.
9. AFFDL Air Slew at High Alpha, Von Karman Gas Dynamic Facility, ARD, Inc., AEDC, V41A-G3A, January 23, 1976.

Contrails